University of Alberta

Effect of Laminar Shear on the Aggregate Structure of Flocculant-dosed Kaolinite Slurries

by

Farid Vaezi Ghobaeiyeh

A thesis submitted to the Faculty of Graduate Studies and Research
in partial fulfillment of the requirements for the degree of

Doctor of Philosophy
in
Chemical Engineering

Department of Chemical and Materials Engineering

©Farid Vaezi Ghobaeiyeh
Spring 2013
Edmonton, Alberta

Permission is hereby granted to the University of Alberta Libraries to reproduce single copies of this thesis and to lend or sell such copies for private, scholarly or scientific research purposes only. Where the thesis is converted to, or otherwise made available in digital form, the University of Alberta will advise potential users of the thesis of these terms.

The author reserves all other publication and other rights in association with the copyright in the thesis and, except as herein before provided, neither the thesis nor any substantial portion thereof may be printed or otherwise reproduced in any material form whatsoever without the author's prior written permission.

Abstract

The research was conducted to investigate effect of hydrodynamic conditioning on the flocculation of the oil sands fine tailings. The main focus was the effect of shearing on the structure of flocculated aggregates and the extent of reflocculation occurring upon cessation of shearing. An experimental technique was developed based on laminar tube flow. This allowed a more realistic estimation of the shear rate to which an aggregate was exposed, and direct sampling of the aggregate to minimize alteration of the aggregate structure by sampling. A combination of aggregate settling velocity and image analysis was used to determine the aggregate structural parameters, i.e. size, shape, density and fractal dimension.

The laminar flow device was used to investigate the flocculation kinetics and evolution of the aggregate structure. Aggregates were formed by flocculation of kaolinite particles, as model clay, with an anionic flocculant under physicochemical conditions similar to those of oil sands tailings. Detailed statistical analysis showed that a dynamic equilibrium flocculation state was established and the formed aggregate structure was statistically reproducible.

The accuracy of aggregate density and fractal dimension measurements using size and settling velocity data was improved by developing a new non-spherical drag coefficient correlation. The new correlation uses only two dimensional geometrical parameters obtained from image analysis. The correlation is applicable to the study of fluid particle dynamics for any fragile and non-spherical particles, including the type produced during the treatment and dewatering of oil sands tailings.

The flocculated aggregates, with well-defined and reproducible structures, were exposed to a wide range of shear rates for different periods of time. The shearing experiments were performed using the laminar tube flow device. The results showed that shearing reduced aggregate size, increased aggregate density and compacted the structure. Also, shearing ultimately produced aggregates having more spherical shapes. Both the magnitude and duration of shearing were found to be important. The degraded aggregates could reflocculate to some degree upon cessation of shearing. The extent of reflocculation was almost independent of the shearing history and the reflocculated aggregates regained much of their original structural properties (i.e. before shearing) with a slight structural compaction.

The results suggest that the controlled shearing and subsequent reflocculation can improve de-watering and consolidation properties of flocculated fine tailings.

Acknowledgment

This project would not have been completed without the help of a number of people. I would like to express my special thanks and gratitude to my supervisor Dr. Sean Sanders and co supervisor Dr. Jacob Masliyah, for their valuable guidance, support and for providing me with resources and funding to conduct my research. Sean's mentorship was essential in conducting the research and his thorough reviews on the thesis improved the writing of the dissertation significantly.

Special thanks to Ms. Terry Runyon, Ms. Leanne Swekla and Mr. Jim Skwarok for their endless help.

Special thanks to Dr. Yadi Maham for his support and mentorship during my teaching assistantship for ChE 243. My gratitude also extends to the staff of the Department of Chemical and Materials Engineering at the University of Alberta.

Also, the pursuit of my education would not have been possible if were not for the encouragement and support of my family, especially my mother.

Finally, I would like to acknowledge the financial support provided by NSERC through Sean and Jacob's Industrial Research Chairs in Pipeline processes and Oil Sands Engineering programs, respectively.

Table of Contents

Chapter 1 **Introduction** 1

1.1. Background 1

1.2. Research objectives 9

1.3. Thesis outline 12

1.4. References 13

Chapter 2 **Flocculation kinetics and aggregate structure of Kaolinite mixtures** 19

2.1. Introduction 19

2.2. Aggregate structure monitoring 23

2.2.1. Measurement of aggregate density and fractal dimension 24

2.2.2. Primary particle density 25

2.2.3. Internal advective flow correction factor 26

2.2.4. Drag coefficient 28

2.2.5. Aggregate shape factor 29

2.3. Experimental method 29

2.3.1. Materials 29

2.3.2. Apparatus and procedures 30

2.4. Results and discussion 33

2.4.1. Aggregate size evolution 33

2.4.2. Aggregate density evolution 37

2.4.3. Aggregate structure 45

2.5. Summary 49

2.6 Nomenclature 51

2.7 References 53

Chapter 3 **An improved non-spherical drag correlation using a new particle shape factor** 57

3.1. Introduction 57

3.2. Previous studies 59

3.2.1. Size and shape descriptors 59

3.2.2. Drag correlations for non-spherical particles 62

3.3. Equation development 68

3.3.1. Side view-shape descriptors 68

3.3.2. Drag coefficients and Reynolds numbers 69

3.3.3. Data bank 70

3.3.4. Data processing and corrections 71

3.3.5. Regression 77

3.4. Results and discussion 78

3.4.1. Correlation development 78

3.4.2. Performance validation of new correlation 89

3.5. Summary 93

3.6. Nomenclature 95

3.7. References 97

Appendices

Appendix 3.1. Particle shape factors described in this study 101

Appendix 3.2. Stokes’ dynamic shape factors for various non-spherical particles 102

Appendix 3.3. Newton’s dynamic shape factors for various non-spherical particles 104

Appendix 3.4. Drag correlations 105

Chapter 4 **New drag coefficient for non-spherical and fragile objects using two dimensional geometrical data obtained from imaging** 107

4.1. Introduction 107

4.2. Equation development 109

4.2.1. Size and shape descriptors 109

4.2.2. Drag coefficients and Reynolds numbers 111

4.2.3. Dynamic shape factors 113

4.3. Data bank 115

4.3.1. Data processing and corrections 115

4.3.2. Regression 116

4.4. Results and discussion 117

4.4.1. Correlation development 117

4.4.2. Performance validation of new correlation 126

4.5. Summary 131

4.6. Nomenclature 133

4.7. References 134

Appendices

Appendix 4.1. Stokes' dynamic shape factors for various non-spherical particles 138

Appendix 4.2. Newton dynamic shape factors for various non-spherical objects 139

Appendix 4.3. Drag correlations 140

Chapter 5 **Shear degradation and reflocculation of flocculated kaolinite mixtures in laminar tube flow** 141

5.1. Introduction 141

5.1.1. Previous studies 142

5.1.2. Shearing devices 147

5.2. Aggregate structure monitoring 150

5.2.1. Size 150

5.2.2. Shape 150

5.2.3.Measurement of aggregate density and fractal dimension 151
5.2.4. Primary particle density 153
5.2.5. Internal advective flow correction factor 154
5.2.6. Aggregate shape and drag coefficient 154
5.3. Material and method 156
5.3.1. Materials 156
5.3.2. Experimental apparatus 158
5.4. Result and discussion 162
5.4.1. Flocculation of dispersed slurry 162
5.4.2. Shearing Zone 166
5.4.3. Reflocculation zone 186
5.5. Summary 210
5.6. Nomenclature 212
5.7. References 214

Appendices

Appendix 5.1. Details of experimental setup and conditions for shearing and reflocculation tests 221

Chapter 6 **Conclusions and Recommendations** 223

6.1. General summary 223
6.2. Novel contributions 226
6.2.1.An experimental technique to monitor structure of aggregates 226
6.2.2.An improved drag correlation for non-spherical particles 227
6.2.3.A novel drag coefficient correlation for fragile non-spherical objects 228
6.2.4. Improved determination of a complete set of aggregate structural parameters 228
6.3. Key findings 230
6.4. Industrial implications 231
6.5. Uncertainties and challenges 232
6.6. Recommendations for future studies 234
6.7. References 235

List of Tables

Table 2.1 F-test and T-test results of aggregate size data for flocculation times $60 \leq t \leq 147$ s 35

Table 2.2 ANOVA test results for comparison of aggregate mean diameters 36

Table 2.3 F-tests and T-tests for aggregate density for $8 \leq t \leq 147$ s 44

Table 2.4 ANOVA results for comparison of aggregate mean effective density 45

Table 2.5 Mass fractal dimension of aggregates for different flocculation times 49

Table 3.1 Summary of data used in this study 71

Table 3.2 Wall effect correction 74

Table 3.3 Comparison of calculated K_{St_V} in this study and values reported in the literature 76

Table 3.4 Comparison of correlations predicting Stokes' dynamic shape factor, N=69 79

Table 3.5 Comparison of correlations predicting Newton's dynamic shape factor 81

Table 3.6 Shape-specific constants and overall constants of Eq. (3.30) 83

Table 3.7 Correlation performance with shape-specific constants for the data used to develop correlation 84

Table 3.8 Correlation performance for the data used to develop correlation. Overall constant used for all shapes, N=702 87

Table 3.9 Comparison of correlation performance in predicting the 702 data points 88

Table 3.10 Correlation performance for the data used to validate the new correlation, N=1080 90

Table 3.11 Summary of statistical analysis comparison of drag coefficient correlations, N=1782 91

Table 4.1 Summary of data used in this study (see Chapter 3) 116

Table 4.2 Comparison of the correlations predicting Stokes' dynamic shape factors. 119

Table 4.3 Comparison of the correlations predicting Newton's dynamic shape factors, N=37 120

Table 4.4 Correlation performance for the data used to develop correlation. Overall constants used for all shapes, N = 702 124

Table 4.5 Comparison of correlations performance in predicting 702 data points 125

Table 4.6 Summary of detailed statistical analysis of correlation performance for the data used to validate the new correlation, N =1080 128

Table 4.7 Summary of statistical analysis comparison of drag coefficient correlations, N=1782 129

Table 5.1 Structural properties of aggregates formed in the flocculation zone 164

Table 5.2 Fractal dimension, D_{F_F}, of flocculated suspension 165

Table 5.3 Fractal dimension of aggregates in shearing and reflocculation zones 206

List of Figures

Fig. 2.1 Scheme of two-stage aggregation process. (1). Destabilization of dispersed particle through a coagulation step, (2). Aggregation of primary flocs using a polymer flocculant 25

Fig. 2.2 Experimental set-up for flocculation tests in laminar tube flocculator 32

Fig. 2.3 Evolution of aggregate size with flocculation time 34

Fig. 2.4 Effect of flocculation time on aggregate mean diameter 37

Fig. 2.5 Aggregate settling velocity data for two different flocculation times 39

Fig. 2.6 Aggregate Re number as a function of aggregate size for flocculation times of 8s and 147s 39

Fig.2.7 Relationship between aggregate size and (a) aggregate porosity, and (b) aggregate effective. Data are shown for flocculation times of 8 and 147 s 40

Fig. 2.8 Evolution of aggregate effective density with flocculation time 42

Fig. 2.9 Harmonic average of aggregate effective density 43

Fig. 2.10 Calculation of mass fractal dimension of aggregates. Lines represent best fit for each of the two flocculation times 46

Fig. 2.11 Effect of flocculation time on the aggregate fractal dimension 48

Fig. 3.1 Wall effect correction of the low Reynolds number data to determine Stokes' dynamic shape factors. Data from Pettyjohn et al. [7] 75

Fig. 3.2 Regression result for the volumetric Stokes' shape factor data correlated with degree of roundness, ϕ. N=69 points; 11 particles shapes 79

Fig. 3.3 Regression result for the volumetric Newton's dynamic shape factor data correlated with degree of roundness, ϕ. N = 37 points; 12 particles shapes 81

Fig. 3.4 Normalized drag coefficient data along with Eqs. (3.31), (3.32) and Ganser correlation (Eq. 3.10) 85

Fig. 3.5 Cumulative distribution of relative error for four drag correlations 92

Fig. 4.1 Scheme of particle projections on different planes 111

Fig. 4.2 Regression result for the side view-Stokes' shape factor data correlated with degree of roundness, ϕ, N = 30 points, 9 particles' shapes 118

Fig. 4.3 Regression result for the side view-Newton's shape factor data correlated with degree of roundness, ϕ. N = 37 points; 12 particles shapes 120

Fig. 4.4 Experimental normalized drag coefficient data along with Eqs. (4.28), (4.29) and Ganser correlation (Eq. 4.12) 122

Fig. 4.5 Cumulative distribution of absolute relative error for four correlations 130

Fig. 5.1 Experimental set-up for shearing and reflocculation experiment 159

Fig. 5.2 Aggregate (a) size and (b) density cumulative distribution for seven flocculation runs at similar conditions to prove reproducibility of flocculation process 163

Fig. 5.3 Change in aggregate size with shear rate at shearing time of (a) τ_S = 60 s, (b) τ_S = 120 s (c) τ_S = 15 s, (d) τ_S = 30 s 168

Fig. 5.4 Effect of shear rate and shearing time on aggregate mean diameter at constant (a) shearing time and (b) constant shear rate 172

Fig. 5.5 Strength factor at four different shearing times of 15 to 120s 173

Fig 5.6 Effect of shear rate and shearing time on degree of roundness (a) τ_S = 60 s, (b) τ_S = 120 s, (c) τ_S = 15 s and (d) τ_S = 30 s 175

Fig. 5.7 Effect of shear rate and shearing time on mean degree of roundness 177

Fig. 5.8 Effect of shear rate and shearing time on aggregate density distribution at (a) τ_S = 60 s, (b) τ_S = 120 s, (c) τ_S = 15 s and (d) τ_S = 30 s 180

Fig. 5.9 Changes in harmonic average effective density after shearing for different shearing times 183

Fig. 5.10 Changes in fractal dimension with shear rate and shearing time 185

Fig. 5.11 Fractal dimension ratio D_{F_S}/D_{F_F} 186

Fig. 5.12 Change in aggregate size distribution upon shearing followed by reflocculation at (a) τ_S = 60 s and $\bar{\gamma}_S$ = 224 s^{-1}, (b) τ_S = 60 s and $\bar{\gamma}_S$ = 411 s^{-1}, (c) τ_S = 60 s and $\bar{\gamma}_S$ = 1331 s^{-1}, (d) τ_S = 15 s and $\bar{\gamma}_S$ = 1348 s^{-1} 188

Fig. 5.13 Change in aggregate Sauter mean diameter, d_{32}, upon shearing followed by reflocculation at shearing times of (a) τ_S = 15 s, (b) τ_S = 30 s, (c) τ_S = 60 s and (d) τ_S = 120 s 191

Fig. 5.14 Degree of reflocculation for different shearing times of τ_S = 15, 30, 60, 120 s 193

Fig. 5.15 Change in cumulative distributions of degree of roundness upon shearing followed by reflocculation at three different shearing condition of (a) τ_S = 15 s, $\bar{\gamma}_S$ = 1348 s^{-1}, (b) τ_S = 30 s, $\bar{\gamma}_S$ = 1379 s^{-1} (c) τ_S = 60 s, $\bar{\gamma}_S$ = 1331 s^{-1} and (d) τ_S = 120 s, $\bar{\gamma}_S$ = 450s^{-1} 195

Fig. 5.16 Change in the average degree of roundness after flocculation, shearing and reflocculation at different shearing times of (a) τ_S = 15 s, (b) τ_S = 30 s, (c) τ_S = 60 s and (d) τ_S = 120 s 198

Fig. 5.17 Change in cumulative distributions of aggregate effective density after flocculation, shearing and reflocculation at four different shearing condition of (a) τ_S = 15 s, $\bar{\gamma}_S$ = 1348 s^{-1}, (b) τ_S = 30 s, $\bar{\gamma}_S$ = 1379 s^{-1} and (c) τ_S = 60 s, $\bar{\gamma}_S$ = 1331 s^{-1} and (d) τ_S = 120 s, $\bar{\gamma}_S$ = 450 s^{-1} 201

Fig. 5.18 Changes in the harmonic mean effective density after flocculation shearing and reflocculation at different shearing times of (a) τ_S = 15 s, (b) τ_S = 30 s, (c) τ_S = 60 s and (d) τ_S = 120s 204

Fig. 5.19 Changes in fractal dimension after flocculation, shearing and reflocculation at different shearing times of (a) τ_S = 15s, (b) τ_S = 30s, (c) τ_S = 60 s and (d) τ_S = 120 s 207

Chapter 1
Introduction

1.1.Background

Oil and gas have been the major source of energy powering the world economy for more than a century. They will likely continue to do so for at least the present century. The global demand for oil is expected to increase by 17% from 84 million barrels per day (mbd) in 2009 to predicted 99 mbd in 2035 [1]. However, conventional crude oil production will reach to an approximate plateau of around 68-69 mbd by 2020, with rising production of natural gas liquids and unconventional oil offsetting a decline in conventional crude oil production [1]. Therefore, unconventional oil sources, such as extra heavy oil and oil sands, play an increasingly important role in world oil supply and there has been a growing interest therein [1].

The production of unconventional oil will rise from 2.3 mbd in 2009 to 9.5 mbd in 2035, and will meet about 10% of world oil demand by 2035, compared with less than 3% today [1]. Canadian oil sands production makes an important contribution to the world energy supply, climbing from about 1.5 mbd in 2010 to predicted 4.2 mbd in 2035 [1,2]. Although oil sands reserves are estimated to be several times larger than conventional oil resources, production is expensive as well as technologically and environmentally challenging [1]. Major challenges in the oil sands industry (compared to conventional oil production) include: higher greenhouse gas emission, water consumption and wastewater accumulation [1,3]. Water plays a critical role in the development of oil sands industry in mineable operations. Other than water consumption in utilities to generate steam, cooling water and hydrogen in upgraders, water is mainly used as an extraction agent to separate bitumen from oil sands. It is estimated that about 10 to 15 barrels of process water is required to produce 1 barrel of bitumen. A significant portion of process water (>80%) is recycled within the extraction plant so on average 2-3 barrels of fresh water make-up for every barrel of bitumen is required [3,4]. In 2010, 85% (around 130 million m^3) of the fresh water intake was supplied from the Athabasca River and was consumed by the four present oil sands operators, CNRL, Shell Canada, Suncor and Syncrude. This intake represents only for 0.6% of average river flow and less than 3% of the lowest winter flow in 2010 [3,4]. The water demand on the Athabasca River will rise with increasing bitumen production. Although growing water demand from the river complicates future expansions, the major challenge is the accumulation of wastewater within the boundaries of mine sites. Such accumulation takes place in the tailings ponds, which are large engineered dam and dyke systems designed to contain the contaminated water and also serve as settling basins enabling water to be separated and recycled [3,4].

Tailing ponds contain contaminated water, sand, fine clays, silts, residual bitumen and other by-products of the oil sands mining and extraction process [4-6]. The fast-settling sand particles segregate from the tailings upon deposition at the edge of the ponds while the fine fraction accumulates as a form of sludge toward the bottom of the tailings ponds. The size and surface electric potential of fine clay particles cause difficulties in separating them from water by a simple settling method [4,6]. The slow-settling fine particle sludge settles only to about 30 wt% solids content after a few years of placement and it is normally referred as mature fine tailings (MFT) [2-7]. Oil sands operators recycle around 80-90% of process water; however, under a zero discharge policy from the tailing ponds, the tailing ponds water inventory increases with time [3,7,8]. The accumulation rate of MFT volume is 20% more than the excavation rate of oil sands from the mine [4]. This accumulation has led to the construction of 176 km^2 of tailing ponds as of 2010 that contain a total MFT volume of 830 million m^3 for all the tailings ponds in the minable area [4-6,8,9]. The MFT inventory is forecasted to reach one billion m^3 in 2014 and about two billion m^3 in 2034 [10].

The growing volume of the tailings ponds requires safe containment, vigilant management and environmentally safe treatment of the fine solids suspension. Tailings ponds are one of the most important challenges and liabilities for the oil sands industry. Moreover, failure of a containment structure or long term leakage to underground water resources would lead to a disaster [2-6]. The tailings ponds challenge has become even more serious after recent introduction of legislation to minimize the environmental impacts. In 2009, Energy Resources Conservation Board (ERCB) of Alberta released Directive 74: “Tailings Performance Criteria and Requirements for Oil Sands Mining Schemes”. This regulation is concerned with tailings management plans to minimize and eventually eliminate long-term storage of fine clay tailings as well as to dewater and render trafficable deposits within five years of generation [11]. Directive 74 obliges minable oil sands companies to reduce fine particles accumulation in tailings and maximize the water recycle. This regulation holds oil sands companies accountable for tailings management in the present and future operations. Mines are subject to shut down and developments are not permitted, if the operators fail to meet the objectives of the directive [11].

The main objective of tailings treatment is to increase water recovery from tailings and remove water so that a trafficable surface and subsequent reclamation can be established within a reasonable timeline [3]. Over the past 40 years, oil sands companies have conducted research to find a robust solution to dispose of the oil sand tailings safely and minimize land disturbance. A recent review has identified 34 process/technology options for tailings treatment in seven major groups: permanent storage, gravity sedimentation, chemical dewatering, mechanical dewatering, thermal drying, biological treatment and combination thereof [5]. Only a few options have been used at the commercial scale and/or have been commercially demonstrated, including gravity sedimentation, composite/consolidated tailings (CT) and thickened tailings (TT) technology [4-6,12].

The gravity sedimentation process is the simplest technology in which tailings are pumped directly to a disposal area and dewatering occurs by gravity settling while the supernatant is recycled to the extraction plant. This process has been relied upon in the oil sands industry over last 40 years. However, it needs vast surface area, has primarily caused the present MFT problem and does not meet the Directive 74 mandates [5-8,12-15].

Two oil sands operators, Suncor and Syncrude, have been using the composite/consolidated tailings (CT) technology at the commercial scale [5,6,16-18]. The CT technology consists of two simultaneous steps: coagulation of previously formed MFT using an inorganic coagulant, typically gypsum, and addition of coarse sand tailings in a controlled condition to induce non-segregating tailings. The coarse sands' weight provides additional force for further densification of the fine sludge, promoting further dewatering and solid-like deposits [4-6,15,17,18]. The CT technology reduces the accumulation of mature fine tailings (MFT) but produces newer MFT and it needs large amounts of additional resources of sands to treat the legacy MFT [5,6,17]. The recycled process water contains a high concentration of calcium ions that has negative impact on the extraction process and causes scaling in pipes and process equipment [4,19]. The CT technology has low energy recovery efficiency and requires a well-controlled operation to minimize inconsistency in making deposits with required specifications [4-6,17].

In the last three decades, extensive research has been conducted to apply flocculation processes in the oil sand fine tailings. This process is sometimes referred as "Fine Paste Technique" or "Thickened Tailings" (TT) process [4,7,17,20-23]. In this proposed method, the run-off stream from coarse tails settling and other fresh fine tailings are fed into a thickener. Polymeric flocculant is added to the slurry for rapid settling of fines. Warm water from the thickener overflow is recycled to the extraction plant. The flocculated sediment (thickener underflow or paste) has a solid content at least 25-30 wt. %, which is pipelined to the mined-out pit or a containment area. The paste is allowed to consolidate through gravity drainage and surface desiccation. After a period of time, a layer of coarse tails can be placed on top of the deposit and this load enhances paste consolidation. Finally, the containment are can be reclaimed as dry land [4-7,12,13,22,23]. This technique would eliminate MFT storage ponds, make warm water available for recycle, which reduces energy costs and greenhouse gas emissions, reduces disturbed land areas and allows for accelerated land reclamation [4,17]. Unlike CT technology, the flocculation process has a negligible effect on the chemistry of the recycled water [4,9].

In a different approach and similar to CT technology, combined TT process and coarse sands addition has potential applications as non-segregating tailings [4-6,17,24,25]. Three oil sand operators, Shell Canada, Suncor and Syncrude, have conducted pilot and large-scale demonstrations of TT (and similar alternatives with sand addition) as a viable technology [5,16,17,26-28]. Shell has implemented this technology at commercial scale[5,17,24].

A similar process, developed by Suncor, uses in-line flocculation for fine tailings treatment [29,30]. The flocculation performance of fine tailings is affected by various parameters including flocculant properties and dosage, mineralogy of the solids, water chemistry of the fine slurry and hydrodynamic conditions of the flocculation process and the subsequent paste handling and transportation methods [4,22,23,26-28]. At present, the composite deposits formed by non-segregating flocculated tailings do not seem to meet the geotechnical standards [4,5]. Therefore, application of flocculation process to produce non-segregating tailings continues to be an important area of study [4,5].

The thickened paste contains large, tenuous and porous aggregates [22,23,26,27]. The physical characteristics of the thickened mixtures are affected by changes in aggregate structure, which in turn depend on the physical and chemical conditions during and after flocculation [20-23,26,27]. One of the sensitive and very important characteristics of a flocculated suspension is its rheological behavior, which affects transportation and disposal of the thickened tailings. The rheological behaviour of concentrated flocculated clay suspensions is strongly controlled by the degree of flocculation, water chemistry and clay surface physico-chemical properties. Flocculated slurries exhibit non-Newtonian fluid behavior where time-dependency and shear-thinning phenomena are common [31-35].

Nguyen and Boger [34] review rheology as applied to tailings dewatering, pipeline transport and consolidation problems. Boger et al. [35] discuss the importance of having a thorough understanding of the rheological characteristics of the thickener underflow, along with the need for rheological studies for the proper design and optimized operation of thickeners, optimum conditions for pipeline transport, disposal method and depositional requirements. Measurements of rheological parameters of a thickener underflow paste are used to predict and/or control dewatering performance and to assess flocculation behavior of clay mineral dispersions. Rheological parameters (such as viscoelastic and yield behavior) can be correlated with the networking size and density of aggregate structures within the paste [33,36,37]. Herrington et al. [38] attempted to link rheological properties of flocculated kaolinite to differences in the aggregate structure. Schaan et al. [39] observed that the rheological behavior of the flocculated kaolinite slurries (used as a model for oil sands fine tailings) changed permanently upon shearing, with no subsequent recovery with time, or upon cessation of shearing. McFarlane et al. [36,37] found that shearing changed the rheology of a flocculated kaolinite slurry and controlled shearing modified the interfacial chemistry and particle interaction to improve consolidation properties of thickened tailings. Watson et al. [40] studied rheological characteristic of flocculated MFT, floc breakage and reflocculation upon shearing and observed an improvement in dewatering properties under a controlled hydrodynamic conditioning. Therefore, it can be concluded that the rheological behavior of the thickened tailings during and after flocculation depends on the hydrodynamic conditions to which the mixture is exposed. In addition, these studies imply that there is likely a correlation between the rheological properties of a flocculated slurry, aggregate-aggregate interactions in the slurry and the structure of individual aggregates. Michaels and Bolger [41] developed a structural model for the aggregate network and correlated the rheological characteristics of a coagulated kaolin suspension with aggregate size, concentration as well as inter-aggregate interactions in the network.

The fact that shearing affects the rheological behavior of these slurries indicates the sensitivity of aggregate structure to shear [33,37,41]. In other words, shearing can change the behavior of flocculated mixtures because of changes in the aggregate structure. Consequent changes in rheological behavior can then cause serious challenges in the pipeline transport of the mixtures from the thickener underflow to the disposal site, and to the geotechnical stability of the reclaimed land [32,34,35].

Physical characteristics (including rheological characteristics) at the thickener underflow outlet are normally used in the design and control thickeners and the downstream transport pipeline [42-44]. However, the deposition pit for the thickened slurry is typically located few kilometers away from the thickener. The thickened slurry delivered to the pit has rheological characteristics very different from those measured at the thickener underflow sampling point because of the shearing done by pumps and during the pipeline transport of the mixture. This causes serious challenges in design and operation of the pipeline and the prediction of the depositional behavior of the mixture as well [35,39,44]. In a rational design approach, physical and rheological properties of the thickened slurry required for final deposition site are considered as the input design data. The design sequence begins at the disposal point and works backward to the thickening stage. This approach involves specification of the rheological requirements for pipeline transport and then the requirements for the material produced by the thickener [35,45]. Therefore, rheological behavior (in terms of response to shearing and compression) during placement at the deposition site, for pipeline transport and for thickening is required for an environmentally and economically feasible tailings disposal system.

As discussed above, a thorough understanding of changes in the rheological characteristics of thickened slurries caused by shearing is very important for the design and optimal operation of thickeners, the pump and pipeline system and the final properties of the deposit. In order to acquire such a thorough understanding, three major steps are required: (a) Shear and compressional rheology measurements, followed by interpretation and predictions of flow properties; (b) Development of the understanding of the relationship between macroscopic rheological behavior and microscopic properties, i.e. aggregate structure of the flocculated suspension; and (c) Relate the microscopic response of flocculated aggregate structure to macroscopic changes in hydrodynamic conditions of the suspension. The present research deals with the third step in an attempt to provide a fundamental understanding of the effect of shearing on the flocculated aggregate structure.

Fundamental studies using actual fine tailings samples are extremely challenging due to constituents' diversity, complexity of interactions among constituents and compositional variations in different sites. Major constituents of oil sands fine tailings are minerals such as kaolinite, illite, smectites, quartz, muscovite, feldspar, chlorite, dolomite allophanes, halloysite, siderite, some metallic oxide compounds, residual bitumen and solid organic matters [4,46,47]. Studies show that the clays in fine tailings can be classified to different fractions (at least three) with distinctly different physical and surface properties [48]. There are some indications of significant interaction among the kaolinite and illite through inter-stratification and clay surface interactions with metallic compounds [48,49]. An additional complicating factor is a significant physical or chemical adsorption of organic materials onto the surface of clay particles [50].

Clays often interact with various compounds within fine tailings, which can interfere with the flocculation process. A model clay system can be used to investigate flocculation mechanisms and structural response to changes in hydrodynamic changes. To avoid difficulties associated with studying a system as complex as oil sand fine tailings, we examine a simpler model system possessing key characteristics that are similar to the actual tailings. The model system chosen for this study consists of kaolinite suspension under physico-chemical conditions similar to that of oil sand tailings, since kaolinite constitutes around 60-80 wt% of clay minerals in oil sands fine tailings [4]. In addition, kaolinite affects the flocculation process the most, compared to the other constituents of the fine tailings. While this simplification does not allow for direct application of results obtained in this research to actual oil sand fine tailings, it does contribute to fundamental mechanistic understanding of oil sands fine tailings thickening technology.

1.2. Research objectives

The purpose of the present study is to evaluate the effect of hydrodynamic conditions on the characteristics of flocculated kaolinite suspensions. The core objective of the research is to investigate how shearing affects the structure of aggregates formed through flocculation of fine clay particles. The research is conducted in three main phases:

a) The first step focuses on the study of the kinetics of flocculation and the specification of important parameters defining structure of the flocculated kaolinite aggregates. The objective of this step is to define a set of physicochemical conditions to obtain large flocculated, tenuous aggregates similar to those formed in the flocculation of oil sand fine tailings. One of the key activities of this step is to ensure it is possible to obtain aggregates with reproducible structural properties.

b) In the second step, the shear degradation of the flocculated aggregates under well-defined shearing conditions is studied. The aggregates studied in this step are formed under conditions defined in the previous step. This is the main focus of the present study.

c) In the third step, the extent of reflocculation and regrowth of the shear-degraded aggregates is investigated. This portion of the research answers an important question as to whether the shear effect on the aggregate structure is completely permanent or if there is a degree of recovery in the aggregate structure.

The objectives of the research are met through the completion of the following major actions:

1. Define a set of conditions to produce flocculated kaolinite aggregates with a well-defined and reproducible structure. Specify kinetics of flocculation in terms of evolution of aggregate structural parameters including size, density and fractal dimension, assuming spherical aggregates.
2. Develop a measurement technique to obtain aggregate structural properties using aggregate settling velocity data combined with an imaging technique

that allows for minimum alteration of the aggregate structure during sampling.

3. Develop a new correlation for a non-spherical particle drag coefficient, which is used to determine the structural properties of tenuous and fragile aggregates.
4. Revisit important parameters describing aggregate structure and improve estimation of aggregate density by considering the non-sphericity of the aggregate in calculation of the aggregate drag coefficient.
5. Investigate the shear degradation of aggregate structure under well-defined shearing conditions
6. Investigate likelihood and extent of reflocculation after cessation of shearing.

One of the important contributions of the present study is the development of an experimental technique to study flocculation, shear degradation and reflocculation processes in laminar tube flow. This approach allows for more realistic estimation of the shear rate magnitude to which an aggregate is exposed, as compared to more complicated shear fields used in previous published studies.

Another important contribution of this dissertation is to present a new correlation to estimate drag coefficients for non-spherical particles. The combination of the new drag correlation, settling velocity measurements and image analysis is used to evaluate structural parameters of the fragile aggregates. The aggregate structural parameters include: size, shape, density and fractal dimension. The measurement technique described in the present study is ideally suited for the study of suspensions containing fragile particles with a highly irregular shape in the micron to millimeter size range, similar to the aggregates formed by flocculation of fine clay particles in a thickening process. Changes in the aggregate structural parameters are used as benchmarks to evaluate the effects of changes in hydrodynamic conditions.

The new non-spherical drag coefficient correlation is used to obtain more accurate calculations of aggregate density using aggregate size and settling velocity data. An accurate estimation of aggregate density, which is lacking in the current literature, is essential in measuring changes in flocculated aggregate structure caused by hydrodynamic conditioning. An important additional contribution of this study is to the field of fluid-particle dynamics, with the introduction of a novel approach used to determine the drag coefficient for a non-spherical particle using only online imaging data.

From an industrial viewpoint, the present study provides better understanding of the relationship between macroscopic changes in the handling and transportation characteristics of flocculated suspensions and the microscopic structural properties of flocculated aggregates found in the suspension. The changes in flocculated aggregate structure that occur with changes in hydrodynamic conditions provide an indication of the strength of the aggregates and their ability to resist to the external forces encountered during the thickening process and subsequent pipeline transport. The knowledge gained through this research will answer one of major questions encountered in dealing with the dynamic behavior of flocculated suspension: how does aggregate structure respond to changes in hydrodynamic conditioning of the suspension? The answer fills a major gap in the fundamental understanding of the rheological characteristics of thickened slurries, which is very important information for the design and optimal operation of thickeners and the pipeline transport system and proper management of the tailings deposit. On the other hand, the probability of reflocculation in a controlled condition after aggregates disruption can improve performance of the thickening process. Moreover, further application of the developed experimental technique will provide the ability to evaluate flocculant performance, help improve thickening processes, optimize the handling and transporting of thickened tailings and improve design criteria and process control strategies. In the long run, improved design, operational conditions and process control will improve fine tailings dewatering, geotechnical properties of reclaimed lands, and minimize land disturbance in an economically feasible approach.

1.3. Thesis Outline

The dissertation is organized in a papers-based format; with Chapters 2 through 5 each containing a manuscript submitted or accepted for publication. Chapter 2 addresses flocculation kinetics of kaolinite particles and conditions required to produce flocculated kaolinite aggregates with a well-defined and reproducible structure. This chapter discusses the experimental technique developed in the present study using laminar tube flow flocculators and describes the measurement techniques and required mathematical equations to determine aggregate structural parameters. It also discusses the development of a dynamic steady state condition for the flocculation of the kaolinite suspension. Chapter 3 introduces a new geometrical shape factor that is easily available from on-line image analysis and describes the development of a new drag coefficient correlation for any non-spherical particle using a new shape factor. This chapter also provides required data and basic equations for Chapter 4, in which another form of the drag coefficient correlation for non-spherical particles is developed to be used specifically with imaging techniques. The novel approach introduced in Chapter 4 links, for the first time, particle-fluid hydrodynamics to online digital imaging measurements. The novel approach also improves the accuracy of the calculation of the aggregate drag coefficient and therefore the accuracy of the calculation of the aggregate density.

Chapter 5 builds on the knowledge gained through Chapters 2, 3 and 4 and describes the use of those contributions to address the core objective of the thesis. Chapter 5 describes the shear degradation of flocculated aggregates under shearing conditions developed using the laminar flow device. It also describes the extent of reflocculation after cessation of shearing. This chapter provides an important contribution to the understanding of changes in aggregate structural behavior with hydrodynamic conditioning.

Chapter 6 provides a summary of the key findings of Chapters 2 to 5 and includes a conclusive discussion of the results. Implications for treating the oil sand fine tailings are considered and recommendations for extending the research through future studies are made.

1.4. References

1. International Energy Agency, “World energy outlook 2010 fact sheet”, (2010). [cited 2012 Oct.], www.iea.org
2. Canadian Association of Petroleum production, “Basic statistics”, (2010). [cited 2012 Oct.], www.capp.ca,
3. Canadian Association of Petroleum production, “The facts on oil sands”, (2010). [cited 2012 Oct.], www.capp.ca
4. Masliyah, J.H., Czarnecki, J., Xu, Z., “Handbook on theory and practices of bitumen recovery from Athabasca oil sands”, Vol. I: “Theoretical basis”, Kingsley Knowledge Publication, Canada, 2011.
5. BGC Engineering Inc., “Oil sands tailings technology review”, Oil Sands Research and Information Network (OSRIN), University of Alberta, School of Energy and the Environment, Edmonton, OSRIN Report No. TR-1, 2010.
6. Sobkowicz, J., “Oil sands tailings technology deployment roadmap”, Project report to Alberta Innovates–Energy and Environment Solutions, Vol. 2, 2012.
7. Scott, J.D., Cymerman, G., “Prediction of viable tailings disposal methods”, Symposium on Sedimentation Consolidation Models, ASCE, San Francisco, 1984, 522-544.
8. Alberta Environment and Sustainable Resource Development (AESRD), Government of Alberta, “Tailings ponds”, (2010). [cited 2012 Oct.], http://environment.alberta.ca/apps/osip/
9. Allen, E.W., (2008). “Process water treatment in Canada’s oil sands industry: I. Target pollutant and treatment objectives”, J. Environ. Eng. Sci., 7, 123-138.
10. Houlihan, R., Haneef, M., “Oil sands tailings: regulatory perspective”. Presented in: 1st International Oil Sands Tailing Conference, Edmonton, 2008, 7-10 December.
11. Energy Resources Conservation Board (ERCB) of Alberta, “Directive 74: Tailings performance criteria and requirements for oil sands mining schemes”, February 3, 2009.

12. Nelson, R., Devenny, D., “Screening study of oil sand tailings technologies and practices”, Proceeding of Tailings and Mine Waste “09”, Banff, Canada, 2009, 1-4 November, 871-880.
13. Lord, E.R., Liu, Y., “Depositional and geotechnical characteristics of paste produced from oil sand tailings”, Tailings and Mine Waste “98”, Proceeding of the Fifth Int. Confer. On Tailings and Mine Waste “98”/Colorado, USA, 1998, 26-28 Jan., 147-157.
14. Kasperski, K.L., (1992). “A review of properties and treatment of oil sands tailings”, AOSTRA Journal of Research 8, 11-53
15. MacKinnon, M.D., (1989). “Development of the tailings pond at Syncrude's oil sands plant: 1978-1987”, AOSTRA Journal of Research 5, 109-133.
16. Simieritsch, T., Obad, J., Dyer, S., “Tailings plan review- An assessment of oil sands company submissions for compliance with ERCB Directive 074: Tailings performance criteria and requirements for oil sands mining”; Ed. R. Lines, The Pembina Institute; Pembina Foundation and Water Matters, 2009, December.
17. Devenny, D.W., “A screening study of oil sand tailings technologies and practices”, Two part reports prepared for Alberta Energy Research Institute, Edmonton, 2010.
18. Matthews, J.G., Shaw, W.H., Mackinnon, M.D., Cuddy, R.G., (2002). “Development of composite tailings technology at Syncrude”, Int. J. Mineral Process., 16, 24-39.
19. MacKinnon, M.D., Matthews, J.G., Shaw, W.H., Cuddy, R.G., (2001). “Water quality issues associated with composite tailings (CT) technology for managing oil sands tailings”, Int. J. Surface Mining 15(4), 235-256.
20. Rao, R., (1980). “Flocculation and dewatering of Alberta oil sands tailings”. Int. J. Miner. Process., 7, 245-253.
21. Hamza, H.A., Stanonik, D.J., Kessick, M.A., (1996). “Flocculation of lime-treated oil sands tailings”, Fuel, 75(3), 280-284.
22. Cymerman, G., Kwong, T., Lord, E., Hamza, H.A., Xu, Y., “Thickening and disposal of fine tails from oil sand processing”, In: Polymer in Mineral

Processing-Proc. 3rd UBC-McGill Int. Symp., (Ed. by) Laskowski, J.S., Metallurgical Society of CIM, Quebec City, 1999, 605-619.

23. Xu, Y., Cymerman, G., “Flocculation of fine oil sand tails”, In: Polymer in Mineral processing-Proc. 3rd UBC-McGill Int. Symp., (Ed. by) Laskowski, J.S., Metallurgical Society of CIM, Quebec City, 1999, 591-604.
24. Shell Canada Ltd., “Muskeg River mine: Tailings management plan”, Submitted to Energy Resources Conservation Board, Calgary, 2010.
25. Matthews, J., Masala, S., “Tailings research at Shell's Muskeg River mine tailings facility”, Proceeding of 13th Int. Conf. Tailings and Mine Waste ‘09, Banff, Canada, 2009, 1-4 November, 405-415.
26. Yuan, X.S., Shaw, W., (2007). "Novel processes for treatment of Syncrude fine transition and marine ore tailings", Canadian Metallurgical Quarterly. 46(3), 265-272.
27. Sworska, A., Laskowski, J.S., Cymerman, G., (2000). "Flocculation of the Syncrude fine tailings: Part I. effect of pH, polymer dosage and Mg^{2+} and Ca^{2+} cations", Int. J. Mineral Process. 60(2), 143-152.
28. Kotylar, L.S., Sparks, B.D., Schutte, R., (1996). “Effects of salt on the flocculation behavior of nanoparticles in oil sands fine tailings”, Clays and Clay Minerals 44(1), 121-131.
29. Jerravipoolvarn, S., Scott, J.D., Chalaturnyk, R.J., “Geotechnical characteristics of laboratory in-line thickened oil sands tailings”, Proceeding of Tailings and Mine Waste “09”, Banff, Canada, 2009, 1-4 November, 813-828.
30. Sanchez, A., “In-line flocculation for MFT treatment”, Presented in 1st Pipeline Transport processes workshop, University of Alberta, Edmonton, 2012, 5-6 June.
31. Johnson, S.B., Franks, G.V., Scales, P.J., Boger, D.V. Heal, T.W., (2000). “Surface chemistry–rheology relationships in concentrated mineral suspensions”, Int. J. Miner. Process. 58, 267–304.
32. Boger, D.V. (2009). “Rheology and the resource industries”, Chem. Eng. Sci., 64(22), 4525-4536.

33. Mills, P.D.A., Goodwin, J.W., Grover, B.W., (1991). “Shear field modification of strongly flocculated suspensions-Aggregate morphology”, Colloid Poly. Sci., 269, 949-963.
34. Nguyen, Q.D., Boger, D.V., (1998). “Application of rheology to solving tailings disposal problems”, Int. J. Miner. Process. 54, 217–233.
35. Boger, D.V., Scales, P.F. Sofra, F., “Rheological concepts” Chap 3 in: “Paste and Thickened Tailings – A Guide”, (Ed. by) Jewell, R., Fourie, A., Second Ed., Australian Centre for Geomechanics, 2010.
36. McFarlane, A.J., Bremmell, K., Addai-Mensah, J., (2005)a. “Microstructure, rheology and dewatering behavior of smectite dispersions during orthokinetic flocculation”, Mineral Eng., 18, 1173-1182.
37. McFarlane, A.J., Addai-Mensah, J., Bremmell, K., (2005)b. “Rheology of flocculated kaolinite dispersions”, Korea-Australia Rheology J., 17(4), 181-190.
38. Herrington, T. M., Midmore, B.R., Watts, J.C., “Flocculation of kaolin suspensions by polyelectrolytes”, Proceedings of “Colloid polymer interactions: particulate, amphiphilic and biological surfaces”, (Ed. by) Tong, P., Dubin, P.L., ACS, Washington, D.C., 1993, 162-181.
39. Schaan, J., Sanders, R.S., Gillies, R.G., McKibben, M.J., Litzenberger, C., Sun, R-J., Shook, C.A., “Effect of shear history on the flow properties of flocculant-dosed thickened tailings slurries”, 16th International Conference on Hydrotransport, Vol. II, Santiago, Chile, 2004, 26-28 April, 403-414.
40. Watson, P., Fenderson, T., Mahmoudkhani, A., Nair, M., Patel, A., Roberts, G., “Breakage and reformation of flocs in oil sands tailings slurries”, Proceedings of Tailings and Mine Waste 2011, Vancouver, Canada, 2011, 6-9, November.
41. Michaels, A.S., Bolger, C.B., (1962). “The plastic flow behavior of flocculated kaolin suspensions”, I & EC Fundamen., 1(3), 153-162.
42. Malhotra, D., Taylor, P.R., Spiller, E., LeVier, M. “Recent advances in mineral processing plant design”, SME Inc., Littleton, Colorado, 2009, 2164-2173.

43. Schoenbrunn, F., Hales, L., Bedell, D., “Strategies for instrumentation and control of thickeners and other solid-liquid separation circuits”, in: Mular, A.L., Halbe, D.N., Barratt, D.J. (Ed.), “Mineral Processing Plant Design, Practice, and Control: Proceedings, Vol. 2”, SME Inc., Littleton, Colorado, 2009, 2164-2173.
44. Gladman, B.J., Usher, S.P., Scales, P.J., “Understanding the thickening process”, Proceedings of Paste 2006 – (Eds by) Jewell, R.J., Lawson,S., Newman, P., Australian Centre for Geomechanics, Limerick, Ireland, 2006, 5-12.
45. Sofra, F., “Rheological assessment – A road map for plant designers and operators”, Proceedings of Paste 2006 – (Eds by) Jewell, R.J., Lawson,S., Newman, P., Australian Centre for Geomechanics, Limerick, Ireland, 2006, 13-23.
46. Cloutis, E.A., Gaffey, M.J., Moslow, T.F., (1995). “Characterization of minerals in oil sands by reflectance spectroscopy”, Fuel, 74 (6), 874-879.
47. Majid, A., Argue, S., Boyko, V., Pleizier, G., L’Ecuyer, P., Tunney, J., Lang, S., (2003). “Characterization of sol-/gel-derived nanoparticles separated from oil sands fine tailing”, Colloids and Surf. A: Physicochem. Eng. Aspects 224 (2003), 33-44.
48. Angle, C.W., Zrobok, R., Hamza, H.A., (1993). “Surface properties and elasticity of oil-sands derived clays found in a sludge pond”; Appl. Clay Sci., 7, 455-470.
49. Omotoso, O.E., Mikula, R.J., (2004). “High surface areas caused by smectitic interstratification of kaolinite and illite in Athabasca oil sands”, Appl. Clay Sci., 25, 37-47.
50. Sparks, B.D., Kotlyar, L.S., O’Carroll, J.B., Chung, K.H., (2003). “Athabasca oil sands: effect of organic coated solids on bitumen recovery and quality”, J. Petrol. Sci. Eng., 39, 417-430.

Chapter 2

Flocculation kinetics and aggregate structure of Kaolinite mixtures[1]

2.1. Introduction

The flocculation of fine particles in water is of importance in many fields, such as chemical and biological wastewater treatment and water purification, and tailings treatment in the mining and oil sands industries.

In the oil sands industry, any water-based process for the extraction of bitumen from oil sand produces a suspension of clay fines. The main component of the fine solids in the tailings is kaolinite, whose particle size is in the colloidal range [1]. Their small size and surface electric potential cause difficulties in settling and consolidation of the fine solid particles. The treatment of the fine solids suspension is one of the most important tailings management issues in the oil sands industry [1, 2]. Recently, some oil sands operators have begun to utilize thickener technology, which involves polymer-induced flocculation. The thickening process allows for production of higher density tailings mixtures and recycling of the separated warm water stream [1, 2].

Normally flocculated fine tailings contain large, tenuous and porous aggregates [1, 2]. The highly irregular 3-dimensional structure of an aggregate and its inherent frangible nature make it difficult to quantify its structure. In addition, the characteristics of flocculated aggregates change depending on the physical and chemical conditions during and after the flocculation process.

It is well known that aggregate size and density are the two most important properties of aggregates [3]. Aggregate density is the density of the porous structure that is made of fine particles and surrounding fluid. Despite the number of comprehensive studies reported in the literature describing the evaluation of aggregate structure, in most of those studies only size distribution results are reported. There are few studies in which aggregate density is measured [4-8].

---

[1] Part of this chapter was published in Vaezi G., F., Sanders, R.S., Masliyah, J.H., *J. Colloid and Interface Sci.* 355 (2011) 96-105.

However, no studies in which the change in aggregate density and aggregate population are monitored during flocculation could be found. Spicer et al. [9] presented changes in the aggregate average density during cyclic shearing. The limitation here arises from the fact that it is difficult to measure the aggregate density accurately.

Normally, the flocculation process takes place in a shear field to provide good particle-flocculant dispersion and particle-particle contact. In many studies, the turbulent shear field occurring within a stirred tank has been used. The random nature of the shear field in a stirred tank limits one's ability to specify the shear rate with good accuracy. In most studies the hydrodynamics of the stirred tank are characterized using an average shear rate, calculated using input power and tank volume. Spicer et al. [9] studied the floc size and density evolution of polystyrene particles in a mixed tank. They considered the average shear rate to be representative of the hydrodynamic conditions inside the tank. However, Bouyer et al. [10, 11] showed that the average shear rate does not correspond to the different shear rates that a floc experiences. They emphasized that regardless of tank type, the floc size distribution is a function of most probable shear rate (mode of dissipation rate distribution curve) and type of impeller. The most probable dissipation rate (or shear rate) is not a straightforward parameter to estimate; instead detailed hydrodynamic studies of the shear field should be conducted. For instance, Bouyer et al.[11] and Coufort et al.[12] used a Particle Image Velocimetry (PIV) technique.

A Couette flow system can also be used to study the flocculation process. Serra et al. [13, 14] studied the aggregation and breakage of latex particles in a Couette flow Rahmani et al. [15] used image analysis to measure the asphaltene floc size in a Couette flow device. Coufort et al. [12] investigated the hydrodynamics of a Taylor-Couette device operating in turbulent flow conditions. They reported results similar to those of Bouyer et al. [10, 11], specifically concerning the importance of the most probable dissipation rate. A Couette flow device has some limitations, particularly in the laminar flow regime. Differential settling of large aggregates can occur to some extent, especially at lower shear rates. This can affect sampling, aggregate structure and size measurement. Although higher shear rates can prevent aggregate settling, instabilities created by Taylor vortices can disturb the fully laminar regime [12, 13]. Furthermore, sampling can be challenging in a Couette flow device.

Sampling from a mixed tank or Couette cell can drastically alter the aggregate size and/or density. Spicer et al. [9] compared the effect of three different sampling techniques on the repeatability of aggregate size measurement. In a similar study conducted by Serra et al. [13, 14], an external circulation loop on a Couette flow system was used to measure the aggregate size. In these studies, the authors did not report the effect of sampling on the diameter distribution, aggregate structure, or the effect of mixture circulation back into the mixed tank. Shearing through the circulation pump, loop and size measurement device can alter the aggregate size distribution and structure. Any sampling method can change the aggregate structure to some extent, and samples may not be representative of the aggregates inside the flocculator. More detailed studies are required to verify that sampling does not affect the aggregate structure.

The shear field associated with laminar tube flow is an excellent alternative to the aforementioned shear fields. Gregory [16-18] used laminar tube flow for qualitative monitoring of size evolution in developing the Photometric Dispersion Analyser (PDA). In Newtonian laminar tube flow inside a straight tube, the shear rate varies linearly with the tube radius. This provides a shear field that is more uniform than that of the mixed tank. The average shear rate for laminar flow inside a straight tube ($\bar{\dot{\gamma}}_{Straight}$) can be easily obtained by integrating shear rate over the tube cross section:

$$\bar{\dot{\gamma}}_{Straight} = \frac{1}{A_t}\int_0^{A_t} \dot{\gamma}(r)\, dA_t \tag{2.1a}$$

where A_t is tube cross sectional area and $\dot{\gamma}(r)$ is shear rate that is given by the Hagen-Poiseuille equation. After substitution of terms into Eq. (2.1a):

$$\bar{\dot{\gamma}}_{Straight} = \frac{4}{\pi D_t^2}\int_0^{\frac{D_t}{2}} \left(\frac{32Q}{3D_t^3}.\frac{2r}{D_t}\right)(2\pi r)d_r = \frac{64Q}{3\pi D_t^3} \tag{2.1b}$$

where D_t is tube internal diameter and Q is volumetric flow rate. This equation gives a much better estimation of the shear rate that an aggregate is exposed to, compared with a global shear rate in a stirred tank. Another advantage is the sampling is much easier and less invasive, as samples can be obtained directly from the tube outlet, minimizing the effect of the sampling step on the aggregate structure.

Because of space limitations and also to study greater aggregate residence times within the tube, tube can be coiled around a cylinder. In a coiled tube, secondary radial circulation increases the mixing and helps to decrease the axial dispersion (and thus residence time distribution). This also provides a more uniform shear rate than a direct laminar tube flow case [18]. In addition, laminar flow can be maintained up to Reynolds numbers of 5000 in the coiled tube [19]. However, in the coiled tube, secondary radial circulation increases the shear rate. Berger et al.[19] and McConalogue [20] give the following correlation to estimate the average shear rate in a coiled tube:

$$\frac{\bar{\dot{\gamma}}_{Straight}}{\bar{\dot{\gamma}}_{Curved}} = 1 - \left[1 - \left(\frac{11.6}{De} \right)^{n} \right]^{\frac{1}{n}} \tag{2.2-a}$$

where De is the Dean number, which is defined as:

$$De = \left(\frac{D_t}{D_C} \right)^{0.5} Re_t \tag{2.2-b}$$

In Eq. (2.2b), D_t is tube internal diameter, D_C is diameter of tube curvature (diameter of cylinder that tube is coiled around) and Re_t is tube flow Reynolds number given by:

$$Re_t = \frac{4 \rho_L \, Q}{\pi \, \mu_L D_t} \tag{2.2-c}$$

where ρ_L and μ_L are liquid density and viscosity, respectively. McConalogue [20] gives the exponent of $n = 0.45$, for $11.6 < De < 3000$.

The objective of the present study is to develop an experimental technique to examine a two-stage flocculation process in a well-defined shear field. Laminar tube flow is used to establish a shear field that is more uniform than that of the mixed tank. The effect of flocculation time on the size and structure of model fine clay particle aggregates, under physico-chemical conditions similar to that of oil sand tailings, is investigated. The two main aggregate structural parameters, size and density, are determined from analysis of aggregate settling velocity measurements. The effect of advective flow through the aggregate porous structure and the effect of Reynolds number on the aggregate drag coefficient are considered while estimating the aggregate density. The aggregate fractal dimension is determined using two different methods. The evolution of the aggregate structure is presented in terms of size, density and fractal dimension. A detailed statistical analysis was undertaken to investigate the change in the aggregate population, which enabled us to examine the occurrence of aggregate structural conformation due to aging.

2.2. Aggregate structure monitoring

Aggregate size and density are the two main parameters needed to describe an aggregate's structure. Many studies have shown that these two parameters can be related using fractal theory [3, 7, 21, 22]. In a fractal model, aggregate density, ρ_a, and size, *L*, are related with a power-law relationship of the form [3, 21, 23, 24]:

$$\rho_{Eff} = (\rho_a - \rho_L) \propto L^{(D_F - 3)} \tag{2.3}$$

where D_F is the mass fractal dimension. It varies in range of 1-3 and larger values of D_F suggest more densely packed aggregates [21, 24].

A similar power law relationship relates the projected area of a fractal aggregate's 2-D image, A_i, and its size [21, 24]:

$$A_i \propto L^{D_i} \tag{2.4-a}$$

The relationship between the fractal dimension of the image, D_i, and the mass fractal dimension D_F, is given by [21, 24]:

$$D_i = D_F \qquad D_F < 2 \tag{2.4-b}$$

$$D_i = 2 \qquad D_F \geq 2 \tag{2.4-c}$$

Bushell et al. [21] suggest using the aggregate maximum length in Eqs. (2.3) and (2.4), while Gregory [3] states the choice of L does not matter as long as the choice is consistent. Our observation also indicates that the choice of size L does not affect the fractal dimension significantly. Here, the area-based aggregate diameter, d_a, is used, which is calculated after measuring the projected area of an aggregate's image, i.e.

$$d_a = \left(\frac{4A_i}{\pi}\right)^{0.5} \tag{2.5}$$

2.2.1. Measurement of aggregate density and fractal dimension

There are several simple techniques to measure the aggregate size; however, density and fractal dimension cannot be measured easily. Gregory [3] has summarized different methods of aggregate density and fractal dimension measurement. Bushell et al. [21] have also reviewed different methods of fractal dimension measurement. Measurement of aggregate sedimentation velocity is more direct, and less invasive than other techniques used to determine aggregate density and fractal dimension. Aggregate size and sedimentation rate can be measured by direct visualization followed by image analysis. This technique has been widely used to estimate the aggregate density in many studies [5, 6, 8, 25, 26, 27]. In general, a force balance on a spherical porous aggregate settling steadily in an infinite medium leads to [6, 21, 27, 28]:

$$\frac{\rho_a - \rho_L}{\rho_P - \rho_L} = 1 - \varepsilon = \frac{3\rho_L \Omega C_D}{4g(\rho_P - \rho_L).d_a} U_a^2 \tag{2.6}$$

The difference between aggregate density, ρ_a, and liquid density, ρ_L, is known as aggregate effective density, ρ_{Eff}. Other than aggregate equivalent diameter, d_a, and settling velocity, U_a, which are measured in a free-settling test, three unknowns are encountered in the Eq. (2.6): ρ_P, primary particle density; C_D, drag coefficient; and Ω, correction factor for advective flow through the aggregate interior. In the subsequent sections, approaches to estimate these three unknowns (ρ_P, Ω and C_D) are described.

2.2.2. Primary particle density

In Eq. (2.6), ρ_P is the density of primary structural units forming the aggregate. The aggregate is comprised of micro flocs that have some internal water as part of their structure. This has been confirmed experimentally by Michaels and Bolger [29], Li and Logan [30], and by Woodfield and Bickert [22] using simulations. In the present study, a two-stage aggregation process is used. The process, which is illustrated in Fig. 2.1, is comprised of:

(1). Destabilization of dispersed primary particles by a coagulation step and formation of micro-flocs, hereafter called primary flocs.

(2). Aggregation of primary flocs into large aggregates using polymer flocculation

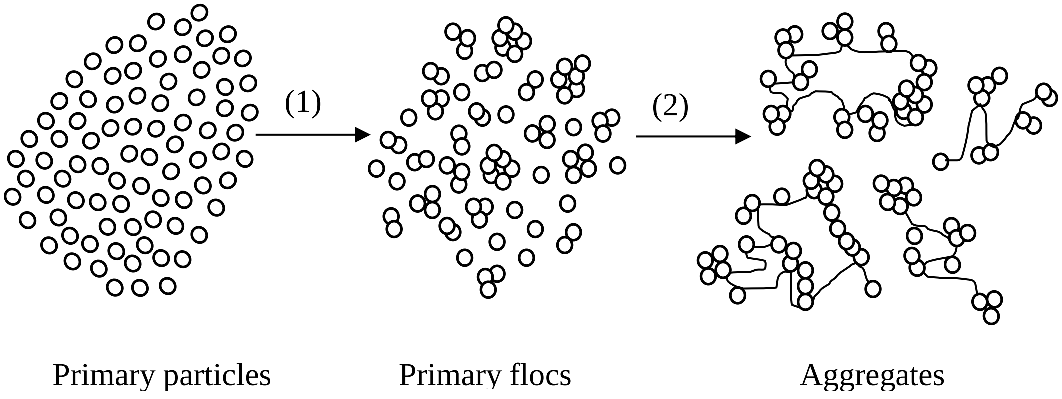

Fig. 2.1. Scheme of two-stage aggregation process. (1). Destabilization of dispersed particle through a coagulation step, (2). Aggregation of primary flocs using a polymer flocculant

The primary floc density can be estimated using the fractal model. Primary floc density scales with the diameter ratio of primary floc to the primary particle with the fractal dimension exponent, so that:

$$\rho_P = \rho_L + (\rho_K - \rho_L) S \left(\frac{d_P}{d_K}\right)^{(D_{PF}-3)} \tag{2.7}$$

where ρ_L is liquid density, ρ_K is primary particle inherent density (in this study, kaolinite density), d_P is primary floc diameter, d_K is primary particle (here, kaolinite) diameter before destabilization, D_{FP} is fractal dimension of primary floc and S is called structural pre factor. Gmachowski [23, 31] used computer simulations to develop a general correlation between S and D_{FP}:

$$S = \left(\sqrt{1.56 - (1.728 - \frac{D_{FP}}{2})^2} - 0.228 \right)^{D_{FP}} \tag{2.8-a}$$

For $1.5 \leq D_{PF} \leq 2.75$, this general form can be reduced to:

$$S \approx 0.42 D_{FP} - 0.22 \tag{2.8-b}$$

2.2.3. Internal advective flow correction factor

The correction factor, Ω, takes account of the advective flow through the aggregate interior. The correction factor is unity for an impermeable spherical aggregate and less than unity for a porous aggregate. Calculation of Ω requires knowledge of aggregate permeability, whose evaluation is usually based on permeability models. For a given aggregate size, the permeability controls the extent of the advection flow [32].

Neale et al. [32] solved the general form of the Brinkman equation to obtain Ω for a highly porous sphere made of porous sub-clusters. They assumed the aggregate was a porous object with a uniform porosity distribution throughout. Vanni [33] solved the Brinkman and Navier-Stokes equations for a non-homogenous aggregate assuming a fractal distribution of the local porosity. For fractal dimension $2 < D_F < 2.5$, he concluded that the uniform aggregate interior structure model, or Neale's simplified solution, gives reasonable results:

$$\Omega = \frac{2\beta^2 \left[1 - (\tanh \beta) / \beta\right]}{2\beta^2 + 3\left[1 - (\tanh \beta) / \beta\right]} \tag{2.9}$$

where β is known as the normalized aggregate equivalent diameter, or the permeability factor, and is expressed by:

$$\beta = \frac{d_a}{2\sqrt{k}} \tag{2.10}$$

where k is the aggregate permeability (m^2) and d_a is the aggregate equivalent diameter. This approach was also confirmed by Li and Logan [30, 34]. This form is used often in the literature because of its simplicity (see Eq. (2.9)). In this study, we use this model to investigate the effect of internal advective flow on aggregate density.

Empirical models are often used to evaluate the aggregate permeability. Lee et al. [6] summarized the six widely employed permeability models. Li and Logan [34] simulated two aggregate structural models, the single-particle fractal model and the cluster-fractal model, and compared the application of three of the six widely used permeability models. Both groups concluded that both the Brinkman and Happel permeability models give good estimates of aggregate permeability. Vanni [33] recommended the use of one of the aforementioned empirical permeability equations along with a shielding coefficient, ξ, to account for short-range particle interactions. Gruy and Cugniet [35] presented experimental results on drag force of permeable model aggregates. For fractal dimensions smaller than 2.5, they recommended the use of the model proposed by Vanni [33]. In this study, the Brinkman permeability model corrected with shielding coefficient is used:

$$k = \frac{d_P^2}{72}\left[3 + \frac{4}{(1-\varepsilon)} - 3.\sqrt{\frac{8}{(1-\varepsilon)} - 3}\right].\frac{1}{\xi} \tag{2.11}$$

where

$$\xi = 1 - 0.6 e^{-10(1-\varepsilon)} \tag{2.12}$$

For fractal dimension $D_F > 2.5$, the permeability effect is negligible and an impermeable aggregate can be assumed. For fractal dimension $D_F < 2$, the rigorous model proposed by Vanni [33] should be solved numerically.

2.2.4. Drag coefficient

There is no generally valid model or correlation to obtain the drag coefficient for a permeable object having a particle Reynolds number, $Re_a > 0.1$ [6, 21]. There are two main approaches used to calculate C_D for a spherical permeable aggregate. In the first approach, Stokes' law is applied to $Re_a > 0.1$, despite the fact that the aggregate size was around 1mm [4, 8, 25, 27]. One should expect that the larger aggregates have Reynolds numbers greater than 0.1 so that Stokes' law is not valid. In the second approach, a C_D-Re correlation has been employed rather than using Stokes' law [21]. Huang [5] used Stokes' law for $Re_a < 1$ and a correlation given by Concha and Almendra [36] for $Re_a > 1$. Johnson et al. [28] reported a correlation for the drag coefficient of a permeable aggregate, but it deviates considerably from many of the results reported in literature [21, 35]. The only available drag coefficient correlation obtained from experimental data for permeable aggregates is given by Masliyah and Polikar [37]. They proposed correlations for a falling permeable sphere with a permeability factor in the range of $15 < \beta < 33$:

$$C_D = \frac{24\Omega}{Re_a} \qquad Re_a \le 0.1 \qquad \text{(2.13-a)}$$

$$C_D = \frac{24\Omega}{Re_a}\left(1 + 0.1315 Re_a^{(0.82-0.05w)}\right) \qquad 0.1 < Re_a \le 7 \qquad \text{(2.13-b)}$$

$$C_D = \frac{24\Omega}{Re_a}\left(1 + 0.0853 Re_a^{(1.093-0.105w)}\right) \qquad 7 < Re_a \le 120 \qquad \text{(2.13-c)}$$

where $w = \log_{10} Re_a$ and Re_a is calculated using a measured settling velocity and the area-based diameter of the aggregate, d_a. The advective flow correction factor, Ω, can be estimated using the model described in previous section. We use this correlation to evaluate the aggregate drag coefficient, assuming it is valid for

$\beta > 33$. This is almost certainly valid since for $\beta > 33$, $\Omega \rightarrow 1$ and the effect of advective flow is negligible [32].

2.2.5. Aggregate shape factor

The correlations described in the previous sections are, strictly speaking, valid only for spherical particles or aggregates. Attempts to measure aggregate shape factor are restricted by the aggregate's fragile structure. In previous studies aggregates are assumed spherical or a constant shape factor is used to estimate the drag coefficient [8, 25, 27, 38]. In this chapter, aggregates are assumed to be spherical. The effect of shape factor on drag coefficient and then on aggregate density will be discussed in Chapter 5.

2.3. Experimental method

2.3.1. Materials

2.3.1.1. Clay slurry

A mass of 125 g of kaolinite (Dry Branch Kaolin Co., Georgia, US) is dispersed in 900 mL deionised water. The inherent density of kaolinite is 2560 kg/m^3 (reported by the supplier) with a moisture content of 4.6 % (w/w) measured by drying at 120°C. To fully disperse the clay, the pH of the slurry is adjusted to 8.70 using a 0.25N NaOH solution. The total mixture volume is then adjusted to 1 L. After the suspension is left to settle overnight, the top 800 mL is decanted. This dispersion and settling step provides a narrow size distribution for the dispersed fine clay. The mean primary particle size is 0.64 ± 0.02 μm, as measured with a Malvern Mastersizer (Hydro 2000SM series). The solids content of the dispersed kaolinite mixture is measured using a Pycnometer and double checked by drying at 120 °C. A typical solids concentration is 50-60 g/L. This stock suspension is used to prepare 3.57 g/L slurry of primary particles through the addition of deionised water. Calcium chloride (0.1 M solution) is added to the prepared clay suspension to obtain 0.325 mM of Ca^{+2} in the suspension. The suspension pH is adjusted to 8.0. The calcium ions destabilize the dispersed primary clay particles and prompt the formation of primary flocs. The average primary floc size was found to be 2.7 ± 0.3μm by Zetasizer (Malvern, Nano-ZS series) and was confirmed to be 2.1 ± 0.3μm using an optical sizing technique (Sysmex, FPIA-3000). The difference in floc diameter is likely due to partial flocs settling in the Zetasizer's measuring cell.

2.3.1.2. Polymer flocculant solution

MAGNAFLOC 1011 polymer flocculant (CIBA Specialty Chemicals) was used for this study. It is a high molecular weight polyacrylamide with approximately 30% degree of anionicity. A concentrated polymer solution of 2 g/L is prepared by dissolving 0.2 g of dry polymer in 100 ml of deionised water. The polymer stock solution is used within two days of preparation. For flocculation experiments, a fresh dilute polymer solution of 6.25 mg/L is prepared by diluting the concentrated stock solution.

2.3.1.3. Settling medium solution

A portion of the 3.57 g/L suspension is flocculated separately in a mixed tank, with the same procedure used for the experiments. The flocculated slurry is filtered using 2 μm filter paper. The filtrate solution is used to fill the settling chamber. This provides identical water chemistry for the flocculated slurry and the liquid in the settling chamber, thus preventing any change in the aggregate structure during the settling velocity experiments. The filtrate was found to behave as a Newtonian fluid with a viscosity of 1.04 mPa.s at 22°C (AR G2 Rheometer, TA Instruments). The temperature of the settling media and clay slurry are checked before each experiment to ensure they are nearly identical. Constant temperature ensures that free convection caused by a temperature gradient and fluid viscosity changes does not affect the settling velocity measurements and hence the calculation of aggregate density.

2.3.2. Apparatus and procedures

A drawing of the experimental apparatus is shown as Fig. 2.2. The apparatus includes two mixed tanks that contain the clay suspension and polymer solution.

The clay suspension and polymer solution are delivered by a peristaltic pump and a gear pump, respectively. Two rotameters measure the flow rates of the clay slurry and polymer solution. Flow meters were calibrated with the same mixtures used during experiments. An in-line mixer (Kenics with L/D=1), with 24 elements and OD of 3/16 inches fitted tightly inside Tygon tubing, is situated upstream of the flocculation tube to promote mixing of the polymer solution and clay suspension. The set-up provides a laminar flow region where the dilute clay suspension is mixed with the polymer solution and the flocculation process proceeds while the mixture flows through the initial length of tubing. The ratio of the suspension to polymer solution flow rate is set at 7/3 to provide final solids and polymer solutions concentrations of 2.5 g/L and 1.875 mg/L, respectively. Flocculation occurs in the "laminar tube flocculator", the section of Tygon tubing attached to the in-line mixer. Different lengths of tubing (L=0.8 to 15.3 m) are used to vary the flocculation time (τ=8 to 147 s). Appendix A1 provides details of experimental conditions. The settling chamber is made from glass and is filled with the settling medium solution. A CCD camera (QICAM Fast 1394 CCD, QImaging designs, Canada), equipped with a macro video zoom lens (Edmund optics Inc.), is mounted on the front face of the settling chamber. The pixel size of the camera is 6.5 μm. The camera is connected to a personal computer which is used to record digital videos of settling aggregates.

An inner tube diameter of 6.4 mm was chosen to obtain a relatively low shear rate in the flocculation tube, which results in the formation of large aggregates. For all experiments, tubes are coiled around a 166 mm cylinder. The flow rate is held constant at 200 ± 5 mL/min. This is the minimum flow rate required to prevent the sedimentation of aggregates inside the flocculation tube. The given flow rate results in an average shear rate of 145 ± 3 s^{-1} in the 6.4 mm ID coiled tube (see Eqs. (2.1) and (2.2)).

Samples are directed from the tube by diverting end of the tube to the settling chamber and the camera is used to capture videos of the falling aggregates. For each experiment, 5-8 samples are directed periodically from the outlet of the flocculation tube, thereby providing random samples of aggregates to prevent biased sampling. A software package, ImagePro Plus 6.1 (Media Cybernetics, USA), is used to control the CCD camera, to capture and to analyze the images. The error associated with the measurement of aggregate diameter is determined by the optical resolution of the camera, which is estimated to be within 10 μm. During the experiments, we found that two different persons could analyse images with less than 5% difference in diameter. Thus, the ultimate error in area-based aggregate diameter would be less than 20-50 μm, for aggregates that are 200-1200 μm in size.

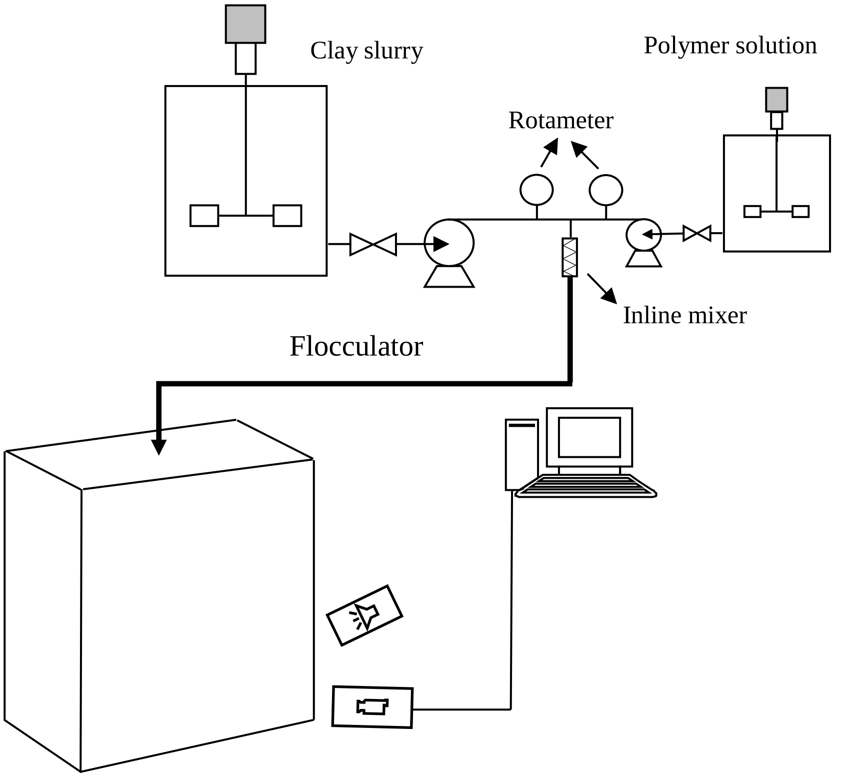

Fig. 2.2. Experimental set-up for flocculation tests in laminar tube flocculator

The terminal settling velocity of an aggregate is evaluated by image analysis. The trajectory of a settling aggregate is tracked and the number of frames in which the aggregate is visible in the field is determined. The settling time is calculated using the number of frames and recording speed of the camera (in frames per second). The setting velocity is calculated as $U_t = \Delta x / \Delta t$, where

Δx is the distance that the aggregate settling distance and Δt is the settling time. Only terminal velocities of falling aggregates with vertical trajectory are measured.

2.4. Results and discussion

2.4.1. Aggregate size evolution

The aggregate size distribution, obtained from image analysis of the settling experiments, is shown as Fig. 2.3. Trends are shown for seven different flocculation times of 8 to 147 s. Each curve shown in this figure involves the analysis of 185–350 aggregates. The results presented in this figure indicate the change in aggregate size distribution with flocculation time. In the early stages of flocculation, the population curve is right-skewed, indicating most aggregates are small and there are few large aggregates. Aggregates grow as they spend more time in the flocculation tube. The interesting feature of Fig. 2.3 is that the size distribution becomes broader, approaching a normal distribution as the flocculation time increases beyond 30 s. The change in the shape of the size distribution curves is likely caused by the fact that the number of aggregate-aggregate and aggregate-tube wall collisions increases with increasing residence time and thus aggregate breakage becomes important. This is a general trend in flocculation processes: in the early stage of the process, aggregation is the dominant mechanism and after aggregates grow larger, fragmentation competes with aggregation. It can be observed that very large aggregates (around d ~ 1700 microns) appear in the mixture at t = 15 s. Larger aggregates are fragmented through breakage, and a dynamic equilibrium is established as flocculation time increases. This explains why the maximum diameter at t = 15 s is greater than that measured at t = 120 s and t = 147 s. Finally, a dynamic equilibrium between aggregation and fragmentation is established. This is depicted in Fig. 2.3 as the size distribution curves for flocculation times of 90 s, 120 s and 147 s overlap, indicating that the aggregate size distribution does not change considerably if the flocculation time is increased beyond 90 s.

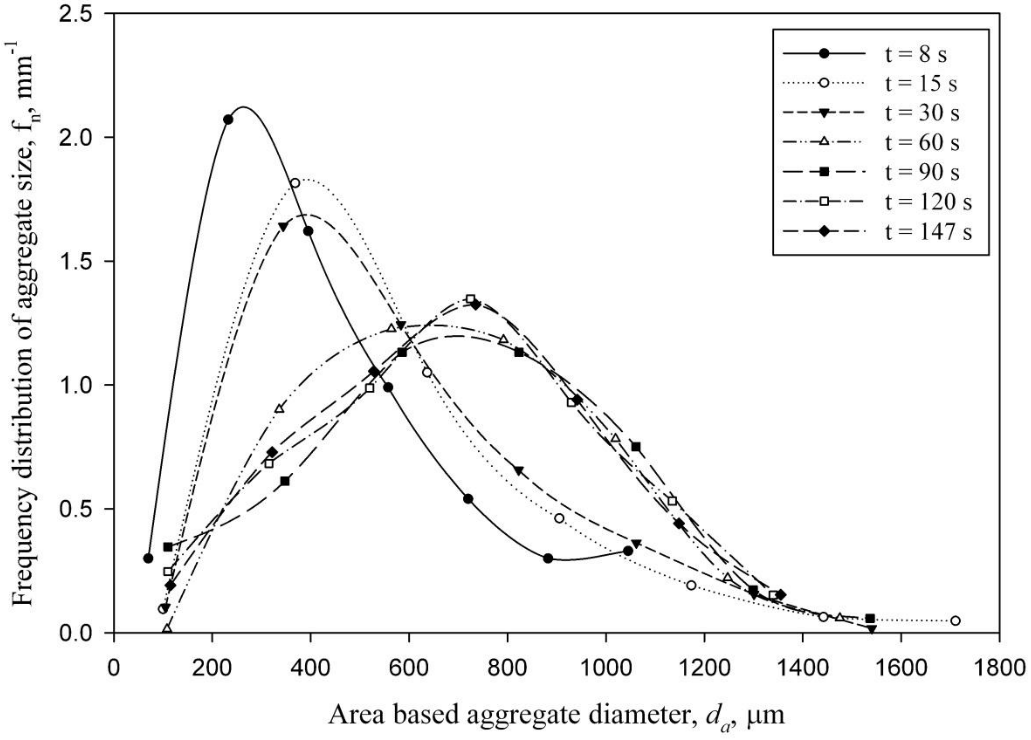

Fig. 2.3. Evolution of aggregate size with flocculation time

The similarity of aggregate size distribution at flocculation times of 60 to 147 s was confirmed by detailed statistical analysis of the population data [39,40]. The F-test to test the equality of variances, and t-tests to test the equality of arithmetic means) were conducted. Table 2.1 summarizes the results of the statistical analyses. All tests described here have a significance level of 5% ($\alpha = 0.05$). Here, the hypothesis H_0 stands for the equality of arithmetic means of two different populations. It can be seen from Table 2.1 that the arithmetic mean of aggregate size data at t = 60 s is likely different from the rest, while the arithmetic means at t = 90, 120 and 147 s are similar. Also, the result shows that the populations at different flocculation times $60 \leq t \leq 147$s have equal variances.

Table 2.1. F-test and T-test results of aggregate size data for flocculation times $60 \leq t \leq 147$ s.

H_0	Equal Variances? (from F-Test result)	p-value of T-test	Reject H_0?
$\bar{d}_{60} = \bar{d}_{90}$	Yes	0.017	Yes
$\bar{d}_{60} = \bar{d}_{120}$	Yes	0.062	No
$\bar{d}_{60} = \bar{d}_{147}$	No	0.007	Yes
$\bar{d}_{90} = \bar{d}_{120}$	Yes	0.720	No
$\bar{d}_{90} = \bar{d}_{147}$	Yes	0.614	No
$\bar{d}_{120} = \bar{d}_{147}$	Yes	0.414	No

An analysis of Variance (ANOVA) test was also carried out to compare the arithmetic means of the populations. The fixed effects model is used here, and in order to perform hypothesis testing using this model, the assumption that the errors are independently and normally distributed must be satisfied 39,40]. The residual plot of size data showed that the residuals do not follow any particular pattern, meaning that the assumption is valid and the fixed effects model can be used. The ANOVA test was done for two cases. In the first, the arithmetic mean diameters at 4 flocculation times of 60 s to 147 s were compared; in the second, 3 flocculation times of 90 s to 147 s were tested. The null hypothesis, H_0, is the equality of arithmetic means and the alternate hypothesis is H_1: $\bar{d}_i \neq \bar{d}_j$ for at least one pair (t_i , t_j) for *i* and *j* = 60, 90, 120, 147 s, where $\bar{d}_i$ is the arithmetic mean of the size population at time *i*. The significance level used here is 5%. The results are summarized in Table 2.2. They show that the test statistic, F_0, is greater than the critical F for comparison of populations at t = 60 s to 147 s. Also, the p-value is less than $\alpha = 0.05$. Both these observations lead to the rejection of H_0, meaning that not all of the four size population arithmetic means are equal. This supports the result of the t-test and the F-test reported in Table 2.1, i.e. that the arithmetic mean of population at t=60 s is different from the other three arithmetic means.

The second ANOVA test is performed to compare the arithmetic mean diameters for t = 90, 120, 147 s. As can be seen from Table 2.2, the value of F_0 is now less than the critical F and the p-value is much larger than $\alpha = 0.05$. This large p-value means that there is very weak evidence against H_0, so it cannot be rejected. In other words, the hypothesis that $\bar{d}_i = \bar{d}_j$ where *i, j* = 60, 90, 120, 147 s is likely correct. Additionally, the arithmetic mean diameter for t = 60 s is significantly different from the arithmetic mean diameters at t=90, 120, 147 s. This implies the aggregate size reaches a steady state condition after 90 s of flocculation.

Table 2.2. ANOVA test results for comparison of aggregate mean diameters

	F_0	p-value	critical F
Comparison of means, for 4 flocculation times of t = 60, 90, 120, 147 s	3.076	0.027	2.613
Comparison of means, for 3 flocculation times of t = 90, 120, 147 s	0.320	0.726	3.007

The steady state conditions (with respect to aggregate diameter) can be seen clearly in Fig. 2.4, which demonstrates how the Sauter mean diameter, d_{32}, (or volume-surface mean diameter) changes with flocculation time. The Sauter mean diameter is defined as:

$$d_{32} = \frac{\sum_{i=1}^{n} N_i . d_i^3}{\sum_{i=1}^{n} N_i . d_i^2} \tag{2.14}$$

where N_i is the number of aggregates with a diameter d_i. The mass-mean diameter, d_{mass}, and the arithmetic mean diameter, d_{10}, follow similar trends, as does d_{32}, but they are not presented here. It is clear that flocculation proceeds rapidly (in less than 10 s) and a maximum diameter occurs 15 s after flocculation starts. This trend confirms the dominance of aggregation in the early stages of flocculation. The rapid flocculation observed here is related to the fact that the particles are already de-stabilized through Calcium ion addition and because the initial clay concentration is relatively high compared to many other works reported in the literature (see, for example [41]). Again, the plateau shown in Fig. 2.4 suggests a balance between the aggregation and fragmentation processes, and hence a dynamic quasi-equilibrium. The trend shown in Fig. 2.4 is in accord with the statistical analyses described previously.

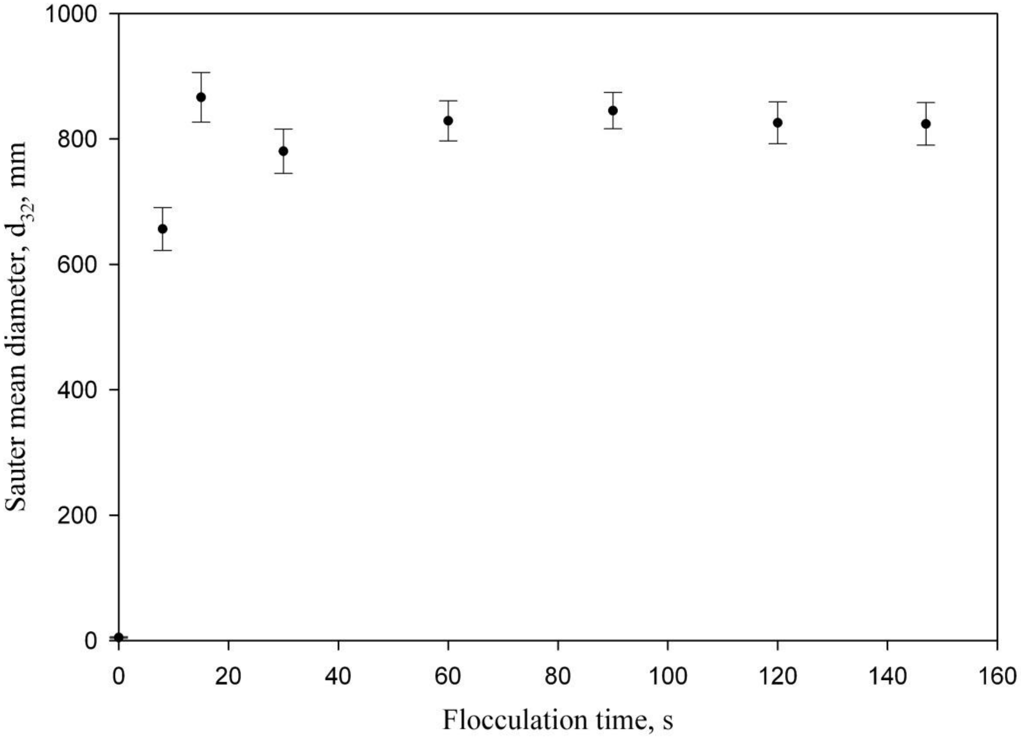

Fig. 2.4. Effect of flocculation time on aggregate mean diameter.

To this point, only the evolution of aggregate size distribution has been discussed. We now examine the evolution of aggregate density and structure.

2.4.2. Aggregate density evolution

The primary floc density, ρ_P, is required in Eq. (2.6) to determine aggregate density (or aggregate porosity). Here, the primary flocs, which represent the primary units of an aggregate, are formed by the destabilization of kaolinite fine particles through the addition of calcium ions. These primary flocs were sensitive to shearing when we tried to measure their size, indicating their fragile nature. The density of the primary flocs was estimated to be $\rho_P = 1625 kg/m^3$ using Eqs. (2.7) and (2.8). A fractal dimension D_{PF} = 2.5 for primary flocs was assumed, and primary floc size was found to be 2.7 μm (see Section 2.3.1.1). The fractal dimension of the flocs that are formed through coagulation of a stable mixture under turbulent conditions in a stirred tank varies between 2.3 and 2.7 [3, 33]. The size and density of the primary particle (Kaolinite particle before destabilization) are 0.64 μm and 2560 kg/m^3, respectively. To estimate ρ_P, these data were applied to Eq. (2.7) along with the structural pre-factor (S) factor that was calculated using Eq. (2.8).

Aggregate settling velocity data for t = 8, 147 s are shown in Fig. 2.5. The aggregate settling velocity exhibits a power law relationship with aggregate area-based diameter as $U_a \propto d_a^{0.83}$ at t = 8 s and $U_a \propto d_a^{0.86}$ at t = 147 s. Similar relationships were observed for other flocculation times. Recall that the exponent for an impermeable sphere in Stokes' regime is 2.0 which gradually decreases with increasing Reynolds number, reaching 0.5 in the Newtonian regime. The corresponding Reynolds number shown in Fig. 2.6 varies from 0.001 to 15 for the data presented in Fig. 2.6. For this range of Reynolds numbers, an exponent less than two is an indication of the fractal-like nature of the aggregates. Also, the Reynolds number range shows that we cannot apply Stokes' law for the entire range of aggregate size-velocity data, considering that for our aggregates, $\beta > 10$. In other words, a drag coefficient correlation to account for the effect of Reynolds number is required. Consequently, Eqs. (2.13) were used to calculate drag coefficient.

The estimated aggregate effective porosity for two flocculation times is shown in Fig. 2.7a. The aggregate porosity was calculated using the set of Eqs. (2.6) and (2.9) through (2.13). These equations were solved numerically using MATLAB. The observed trend between the aggregate porosity and diameter confirms that aggregate porosity increases with size. Also, the data show that the aggregate is primarily comprised of liquid. For example, for an aggregate of d_a = 1000 μm, ε is about 0.95, meaning only 5% of the aggregate volume is made up of solids. This result is in agreement with the data reported in literature for aggregate porosity [5-8, 27].

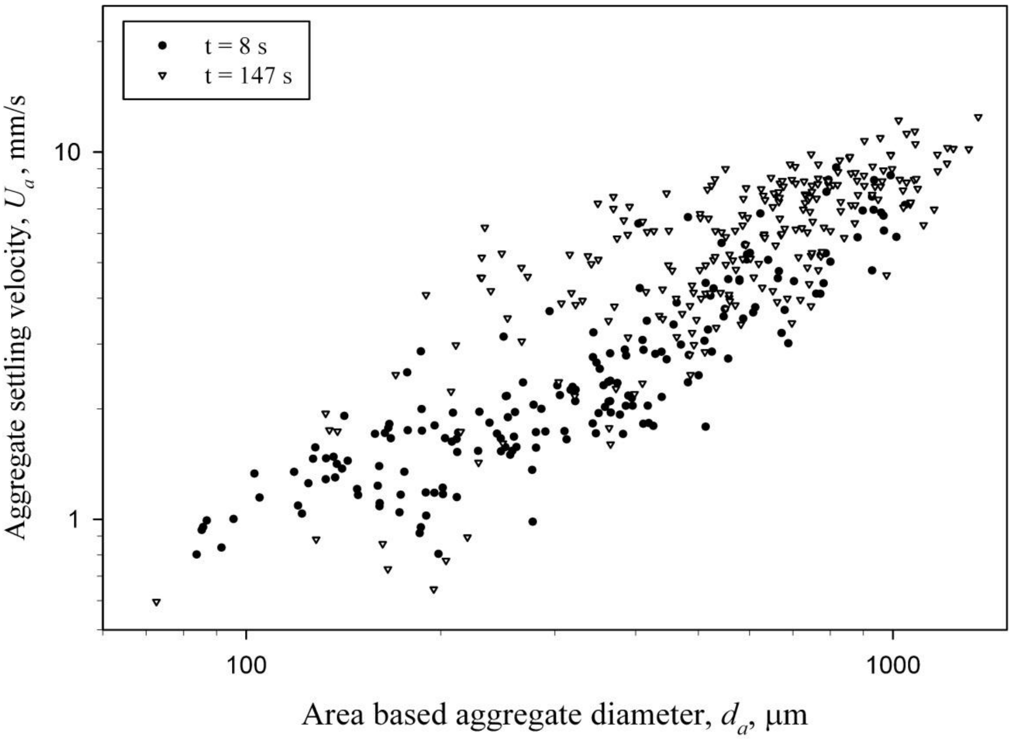

Fig. 2.5. Aggregate settling velocity data for two different flocculation times.

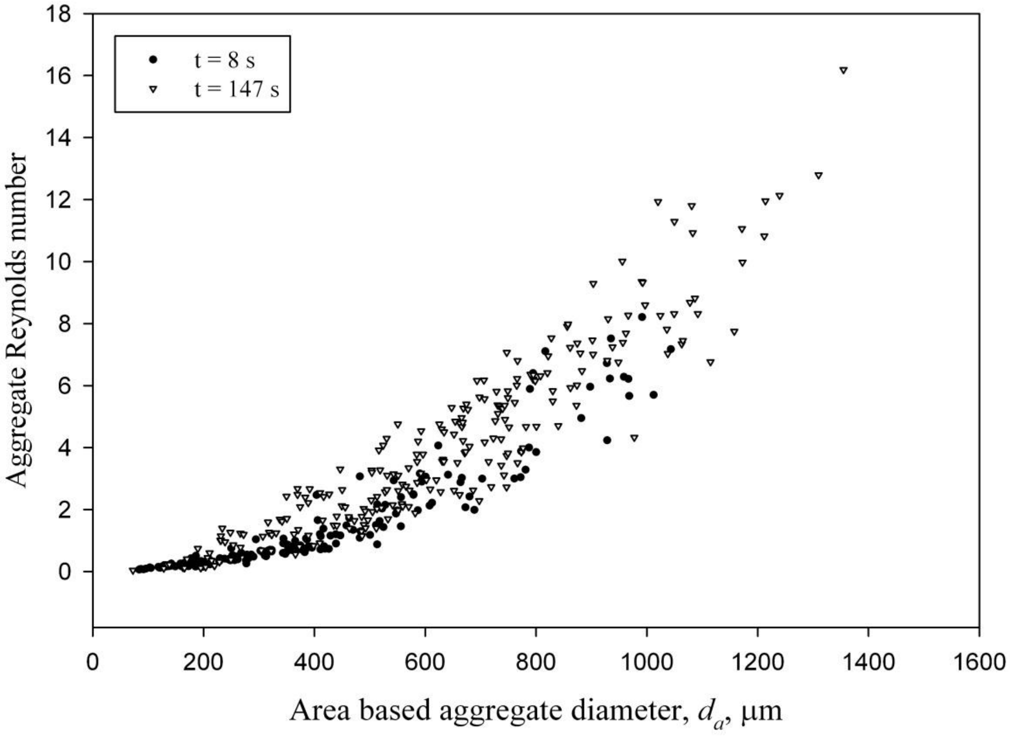

Fig. 2.6. Aggregate Re number as a function of aggregate size for flocculation times of 8s and 147s.

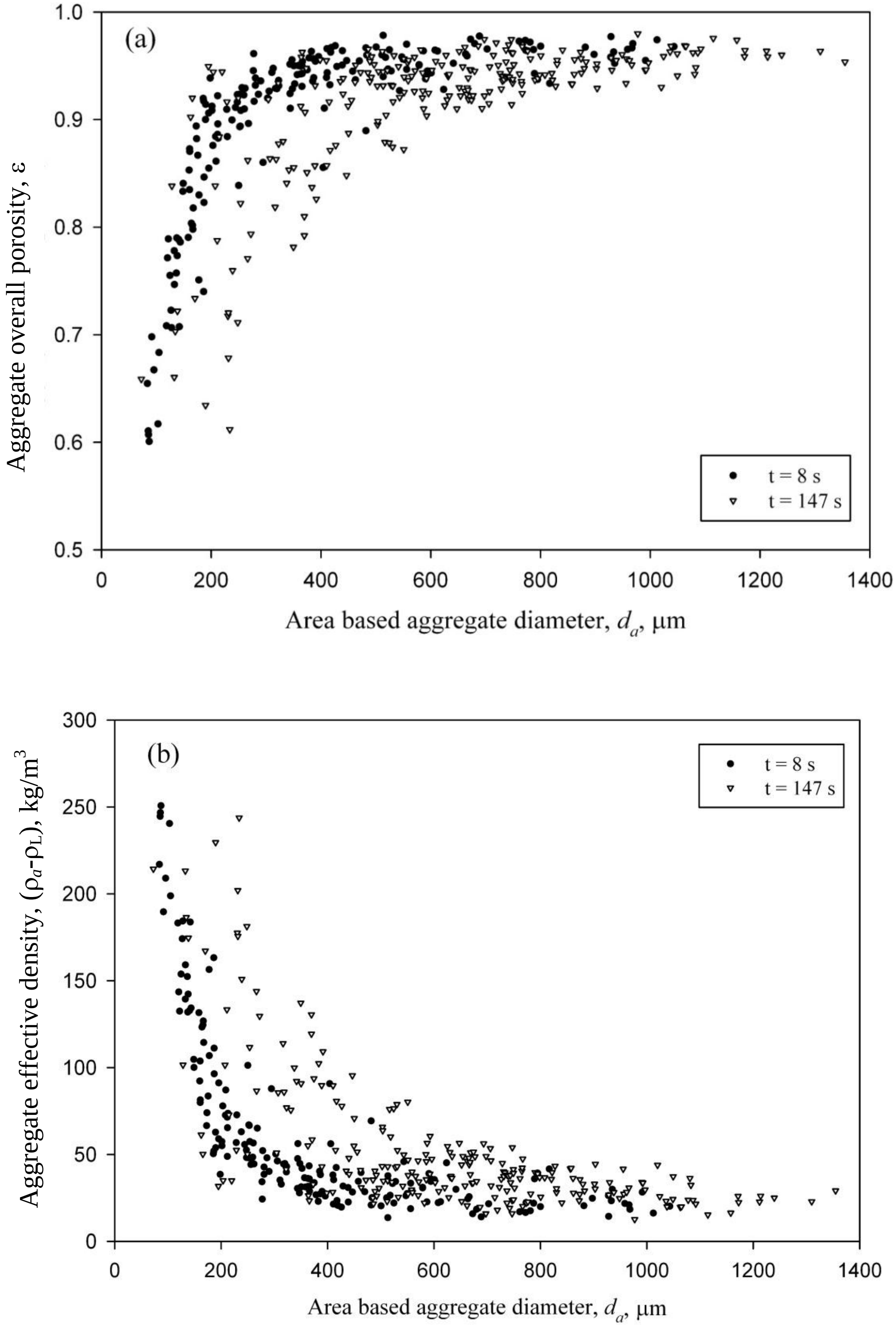

Fig.2.7. Relationship between aggregate size and (a) aggregate porosity, and (b) aggregate effective. Data are shown for flocculation times of 8 and 147 s.

The effective aggregate density $\left(\rho_a - \rho_L\right)$ was calculated using Eq. (2.6) after determining the aggregate porosity. Fig. 2.7b shows how the aggregate effective density changes with diameter for t = 8, 147 s. The result indicates that an aggregate effective density is typically around 10-250 kg/m^3, meaning its density is near the liquid density. This is not surprising as about 95% of aggregate structure is occupied by liquid. The density-diameter trend is common among all flocculation times, indicating that the aggregate effective density decreases as floc size increases in a power law form. This is a feature of a fractal-like object and the result is in good agreement with previously reported results for aggregates of various materials [6, 8, 39]. The rapid decrease in the density with aggregate diameter shows that the size of the pores between primary flocs increases rapidly for larger aggregates.

Number frequency plots of aggregate effective density are shown in Fig. 2.8 for seven different flocculation times. The graph depicts the evolution of aggregate density during the flocculation. We can see in Fig. 2.8 that aggregate density distribution is somewhat broader in the early stages of flocculation (t = 8 s). As aggregates grow, they become less dense. There is no significant difference in density distribution for flocculation times of 15 s to 120 s, indicating that the density population does not change significantly despite the fact that the change in the aggregate size in first 60 seconds of flocculation is significant (see previous section). This is likely because of aggregate-aggregate, aggregate-tube wall contacts and shear force that compact the aggregates. The compaction forces squeeze part of liquid out of the aggregate structure leading to an increase in the aggregate density. This partly compensates for the decrease in density that occurs with increasing aggregate size (see Fig. 2.7b). However, upon compaction, the aggregate size does not change considerably unless breakage occurs. Interestingly, as Fig. 2.8 shows, the density distribution seems to shift slightly towards more dense aggregates at t = 147 s. This behaviour is investigated with statistical analysis in the subsequent sections.

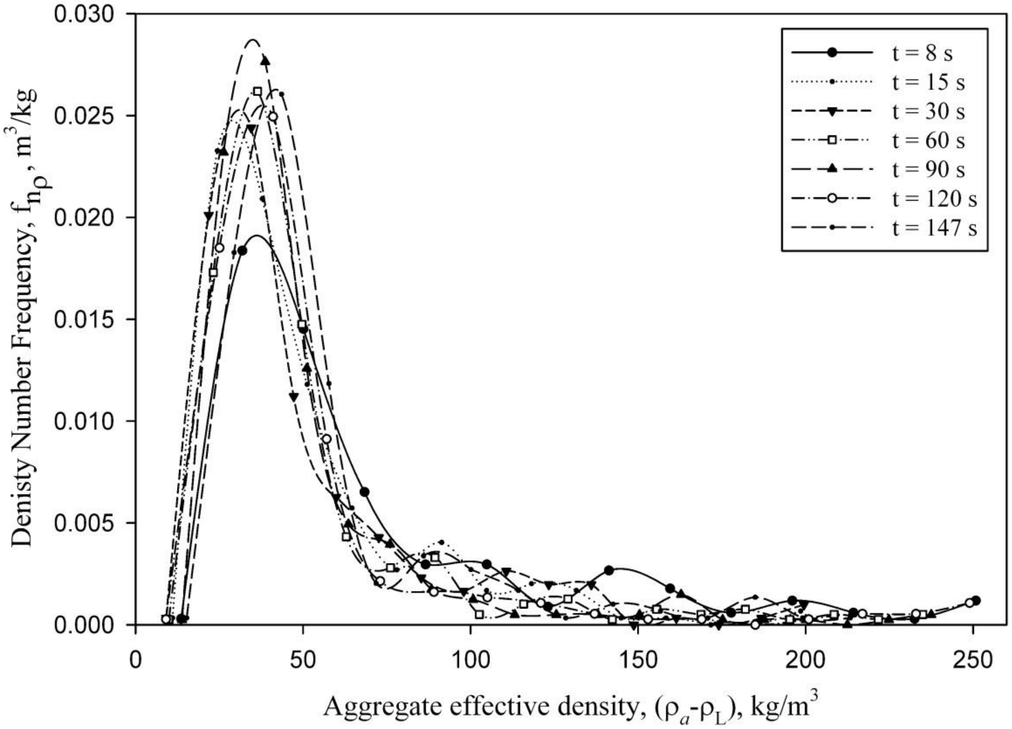

Fig. 2.8. Evolution of aggregate effective density with flocculation time.

The harmonic mean aggregate density is calculated using Eq. (2.15):

$$\bar{\rho}_a - \rho_L = \left(\frac{1}{N_T} \sum_{i=1}^{N_T} \frac{N_i}{\rho_{a_i}} \right)^{-1} - \rho_L \qquad (2.15)$$

and illustrated in Fig. 2.9 for different flocculation times. The estimated average effective density decreases quickly as aggregate size increases. For the primary flocs, the average effective density is 625 kg/m^3 and it decreases to 60 kg/m^3 in the first 8 s of the flocculation process. Aggregates appear within 10 s, and their size increases with increasing flocculation time for 90 s. After flocculation times of 15 s, the mean aggregate effective density does not change significantly, although aggregates grow larger as they spend more time in the flocculator.

As described previously, this is caused by simultaneous aggregate growth, which is associated with a density decrease, and aggregate compaction, which increases density. At longer flocculation times (e.g. t = 147 s), the harmonic average aggregate effective density increases slightly, whereas the aggregate mean Sauter diameter does not change (see Fig. 2.4). This may be governed by aggregate aging and structural conformation.

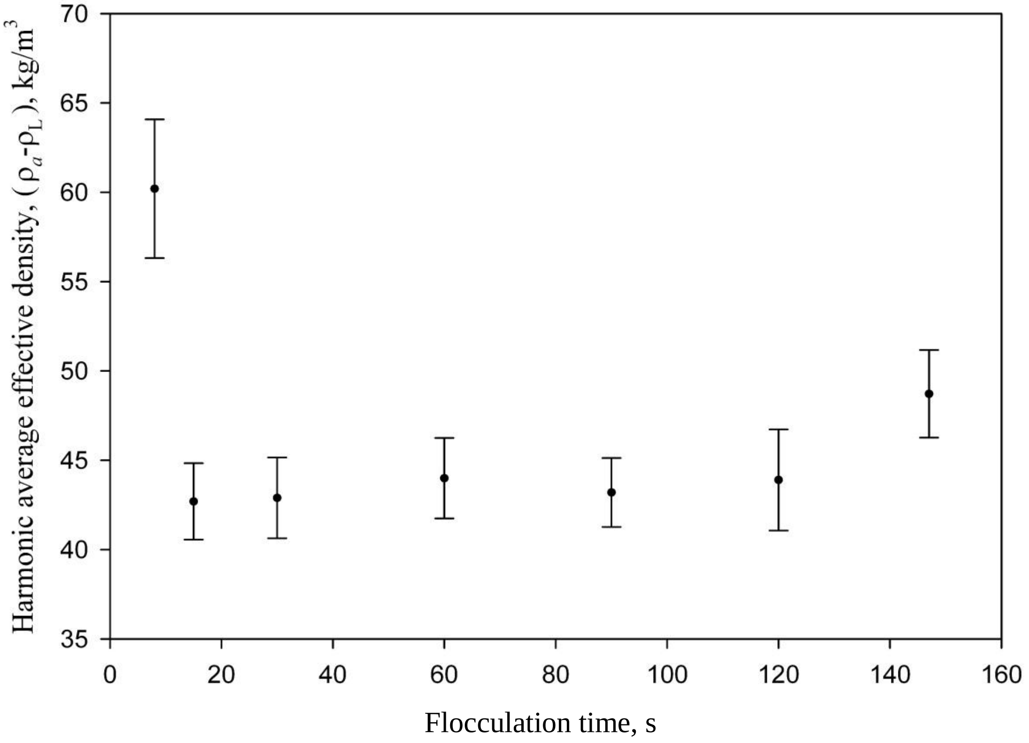

Fig. 2.9. Harmonic average of aggregate effective density.

The results presented in Figs. 2.8 and 2.9 indicate that longer flocculation times may lead to the establishment of a new quasi equilibrium state due to structural conformation phenomenon (or aging). We checked the similarity of aggregate density distribution at all flocculation times and occurrence of aging at longer flocculation times by detailed statistical analysis of the population data shown in the Fig. 9 [39, 40]. For this purpose, the F-test, t-test and ANOVA test were conducted.

The statistical analyses methods are described in Section 4.1. Table 2.3 summarizes the results obtained from the F-test and t-tests. The tests have a significance level of 5 % ($\alpha = 0.05$). Based on the results of Table 2.3, it can be concluded that the arithmetic mean density at $t = 8$ s is different from any other residence time (p-values are less than 0.05, so hypothesis H_0 is rejected). On the other hand, all the p-values for paired t-tests between arithmetic mean densities at $t \geq 15$ s greater than 0.05, meaning hypothesis H_0 is not rejected. In other words, the arithmetic mean densities at $t \geq 15$ s are statistically identical. However, the p-values for a paired test of any residence time and t=147s are slightly greater than 0.05. This shows the statistical test is sensitive to the number of data points and arithmetic mean density at t=147s might be different than those at t=15 to 120s.

Table 2.3. F-tests and T-tests for aggregate density for times of $8 \leq t \leq 147$ s.

H_0	Equal Variances? From F-test	p-value of T-test	Reject H_0?
$\bar{\rho}_8 = \bar{\rho}_{15}$	No	$2.62 * 10^{-5}$	Yes
$\bar{\rho}_8 = \bar{\rho}_{30}$	No	$4.83 * 10^{-5}$	Yes
$\bar{\rho}_8 = \bar{\rho}_{60}$	No	$1.41 * 10^{-4}$	Yes
$\bar{\rho}_8 = \bar{\rho}_{90}$	No	$3.11 * 10^{-5}$	Yes
$\bar{\rho}_8 = \bar{\rho}_{120}$	No	$4.34 * 10^{-4}$	Yes
$\bar{\rho}_8 = \bar{\rho}_{147}$	No	$6.13 * 10^{-3}$	Yes
$\bar{\rho}_{15} = \bar{\rho}_{30}$	Yes	0.891	No
$\bar{\rho}_{15} = \bar{\rho}_{60}$	No	0.596	No
$\bar{\rho}_{15} = \bar{\rho}_{90}$	Yes	0.838	No
$\bar{\rho}_{15} = \bar{\rho}_{120}$	No	0.598	No
$\bar{\rho}_{15} = \bar{\rho}_{147}$	Yes	0.056	No
$\bar{\rho}_{30} = \bar{\rho}_{60}$	Yes	0.707	No
$\bar{\rho}_{30} = \bar{\rho}_{90}$	Yes	0.954	No
$\bar{\rho}_{30} = \bar{\rho}_{120}$	No	0.691	No
$\bar{\rho}_{30} = \bar{\rho}_{147}$	Yes	0.083	No
$\bar{\rho}_{60} = \bar{\rho}_{90}$	No	0.725	No
$\bar{\rho}_{60} = \bar{\rho}_{120}$	No	0.949	No
$\bar{\rho}_{60} = \bar{\rho}_{147}$	Yes	0.176	No
$\bar{\rho}_{90} = \bar{\rho}_{120}$	No	0.711	No
$\bar{\rho}_{90} = \bar{\rho}_{147}$	Yes	0.072	No
$\bar{\rho}_{120} = \bar{\rho}_{147}$	No	0.127	No

To check the probability of equality for the density data more accurately, an ANOVA test is also conducted on the six data sets (t = 15 s to 147 s). Here, the null hypothesis, H_0, is the equality of the arithmetic means of densities or: $\bar{\rho}_{15} = \bar{\rho}_{30} = \bar{\rho}_{60} = \bar{\rho}_{90} = \bar{\rho}_{120} = \bar{\rho}_{147}$ and the alternate hypothesis is H_1: $\bar{\rho}_i \neq \bar{\rho}_j$ for at least one pair (t_i , t_j) for *i* and j = 15, 30, 60, 90, 120, 147 s, where $\overline{\rho}_i$ is the arithmetic mean of effective density population at time *i*. Table 2.4 shows that the test statistic, $F_0 < F$ while $p > 0.05$. This implies that H_0 cannot be rejected; thus, the six arithmetic mean densities obtained from t = 15, 30, 60, 90, 120, 147 s are still statistically equal.

Table 2.4. ANOVA results for comparison of aggregate mean effective density

	F_0	P-value	Critical F
Comparison of density means, for 5 flocculation times of t = 15, 30, 60, 90, 120, 147 s	0.845	0.518	2.220

In summary, the F-tests did not show any specific trend on equality of variances at different flocculation times. The t-Test and ANOVA test results showed that the arithmetic mean density at t = 8 s is different from any other flocculation time. On the other hand, the arithmetic mean densities at t ≥ 15 s are statistically identical. The equality of the arithmetic mean densities at t ≥ 15 does not support the slight increase in the mean aggregate density at t = 147 s indicated by Fig. 2.9. However, the statistical test showed a sensitivity to the number of data points at t = 147 s. Further investigation is required to confirm that aggregate aging may occur at longer flocculation times.

2.4.3. Aggregate structure

Fig. 2.10 demonstrates how the average aggregate mass fractal dimension was calculated by regression of aggregate effective density and area-based diameter using Eq. (2.3). A similar result was obtained by regression of aggregate effective density and Feret diameter. This is in agreement with Gregory’s statement that the choice of L in Eq. (2.3) does not matter [3]. Fig. 2.10 illustrates the best fit lines for t = 8, 147 s. The data are scattered around the best fit line, indicating substantial variation in aggregate density for a given diameter. A similar trend was observed in Figs. 2.7.

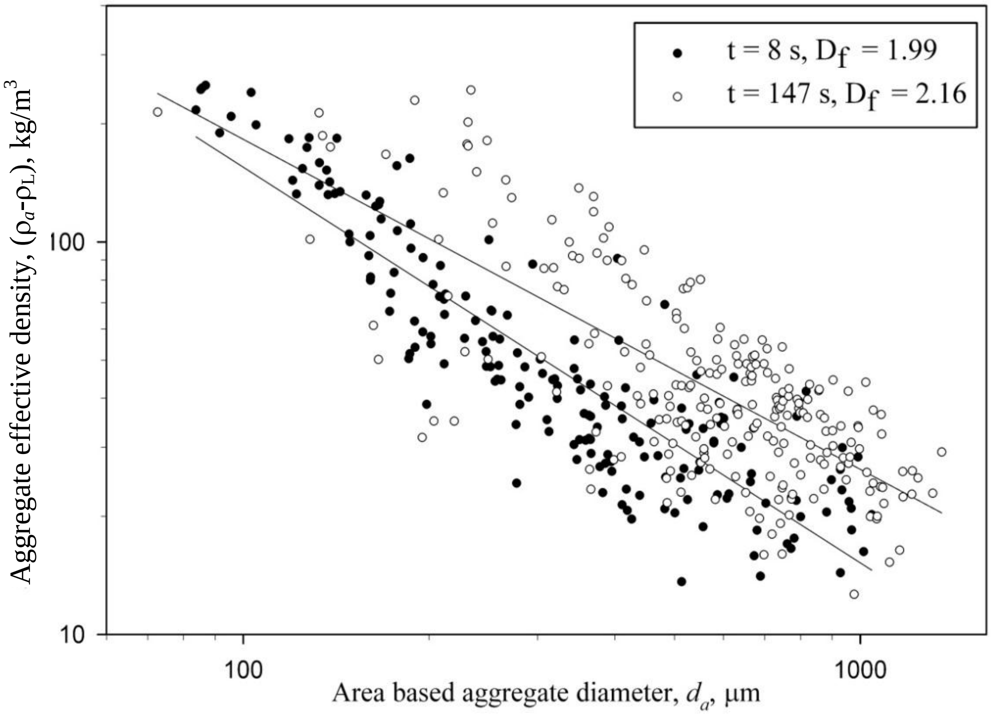

Fig. 2.10. Calculation of mass fractal dimension of aggregates. Lines represent best fit for each of the two flocculation times.

There are three reasons for the scatter in the aggregate density data. An aggregate's history and specifically, how it is formed, can affect its structure and hence its density. Aggregates can have different individual residence times in the flocculation tube because of laminar tube flow dispersion. In addition, when an aggregate collides many times with other aggregates or the tube wall and the collision force does not exceed the aggregate strength, the aggregate density increases. Otherwise it breaks down to form smaller aggregates. As a result, aggregates with identical diameters and shapes can have different porosities/or densities. In other words, an aggregate produced by breakage of a larger aggregate can be denser than an aggregate produced through aggregation of smaller ones.

The second reason is that aggregates are not spherical, but generally irregularly shaped. As a result, the terminal velocity of an aggregate can change substantially with aggregate shape and orientation while settling (see Fig. 2.5).

The orientation affects the drag force, not only because the flow pattern is affected, but also because the drag force depends on the projected area perpendicular to the settling direction. As Lerman [42] stated, the expected settling rates, from fastest to slowest, are for a sphere, a needle, and a disc, respectively. A disc or cylinder-like aggregate may settle much more slowly than a spherical one with the same volume, even though the average area-based diameter of the disc or cylinder may be larger than that of the spherical aggregate.

The third reason for the scatter in the density data of Fig. 2.10 (and Figs. 2.7) is that no particle sizing and density estimation method is perfect for measuring the aggregate size and density. Image analysis has specific advantages and disadvantages. With an imaging technique, we measure the projected area of the aggregate on a plane parallel to the settling direction, while in reality the projected area on a plane perpendicular to the settling direction should be measured. Unfortunately, it is very difficult to measure the projected area for a fragile aggregate. In addition, images are two dimensional rather than three dimensional, meaning that some detailed information about the geometry of the aggregate is not considered. Despite these limitations, image analysis has been used extensively to measure aggregate structural parameters and changes in its morphology. This technique also gives crucial qualitative information about the structure of an aggregate because we are able to see the aggregate.

These three phenomena explain the high degree of scatter in the density measurements and the relatively low regression factor of the mass fractal dimension estimation (see Fig. 2.10). Nevertheless, as Gregory [3] and Bushell et al. [21] note, the settling velocity measurement technique is widely used to measure the aggregate density and fractal dimension. The estimated fractal dimension has been used as an index of aggregate structure with confidence [3, 21, 24].

The mass fractal dimension of aggregates, D_F, for seven different flocculation times is calculated using aggregate diameter and density data (see Eq. (2.3)) and is shown graphically in Fig. 2.11. This figure also shows image fractal dimensions calculated using Eqs. (2.4), which gives $D_i \cong 2.0$. Both methods used to calculate fractal dimension (Eqs. (2.3) to (2.4)) give similar results considering that fractal dimension of an image cannot exceed 2 because of the image geometric opacity. We can confidently rely on the fractal dimension data obtained using either method as they are in excellent agreement. Both show $D_F = 2.0$.

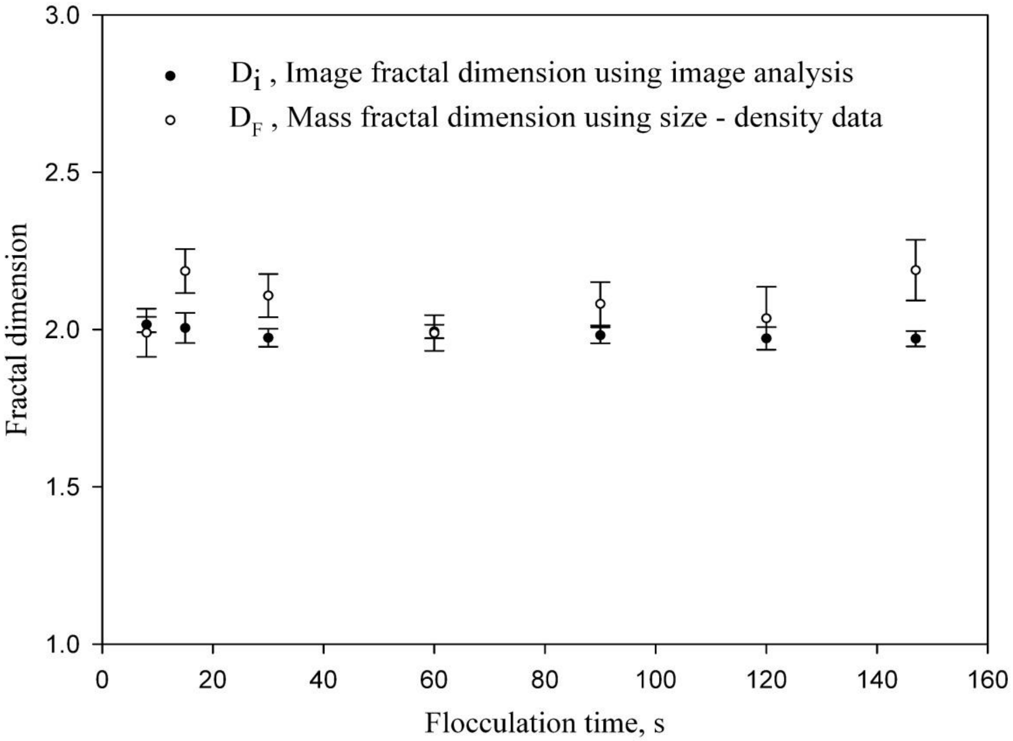

Fig. 2.11. Effect of flocculation time on the aggregate fractal dimension.

The mass fractal dimension of a primary floc was assumed to be 2.5. The aggregation process proceeds quickly after mixing of the destabilized slurry and flocculant; and, mass fractal dimension falls to around 2.0 at t = 8 s and stays nearly constant at 2.0 for t ≥ 15 s. The slight variations of the mass fractal dimension around $D_F = 2.0$ can be consequences of fractal-like nature of aggregates not mathematically ideal fractal aggregates, velocity data scatter, error from density calculation and data regression. These variations might be important in the context of fractal theory, but statistically speaking, the calculated fractal dimensions are constant at different flocculation times.

Mass fractal dimension is an indication of the compactness of an aggregate structure. The fractal dimension data shown in Fig. 2.11 indicate that aggregates formed in our experiments are relatively compact. This makes us more confident about our decision to use Vanni's model to calculate the advective flow correction factor, Ω. The regression factors of mass fractal dimension calculation reported in Table 2.5 are in good agreement with similar studies (see, for example [6, 27]).

Table 2.5. Mass fractal dimension of aggregates for different flocculation times

Flocculation time, s	0	8	15	30	60	90	120	147
Fractal dimension	2.5*	1.99	2.19	2.11	1.99	2.08	2.04	2.19
Regression factor	-	0.792	0.743	0.736	0.834	0.720	0.607	0.593
Number of data points	-	185	225	239	297	326	233	235

* Assumed based on literature data

2.5. Summary

This chapter presented an experimental technique developed to study aggregate structure and kinetics of a two-stage flocculation process using a laminar shear field. Laminar tube flow was shown to be a well-characterized and uniform shear field in which to monitor the flocculation process, especially compared with more conventional geometries, such as stirred tanks that have turbulent hydrodynamics with a random nature.

It also allowed for direct aggregate sampling where their structures were less altered by the sampling as compared to other sampling methods.

The two main aggregate structural parameters, aggregate size and density, were determined from image analysis and settling velocity measurements. Large numbers of aggregates were analyzed to ensure that the results were consistent and statistically representative. Aggregate fractal diameter was calculated using two methods, through a size-density relationship and through image analysis. The methods provided results that were in good agreement.

The kinetics of the flocculation process, i.e. the evolution of aggregate size, density and fractal dimension, was investigated. Results showed that aggregates grow quickly to become relatively tenuous with an open structure in the early stages of the flocculation process. A dynamic steady state condition appeared after 90 s of flocculation time, for the experimental conditions studied here. Aggregate size evolution data and a detailed statistical analysis confirmed that aggregate size did not change beyond the steady state condition.

Aggregate density increases slightly at longer flocculation times, meaning that aggregate aging might have occurred. However, a detailed statistical analysis did not support this hypothesis, implying that the aggregate structural conformation was unlikely to have occurred for the experimental conditions studied here. Further experiments are required to confirm that aggregate aging would not occur at longer flocculation times. The aggregates formed in the laminar tube flow flocculation experiments conducted here had a mass fractal dimension around 2, indicating that the aggregate structure was relatively open.

One of the most important findings of this study is the definition of a set of conditions, in terms of flocculation procedure and process condition, to produce aggregates with defined and reproducible structure. In Chapter 5, we will use these conditions to produce aggregates with a defined structure and then study the effect of shear degradation on the aggregate structure.

2.6. Nomenclature

A_i	Projected area of aggregate (l^2)
C_D	Drag coefficient
d_{32}	Sauter mean diameter (l)
d_a	Aggregate area-based equivalent diameter (l)
$\bar{d}_i$	Arithmetic mean of aggregate size population at time *i* (l)
d_i	Aggregate size at size interval of *i* (l)
D_C	Curvature diameter for a coiled tube, diameter of cylinder tube coiled around (l)
D_F	Mass fractal dimension
D_i	Image fractal dimension
d_K	Dispersed Kaolinite diameter (l)
d_P	Primary floc diameter (l)
D_{PF}	Mass fractal dimension of primary flocs
D_t	Tube internal diameter (l)
De	Dean number for a curved tube
f_{n_d}	Frequency distribution of size, mm^{-1}
F_{n_d}	Cumulative aggregate size distribution, less than %
f_{n_ρ}	Aggregate density number frequency, m^3/kg
F_{n_ρ}	Cumulative aggregate density distribution, less than %
g	Gravitational acceleration ($l\ T^{-2}$)
k	Aggregate permeability (l^2)
L	Aggregate size (l)
N_i	Number of aggregate with size d_i
N_T	Total number of aggregates
Q	volumetric flow rate (l^3T^{-1})
Re_a	Area-based aggregate Reynolds number, $\mathrm{Re}_a = \dfrac{\rho_L U_a d_a}{\mu_L}$
Re_t	Reynolds number inside a tube $\mathrm{Re}_t = \dfrac{4\rho_L Q}{\pi\ \mu_L\ D_t}$
S	Structural pre factor

t	Flocculation time (T)
U_a	Aggregate settling velocity (l T^{-1})
α	Significance level
β	Permeability factor
ε	Aggregate overall porosity
$\bar{\dot{\gamma}}_{Curved}$	Average shear rate in a coiled tube (T^{-1})
$\bar{\dot{\gamma}}_{Straight}$	Average shear rate in a straight tube (T^{-1})
Ω	Advective flow correction factor
ξ	Shielding coefficient of particles interaction
μ_L	Liquid viscosity, (M l^{-1}T^{-1})
ρ_a	Aggregate density (M l^{-3})
ρ_{Eff}	Aggregate effective density, (M l^{-3})
ρ_K	Kaolinite density (M l^{-3})
ρ_L	Liquid density (M l^{-3})
ρ_P	Primary floc density (M l^{-3})
$\bar{\rho}_i$	Arithmetic mean of effective density population at time i (M l^{-3})
Δx	Aggregate settling distance (l)
Δt	Aggregate settling time (T)

2.7. References

1. Cymerman, G., Kwong, T., Lord, E., Hamza, H.A., Xu, Y., “Thickening and disposal of fine tails from oil sand processing”, In: Polymer in Mineral Processing-Proc. 3rd UBC-McGill Int. Symp., (Ed. By) Laskowski, J.S., Metallurgical Society of CIM, Quebec City, 1999, 605-619.
2. Xu, Y., Cymerman, G., “Flocculation of fine oil sand tails”, In: Polymer in Mineral processing-Proc. 3rd UBC-McGill Int. Symp., (Ed. By) Laskowski, J.S., Metallurgical Society of CIM, Quebec City, 1999, 591-604.
3. J. Gregory, (1997). “The Density of Particle Aggregates”, Wat. Sci. Technol., 36, 1-13
4. Farrow, J.B., Johnston, R.R.M., Simic, K., Swift, J.D., (2000). “Consolidation and aggregate densification during gravity thickening”, Chem Eng J. 80, 141-148
5. Huang, H. (1993). “Porosity-size relationship of drilling mud flocs: fractal structure”, Clays and clay Minerals 41, 373-379.
6. Lee, D. J., Chen, G. W., Liao, Y. C., Hsieh, C. C. (1996). “On the free-settling test for estimating activated sludge floc density”, Water Res. 30, 541-550.
7. Li, D.H., Ganczarczyk, J.J, (1989). “Fractal geometry of particle aggregates generated in water and wastewater treatment processes”, Envir. Sci. & Technol., 23, 1385-1389.
8. Tambo, N., Watanabe, Y., (1979). “Physical characteristics of flocs-I The floc density function and aluminum floc”, Water Res., 13, 409-419.
9. Spicer, P.T., Pratsinis, S.E., Raper, J., Amal, R., Bushell, G., (1998). “Effect of shear schedule on particle size, density, and structure during flocculation in stirred tank”, Powder Technol., 97, 26-34.
10. Bouyer, D., Liné, A., Do-Quang, Z., (2004). “Experimental analysis of floc size distribution under different hydrodynamics in a mixing tank”, AICHE J. 50, 2064-2081.
11. Bouyer, D., Coufort, C., Live, A., Do-Quang, Z., (2005). “Experimental analysis of floc size distribution in a 1-L jar under different hydrodynamics

and physiochemical conditions”, J. of Colloid and Interface Sci., 292, 413-428.

12. Coufort, C., Bouyer, D., Line, A., (2005). “Flocculation related to local hydrodynamics in a Taylor-Couette reactor and in a jar”, Chem. Eng. Sci., 60, 2179-2192.
13. Serra, T., Colomer, J., Casamitjana, X., (1997). “Aggregation and breakup of particles in a shear flow”, J. Colloid and Interface Sci., 187, 466-73.
14. Serra, T., Casamitjana, X., (1998). “Effect of the shear and volume fraction on the aggregation and breakup of particles”, AIChE J., 44, 1724-1730.
15. Rahmani, N.H.G. , Dabros, T., Masliyah, J.H., (2004). “Evolution of asphaltene floc size distribution in organic solvents under shear”, Chem. Eng. Sci., 59, 685-697.
16. Gregory, J., (1981). “Flocculation in laminar tube flow”, Chem. Eng. Sci. 36, 1789-1794.
17. Gregory, J., (1985). “Turbidity fluctuations in flowing suspensions”, J. Colloid Interface Sci. 105, 357.
18. Gregory, J., (1987). “Laminar dispersion and the monitoring of flocculation processes”. J. of Colloid and Interface Science 118, 397-409.
19. Berger, S.A., Talbot, L., Yao, L.S., (1983). “Flow in curved pipes”. Ann. Rev. of Fluid Mech., 15, 461-512.
20. McConalogue, D.J., (1970). “The effect of secondary flow on the laminar dispersion of an injected substance in a curved tube”, Proc. Roy. Soc. Lond. A., 315, 99-113.
21. Bushell, G.C., Yan, Y.D., Woodfield, D., Raper, J., Amal, R. (2002). “On techniques for the measurement of the mass fractal dimension of aggregates”, Adv. Colloid Interface Sci. 95, 1-50.
22. Woodfield, D., Bickert, G. (2001). “An improved permeability model for fractal aggregates settling in creeping flow”, Water Res., 35, 3801-3806.
23. Gmachowski, L., (1996). “Hydrodynamics of aggregated media”, J Colloid Interface Sci. 178, 80-86.

24. Jarvis, P., Jefferson, B., Parsons, S. A., (2005). "Measuring floc structural characteristics" Reviews in Environ. Sci. Biotechnol. 4, 1-18.
25. Nasser, M.S., James, A.E., (2007). "Effect of polyacrylamide polymers on floc size and rheological behavior of kaolinite suspensions", Colloids Surf. A PhysicoChem. Eng. Aspects, 301, 311–322.
26. Klimpel, R.C., Hogg, R., (1991). "Evaluation of floc structures", Colloids Surf., 55, 279-288.
27. Li, D., Ganczarczyk, J.J., (1992). "Advective transport in activated sludge flocs", Water Environ. Res., 64, 236-240.
28. Johnson, C.P., Li, X., Logan, B.E., (1996). "Settling velocities of fractal aggregates", Environ. Sci. Technol., 30, 1911-1918.
29. Michaels, A.S., Bolger, J.C., (1962). "Settling rates and sediment volumes of flocculated Kaolin suspensions", Ind. Eng. Chem. Fundamen. 1, 24-33.
30. Li, X.Y., Logan, B.E., (1997). "Collision frequencies between fractal aggregates and small particles in a turbulent sheared fluid", Environ. Sci. Technol., 31, 1237-1242.
31. Gmachowski, L., (2000). "Estimation of the dynamic size of fractal aggregates" Colloids Surf. A Physicochem. Eng. Aspects, 170, 209-216.
32. Neale, G., Epstein, N., Nader, W., (1973). "Creeping flow relative to permeable spheres", Chem. Eng. Sci., 28, 1865-1874.
33. Vanni, M., (2000). "Creeping flow over spherical permeable aggregates", Chem. Eng. Sci., 55, 685-698.
34. Li, X., Logan, B.E., (2001). "Permeability of fractal aggregates", Water Res., 35, 3373-3380.
35. Gruy, F., Cugniet, P., (2004). "Experimental study of small aggregate settling", J. Colloid Interface Sci., 272, 465-471.
36. Concha, F., Almendra, E.R., (1979). "Settling velocities of particulate systems, 1. Settling velocities of individual spherical particles", Int. J. Miner. Process. 5, 349-367.
37. Masliyah, J.H., Polikar, M., (1980). "Terminal velocity of porous spheres", Can. J. Chem. Eng., 58, 299-302.

38. Námer, J., Ganczarczyk, J.J, (1993). “Settling properties of digested sludge particle aggregates”, Water Res. 27, 1285-1294.
39. Montgomery, D.C., “Applied statistics and probability for engineers”, John Wiley, New York, 1999.
40. Montgomery, D.C., “Design and analysis of experiments”, John Wiley, New York, 2001.
41. Biggs, C.A., Lant, P.A., (2000). “Activated sludge flocculation: On-line determination of floc size and the effect of shear “, Water Res. 34, 2542-2550.
42. Lerman, A., “Geochemical processes: water and sediment environment”, Wiley, Newyork, 1979.

Chapter 3

An improved non-spherical drag correlation using a new particle shape factor

3.1. Introduction

An array of processes in the chemical, mineral and metallurgical industries involve the settling of non-spherical solid particles in a stagnant fluid or interaction between solid particles and a moving fluid. Examples include sedimentation of sludge in water treatment and aggregates in flocculation processes, slurry pipeline transportation, fluidized bed systems and multi-phase reactors. Similar fluid-particle interactions are encountered in fields as disparate as meteorology and geology. Meteorology involves the study of the growth and free fall of rain, snow and hailstones as well as pollutant transport in the atmosphere. In geology, the natural transport of sedimentary grains and biological floc motions in rivers and oceans are of interest.

The literature abounds with experimental, theoretical and computational studies describing various aspects of the motion of a spherical particle in an incompressible viscous media, especially at low to intermediate Reynolds numbers [1]. Numerous empirical correlations that describe the steady settling of a sphere in a quiescent media at higher Reynolds numbers can be found [1-4]. Based on a combination of computational results and experimental correlations, it is now possible to predict the drag force on a moving spherical particle in a viscous media. The results are normally represented by a drag coefficient correlation. In most conditions of practical interest, the sphere drag coefficient, C_{D_S}, correlates with the particle Reynolds number, *Re*, with reasonable accuracy [5]:

$$C_{D_S} = f_1(Re) \tag{3.1}$$

In contrast, theoretical studies on non-spherical particles are limited to creeping flows and idealized shapes, mostly axisymmetric and slender bodies [1,6]. The limitation arises from the fact that at higher Reynolds numbers, the flow around a non-spherical particle is very complex. The complex flow pattern is a consequence of flow separation, oscillation, rotation and instability of the particle orientation [1,5]. It is generally recognized, and supported by experiments, that non-spherical particles have greater drag coefficients than a sphere under similar flow conditions [1,5,7]. Dimensional analysis shows that the drag coefficient for a non-spherical particle can be estimated from its Reynolds number, a shape descriptor, Λ, and an orientation descriptor, Γ [5]:

$$C_D = f_2\left(Re, \Lambda, \Gamma\right) \tag{3.2}$$

There are two distinct approaches to estimate the drag coefficient of a non-spherical particle. The first approach uses a shape-specific correlation. The second approach is based on a universal correlation applicable for any shape and orientation. Shape-specific correlations are numerous as there are many possible particle shapes. However, they are unlikely to predict drag coefficients of highly irregular particles to any reasonable degree of accuracy. The universal correlation approach, which has become increasingly popular over the past 20 years, typically requires specifying one to three parameters as shape and orientation descriptors. The main obstacle in developing a universally applicable correlation is the inherent difficulty in describing the size, shape and orientation of a non-spherical particle unambiguously. Furthermore, these shape and orientation descriptors are based on particle geometrical measurements that are often difficult or impossible to make in most practical applications, such as online particle characterization.

The primary objective of this study is to obtain a reliable, generalized and accurate correlation that predicts the drag coefficient of non-spherical particles using a minimum number of geometrical parameters. Subsequent to a thorough review of the shape descriptions of non-spherical particles, a new shape factor is defined after evaluating all possible shape factors that can be defined using different geometrical parameters. Side view-geometrical parameters that are determined after particle projection in a plane parallel to the direction of its motion have been taken into consideration. The new shape factor is then used to correlate experimental drag data. An extensive bank of experimental data, taken from the literature, is presented with the intention of covering as many shapes as possible. Predictions of the drag coefficient using the new correlation are evaluated against experimental measurements and compared with two of the more accurate drag correlations available in the literature.

3.2. Previous studies

3.2.1. Size and shape descriptors

Natural and man-made solid particles occur in almost every imaginable shape. There is not a single approach to accurately describe the size and shape of non-spherical particles, particularly irregular ones. In fact, the problem of accurately predicting particle drag is really a problem of describing the size and shape of irregular non-spherical particles.

Size and shape descriptors are normally evaluated using some combination of four geometric factors [1]:

- volume,
- surface area,
- projected area normal to a specific plane,
- projected perimeter normal to a specific plane

Clift et al. [1] provide a summary of methods used to quantify the size and shape of a non-spherical particle.

Below, we review some of the most common size and shape descriptors found in drag coefficient correlations. In each case, we describe how the geometric factors are used. The merits of different approaches are summarized.

3.2.1.1. Size

One of the most common methods of specifying the size of non-spherical particles is on the basis of an “equivalent sphere,” defined as a sphere with the same value of one of the four geometric parameters listed above. The volume-equivalent sphere diameter, or nominal diameter, d_V, is defined as [1,8]:

$$d_V = \left(\frac{6V_P}{\pi}\right)^{\frac{1}{3}} \qquad (3.3)$$

This definition has been used extensively to define the Reynolds number and drag coefficient [1,4,8,9].

A similar size descriptor is defined as the diameter of a sphere with the same projected area of the particle in a plane normal to the direction of flow [1,8]:

$$d_P = \left(\frac{4A_P}{\pi} \right)^{\frac{1}{2}} \tag{3.4}$$

Only a few drag coefficient correlations are based on the normal view-projected area equivalent sphere diameter, d_P. In some studies, the ratio of $\left(d_P / d_V\right)$ is used as a pertinent shape factor describing particle orientation in drag coefficient correlations [9-14]. However, it is not easy to estimate d_V and d_P in many practical applications due to the difficulties in measuring particle volume and particle projected area on a plane perpendicular to the direction of motion.

3.2.1.2. Shape factors

A particle shape factor is normally described as the ratio of one of the characteristic geometric factors to the corresponding value for an equivalent sphere. For example, the Wadell sphericity, ψ , is defined as the ratio of the surface area of the volume-equivalent sphere to the actual surface area of the particle, S, [1]:

$$\psi = \frac{\pi\, d_V^2}{S} \tag{3.5}$$

Sphericity is perhaps the shape factor used most frequently in existing drag correlations. However it provides no information about particle orientation [4,7,9-12,14-18]. Haider and Levenspiel [4] note that sphericity is the best shape factor to describe isometric particles, but it performs poorly in describing non-isometric particles. Furthermore, it is difficult and sometimes impossible to determine the sphericity for highly irregular particles due to difficulties associated with the measurement of particle surface area [1,5,19]. This difficulty is often encountered in online particle geometry identifications. Bowen and Masliyah [20] also showed that the drag coefficient of axisymmetric particles did not correlate well with sphericity in the viscous regime. Consequently, in some studies a second (and sometimes even third) shape factor is used to correlate the drag coefficient data [9-12,18].

Particle circularity, c, which is also referred to as surface sphericity, is defined as follows [1]:

$$c = \frac{\pi\, d_P}{P_P} \tag{3.6}$$

where P_P is the projected perimeter of the particle in a plane normal to its direction of motion and d_P is given by Eq. (3.4). It is easier to measure the circularity of a particle than its sphericity because d_P and P_P can be determined from microscopic or photographic analysis.

It is interesting to note that circularity has been rarely used to correlate the particle drag coefficient. In fact, to the authors' knowledge, Tran-Cong et al. [21] may provide the only example. One of the disadvantages of using circularity is that it may yield identical values for objects of different shape. For example, a cylinder falling axially and a sphere have the same circularity. For online measurement of particle shape, circularity does not provide any advantage because it is extremely difficult to obtain the projection of a particle shape on a plane normal to the direction of motion.

Many authors [e.g. 5,19,22-27] attempted to use the Corey shape factor, β, which is defined as:

$$\beta = \frac{Z}{\sqrt{X\,Y}} \quad ; \quad X > Y > Z \tag{3.7}$$

where X, Y and Z are the lengths of the three principal axes of a particles. The Corey shape factor is defined to correspond with the observation that in transition and turbulent regimes, particles usually orient themselves such that they present the maximum projected area to the passing fluid [19,22]. Here, the maximum projected area is approximated by $X\,Y$. The Corey shape factor can also describe the relative flatness of a particle [19].

Unlike sphericity, the Corey shape factor does not require characterization of particle surface. For this reason, a number of researchers have found this shape factor appropriate in correlating their experimental results [5,19,22]; however, Alger and Simons [28] showed its relative inadequacy for their own data. Recently, Loth [27] attempted to apply the Corey shape factor to Ganser's method [9]. While his results are promising, he noted the uncertainty associated with correlations based on the Corey shape factor and suggested they be used only to obtain a rough estimate of the drag coefficient. It appears that further investigation in application of the Corey shape factor might be beneficial.

Bowen and Masliyah [20] introduced another shape factor, Σ:

$$\Sigma = \frac{S}{S'_P} = \frac{\pi S}{P_I^2} \tag{3.8}$$

where S'_P is surface area of a sphere with the diameter of an equivalent circle that has same side view-projected perimeter, P_I, as the non-spherical particle. They found this shape factor to be most useful for axisymmetric particles with creeping flow parallel to the axis of symmetry [1,20]. There has been no investigation of the applicability of this shape factor in transition and turbulent flow regimes.

Many other shape factors have been defined, e.g. Heywood volumetric shape factor, Janke shape factor, Hofmann shape entropy [1,29]. However, they have not been used in many applications because of their complexity and/or inadequacy over a broad range of particle shape.

The number and variety of shape factors as summarized above indicates that it is nearly impossible to unambiguously describe a particle's shape and orientation. Clearly, each shape factor has its merits and limitations. One of the most important considerations in selecting a shape factor, then, is the particle characterization techniques used. This will be demonstrated subsequently.

3.2.2. Drag correlations for non-spherical particles

Two different approaches are available to predict the drag coefficient of a non-spherical particle. In the first approach, an expression is developed for a specific particle shape and orientation. In the second approach, a "universal" correlation is developed for a broad range of particle shapes and orientations. Shape-specific correlations are generally more accurate than universal correlations. However, each particle shape requires a different expression and shape-specific correlations are also not suitable for irregularly shaped particles. The universal drag expression is more useful for design and engineering applications, despite the fact that it may be less accurate than shape-specific correlations.

Many attempts to obtain shape-specific drag coefficients using computational modeling and experimental measurements are reported in the literature. For example, Michael [30] solved the Navier-Stokes equations for a disk in the Reynolds number range of 1.5 to 50. Davis [31] presented an analytical method used to calculate the drag on disks in the creeping flow regime. Masliyah and Epstein [32] numerically evaluated skin and form drag coefficients of oblate and prolate spheroids with aspect ratios of 0.2, 0.5 and 0.9 for $Re \leq 100$. Pitter et al. [33] extended Masliyah and Epstein's [32] results to an aspect ratio of 0.05 and compared numerical results with some experimental data.

Computation-based approaches, such as the one described by Pitter et al. [33], provide a fundamental understanding of the fluid-particle interactions and flow field around particles. However, this method is time consuming and costly in terms of computational power and generally does not provide accurate results for transition and turbulent regimes. Furthermore, any drag expression obtained through numerical simulation should be validated by conducting experiments.

There are also numerous examples of shape-specific empirical correlations based on experimental measurements. Ui et al. [34] presented empirical correlations for disks and cylinders at low Reynolds numbers ($Re < 1$). McKay et al. [35] correlated their own experimental data for cylinders with aspect ratios of 0.25 to 5 over a broad range of Reynolds numbers. Unnikrishnan and Chhabra [14] obtained a drag coefficient correlation for cylinders with aspect ratios of 0.05 to 2 for $0.2 < Re < 180$ using experimental data. Militzer et al. [36] developed a drag coefficient correlation for spheroidal particles for Reynolds numbers between 1 and 200. Sharma and Chhabra [37] reported an experimental drag coefficient for cones with *0.8 < Re < 475*. Madhav and Chhabra [17] developed an experimental drag correlation for *0.1 < Re < 400*. They claimed that when the volume-equivalent sphere diameter is used to calculate the Reynolds number, a single correlation can provide a reasonable estimate of the drag coefficient for cylinders, needles and rectangular prisms.

In summary, shape-specific correlations are beneficial for specific processes where the particle shape is well defined and a correlation was previously developed. The reality is that the diversity of particle shapes, particularly for applications involving irregular particles, requires tremendous effort to develop individual correlations for each particle shape.

In the second approach, a single correlation is developed as a universal expression for all shapes and orientations of non-spherical particles. Universal correlations are superior to shape-specific correlations as they can be applied to nearly any shape, making them quite useful for practical applications. For example, Pettyjohn and Christiansen [7] collected a data bank for the drag coefficient of spheres and four isometric non-spherical particles covering a broad range of Reynolds numbers. They attempted to correlate two dynamic shape factors, defined for Stokes' and Newton's regimes, with sphericity. These dynamic shape factors are discussed subsequently. For the intermediate region, they presented a graph comprised of curves plotted for constant sphericity. Instead of a graph for the intermediate region, Geldart [38,39] proposed a simple interpolation based only on the Reynolds number to use Pettyjohn and Christiansen's correlation for dynamic shape factors. The Pettyjohn and Christiansen [7] data bank has been used extensively in many studies [9,11,18,27].

Haider and Levenspiel [4] developed a drag coefficient correlation for spherical and non-spherical particles using experimental data reported in the literature. Their drag correlation takes the general form of [4]:

$$C_{D_V} = \frac{24}{Re_V}(1 + B_1\, Re_V^{B_2}) + \frac{B_3}{\left(1 + \dfrac{B_4}{Re_V}\right)} \tag{3.9}$$

Where Re_V is based on the volume-equivalent sphere diameter and C_{D_V} is the volume-equivalent sphere drag coefficient, hereafter denoted the volumetric drag coefficient. The constants B_1 to B_4 were assumed to be functions of sphericity and were found by regression of the experimental data (419 data points for isometric solids, 87 data points for disks and non-isometric solids and 408 data points for spheres). This correlation gives poor predictions for particles having a sphericity of less than 0.67 [4,6].

Ganser [9] revisited Haider and Levenspiel's work and introduced a universal drag correlation:

$$C_D^* = \frac{24}{Re^*}(1 + 0.1118 Re^{*0.6567}) + \frac{0.4305}{\left(1 + \frac{3305}{Re^*}\right)} \qquad (3.10)$$

where the normalized drag coefficient, C_D^*, and the normalized Reynolds number, Re^*, are defined as [9]:

$$C_D^* = \frac{C_{D_V}}{K_{N_V}} \qquad (3.11)$$

$$Re^* = Re_V K_{St_V} K_{N_V} \qquad (3.12)$$

Ganser [9] normalized the Reynolds number using two dynamic shape factors, K_{St_V} and K_{N_V}, defined for creeping flow and turbulent flow regimes respectively. Stokes' dynamic shape factor, K_{St_V}, is defined as the ratio of the drag coefficient of the volume-equivalent sphere to that of the non-spherical particle in the creeping flow regime, i.e. Stokes' regime [1,7,9-11]:

$$K_{St_V} = \left(\frac{\left({}^{24}\!/_{\mathrm{Re}_V} \right)}{C_{D_V}} \right)_{Stokes} \qquad (3.13)$$

Stokes' dynamic shape factor is also equivalent to the ratio of the settling velocity of the non-spherical particle to that of the volume-equivalent sphere with identical particle density settling in the same fluid. There have been many different theoretical and experimental attempts to correlate Stokes' shape factor with a geometrical shape factor, mostly with sphericity [1,7,10-13,18,20,23,27, 40]. Leith [11] introduced an expression for K_{St_V} based on the concept that in the creeping flow regime, form drag comprises one-third of the total drag on a sphere (See Appendix 3.4). He developed a simple expression based on particle sphericity. Its theoretical foundation and reasonable accuracy make it more useful than many other expressions found in the literature, e.g. [7,9,10,20,27].

Newton's dynamic shape factor, K_{N_V} , is defined as ratio of the drag coefficient of a non-spherical particle, C_{D_V} , to that of a sphere, C_{D_S} , in the fully turbulent regime, i.e. Newton's regime [7,15]:

$$K_{N_V} = \left(\frac{C_{D_V}}{C_{D_S}}\right)_{Newton} \tag{3.14}$$

Thompson and Clark [15] defined this dynamic shape factor at Re_V = *10,000*. They attempted to correlate the drag coefficient with K_{N_V} instead of using a geometrical shape factor, regardless of flow regime. They also tried to correlate K_{N_V} with particle sphericity; however, the result was not satisfactory. Ganser [9] modified Thompson and Clark's approach and correlated K_{N_V} with sphericity (See Appendix 3.4). Recently, Loth [27] correlated K_{N_V} with the Corey shape factor but the result was unsatisfactory.

Chhabra et al. [6] provide a critical review of available empirical correlations. They collected the experimental results of 19 independent studies, which included many different particle shapes. Their comparison showed that the Ganser correlation provided the most accurate predictions of the drag coefficient, as of 1999. They also noted that further improvement in the accuracy of predictions could only be achieved by using additional shape/orientation descriptors [6]. Recently, Hölzer and Sommerfeld [18] correlated data taken from the literature using three shape factors: Wadell sphericity, cross-wise sphericity and length-wise sphericity. Cross-wise and length-wise sphericities were used as orientation descriptors where cross-wise sphericity is related to (d_P/d_V). Here, this correlation will be referred to as the H & S correlation. It was shown that the H & S correlation provides more accurate predictions for disks and plates compared with the Haider and Levenspiel [4] and Ganser correlations. No improvement was observed for spheres, isometric particles, cuboids and cylinders [18]. Hölzer and Sommerfeld [18] reported that, overall, predictions by the H & S correlation are more accurate than those obtained using the Ganser correlation. They claim that the H & S correlation is the most accurate because it is based on three shape/orientation factors. However, they recognize that it is likely impossible to obtain length-wise sphericity for many applications and suggest that length-wise sphericity can be approximated with cross-wise sphericity. This approximation reduced the H & S correlation to the same degree of accuracy and complexity as the Ganser correlation, with each having two shape/orientation factors of sphericity and a (d_P/d_V) dependent factor (cross-wise sphericity).

Previous studies focused on finding out a way to describe the orientation of a settling non-spherical particle. However, orientation may change in different flow regimes. Studies show that in a completely viscous regime, a particle settles in the orientation that it is positioned [1], meaning orientation is stable during settling. In transition and turbulent regimes, however, a particle is likely to be oriented such that its greatest projected area is normal to the direction of motion [1,19,22]. We refer to this orientation as the preferred orientation. In other words, description of particle orientation may not be required except in creeping flow regime. Furthermore, in transition and turbulent regimes, most of non-spherical particles do not have a stable orientation (including the preferred orientation) and thus an orientation descriptor is not appropriate. For example, a disk can have regular oscillation, glide-tumble and tumble pattern in which the disk even rotates through 360°. Such behaviour depends on the thickness-to-diameter ratio, Reynolds number and the ratio of disk-to-fluid density. This means that the disk has an unstable orientation that cannot be described easily with any orientation descriptor [5,46]. Therefore, the exposure of the greatest projected area to the flow, i.e. preferred orientation, is a trajectory-averaged approximation. This approximation is to be used to develop a new drag correlation using a single shape factor in subsequent sections.

As previously described, most of the available shape factors require the measurement of particle surface area, which is difficult to obtain for fragile particles and particles with highly irregular shapes and/or rough surfaces. Therefore, we define a new shape factor that can be determined with a minimum number of geometrical parameters. The result of our analysis showed that the combination of this new shape factor, the preferred orientation approximation and the volume-equivalent sphere diameter allow us to correlate drag data with reasonable accuracy.

3.3. Equation development

In many applications, online particle characterization techniques are used, in which the particle geometry is assessed using a two-dimensional view of the particle in a plane parallel to the direction of motion. This view does not provide any information about the volume, the surface area and the projected area of the particle on a plane perpendicular to the direction of flow. Therefore, we analyzed combinations of different geometrical factors to find the most appropriate shape descriptor, with an emphasis on the geometrical factors readily obtained from a side view of the particle.

3.3.1. Side view-shape descriptors

Possible combinations of different measurable geometrical factors can lead to many different ways to describe particle shape [1,20]. Nevertheless, most of these shape factors require geometrical properties that are difficult to measure. We define here a number of shape factors, using mainly side view-geometrical information. Appendix 3.1 summarizes these shape factors. Our attempts to correlate non-spherical drag data with the shape factors defined in Appendix 3.1 show that the most useful shape factor is “degree of roundness,” ϕ. It is defined as the ratio of the side view-projected area of the particle to the area of a circle having the identical side view-projected perimeter as the particle:

$$\phi = \frac{4\pi A_I}{P_I^2} \tag{3.15}$$

where A_I and P_I are the side view-projected area and the side view-projected perimeter of the particle respectively, that are obtained from projection of particle in a plane parallel to the direction of motion. For a sphere, the degree of roundness is unity and for a non-spherical object it is less than one.

3.3.2. Drag coefficients and Reynolds numbers

The drag coefficient, C_D, for a particle moving with a uniform velocity of U in an infinite quiescent fluid is defined in terms of the drag force, F_D, and the force attributed to the dynamic pressure:

$$C_D = \frac{2F_D}{\rho_L A U^2} \tag{3.16}$$

where ρ_L is the density of the fluid and A is the characteristic surface area of the particle.

In the case of a freely settling particle, the drag force is balanced by the particle's immersed weight, $(\rho_P - \rho_L) g V_P$. The steady-state force balance leads to following expression:

$$C_D = \frac{2g(\rho_P - \rho_L)V_P}{A\rho_L U^2} \tag{3.17}$$

where ρ_P is the particle density, g is the gravitational acceleration and V_P is the particle volume. Two forms for determination of the non-spherical drag coefficient can be found in the literature, depending on the definition of A. In the main body of the literature, experimentally determined drag coefficients are reported in the form of a volumetric drag coefficient, C_{D_V}. In this form, the projected area of the volume-equivalent sphere, $(A_V = \pi d_V^2/4)$, is substituted for A in Eq. (3.17) [4,7,9-11,26,31,41-43]:

$$C_{D_V} = \frac{4g(\rho_P - \rho_L)d_V}{3\rho_L U^2} \tag{3.18}$$

The second form relies on the classic definition of the drag coefficient, where the actual projected area of the particle in a plane perpendicular to the direction of motion, A_P, is substituted for A in Eq. (3.17) [14,17,21,28,35,37,44,45]:

$$C_{D_P} = \frac{4g(\rho_P - \rho)d_V^3}{3d_P^2\,\rho_L U^2} \tag{3.19}$$

These two forms of the drag coefficient are related through the ratio of $(d_P/d_V)^2$.

The non-spherical particle's Reynolds number can be defined using different characteristic particle length scales. For example, in many studies particle-characteristic diameter, e.g. diameter for a cylinder, is employed [14,45,46]. Other studies use hydraulic diameter [44] or surface area-equivalent sphere diameter [28] to determine the Reynolds number. The most widely used definition of the Reynolds number is based on the volume-equivalent sphere diameter, d_V [4,7,9,17,22,35,37,41,43]:

$$\mathrm{Re}_V = \frac{\rho_L U\, d_V}{\mu_L} \tag{3.20}$$

A few studies mention that drag data are correlated more effectively with Re_V than with any other form of the Reynolds number [17,19]. In this study, Re_V is used to develop the drag coefficient correlation.

3.3.3. Data bank

In order to cover a wide range of conditions, in terms of hydrodynamics and particle shape, more than 2100 experimental data points reported in the literature were collected. Table 3.1 summarizes the data bank collected for this study. Part of this voluminous data bank was used to develop a new drag coefficient correlation; the remainder was used to validate the performance of the new drag correlation.

Table 3.1. Summary of data used in this study.

Investigator(s)	Particle shape	N	Re_V	Used in*
Baba and Komar [24]	Irregular sand grain (ellipsoidal)	72	0.04 - 2.2	V
Heiss and Coull [10]	Cylinders and prisms	24	<0.1	C
Issacs and Thodos [45]	Cylinders	6	200 – 60e3	C
Johnson et al. [12]	Plate like prisms	62	0.1 - 1.6	C / V
Komar [43]	Cylinders	29	0.09 - 3	C / V
Lasso and Weidman [41]	Cylinders	66	0.05 - 1.5	C / V
List and Schemenauer [53]	Broad-branched crystal, cones, dendrite, disk, hexagonal plate, stellar crystal with plates, stellar crystal	340	0.03 - 875	V
McKay et al. [35]	Cylinder	66	9 - 5,700	C / V
Pettyjohn and Christiansen [7]	Cube, cube octahedron, octahedron, sphere, tetrahedron	635	2e-5 - 22,650	C
Data of Corey, Malaika, Wilde and Schulz through Schulz et al. [19], McNown et al. [22]	Cylinders, double cones, spheroid, square prism, natural sedimentary sands (ellipsoidal), sand grains from rock crusher fragments and gravels	421	1e-3-18e3	C/ V
Sharma and Chhabra [37]	Cones	8	0.5 - 292	V
Sheaffer [13]	Plate like prisms	40	0.07 - 0.4	C / V
Squires and Squires [44]	Thin disks, falling axially	50	0.002 - 5.4	V
Stringham et al. [5]	Cylinders, disks, oblate, prolate	186	6 - 94,000	C / V
Unnikrishnan and Chhabra [14]	Cylinders and sphere	11	0.2 - 180	C / V
Wang et al [54]	Hemisphere and spherical caps	72	26 - 13,390	V
Willmarth et al. [46]	Thin disks	54	0.4 - 6,300	C / V

* C = Correlation; V = Validation; N = Number of data points

3.3.4. Data processing and corrections

Fluid properties, particle geometrical factors and measured hydrodynamic parameters were extracted from the collected experimental data (see Table 3.1). Reynolds numbers, drag coefficients and shape factors were calculated using the equations defined in Sections 3.2 and 3.3. The collected data were examined carefully and any outliers were excluded from further analysis.

For cases where the orientation was not reported, a preferred orientation was assumed. The preferred orientation assumes exposure of the maximum projected area normal to the direction of motion. This assumption is valid at high Reynolds numbers and is supported by experimental observations [1,5,19,22]. However, in fully viscous regime, particles do not have a preferred orientation [1,10]. Therefore, the preferred orientation assumption may influence the relationship between drag coefficient and geometrical shape factor for some measurements in the Stokes' regime. A second assumption, related to the side view, was made. In order to calculate the degree of roundness, a side view of the particle in which the largest axis of the particle was visible was chosen. The primary consequence of adopting these assumptions is that the largest axis of the particle is assumed to be perpendicular to the direction of the particle's motion.

3.3.4.1. Wall effect

In some of the studies, the effect of the size of the settling chamber on particle settling velocity is not considered. This can cause error and disagreement in combining uncorrected data with corrected data. It is known that the terminal settling velocity of a particle is influenced by the size of the settling chamber in which experiments are carried out [1,47-49]. The retarding effect is caused by upward flow of fluid to balance downward flow of the solid particle and that of fluid dragged down with the particle. This phenomenon is known as the "wall effect." A number of studies to investigate the wall effect, especially on settling of spheres at $Re \leq 47,000$, have been conducted [1,22,47-49]. The results show that boundary influence becomes less important in intermediate and turbulent regimes [1,22,48]. In contrast, little quantitative information is known about the importance of the wall effect on settling velocities of non-spherical particles. Clift et al. [1] provide some theoretical analysis for the wall effect on the settling of axisymmetric shapes in the creeping flow regime. Chhabra [47] experimentally investigated the importance of the wall effect on the settling of cylinders, needles, disks, plates, cubes and parallel-pipeds for $Re \leq 7$. The results revealed that each of these shapes, except for needle-like cylinders with aspect ratios greater than 10, experienced a smaller wall effect than a volume-equivalent sphere.

Studies show that the ratio of measured settling velocity, U_m, to the settling velocity of the particle in an infinite media, U, depends on the ratio of the particle diameter to the diameter of the settling chamber. This dependency is satisfactorily described by a linear expression [1,22,47-49]:

$$f = \frac{U_m}{U} = 1 - \alpha\left(\frac{d_V}{D}\right) \tag{3.21}$$

where D is characteristic diameter of the settling chamber.

Accordingly, the measured drag coefficient, $C_{D_{Vm}}$, can be corrected using:

$$\frac{C_{D_V}}{C_{D_{Vm}}} = f^2 \tag{3.22}$$

For the creeping flow regime:

$$\frac{K_{St_V}}{K_{St_{Vm}}} = f^{-1} \tag{3.23}$$

where $K_{St_{Vm}}$ is the measured Stokes' shape factor. In some of the studies listed in Table 3.1, the wall effect has been considered by conducting experiments in settling chambers with different diameters [12-14,17,37] and/or with different particle sizes [7,10]. In some cases, the wall effect correction applicable for spheres was utilized [19,22,41]. In other studies, the wall effect was not taken into account, especially for intermediate and turbulent regime data [5,7,19,24,43].

We investigated the importance of the type of wall correction by analyzing the data reported by Baba and Komar [24] for ellipsoid-like sand grains. Two different correction factors were calculated using the method described by Chhabra [47] for non-spherical particles and the method of DiFelice [49] and Chhabra et al. [48] for spheres. The relative difference of the corrected velocities using two different types of wall correction correlations was about 1%. This implies that the type of correction factor used does not affect the corrected velocity, particularly in the intermediate and turbulent regimes, where boundary influence is less important. Consequently, wall correction factors were calculated using the method given by Chhabra et al. [48] for spheres, which is applicable for a broad range of Reynolds numbers. For those measurements where the settling velocity was not measured in a cylindrical chamber, the equivalent circle diameter is substituted for D in Eq. (3.21). A summary of the wall correction calculations is shown in Table 3.2.

Table 3.2. Wall effect correction

Data source	Settling chamber	Re_V	$\frac{d_V}{D}$	f
Baba and Komar [24]	Cylindrical, D = 0.33 m	0.09 - 2.1	0.016 - 0.05	0.985 - 0.9642
Corey data through Schulz et al. [19]	Rectangular, 0.25×0.28 m^2	270 - 2,310	0.006 - 0.024	0.9993 - 0.99996
Komar [43]	Cylindrical, D = 0.33 m	0.09 - 1.44	0.016 - 0.044	0.9147 - 0.9646
Pettyjohn and Christiansen [7]	Rectangular, 0.5×0.5 m^2	0.09 - 22,630	0.002 - 0.028	0.9398 - 0.9999
Schulz data through Schulz et al. [19]	Cylindrical, D = 0.15 m	3.4 - 216.8	0.001 - 0.01	0.9956 - 0.99997
Wang et al. [54]	Rectangular, 0.15×0.135 m^2	26 - 13,390	0.03 - 0.11	0.9846 - 0.9989
Wilde data through Schulz [19]	Cylindrical, D = 0.25 m	4.7 - 21,643	0.014 - 0.1	0.9579 - 0.9997

Table 3.2 shows that the correction factor, f, approaches unity at smaller (d_V/D) and/or higher Reynolds numbers, meaning the container wall effect becomes less important for these conditions.

After correcting the data for the wall effect (where applicable), they were classified based on particle shape and flow regime for further processing. In the subsequent sections, Stokes' dynamic shape factor, K_{St}, and Newton's shape factor, K_N, are discussed.

3.3.4.2. Stokes' dynamic shape factor

Figure 3.1 illustrates how the volumetric Stokes' shape factor, K_{St_V}, for four particles are corrected for the wall effect. Values of the corrected Stokes' shape factor are the intercept on a vertical axis and are obtained by applying a least squares regression method to the measured Stokes' shape factor, $K_{St_{V_m}}$, calculated using the measured settling velocity, U_m. Only data for which $Re_V < 0.1$ are used.

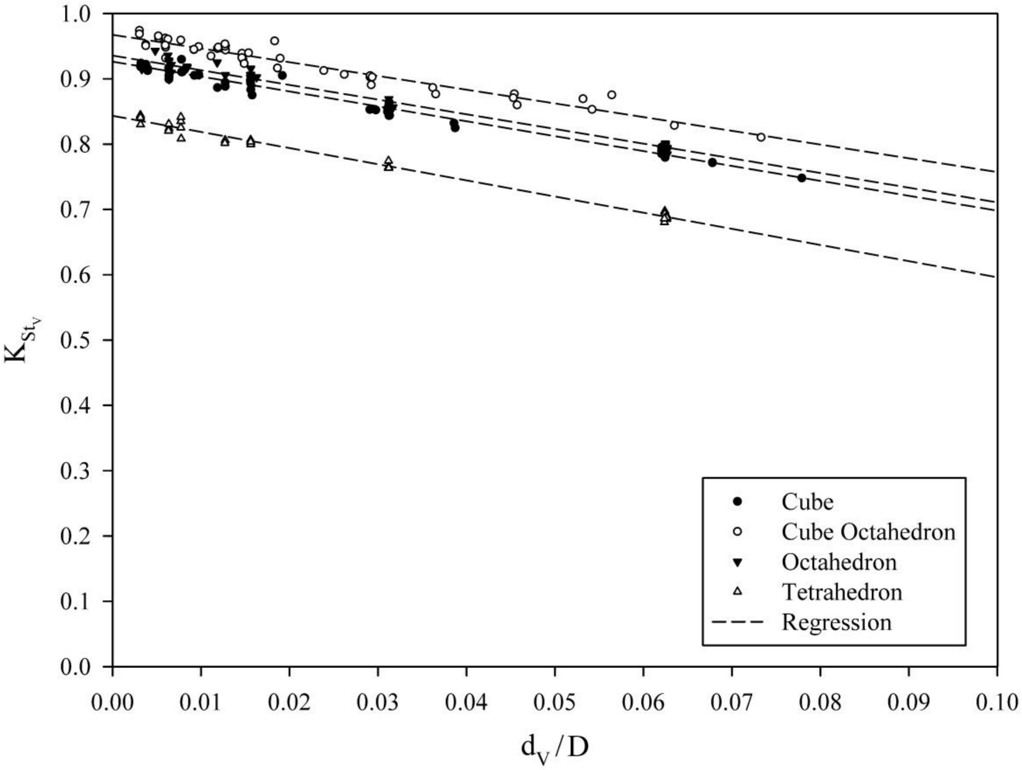

Fig. 3.1. Wall effect correction of the low Reynolds number data to determine Stokes' dynamic shape factors. Data from Pettyjohn et al. [7].

Appendix 3.2 lists Stokes' shape factors, along with the corresponding geometrical shape factors and reported orientation, for 11 different non-spherical particles. This table is used to develop a correlation for Stokes' dynamic shape factor, K_{St_V}. Stokes' shape factors for a cube, cube octahedron, double cone, ellipsoidal sand, octahedron and tetrahedron are corrected for the wall effect using the method described in Section 3.3.5.1.

Calculated values of the volumetric Stokes' dynamic shape factor of selected particles are compared with those reported in the literature. As Table 3.3 shows there is excellent agreement between Stokes' shape factor calculated in this study and those taken directly from the literature [7,9,10,19,22,41]. Note also there is good agreement between values reported by Lasso and Weidman [41] and Heiss and Coull [10] for cylinders falling in axial orientation. Since the Lasso and

Weidman [47] data are for $Re_V > 0.1$, we used the data reported by Heiss and Coull [10].

Table 3.3. Comparison of calculated K_{St_V} in this study and values reported in the literature.

Object	Orientation	Volumetric Stokes' dynamic shape factor, K_{St_V}					
		Present study	Pettyjohn et al. [7]	Ganser [9]	Heiss et al. [10]	Schulz et al. [19], McNown et al. [22]	Lasso et al. [41]
Cube	-	0.926	0.929	0.928	0.926	0.929	-
Cube octahedron	-	0.969	0.972	0.969	-	-	-
Cylinder, E=0.25	Axial wise	-	-	-	0.762	0.760	0.774
Cylinder, E=0.5	Axial wise	-	-	-	0.864	-	0.878
Cylinder, E=1	Axial wise	-	-	-	0.958	-	0.956
Cylinder, E=2	Axial wise	-	-	-	0.975	-	0.977
Cylinder, E=3	Axial wise	-	-	-	0.958	-	0.962
Cylinder, E=4	Axial wise	-	-	-	0.929	-	0.936
Cylinder, E=1	Round wise	-	-	-	0.945	0.967	-
Cylinder, E=4	Round wise	-	-	-	0.758	0.793	-
Octahedron	-	0.936	0.939	0.936	-	-	-
Prism, E=4	Edge wise	-	-	-	0.760	0.705	-
Tetrahedron	-	0.843	0.846	0.842	-	-	-

3.3.4.3. Newton's dynamic shape factor

As explained in Sections 3.2.2 and 3.3.2, at a sufficiently large Reynolds number, a particle of any shape experiences a fully turbulent regime called Newton's regime, where the drag coefficient is approximately constant. Thompson and Clark [15] suggested that Newton's shape factor be evaluated at $Re_V = 10{,}000$. Ganser [9] modified this criterion to $10^4 \le Re^* \le 10^5$ for isometric particles and $Re^* \ge 10^{2.5}$ for disks. The criterion ensures that any non-spherical particle is fully in Newton's regime, meaning that the drag coefficient is constant. However, for some non-spherical particles, experimental data are not available at very high Reynolds numbers.

Examination of the experimental data shows that some non-spherical particles are fully in Newton's regime at Reynolds numbers as low as 200.

Therefore, for those geometries where the experimental drag coefficients at high Reynolds numbers are not reported, we examined the C_{D_V} - Re_V curves plotted using the collected data. For any non-spherical particle, its C_{D_V} - Re_V curve flattens rather quickly at lower Reynolds numbers compared to the same curve drawn for a sphere. For six particle shapes reported by Schulz et al. [19], Newton's shape factors are determined at the maximum Reynolds number reported.

The volume-equivalent Newton's shape factor, K_{N_V}, is calculated using Eq. (3.14). Appendix 3.3 lists Newton's shape factors along with the corresponding geometrical shape factors for 12 different particle shapes. The average of the sphere drag coefficient at Newton's regime reported in 4 references, as $C_{D_S} = 0.450 \pm 0.01$, is used to determine K_{N_V} [1,7,9,50].

3.3.5. Regression

In the present study, correlations are developed using the least squares regression method. Correlation constants are determined by minimizing the *sum of squares error, SSR,* defined as:

$$SSR = \sum_{i=1}^{N} \left(Y_{\exp} - Y_{cal}\right)^2 \tag{3.24}$$

where Y_{exp} is the experimentally measured value and Y_{cal} is the value calculated with a given correlation. The *sum of squares error, SSR*, for Stokes' and Newton's dynamic shape factors are defined linearly. For the drag coefficient data, *SSR* is defined logarithmically [2-4,9]:

$$SSR_{C_D} = \sum_{i=1}^{N} \left(\log\left(C^*_{D,\exp}\right) - \log\left(C^*_{D,cal}\right)\right)^2 \tag{3.25}$$

The goodness of fit is normally measured by *root mean square, RMS,* deviation [4,9]. The *RMS* deviation measures the average fractional displacement of the measured values, Y_{exp}, from the value calculated using the correlation, Y_{cal}. Mathematically, *RMS* is defined as:

$$RMS = \left(\frac{SSR}{N} \right)^{\frac{1}{2}} \tag{3.26}$$

where N is the number of data points used in the regression. The goodness of fit can also be assessed using absolute relative error:

$$\%E = \frac{\left| Y_{\exp} - Y_{cal} \right|}{Y_{\exp}} \times 100 \tag{3.27-a}$$

In the present study, we calculate two absolute relative errors, E_{Max} and E_{Ave}:

$$\%E_{Max} = \max(E_i), \; i = 1 \, to \, N \tag{3.27-b}$$

$$\%E_{Ave} = \frac{\sum_{i=1}^{N} E_i}{N} \tag{3.27-b}$$

3.4. Results and discussion

3.4.1. Correlation development

3.4.1.1. Stokes' dynamic shape factor

Stokes' shape factor, K_{St_V}, is correlated with the degree of roundness, ϕ, using the 69 data points for 11 different shapes reported in Appendix 3.2:

$$K_{St_V} = 1.5195 - 0.4016\sqrt{\phi}\ln(\phi) - 1.4989\, e^{-\phi} \tag{3.28-a}$$

The result is illustrated in Fig. 3.2, where experimental K_{St_V} data are plotted against the degree of roundness along with the correlation of Eq. (3.28-a). As seen from this graph, the correlation predicts the experimental data well. A simpler form that gives $K_{St_V} = 1.0$ for a sphere is:

$$K_{St_V} = \phi^{0.3291} \tag{3.28-b}$$

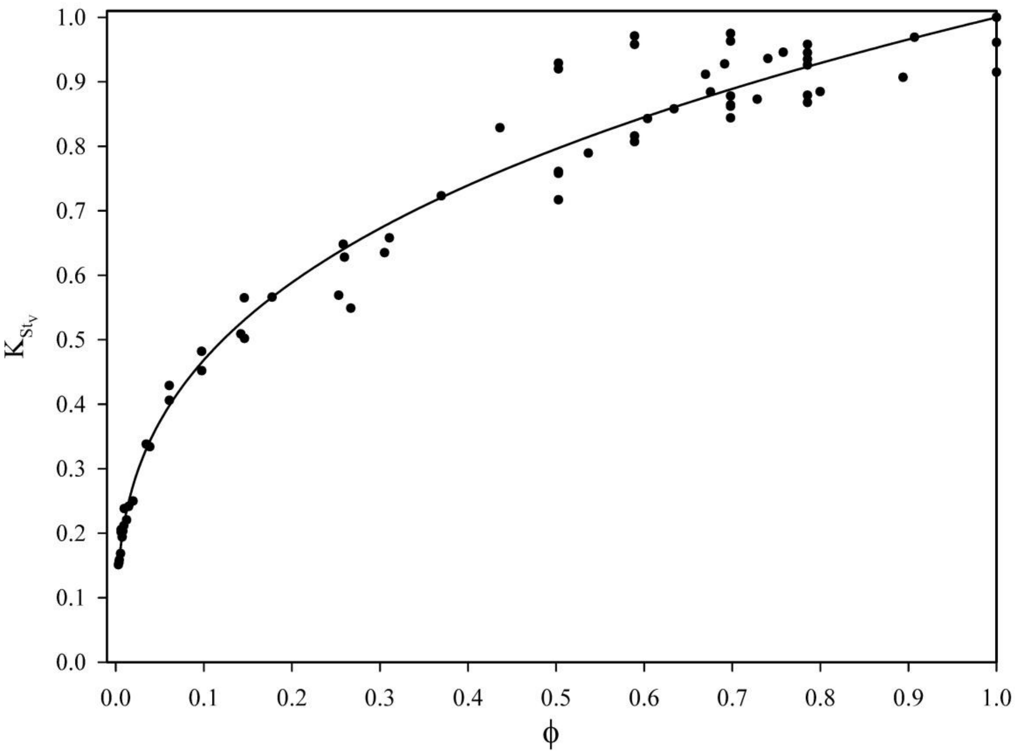

Fig. 3.2. Regression result for the volumetric Stokes' shape factor data correlated with degree of roundness, ϕ . N=69 points; 11 particles shapes.

The goodness of fit and regression results are reported in Table 3.4. The results are also compared with predictions obtained using the Leith formula, which is employed in the Ganser correlation [9]. The new correlation, based on degree of roundness, ϕ , can be said to be more accurate than the Leith formula, because it has lower *RMS*, E_{Max} and E_{Ave} values.

Table 3.4. Comparison of correlations predicting Stokes' dynamic shape factor, N=69

	Shape factor	Eq.	R^2	*RMS*	% E_{Max}	% E_{Ave}
K_{St_V} , using Leith expression	ψ , $\frac{d_P}{d_V}$	-	-	0.060	30.8	7.8
K_{St_V} , New correlation	ϕ	(3.28-a)	97.5	0.043	17.6	5.0
K_{St_V} , New correlation	ϕ	(3.28-b)	97.3	0.045	17.9	4.9

Despite the fact that the Leith expression has a theoretical foundation, it has three disadvantages. In many applications, it is both very difficult and inaccurate to obtain the geometrical information required to determine the two shape factors used in the Leith expression. For instance, there is no accurate way to measure the surface area of a very irregular non-spherical particle with a rough surface, or the volume and surface area of a fragile particle. The second disadvantage of the Leith expression is that it uses sphericity. As explained previously, there are studies that show sphericity does not correlate well with drag coefficient data [1,19,20]. The third disadvantage of the Leith formula is that two versions are required: one for isometric particles and one for non-isometric particles. For non-isometric particles, two shape factors are required: sphericity and $\left(d_P/d_V\right)$. In some circumstances, differentiation of non-isometricity is not very clear. Christiansen and Barker [51] introduced a criterion to specify non-isometricity of a particle based on the ratio of its longest to shortest length. However, it is not an exact criterion based on strong evidence.

3.4.1.2. Newton's dynamic shape factor

Newton's dynamic shape factor, reported in Appendix 3.3, is correlated with the degree of roundness, ϕ, using 37 data points for 12 different shapes:

$$\ln\left(K_{N_V}\right) = 2.0214\left(-\ln\phi\right)^{0.5749} \qquad (3.29)$$

The result is shown in Fig. 3.3, in which experimental Newton's dynamic shape factors, reported in Appendix 3.3, are plotted versus the degree of roundness along with prediction of Eq. (3.29).

Table 3.5 gives goodness of fits and regression results for the volumetric Newton's dynamic shape factor. The results are compared with the prediction of the Ganser expression. The new K_{N_V} correlated with ϕ has lower *RMS* deviation than the Ganser expression correlated with sphericity, but it has slightly higher E_{Ave} and E_{Max}. It is worth mentioning that Ganser [9] did not correct the drag data for the wall effect in intermediate and turbulent regimes. Overall, predictions of

K_{N_V} using the new correlation compare favorably to predictions obtained using the Ganser correlation.

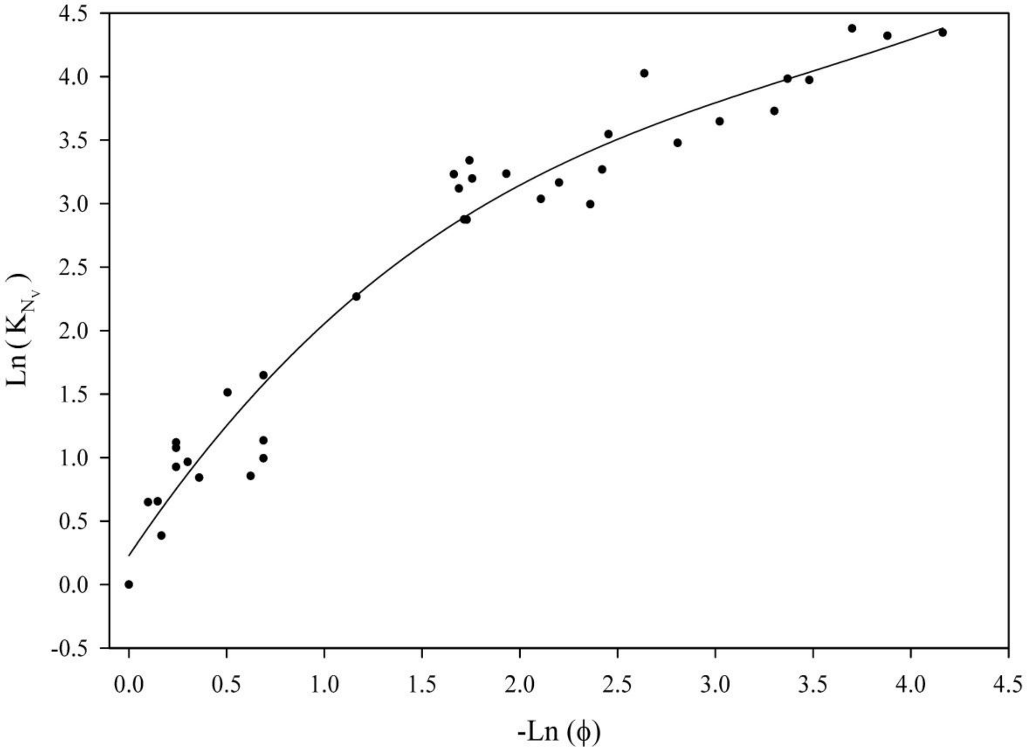

Fig. 3.3. Regression result for the volumetric Newton's dynamic shape factor data correlated with degree of roundness, ϕ. N = 37 points; 12 particles shapes.

Table 3.5. Comparison of correlations predicting Newton's dynamic shape factor

	Shape factor	R^2	*RMS*	% E_{Max}	% E_{Ave}
K_{N_V} , Ganser [9]	ψ	-	7.57	53.0	20.4
K_{N_V} , Eq. (3.29)	ϕ	96	6.15	84.4	22.5

3.4.1.3. Drag correlation

We developed the new correlation based on the form of the correlation reported by Ganser [9]. The correlation predicts that the normalized drag coefficient depends only on the normalized Reynolds number:

$$C_D^* = \frac{24}{Re^*}(1 + B_1 Re^{*B_2}) + \frac{B_3}{\left(1 + \frac{B_4}{Re^*}\right)} \qquad (3.30)$$

The normalized drag coefficient, C_D^*, and the normalized Reynolds number, Re^*, are defined by Eqs. (3.11) and (3.12), respectively. Values of Stokes' and Newton's dynamic shape factors (K_{St_V} and K_{N_V}, respectively) are required to normalize the drag coefficient and Reynolds number. In this study, K_{St_V} and K_{N_V} data given in Appendixes 3.2 and 3.3 are used to determine constants of Eq. (3.30), B_1 to B_4. A different approach is to use correlations to calculate K_{St_V} and K_{N_V} instead of using experimental data. Ganser [9] used experimentally determined values of K_{St_V}; for K_{N_V}, he used the correlation that he developed.

Note that each data point needs a value for K_{St_V} and K_{N_V}. For non-isometric particles and some isometric ones, K_{St_V} depends on orientation. However, orientation of a settling particle can change so that the maximum projected area is exposed normal to the direction of flow in intermediate and Newton's regimes. This orientation is likely unstable due to possible oscillation and tumbling motion, meaning that drag data in intermediate and turbulent regime has a degree of uncertainty [1,5,45,46]. Consequently, any drag correlation for these regions can be considered to be stochastic when the orientation is not known, or when the orientation changes due to the change in flow regime. The "Preferred Orientation Assumption," as a time-averaged orientation, can reduce uncertainty in drag prediction. A different approach to reduce the uncertainty is to use an average value of K_{St_V} for two extreme orientations. Ganser [9] applied the later approach to K_{St_V} of the non-isometric particles. Here the reader is reminded that most shape factors, including sphericity (ψ) and degree of roundness (ϕ), provide no information about particle orientation.

Table 3.6 reports the values of the universal drag correlation constants B_1 to B_4 of Eq. (3.30), for 1,042 data points and 12 different particles. These coefficients are obtained by minimizing the sum of squares error (*SSR*). The regression coefficients are all greater than 99%, implying that all fits were outstanding. For spheres, coefficients reported by Haider and Levenspiel (1989) are used directly as they are obtained using a large data set of 408 points.

Table 3.6. Shape-specific constants and overall constants of Eq. (3.30)

Object	N	B_1	B_2	B_3	B_4	R^2
Cube*	179	0.0907	0.6443	0.4558	2980	99.999878
Cube Octahedron	170	0.1115	0.646	0.4048	2382	99.999993
Cylinder, L/D=0.25	12	0.1000	0.6848	0.4258	2805.5	98.411497
Cylinder, L/D=1	16	0.101	0.6325	0.3825	1792.5	99.959073
Cylinder, L/D=4	43	0.1485	0.6745	0.2754	3688.6	99.830530
Double Cone, D-1	11	0.1000	0.6484	0.4854	1117	99.799753
Double Cone, D-4	7	0.1108	0.6632	0.4954	1156	99.744002
Octahedron	93	0.1015	0.6525	0.4652	3757.5	99.999996
Prism, P-4	8	0.0980	0.7074	0.4254	6110	99.724536
Sphere*	408	0.1806	0.6459	0.4251	6881	99.866726
Spheriod, E-4	14	0.1118	0.6567	0.4305	3305	99.999968
Tetrahedron	81	0.0782	0.6985	0.3921	1665.4	99.999998
Regression of all data together	**702**	**0.0998**	**0.6864**	**0.4025**	**3210**	**99.999800**

* Reported constants by Haier and Levenspiel [4]

Table 3.7 reports the detailed statistical results describing the performance of the new correlation. Additionally, the performance of the Ganser correlation is evaluated for comparison. The new correlation developed here has lower *RMS* deviation, E_{Max} and E_{Ave} compared with the Ganser correlation.

Ganser [9] reported shape-specific constants for four isometric shapes: cube, cube octahedron, octahedron and tetrahedron. To calculate the drag coefficient for other shapes using the Ganser correlation, we used the overall constants he reported (see Eq. 3.10). To normalize the Reynolds number and the drag coefficient, experimental Stokes' and Newton's dynamic shape factors reported in Appendixes 3.2 and 3.3 are used.

Table 3.7. Correlation performance with shape-specific constants for the data used for correlation

Object	Ref.	N	C_{D_V}, present correlation			C_{D_V}, Ganser correlation*		
			RMS	% E_{Max}	% E_{Ave}	*RMS*	% E_{Max}	% E_{Ave}
Cube	[7,19]	179	0.021	22.7	3.4	0.023	26	3.8
Cube octahedron	[7]	170	0.020	13.9	3.4	0.020	13.9	3.4
Cylinder E=0.25*	[14,19]	12	0.046	15.9	10.4	0.054	21.3	11.5
cylinder E=1*	[14,19,35,41]	16	0.038	23	6.7	0.054	29.2	10.6
Cylinder E=4*	[5,19,43]	43	0.017	22.2	6.3	0.097	35.3	18.1
Double cone E=1*	[19]	11	0.033	9.9	7.3	0.045	18.9	8.3
Double cone E=4*	[19]	7	0.052	17.9	10.1	0.069	22.4	12.6
Octahedron	[7]	93	0.016	11.9	3.1	0.020	16	3.3
Prism E=4*	[19]	8	0.053	17.6	10.8	0.066	19.4	13.4
Sphere	[7]	68	0.023	15.8	4.1	0.023	15.8	4.1
Spheriod E=4*	[19]	14	0.094	30.7	14.3	0.094	30.7	14.3
Tetrahedron	[7]	81	0.018	13	3	0.016	14	2.4

* Used overall constants used when shape-specific constants were not calculated in [9]; see Eq. (3.10).

Some objects have limited number of data points, such as double cones and prisms. For those particles, the shape-specific coefficient reported in Table 3.6 can provide only rough estimates of the related constants of B_1 to B_4.

Nevertheless, our main interest is to obtain a universal drag coefficient applicable to any particle. Therefore, regression was performed using all the drag data, or 702 data points. Table 3.6 also gives the corresponding values for regression of all 702 data points including 68 data points for the spheres. The present correlation is developed using 618 data points for seven isometric particles (cube, cube octahedron, cylinder and double cone with $E = 1$, octahedron, sphere and tetrahedron) and 84 data points for five non-isometric particles (cylinder with $E = 0.25$, 4, double cone, prism and spheroid with $E = 4$). In comparison, Ganser [9] used 630 data points for four isometric particles (cube, cube octahedron, octahedron and tetrahedron) and 101 data points for disks.

Substitution of overall constants in Eq. (3.30) yields the universal expression for the drag coefficient:

$$C_D^* = \frac{24}{Re^*}(1 + 0.0998\,Re^{*\,0.6864}) + \frac{0.4025}{\left(1 + \dfrac{3210}{Re^*}\right)} \qquad (3.31)$$

Loth [27] proposed a simpler form of drag correlation which is a modified version of that given by Cheng [52]. The regression yields the following expression:

$$C_D^* = \frac{24}{Re^*} + 0.5 \tag{3.32}$$

Fig. 3.4 illustrates a plot of $C_D^* - Re^*$ (log - log scale) for the 702 experimental data points used to develop the new correlation, along with the correlation given by Eqs. (3.31), (3.32) and the Ganser correlation, Eq. (3.10). The graph depicts that experimental data are well predicted with these correlations.

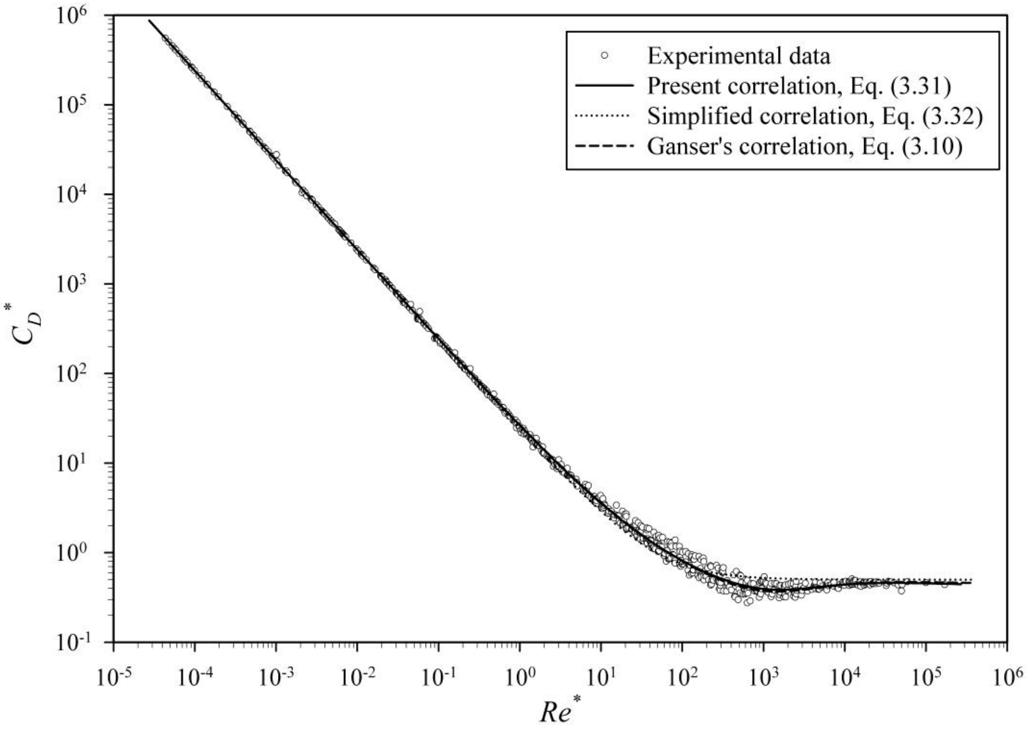

Fig. 3.4. Normalized drag coefficient data along with Eqs. (3.31), (3.32) and Ganser correlation (Eq. 3.10).

Table 3.8 provides detailed statistical information about the performance of Eq. (3.31). For comparison, the performance of the Ganser correlation is also given. Comparison of *RMS* deviation, E_{Max} and E_{Ave} of corresponding shapes show that the new correlation yields results similar to the Ganser correlation when the experimental Stokes' and Newton's dynamic shape factors are used. In contrast, when dynamic shape factors are estimated using related correlations, the Ganser correlation has less error than the new correlation, as indicated by the values of RMS and E_{Max} shown in Table 3.8.

The performance of the new correlation is compromised somewhat when dynamic shape factors are estimated, which is likely related to the broad diversity in particle shapes associated with the data used in its development. That said, the mean relative error for the entire data set is less than 10% in both cases. In terms of comparing the Ganser correlation with the one developed here, it is worth noting that the Ganser correlation requires two shape factors, ψ and $\left(d_P/d_V\right)$ (see Appendix 3.4), which can be difficult for many types of non-isometric particles.

Table 3.8. Correlation performance for the data used to develop correlation. Overall constant used for all shapes, N=702.

Object	Ref.	N	Experimental Stokes' and Newton's dynamic shape factors						Stokes' and Newton's dynamic shape factors by correlations					
			Pesent correlation, Eq. (3.31)			Ganser correlation			Present correlation, Eq. (3.31)			Ganser correlation		
			RMS	% E_{Max}	% E_{Ave}	*RMS*	% E_{Max}	% E_{Ave}	*RMS*	% E_{Max}	% E_{Ave}	*RMS*	% E_{Max}	% E_{Ave}
Cube	[7]	179	0.051	53.2	8.9	0.047	45.6	8.3	0.047	28.5	7	0.041	40.2	7.2
Cube octahedron	[7]	170	0.019	18.8	3	0.019	15.1	3	0.033	23.5	5.4	0.019	16.7	3.3
Cylinder, E=0.25	[14,19,22]	12	0.049	17.1	10.8	0.054	21.3	11.5	0.039	18.9	7	0.069	33.9	9.1
cylinder, E=1	[14,19,22, 35]	16	0.058	31.8	11.5	0.054	29.2	10.6	0.058	31	12	0.042	22.3	7.5
Cylinder, E=4	[5,19,22, 43]	43	0.091	34.6	16.9	0.097	74.3	35.3	0.135	130.4	26.7	0.084	74.3	35.3
Double cone, E=1	[19,22]	11	0.036	14.9	6.7	0.045	18.9	8.3	0.074	28.7	10.8	0.119	40.9	16.8
Double cone, E=4	[19,22]	7	0.064	19.8	11.6	0.069	22.4	12.6	0.120	55.3	28.8	0.075	22.5	14.3
Octahedron	[7]	93	0.032	24	5.1	0.028	18.8	4.8	0.044	29.4	8.6	0.023	14.5	3.8
Prism, E=4	[19,22]	8	0.062	19.8	12.7	0.066	19.4	13.4	0.069	42.8	12.7	0.039	20.9	7.1
Sphere	[7,19]	68	0.065	28.4	9.6	0.069	30.5	10	0.061	27.4	9.5	0.069	30.5	10
Spheriod, E=4	[19,22]	14	0.085	27.1	13.3	0.094	30.7	14.3	0.091	82.3	16.2	0.053	18.2	10.4
Tetrahedron	[7]	81	0.035	18.6	6.1	0.038	20.7	6.4	0.044	29.7	6.1	0.034	19.2	6
Overall		**702**	**0.048**	**53.2**	**9.7**	**0.049**	**45.6**	**7.5**	**0.058**	**130.4**	**8.8**	**0.046**	**74.3**	**6.8**

The performance of four different correlations is illustrated in Table 3.9 by reporting *RMS* deviation, E_{Max} and E_{Ave} associated with each. Again, correlation performance when the dynamic shape factors are calculated from experimental data is shown separately from the case where correlations are used to determine the dynamic shape factors. Overall performance of the new correlation is comparable with the Ganser correlation. Both correlations have $E_{Ave} \leq 10\%$. The Ganser correlation has lower $E_{Max} = 74\%$ compared to present correlation with $E_{Max} = 130\%$, both of which correspond to the case of a cylinder with an aspect ratio of 4 at $Re_V = 24{,}400$ having regular oscillation and rotation about vertical axis [5]. This might be because of uncertainty in measurement or poor prediction due to unstable orientation. In terms of the standard statistical analysis of correlation accuracy, we can say that the H & S correlation is less accurate than the Ganser correlation and the new one proposed here. The maximum relative error for the H&S correlation ($E_{Max} = 60\%$) occurs for a cube octahedron at $Rev = 348$ [7]. For the same data point, our correlation has $E_{Max} = 52\%$ and the Ganser correlation gives $E_{Max} = 13\%$.

The simplified correlation (Eq. 3.32) is the least accurate, as one would expect based on its formulation. The reality, though, is that its performance, on average, is not much worse than the other correlations (see Table 3.9).

Table 3.9. Comparison of correlation performance in predicting the 702 data points.

C_{D_V} correlation	Shape factor	Stokes' and Newton's dynamic shape factors	*RMS*	% E_{Max}	% E_{Ave}	% of data predicted within ±20 %
Eq. (3.31)	ϕ	Experimental K_{St_V}, K_{N_V}	0.048	53.2	9.7	92.7
		K_{St_V}, K_{N_V} by correlation	0.058	130	8.8	89.3
Cheng fit, Eq. (3.32)	ϕ	Experimental K_{St_V}, K_{N_V}	0.081	95.6	12.9	79.8
		K_{St_V}, K_{N_V} by correlation	0.083	156	13.3	84.6
Ganser, [9]	ψ, $\frac{d_P}{d_V}$	Experimental K_{St_V}, K_{N_V}	0.049	45.6	7.5	91.6
		K_{St_V}, K_{N_V} by correlation	0.046	74.3	6.8	92.3
H & S, [18]	ψ, $\frac{d_P}{d_V}$	Does not require calculation of dynamic shape factors	0.078	60	10.4	86.2

Table 3.9 also provides the statistical percentage of data predicted within ± 20% of experimental data by different correlations. Overall prediction of C_{D_V} by the Ganser correlation with 92.3% of data predicted has a slightly lower error band than the present correlation that predicted 89.3% of data within ± 20%. The H & S correlation does not provide any better prediction for this data set, with 86.2% of calculated values within ± 20% of the experimental values.

3.4.2. Performance validation of new correlation

Performance of the new correlation is also investigated by predicting 1,080 non-spherical drag coefficient data points not used to develop the correlation. Table 3.10 provides a detailed comparison of the new correlation with the Ganser correlation. The present correlation predicts C_{D_V} of five particle types (hemisphere and spherical caps, oblate, prolate, stellar crystals and dendrites) better than the Ganser correlation, having lower *RMS* deviation, E_{Max} and E_{Ave}. On the other hand, the Ganser correlation provides better predictions for five particle types (cones, cylinders, plate like prisms, hexagonal plates and broad-branched crystals). For sand and gravel and prisms, two correlations provide similar predictions. Neither correlation provides particularly good drag coefficient predictions for disks. The present correlation has higher E_{Max} = 123.4% for a disk with diameter to thickness ratio of 10 and particle-to-fluid density ratio of 10.3 at $Re_V = 22{,}200$ [5]. For this condition, a disk has very chaotic motion with gliding and tumbling fall behavior [5,46], meaning that the measured drag coefficient has a high degree of uncertainty because of unstable orientation and error associated with the settling velocity measurement.

Table 3.10. Correlation performance for the data used to validate the new correlation, N=1,080.

Objects	E	ϕ	ψ	N	Re_V range	C_{D_V} , present correlation			C_{D_V} , Ganser correlation		
						RMS	% E_{Max}	% E_{Ave}	*RMS*	% E_{Max}	% E_{Ave}
Broad branched crystal [53]	25	0.12	0.28	41	0.08 - 46	0.035	15.7	7.4	0.027	16.0	4.9
Cone [37]; 90° cone-spherical segment; 70° cone-spherical segment; 90° cone-hemisphere segment; 90° tear drop [53]	0.9-2.1	0.52-0.75	0.78-0.98	69	0.5 - 875	0.144	76.0	34.8	0.146	64.0	19.5
Cylinders [5,14,35,41,43]	0.25-9.1	0.28-0.78	0.60-0.87	97	0.04 - 10,000	0.104	97.5	19.5	0.082	60.0	14.7
Dendrite [53]	25	0.12	0.27	50	0.03 - 93	0.075	20.4	15.8	0.107	28.0	21.6
Disk [5,44,46,53]	7.9-1602	0.002-0.31	0.019-0.53	180	0.002 - 25,000	0.139	123.4	26.9	0.136	89.7	21.7
Hemisphere and spherical caps [54]	1.09-2	0.75-0.98	0.84-0.99	72	26 - 13,390	0.214	69.8	35.5	0.238	63.3	38.2
Hexagonal plate [53]	25	0.12	0.30	41	0.06 - 38	0.036	16.6	8.0	0.029	14.7	4.9
Oblate [5]	0.5	0.86	0.94	38	13. - 41,500	0.104	31.8	19.5	0.178	44.9	30.7
Plate like prisms [12]	0.2-4	0.30-0.79	0.59-0.81	22	0.1 - 1.6	0.085	44.1	16.5	0.044	34.5	5.8
Prism [19]	0.25	0.50	0.64	4	11 - 92.4	0.019	5.5	3.9	0.005	5.0	3.5
Prolate [5]	0.5	0.84	0.95	34	14 - 94,000	0.075	38.6	14.4	0.131	40.3	23.4
Sands and gravel [19,24]	1.3-5.2	0.43-0.98	0.58-0.99	337	0.04 - 17,914	0.154	58.6	25.6	0.134	61.9	21.2
Steller crystal with plates, steller crystal [53]	25	0.12	0.28-0.30	48	0.02 - 96	0.079	31.5	15.0	0.129	36.4	23.9
Overall	0.25-1602	0.002-0.98	0.019-0.99	1080	0.02 - 94,000	0.133	123.4	22.8	0.135	89.7	20.8

For 1,080 data points, both correlations predict C_{D_V} with similar *RMS* deviation of 0.133-0.135 and E_{Ave} around 20.8 - 22.8 %, but higher E_{Max} (123.4%) for the correlation developed in the present study.

Table 3.11 compares the performance statistics of the Ganser, H & S and present correlations tested using the entire data bank, comprised of 1,782 data points. Chhabra et al. [6] reported that the Ganser correlation was the most accurate available correlation, as of 1999. Recently, Hölzer and Sommerfeld [18] reported that the H & S correlation is the most exact correlation for arbitrary shaped particles. Appendix 3.4 lists each of these two drag correlations, along with the new correlation developed here.

Table 3.11. Summary of statistical analysis comparison of drag coefficient correlations, N=1,782.

Data for validation	Shape factor	*RMS*	% E_{Max}	% E_{Ave}	Within ± 25 %	Within ± 40 %	Within ± 45 %
Eq. (3.31)	ϕ	0.109	130.4	17.3	77.5	92.0	94.1
Ganser [9]	ψ , $\frac{d_P}{d_V}$	0.109	89.7	15.3	77.2	92.3	95.1
H & S [18]	ψ , $\frac{d_P}{d_V}$	0.109	85.4	15.5	80.4	92.5	94.6
Cheng fit, Eq. (3.32)	ϕ	0.124	183.6	21.8	70.3	88.4	91.0

Comparison of C_{D_V} predictions shows that all three correlations have similar *RMS* deviation of 0.109. The new correlation developed in this study has slightly higher E_{Ave} than the H & S and Ganser correlations. However, statistically speaking, three correlations demonstrate similar accuracy, having similar *RMS* deviation range, and E_{Ave} around 15.3 -17.3%. This is clearly shown in Fig. 3.5 where cumulative absolute relative errors of the correlations are compared. The graph shows that three correlations have similar ability to predict C_{D_V}. Both Table 3.11 and Fig. 3.5 show that the new correlation developed here has a higher E_{Max} value than the H & S and Ganser correlations. The simplified Cheng-like fit, Eq. (3.32), has poorer performance in comparison with Eq. (3.31) owing to its form.

The statistical percentages of the data predicted within ±25, ±40 and ±45 % of 1,782 experimental data are also reported in Table 3.11. All three correlations, predict about 80% of the experimental data within ±25% and more than 92% of the experimental data within ±40 %.

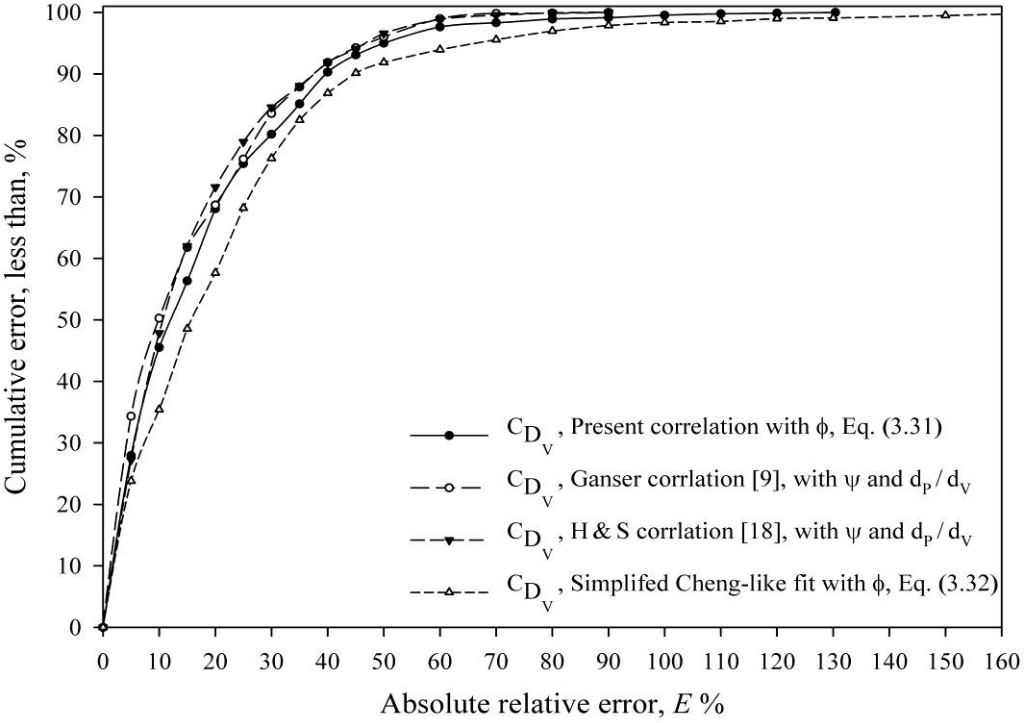

Fig. 3.5. Cumulative distribution of relative error for four drag correlations

The best feature of the correlation developed in the present study is that it uses only one shape factor compared to the other correlations (H & S and Ganser) in which two shape factors, sphericity and (d_P/d_V), are used. Furthermore, the new shape factor used in the new correlation, degree of roundness, is determined more easily and with higher degree of accuracy than ψ and (d_P/d_V).

3.5. Summary

The present study makes two important contributions to the prediction of drag coefficients for any non-spherical particle:

- A new shape factor, “degree of roundness” (ϕ), is defined; and
- A new correlation to predict drag coefficient based on this shape factor is developed and tested.

The new shape factor uses particle geometrical information obtained from a side projected view of the particle in a plane parallel to the particle’s direction of motion. From this view, the particle’s side view-projected area and side view-projected perimeter are determined and used to calculate the degree of roundness. This approach has numerous advantages over commonly used shape factors such as sphericity which, for example, requires measurement of particle surface area and volume. These particle geometrical parameters are not available from typical on-line imaging measurements, where the moving particle is viewed from the side. Such measurements are common in the monitoring and controlling of coagulation, flocculation, sedimentation and pipeline transport processes, and are of particular value for fragile particles. For particles of this type, direct measurement of geometrical factors is very challenging and often impossible.

The new universal drag coefficient correlation proposed here, based on degree of roundness and volume-equivalent sphere diameter, is able to predict experimental drag data in the subcritical regime ($1.5 \times 10^{-5} < Re_V < 1.7 \times 10^{5}$) with a degree of accuracy similar to that associated with the correlations developed by Ganser [9] and Hölzer and Sommerfeld (See Appendix 3.4 for summary of the equations) [18].The advantage of the new correlation is that it is based on a single shape factor (ϕ) while the other two correlations require sphericity (ψ) and $\left(d_P/d_V\right)$ as inputs. The difficulties inherent in measuring sphericity for non-isometric, highly irregular and/or fragile particles are avoided when the new drag coefficient correlation is used.

The results presented here also provide the basis for greatly improved online size and density measurement of highly irregular and fragile particles (e.g. clay aggregates). This application is described in detail in Chapter 4.

3.6. Nomenclature

A	Particle characteristic projected area (L^2)
A_I	Side view-projected area of particle (L^2)
A_P	Normal view-projected area of particle (L^2)
c	Circularity
C_D^*	Normalized drag coefficient
C_{D_P}	Projected area equivalent sphere drag coefficient
C_{D_S}	Sphere drag coefficient
C_{D_V}	Volume equivalent sphere drag coefficient
$C_{D_{V_m}}$	Measured volume equivalent sphere drag coefficient
D	Settling container diameter (L)
d_V	Volume equivalent sphere diameter (L)
d_P	Normal view-projected area equivalent sphere diameter (L)
E	Particle aspect ratio
E_{Ave}	Percentage of average absolute relative error, %
E_{Max}	Percentage of maximum absolute relative error, %
F_D	Drag force ($M\ L\ T^{-2}$)
f	Wall effect correction factor
g	Gravitational acceleration ($L\ T^{-2}$)
K_{St_V}	Volumetric Stokes' dynamic shape factor
$K_{St_{V_m}}$	Measured volumetric Stokes' dynamic shape factor
K_{N_V}	Volumetric Newton's dynamic shape factor
N	Numbers of data points
P_I	Side view-projected perimeter (L)
P_P	Projected perimeter of particle on a plane normal to its direction of motion (L)
Re^*	Normalized Reynolds number
Re_V	Volumetric Reynolds number
S	Particle surface area (L^2)

S'_P	Surface area of a sphere with a diameter of equivalent circle having same side view-projected perimeter (L^2)
U	Particle settling velocity in infinite medium ($L\ T^{-1}$)
U_m	Measured particle settling velocity in a finite container ($L\ T^{-1}$)
V	Particle volume (L^3)
X	Longest principal axis of particle (L)
Y	Mid principal axis of particle (L)
Z	Shortest principal axis of particle (L)
Γ	Size descriptor (L)
$\mathit{\Lambda}$	Shape descriptor
$\mathit{\Sigma}$	Bowen-Masliyah shape factor
α	Correlation constant
β	Corey shape factor
ϕ	Degree of roundness
μ_L	Liquid viscosity, ($M\ L^{-1}\ T^{-1}$)
ρ_L	Liquid density ($M\ L^{-3}$)
ρ_P	Particle density ($M\ L^{-3}$)
ψ	Wadell sphericity

3.7. References

1. Clift, R., Grace, J.R., Weber, M.E., “Bubbles, drops and particles”, Academic Press, New York, 1978.
2. Turton, R., Levenspiel, O., (1986). “A short note on the drag correlation for spheres”, Powder Tech. 47, 83-86.
3. Khan, A.R., Richardson, J.F., (1987). “The resistance to motion of a solid sphere in a fluid”, Chem. Eng. Commun. 62, 135-150.
4. Haider, A., Levenspiel, O., (1989). “Drag coefficient and terminal velocity of spherical and non-spherical particles”, Powder Technol. 58, 63–70.
5. Stringham, G.E., Simons, D.B., Guy, H.P., “The behavior of large particles falling in quiescent liquids”, US Geol. Surv. Prof. Pap., Vol. 562-C 1969.
6. Chhabra, R.P., Agarwal, L., Sinha, N.K., (1999). “Drag on non-spherical particles: an evaluation of available methods”, Powder Technol. 101, 288–295.
7. Pettyjohn, E.S., Christiansen, E.B., (1948). “Effect of particle shape on free settling rates of isometric particles”, Chem. Eng. Prog. 44, 157–172.
8. Torobin, L.B., Gauvin, W.H., (1960). “Fundamental aspects of solid–gas flow: Part IV. The effects of particle rotation, roughness and shape”, Can. J. Chem. Eng. 38, 142–153.
9. Ganser, G.H., (1993). “A rational approach to drag prediction of spherical and non-spherical particles”, Powder Technol. 77, 143-152.
10. Heiss, J.H., Coull, J., (1952). “The effect of orientation and shape on the settling velocity of non-isometric particles in a viscous medium”, Chem. Eng. Prog. 48, 133-140.
11. Leith, D., (1987). “Drag on non-spherical objects”, Aerosol. Sci. Tech. 6, 153–161.
12. Johnson, D.L., Leith, D., Reist, P.C., (1987). “Drag on non-spherical, orthotropic aerosol particles”, J. Aerosol. Sci. 18, 87-97.
13. Sheaffer, A., (1987). “Drag on modified rectangular prisms”, J. Aerosol. Sci. 18, 11-16.

14. Unnikrishnan, A., Chhabra, R.P., (1991). “An experimental study of motion of cylinders in Newtonian fluids: wall effect and drag coefficient”, Can. J. Chem. Eng. 69, 729-735.
15. Thompson, T.L., Clark, N.N., (1991). “A holistic approach to particle drag prediction”, Powder Technol. 67, 57–66.
16. Chien, S.F., (1994). “Settling velocity of irregularly shaped particles”, SPE Drilling and Completion, 9, 281-289.
17. Madhav, G.V., Chhabra, R.P., (1995). “Drag on non-spherical particles in viscous fluids”, Int. J. Miner. Process. 43, 15–29.
18. Hölzer, A., Sommerfeld, M., (2008). “New simple correlation formula for the drag coefficient of non-spherical particles”, Powder Technol. 184, 361-365.
19. Schulz, E.F., Wilde, R.H., Albertson, M.L., “Influence of shape on fall velocity of sedimentary particles”, Report prepared for the Missouri river division, Corps of Engineers, U.S. Army through Colorado, A&M research foundation, Fort Collins CO., 1954.
20. Bowen, B.D., Masliyah, J.H., (1973). “Drag force on isolated axisymmetric particles in Stokes flow”, Can. J. Chem. Eng., 51, 8-15.
21. Tran-Cong, S., Gay, M., .Michaelides, E.E., (2004). “Drag coefficients of irregularly shaped particles”, Powder Technol. 139, 21–32.
22. McNown, J.S., Malaika, J., (1950). “Effect of particle shape on settling velocity at low Reynolds numbers”, Am. Geophys. Union, Trans. 31, 74-82.
23. Komar, P.D., Reimers, C.E., (1978). “Grain shape effects on settling rates”, J. Geol. 86, 193-209.
24. Baba, J., Komar, P.D., (1981). “Settling velocities of irregular grains at low Reynolds numbers”, J. Sediment. Petrol. 51, 121-128.
25. Dressel, M., (1985). “Dynamic shape factors for particle shape characterization”, Part. Charact. 2, 62–66.
26. Swamee, P.K., Ojha, C.S.P., (1989). “Drag coefficient and fall velocity of non-spherical particles”, J. Hydraul. Eng. 117, 660-667.
27. Loth, E., (2008). “Drag of non-spherical solid particles of regular and irregular shape”, Powder Technol. 182, 342-353.

28. Alger, G.R., Simons, D.B., (1968). "Fall velocity of irregular shaped particles", J. Hyd. Eng. Div., Proceedings of ASCE, 94, 721-737.
29. Le Roux, J.P., (1997). "Comparison of sphericity indices as related to the hydraulic equivalence of settling grains", J. Sedimen. Res. 67, 527-530.
30. Michael, P., (1966). "Steady motion of a disk in a viscous fluid", Phys. Fluids 9, 466-471.
31. Davis, A.M.J., (1990). "Stokes drag on a disk sedimenting toward a plane or with other disks; additional effects of a side wall or free surface", Phys. Fluids A 2, 301-312.
32. Masliyah, J.H., Epstein, N., (1970). "Numerical study of the steady flow past spheroids", J. Fluid Mech. 44, 493-512.
33. Pitter, R.L., Pruppacher, H.R., (1973). "A numerical study of viscous flow past a thin oblate spheroid at low and intermediate Reynolds numbers", J. Atmospheric Sci. 30, 125-134.
34. Ui, T.J., Hussey, R.G., (1984). "Stokes drag on a cylinder in axial motion", Phys. Fluid 27, 787-795.
35. McKay, G., Murphy, W.R., Hillis, M., (1988). "Settling characteristics of disks and cylinders", Chem Eng. Res. Des. 66, 107-112.
36. Militzer, J., Kan, J.M., Hamdullahpur, F., Amyotte, P.R., Al Taweel, A.M., (1989). "Drag coefficient for axisymmetric flow around individual spheroidal particles", Powder Technol. 57, 193-195.
37. Sharma, M.K., Chhabra, R.P., (1991). "An experimental study of free fall of cone in Newtonian and non-Newtonian media: drag coefficient and wall effects", Chem. Eng. Process. 30, 61-67.
38. Geldart, D., "Gas fluidization technology", Chap. 6, John Wiley and Sons Inc., New York, 1986.
39. Geldart, D., (1990). "Estimation of basic particle properties for use in fluid-particle process calculation", Powder Technol. 60, 1-13.
40. Lee, C.T., Leith, D., (1989). "Drag force on agglomerated spheres in creeping flow", J. Aerosol Sci. 20, 501-513.

41. Lasso, I.A., Weidman, P.D., (1986). “Stokes drag on hollow cylinders and conglomerates”, Phys. Fluids 29, 3921–3934.
42. Agarwal,, N., Chhabra, R.P., (2007). “Settling velocity of cubes in Newtonian and power law liquids”, Powder Technol. 178, 17-21.
43. Komar, P.D., (1980). “Settling velocities of circular cylinders at low Reynolds numbers”, J. Geol. 88, 327-336.
44. Squires, L., Squires Jr., W., (1973). “The sedimentation of thin disks”, Trans. Am. Inst. Chem. Eng. 33, 1-12.
45. Isaacs, J.L., Thodos, G., (1967). “The free settling of solid cylindrical particles in the turbulent regime”, Can. J. Chem. Eng. 45, 150-155.
46. Willmarth, W.W., Hawk, N.E., Harvey, R.L., (1964). “Steady and unsteady motions and wakes of freely falling disks”, Phys. Fluids 7, 197–208.
47. Chhabra, R.P., (1995). “Wall effects on free settling velocity of non-spherical particles in viscous media in cylindrical tubes”, Powder Technol. 85, 83-90.
48. Chhabra, R.P., Agarwal, S., Chaudhary, K., (2003). “A note on wall effect on the terminal falling velocity of a sphere in quiescent Newtonian media in cylindrical tubes”, Powder Technol. 129, 53-58.
49. Di Felice, R., (1996). “A relationship for the wall effect on the settling velocity of a sphere at any flow regime”, Int. J. Multiphase flow 22, 527-533.
50. Perry, R.H., Green, D.W., “Perry’s Chemical Engineers’ Handbook”, 7th Ed. McGraw-Hill, 1997.
51. Christiansen, E.B., Barker, D.H., (1965). “The effect of shape and density on the free settling of particles at high Reynolds number”, AIChE J. 11, 145–151.
52. Cheng, N.S., (1997). “Simplified settling velocity formula for sediment particle”, J. Hydraul. Eng. 123, 149–152.
53. List, R., Schemenauer, R.S., (1971). “Free – fall behaviour of planar snow crystals”, conical graupel and small hail, J. Atmos. Sci. 28, 110–115.
54. Wang, J., Qi, H., You, C., (2009). “Experimental study of sedimentation characteristics of spheroidal particles, Particuology 7, 264-268.

Appendix 3.1. Particle shape factors described in this study

Name	Notation	Definition
Wadell sphericity	$\psi = \frac{\pi d_V^2}{S}$	$\frac{\text{Surface area of volume equivalent sphere}}{\text{Actual surface are of particle}}$
Degree of roundness	$\phi = \frac{A_I}{\left(\frac{\pi}{4}\left(\frac{P_I}{\pi}\right)^2\right)}$	$\frac{\text{Side view–projected area of particle}}{\text{Area of side view – projected perimeter equivalent circle}}$
Side view-Sphericity 1	$\psi' = \frac{\pi d_I^2}{\pi L_{\max}^2}$	$\frac{\text{Surface area of side view – projected area equivalent sphere}}{\text{Surface area of a sphere with diameter of maximum side view – length}}$
Side view-Sphericity 2	$\psi'' = \frac{\pi d_I^2}{\pi (HL_{\max})^2}$	$\frac{\text{Surface area of side view – projected area equivalent sphere}}{\text{Surface area of a sphere with diameter of maximum side view – horizontal length}}$
Wadell circularity	$C = \frac{\pi d_P}{P_P}$	$\frac{\text{Perimeter of normal projected – area equvalent circle}}{\text{Normal projected - Perimeter of particle on plane normal to flow}}$
Side view-circularity 1	$C' = \frac{\pi d_I}{P_I} = \phi^{\frac{1}{2}}$	$\frac{\text{Perimeter of side view – projected area equivalent sphere}}{\text{Side view – projected perimeter of particle on plane parallel to flow}}$
Side view-circularity 2	$C'' = \frac{\pi (HD_{\max})}{P_I}$	$\frac{\text{Perimeter of circumcribing circle with diameter of maximum side view – horizontal length}}{\text{Side perimeter of particle on plane parallel to flow}}$
Corey shape factor	$\beta = \frac{Z}{\sqrt{X\ Y}}$	$\frac{\text{Shortest axis length}}{\sqrt{(\text{Longest axis length})(\text{Intermediate axis length})}}$
Side view-Corey shape factor 1	$\beta' \approx \frac{L_{\min}}{\sqrt{L_{\max}\ d_I}}$	$\frac{\text{Shortest side view – length}}{\sqrt{(\text{Longest side view – length})(\text{Intermediate side view – length})}}$
Side view-Corey shape factor 2	$\beta'' \approx \frac{L_{\min}}{L_{\max}}$	$\frac{\text{Shortest side view – length}}{\text{Longest side view – length}}$
Bowen-Masliyah Shape factor	$\Sigma = \frac{S}{\pi\left(\frac{P_I}{\pi}\right)^2}$	$\frac{\text{Surface area of particle}}{\text{Surface area of side view – projected perimeter equivalent sphere}}$
Side view-Bowen-Masliyah Shape factor 1	$\Sigma' = \frac{\pi L_{\max}^2}{\pi\left(\frac{P_I}{\pi}\right)^2}$	$\frac{\text{Surface area of a sphere with diameter of maximum side view – length}}{\text{Surface area of side view – projected perimeter equivalent sphere}}$
Side view-Bowen-Masliyah Shape factor 2	$\Sigma'' = \frac{\pi (HL_{\max})^2}{\pi\left(\frac{P_I}{\pi}\right)^2}$	$\frac{\text{Surface area of a sphere with diameter of maximum side view – horizontal length}}{\text{Surface area of sphere with maximum horizontal diameter}}$

Appendix 3.2. Stokes' dynamic shape factors for various non-spherical particles

Object	Orientation	E	$\frac{d_V}{d_I}$	$\frac{d_P}{d_V}$	ϕ	ψ	K_{St_V}	Data origin
Cube	-	1.0	1.100	0.910	0.785	0.806	0.926	[7]
Cube octahedron	-	1.2	0.908	1.102	0.907	0.905	0.969	[7]
Cylinder	Axial	0.25	1.278	1.387	0.503	0.693	0.761	[10, 22]
Cylinder	Axial	0.5	1.139	1.101	0.698	0.826	0.864	[10, 41]
Cylinder	Axial	1.0	1.015	0.874	0.785	0.874	0.958	[10, 41]
Cylinder	Axial	1.5	0.943	0.767	0.754	0.849	0.975	[10, 41]
Cylinder	Axial	2.0	0.904	0.693	0.698	0.832	0.975	[10, 41]
Cylinder	Axial	3.0	0.845	0.606	0.589	0.779	0.958	[10, 41]
Cylinder	Axial	4.0	0.805	0.550	0.503	0.734	0.929	[10, 41]
Cylinder	Round wise	0.25	0.721	0.782	1.000	0.693	0.915	[10]
Cylinder	Round wise	0.5	0.909	0.878	1.000	0.826	0.961	[10]
Cylinder	Round wise	1.0	1.015	0.986	0.785	0.874	0.945	[10]
Cylinder	Round wise	2.0	0.904	1.106	0.698	0.832	0.878	[10]
Cylinder	Round wise	3.0	0.845	1.184	0.589	0.779	0.807	[10]
Cylinder	Round wise	4.0	0.805	1.242	0.503	0.734	0.758	[10]
Disk	Horizontal	342	2.682	6.106	0.009	0.053	0.212	[44]
Disk	Horizontal	212	2.478	5.211	0.015	0.073	0.242	[44]
Disk	Horizontal	520	2.877	7.025	0.006	0.040	0.206	[44]
Disk	Horizontal	323	2.658	5.995	0.010	0.055	0.238	[44]
Disk	Horizontal	783	3.080	8.050	0.004	0.031	0.158	[44]
Disk	Horizontal	431	2.788	6.598	0.007	0.046	0.194	[44]
Disk	Horizontal	387	2.738	6.364	0.008	0.049	0.203	[44]
Disk	Horizontal	254	2.553	5.532	0.012	0.065	0.221	[44]
Disk	Horizontal	158	2.358	4.721	0.020	0.089	0.250	[44]
Disk	Horizontal	1,052	3.235	8.886	0.003	0.025	0.151	[44]
Disk	Horizontal	890	3.146	8.402	0.004	0.028	0.154	[44]
Disk	Horizontal	579	2.929	7.283	0.005	0.038	0.169	[44]
Disk	Horizontal	520	2.877	7.025	0.006	0.040	0.202	[44]
Double cone	POA	1.0	0.995	1.260	0.785	0.891	0.879	[19]
Double cone	POA	4.0	0.790	1.267	0.370	0.770	0.723	[19]
Ellipsoidal sand	POA	3.2	0.841	1.274	0.634	0.804	0.858	[24]
Ellipsoidal sand	POA	2.6	0.979	1.251	0.728	0.899	0.873	[24]
Ellipsoidal sand	POA	1.7	0.973	1.132	0.894	0.962	0.907	[24]
Ellipsoidal sand	POA	2.8	0.932	1.420	0.691	0.735	0.928	[24]
Ellipsoidal sand	POA	2.9	0.995	1.275	0.675	0.895	0.884	[24]
Ellipsoidal sand	POA	2.2	0.970	1.283	0.800	0.842	0.885	[24]
Ellipsoidal sand	POA	3.0	0.921	1.216	0.670	0.908	0.912	[24]
Ellipsoidal sand	POA	5.2	0.983	1.671	0.436	0.610	0.829	[24]
Ellipsoidal sand	POA	2.4	0.893	1.253	0.758	0.836	0.946	[24]
Spheroid	POA	4.0	0.794	1.260	0.537	0.785	0.790	[19]
Octahedron	-	1.4	1.018	1.169	0.741	0.846	0.936	[7]
Plate	Given	10.0	0.944	1.498	0.260	0.557	0.628	[12]
Plate	Given	10.3	1.621	1.980	0.253	0.428	0.569	[12]

Plate	Given	15.6	1.097	1.807	0.178	0.465	0.566	[12]
Plate	Given	2.0	2.034	0.695	0.258	0.359	0.648	[12]
Plate	Given	20.1	1.440	2.203	0.142	0.359	0.509	[12]
Plate	Given	4.0	2.545	0.785	0.267	0.298	0.549	[12]
Plate	Given	8.0	1.231	1.618	0.311	0.555	0.658	[12]
Plate	Given	19.4	1.427	2.176	0.146	0.366	0.502	[13]
Plate	Given	19.5	1.432	2.180	0.146	0.365	0.565	[13]
Plate	Given	30.2	1.361	2.371	0.098	0.315	0.452	[13]
Plate	Given	30.2	1.352	2.364	0.098	0.316	0.482	[13]
Plate	Given	49.6	1.233	2.555	0.061	0.273	0.406	[13]
Plate	Given	49.7	1.232	2.556	0.061	0.273	0.429	[13]
Plate	Given	8.2	1.244	1.636	0.305	0.548	0.635	[13]
Plate	Given	79.5	1.131	2.753	0.039	0.237	0.334	[13]
Plate	Given	88.9	1.121	2.820	0.035	0.226	0.338	[13]
Prism	Given	4.0	0.693	0.722	0.785	0.640	0.868	[10]
Prism	Given	2.0	0.873	0.810	0.785	0.762	0.935	[10]
Prism	Given	0.5	0.980	1.021	0.698	0.768	0.862	[10]
Prism	Given	0.3	0.916	1.092	0.589	0.719	0.816	[10]
Prism	Given	0.3	0.873	1.146	0.503	0.677	0.760	[10]
Prism	Given	0.3	1.385	1.444	0.503	0.640	0.717	[10]
Prism	Given	0.5	1.234	1.146	0.698	0.762	0.844	[10]
Prism	Given	2.0	0.980	0.722	0.698	0.768	0.963	[10]
Prism	Given	3.0	0.916	0.631	0.589	0.719	0.971	[10]
Prism	Given	4.0	0.873	0.573	0.503	0.677	0.920	[10]
Sphere	-	1.0	1.000	1.000	1.000	1.000	1.000	[7]
Tetrahedron	-	1.2	0.844	1.222	0.604	0.671	0.843	[7]

[*] POA: Preferred Orientation Assumption

Appendix 3.3. Newton's dynamic shape factors for various non-spherical particles

Object	E	Re*	$\frac{d_V}{d_I}$	$\frac{d_P}{d_V}$	ϕ	ψ	K_{N_V}	Data origin
Cube	-	6 - 36$\times$10^3	1.100	0.910	0.785	0.806	3.062	[7]
Cube octahedron	-	4 - 24$\times$10^3	0.908	1.102	0.907	0.905	1.913	[7]
Cylinder	2	2$\times$10^4	0.904	1.106	0.698	0.832	2.322	[45]
Cylinder	1	300	1.015	0.986	0.785	0.874	2.526	[19]
Cylinder	0.25	787	0.782	1.387	0.503	0.693	5.196	[19]
Cylinder	4	2 - 21$\times$10^3	0.805	1.242	0.503	0.734	2.704	[5, 19, 45]
Double cone	1	1 - 2.1$\times$10^3	1.005	1.260	0.785	0.891	2.933	[19]
Double cone	4	1 -1.7$\times$10^3	0.789	1.267	0.370	0.770	2.898	[19]
Octahedron		4 - 33$\times$10^3	1.017	1.169	0.740	0.846	2.627	[7]
Oblate	2	4 - 7.6$\times$10^4	0.879		0.863	0.966	1.926	[5]
Prism	4	705	0.872	0.572	0.503	0.677	3.111	[19]
Prolate	2	2 - 1.3$\times$10^5	1.110		0.847	0.947	1.471	[5]
Sphere		1 - 17$\times$10^4	1.000	1.000	1.000	1.000	1.000	[7]
Spheroid	4	2,350	0.794	1.260	0.537	0.785	2.353	[19]
Tetrahedron	-	5 - 51$\times$10^3	0.844	1.221	0.604	0.671	4.540	[7]
Disk	7.9	13,631	1.433	1.743	0.312	0.526	9.649	[46]
Disk	14.5	7,927	1.584	2.130	0.190	0.387	25.303	[46]
Disk	14.9	3,028	1.592	2.151	0.185	0.382	22.617	[46]
Disk	15.4	22,545	1.600	2.173	0.180	0.375	17.729	[46]
Disk	15.6	5,256	1.604	2.184	0.178	0.372	17.701	[46]
Disk	15.9	13,692	1.608	2.195	0.175	0.369	28.224	[46]
Disk	16.1	4,485	1.613	2.207	0.173	0.365	24.467	[46]
Disk	19.6	21,271	1.666	2.356	0.145	0.327	25.407	[46]
Disk	23.8	391	1.721	2.513	0.122	0.292	20.831	[46]
Disk	26.3	355	1.750	2.598	0.111	0.275	23.706	[46]
Disk	31.3	395	1.800	2.752	0.094	0.248	19.988	[46]
Disk	33.3	418	1.820	2.811	0.089	0.239	26.266	[46]
Disk	34.5	3,063	1.830	2.843	0.086	0.234	34.675	[46]
Disk	41.8	74,723	1.890	3.033	0.072	0.208	56.003	[46]
Disk	50	387	1.947	3.218	0.060	0.186	32.384	[46]
Disk	62.5	432	2.021	3.467	0.049	0.161	38.361	[46]
Disk	83.3	453	2.120	3.816	0.037	0.134	41.623	[46]
Disk	89.3	444	2.145	3.904	0.034	0.128	53.661	[46]
Disk	100	314	2.186	4.055	0.031	0.119	53.138	[46]
Disk	125	506	2.268	4.368	0.025	0.103	79.769	[46]
Disk	150	526	2.339	4.643	0.021	0.092	75.275	[46]
Disk	200	574	2.453	5.109	0.017	0.076	77.183	[46]

Appendix 3.4. Drag correlations

Reference	Drag correlations	Geometrical shape factor(s)	Dynamic shape factors
Present study	$\frac{C_{D_V}}{K_{N_V}}=\frac{24}{\left(Re_V K_{St_V} K_{N_V}\right)}\left(1+0.0998\left(Re_V K_{St_V} K_{N_V}\right)^{0.6864}\right)+\frac{0.4025}{\left(1+\frac{3210}{\left(Re_V K_{St_V} K_{N_V}\right)}\right)}$	Degree of roundness (ϕ)	$K_{St_V}=\phi^{0.3291}$ $\ln\left(K_{N_V}\right)=2.0214\left(-\ln\phi\right)^{0.5749}$
Present study, Cheng-like fit	$\frac{C_{D_V}}{K_{N_V}}=\frac{24}{\left(Re_V K_{St_V} K_{N_V}\right)}+0.5$	Degree of roundness (ϕ)	$K_{St_V}=\phi^{0.3291}$ $\ln\left(K_{N_V}\right)=2.0214\left(-\ln\phi\right)^{0.5749}$
Ganser [9]	$\frac{C_{D_V}}{K_{N_V}}=\frac{24}{\left(Re_V K_{St_V} K_{N_V}\right)}\left(1+0.1118\left(Re_V K_{St_V} K_{N_V}\right)^{0.6567}\right)+\frac{0.4305}{\left(1+\frac{3305}{\left(Re_V K_{St_V} K_{N_V}\right)}\right)}$	Sphericity (ψ) and $\frac{d_P}{d_V}$	For non-isometric particles: $K_{St_V}=\left(\frac{1}{3}\frac{d_P}{d_V}+\frac{2}{3}\frac{1}{\sqrt{\psi}}\right)^{-1}$ For isometric particles: $K_{St_V}=\left(\frac{1}{3}+\frac{2}{3}\frac{1}{\sqrt{\psi}}\right)^{-1}$ $K_{N_V}=10^{1.8148(-Log\psi)^{0.5743}}$
Hölzer and Sommerfeld [18]	$C_{D_V}=\frac{8}{Re_V}\frac{d_P}{d_V}+\frac{16}{Re_V}\frac{1}{\sqrt{\psi}}+\frac{3}{\sqrt{\mathrm{Re}_V}}\frac{1}{\psi^{0.75}}+0.42\left(\frac{d_P}{d_V}\right)^2 10^{0.4(-\log\psi)^{0.2}}$	Sphericity (ψ) and $\frac{d_P}{d_V}$	Does need dynamic shape factors

Chapter 4

New drag coefficient for non-spherical and fragile objects using two dimensional geometrical data obtained from imaging

4.1. Introduction

The interaction of a moving particle with the surrounding fluid is encountered in many applications. The study of this interaction raises a lot of interest in industrial and research fields. In industrial cases, online monitoring of fluid-particle hydrodynamics provides an appropriate basis to control and optimize the process. For instance, in a fluidized bed system, where the fluidization velocity of particles can vary due to particle size distribution or particle breakage [1], online estimation of the particles' settling velocities can be used to monitor and control the process. For such cases where direct velocity measurement is not applicable, the settling velocities of the particles with a given density can be estimated after online identification of the particle size and shape. Another industrial example is removal of particles in water and the wastewater treatment systems using flocculation-clarification processes. In such cases, settling velocity, size and density of aggregates profoundly affect efficiency of solid-liquid separation and effluent quality [2,3]. Therefore, online measurement of the aggregates' settling properties is very crucial. In research studies, online measurement of fluid-particle interaction is a classical and non-invasive technique for particle characterization. For example, the density of a particle can be determined after quantifying the geometry and settling velocity of the particle. This indirect technique is extensively used to estimate structural properties of porous and fragile aggregates [3-10]. The classical way to describe fluid-particle hydrodynamics is a particle drag coefficient; hence, a reliable evaluation of the drag coefficient is highly desirable.

In earlier studies, the drag force experienced by spheres moving through a fluid has been investigated. An extensive set of experimental data combined with computational results permits us to predict the drag force on a moving spherical particle in a viscous media [11-13]. Many subsequent studies have focused on the drag force on non-spherical particles [14-32]. Other than variables that affect the drag force on a sphere, drag force on a non-spherical particle depends on particle shape and orientation. This complex dependency restricts the study of non-spherical drag using theoretical and computational methods. Therefore, empirical drag correlations are developed using experimental drag data to predict non-spherical drag coefficients [11,15,16,33-42]. The correlations developed by Ganser [39] and Hölzer and Sommerfeld [42] predict non-spherical drag with reasonable accuracy [40-42] (see also Chapter 3). Here, these correlations will be referred to as the Ganser correlation and the H & S correlation. These correlations require two geometrical descriptors to capture particle shape and orientation. The required descriptors are determined using particle volume, surface area and projected area in a plane perpendicular to the direction of motion. For a particle with well-defined shape, these geometrical factors can be easily determined. However, in most practical applications, particles have highly irregular shapes and/or rough surfaces. For these types of particles, accurate determination of particle surface area is very difficult. In Chapter 3, we developed a new universal drag correlation that uses particle volume and a shape factor denoted the “degree of roundness”. The degree of roundness is defined using geometrical parameters that are obtained from projection of the particle in a plane parallel to the direction of motion. Detailed statistical analysis performed in Chapter 3 proves the new correlation has similar accuracy as the Ganser and H & S correlations. The first important feature of our correlation is that it uses only a single shape factor to describe the non-sphericity of a particle. The second feature is that the required shape factor, that is the degree of roundness, is not determined using particle volume and surface area, but rather by using projected area and perimeter in a plane parallel to the direction of motion. In comparison, the Ganser and H & S correlations require two shape factors which are not easy to determine in many circumstances [39,42].

The correlation developed in Chapter 3 predicts non-spherical drag coefficient accurately by using particle volume and degree of roundness.

However, there are situations where measurements of particle volume are very challenging and sometimes impossible. For instance, the volume of a highly irregular and fragile aggregate formed through the flocculation process cannot be measured, since any sampling method may change the aggregate's size and volume [10]. In such cases, online imaging techniques are often employed to quantify the geometry of particles. However, an obstacle to improving the accuracy and expanding the applications of imaging techniques is their intrinsic limitations in measuring particle volume. Typically, online imaging techniques do not directly measure particle volume but instead capture two-dimensional images of the particles from the side [2-10,43]. Additionally, a reliable approach to link particle-fluid hydrodynamics to online imaging techniques is lacking.

The primary objective of the present study is to define a novel approach for predicting the drag coefficient using geometrical data obtained from online imaging techniques. The intention is to use only particle geometrical data obtained from side projection of the particle in a plane parallel to the direction of its motion. To that end, new forms of size descriptor, drag coefficient and Reynolds number are defined. The combination of degree of roundness, the new forms of drag coefficient and a size descriptor is applied to correlate experimental drag data. An extensive bank of experimental data taken from the literature is used with the intention of covering as many shapes as possible. Predictions of drag data using the new correlation are assessed against experimental data and compared with three of the more accurate drag correlations, the Ganser and H & S correlations, and the correlation developed in Chapter 3.

4.2. Equation development

4.2.1. Size and shape descriptors

In Chapter 3, the most common size and shape descriptors used in drag coefficient correlations were reviewed and their advantages and disadvantages were discussed. Volume-equivalent sphere diameter has been used extensively to define the Reynolds number and drag coefficient [11,14-23,29-42]. It is the diameter of an equivalent sphere having a volume equal to particle volume:

$$d_V = \left(\frac{6V_P}{\pi} \right)^{\frac{1}{3}} \tag{4.1}$$

where V_P is particle volume that is lacking in online measurements taken using imaging techniques [4,10,43].

One can define an equivalent sphere diameter having the same side view-projected area as that of a particle in a plane parallel to the direction of motion:

$$d_I = \left(\frac{4A_I}{\pi} \right)^{\frac{1}{2}} \tag{4.2}$$

where A_I is the side view-projected area of particle in a plane parallel to the direction of the particle's motion and d_I is named the side view-area equivalent sphere diameter. The side view-area equivalent sphere diameter, d_I, has been used as a size descriptor in online particle identification applications using imaging techniques. There are many studies that have used d_I to characterize size, then estimate the density of a porous and fragile aggregate using its settling velocity data. [2-10,43].

The side view-area equivalent sphere diameter, d_I, should be distinguished from d_P, which is another equivalent diameter defined using projected area of the particle in a plane perpendicular to the direction of motion:

$$d_P = \left(\frac{4A_P}{\pi} \right)^{\frac{1}{2}} \tag{4.3}$$

where A_P is the projected area of the particle in a plane perpendicular to the direction of particle's motion. This normal projected-area equivalent sphere diameter has been used in prior drag correlations [11,33,39,42]. Figure 4.1 exemplifies two different views of a cylinder falling axially to determine A_P and A_I.

We successfully developed a new drag correlation using degree of roundness, ϕ (see Eq. 4.4). It is defined as the ratio of the side view-projected area of the particle to the area of a circle having the equivalent side view-projected perimeter as the particle:

$$\phi = \frac{4\pi A_I}{P_I^2} \tag{4.4}$$

where A_I and P_I are the side view-projected area and the side view-projected perimeter of the particle respectively, that are obtained from projection of particle in a plane parallel to the direction of motion. For a sphere, the degree of roundness is unity and for a non-spherical object it is less than one.

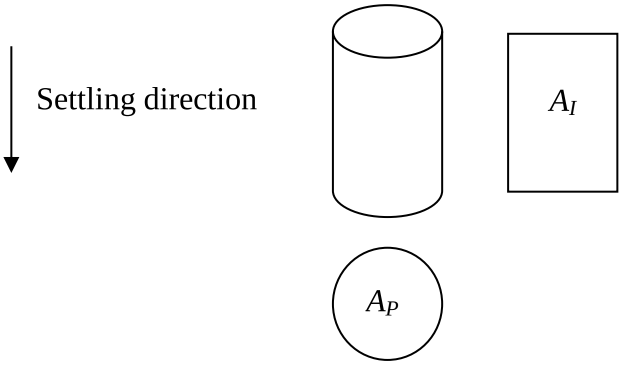

Fig 4.1. Scheme of particle projections on different planes.

4.2.2. Drag coefficients and Reynolds numbers

Force balance on a steadily settling particle with a uniform velocity of U in an infinite quiescent fluid leads to a expression for drag coefficient, C_D:

$$C_D = \frac{2g(\rho_P - \rho_L)V_P}{A\rho_L U^2} \tag{4.5}$$

where ρ_P is the density of the particle, ρ_L is the density of the fluid, g is the gravitational acceleration, V_P is the particle volume and A is a characteristic projected area of the particle. Two different forms of drag coefficient are used in the literature, depending on what projected area of the particle is substituted for A in Eq. (4.5) (See Chapter 3). The most common form of drag coefficient is the volumetric drag coefficient, C_{D_V}, in which the projected area of the volume-equivalent sphere, $A_V = \pi d_V^2/4$, is substituted for A in Eq. (4.5) [11]:

$$C_{D_V} = \frac{4g(\rho_P - \rho_L)d_V}{3\rho_L U^2} \tag{4.6}$$

Here, we define a new form of drag coefficient that uses the side view-projected area, A$_I$. In cases where the particle volume, V_P, is not available, we propose to approximate the particle volume in Eq. (4.5) using the side view-area equivalent sphere diameter, d_I:

$$V_I = \frac{\pi}{6} d_I^3 \tag{4.7}$$

Here, we denote this volume as side view-volume, which is not the actual or measured volume of the particle, V_P, as it is in Eq. (4.6). Substitution of this approximation into Eq. (4.5) leads to a new form of drag coefficient:

$$C_{D_I} = \frac{2g(\rho_P - \rho)V_I}{A_I\, \rho_L U^2} = \frac{4g(\rho_P - \rho)d_I}{3\rho_L U^2} \tag{4.8}$$

where C_{D_I} is named side view-area equivalent sphere drag coefficient. The main feature of C_{D_I} definition is that it only uses two-dimensional geometrical data obtained from projection of the particle in a plane parallel to the direction of motion.

It is obvious that numerical values of C_{D_V} and C_{D_I} are not identical, but they can be related after combining Eqs. (4.6) and (4.8):

$$C_{D_I} = C_{D_V} \frac{V_I}{V_P} \frac{A_V}{A_I} = C_{D_V} \frac{d_I}{d_V} \tag{4.9}$$

For a non-spherical particle, the Reynolds number is defined in different ways in the literature. The most widely used definition of a particle's Reynolds number is the one which is based on the volume-equivalent sphere diameter, d_V [11,40]:

$$Re_V = \frac{\rho_L U\, d_V}{\mu_L} \tag{4.10}$$

where μ_L is the viscosity of the fluid and Re_V is the volumetric Reynolds number.

Similar to drag coefficient, we define a new form of Reynolds number using the side view-area equivalent sphere diameter, d$_I$:

$$Re_I = \frac{\rho_L U\, d_I}{\mu_L} \tag{4.11}$$

where Re_I is named the side view-Reynolds number. The volumetric and side view-Reynolds numbers are easily related by the ratio of $\left(d_I / d_V\right)$.

4.2.3. Dynamic shape factors

Ganser [39] introduced a universal correlation:

$$C_D^* = \frac{24}{Re^*}(1+0.1118\,Re^{*0.6567}) + \frac{0.4305}{\left(1+\frac{3305}{Re^*}\right)} \tag{4.12}$$

where the normalized drag coefficient, C_D^*, and the normalized Reynolds number, Re^*, are defined as [39]:

$$C_D^* = \frac{C_{D_V}}{K_{N_V}} \tag{4.13}$$

$$Re^* = Re_V\, K_{St_V} K_{N_V} \tag{4.14}$$

In the Ganser correlation, the Reynolds number is normalized using two volumetric dynamic shape factors, K_{St_V} and K_{N_V}, defined for creeping and turbulent flow regimes respectively. The volumetric Stokes' shape factor, K_{St_V}, is defined as the ratio of the volume-equivalent sphere drag coefficient to that of the non-spherical particle in the creeping flow regime [11,16,33]:

$$K_{St_V} = \left(\frac{\left(24 / \mathrm{Re}_V\right)}{C_{D_V}}\right)_{Stokes} \tag{4.15}$$

There are numerous theoretical and experimental attempts to correlate the volumetric Stokes' shape factor with a geometrical shape factor, mostly with sphericity [11,15,16,33,39,41,44]. Leith [33] introduced an expression for K_{St_V} based on the concept that, in the creeping flow regime, form drag comprises one-third of the total drag on a sphere. The expression uses two shape factors of $\left(d_P / d_V\right)$ and sphericity, ψ. The theoretical foundation and reasonable accuracy of the Leith expression makes it more useful than many other expressions found in the literature [15,16,39,41,44]. Ganser [39] used the Leith expression to develop the Ganser correlation. In Chapter 3, we developed a new K_{St_V} correlation using a single shape factor: degree of roundness. The main advantages of the new K_{St_V} correlation are improved accuracy compared to the similar K_{St_V} correlations and the ability to use the single shape factor of degree of roundness, ϕ, instead of sphericity, ψ, and $\left(d_P/d_V\right)$.

The volumetric Newton's shape factor, K_{N_V}, is defined as ratio of the drag coefficient of a non-spherical particle, C_{D_V}, to that of a sphere, C_{D_S}, in the fully turbulent regime [15,37]:

$$K_{N_V} = \left(\frac{C_{D_V}}{C_{D_S}}\right)_{Newton} \tag{4.16}$$

Thompson and Clark [37] defined this dynamic shape factor at the Re_V = 10,000. They attempted to correlate the drag coefficient with K_{N_V} instead of using a geometrical shape factor. Ganser [39] modified Thompson and Clark's approach and correlated K_{N_V} with sphericity. We successfully correlated K_{N_V} with the degree of roundness, ϕ (see Eq. 3.29), which has a similar accuracy to that of the K_{N_V} expression correlated using sphericity, ψ.

In cases where particle volumetric data is not available, we introduce a new form of Stokes' dynamic factor named side view-Stokes' shape factor, K_{St_I}, which is defined in Eq. (4.17) after combing Eqs. (4.9), (4.11) and (4.15):

$$K_{St_I} = \left(\frac{\left(24/\mathrm{Re}_I\right)}{C_{D_I}}\right)_{Stokes} = K_{St_V}\left(\frac{d_V}{d_I}\right)^2 \tag{4.17}$$

Similarly, after combining Eqs. (4.8), (4.9) and (4.16), a side view-Newton's shape factor, K_{N_I}, is defined as:

$$K_{N_I} = \left(\frac{C_{D_I}}{C_{D_S}}\right)_{Newton} = K_{N_V}\left(\frac{d_I}{d_V}\right) \tag{4.18}$$

A favorable outcome of defining side view-dynamic shape factors is that they do not influence the normalization of the drag equation. In other words, normalization using the volume-equivalent dynamic shape factors and normalization using the side view-dynamic shape factors lead to the same normalized Reynolds number and drag coefficient:

$$Re^* = \mathrm{Re}_V\, K_{St_V} K_{N_V} = Re_I K_{St_I} K_{N_I} \tag{4.19}$$

$$C_D^* = \frac{C_{D_V}}{K_{N_V}} = \frac{C_{D_I}}{K_{N_I}} \tag{4.20}$$

The independency of Re^* and C_D^* from their definitions, provides the basis to correlate C_{D_I} with Re_I and degree of roundness using a universal $C_D^* - Re^*$ expression.

4.3. Data bank

4.3.1. Data processing and corrections

In the present study, we use the same experimental data bank collected from the literature presented in Chapter 3. Table 4.1 summarizes the data bank which consists of more than 2,100 experimental data points that cover a wide range of conditions in terms of hydrodynamics and particle shapes.

Part of this voluminous data bank was used to develop the new drag coefficient correlation and the remainder was used to validate the performance of the new drag correlation. For cases where the orientation was not reported, we assume that the largest axis of the particle is perpendicular to the direction of the particle’s motion. The required assumptions related to data processing and wall effect corrections are described in detail in Chapter 3.

Table 4.1. Summary of data used in this study (see Chapter 3).

Investigator(s)	Particle shape(s)	N*	Re_V	Used in*
Baba and Komar [31]	Irregular sand grain (ellipsoidal)	72	0.04 - 2.2	V
Heiss and Coull [16]	Cylinders and prisms	24	< 0.1	C
Issacs and Thodos [25]	Cylinders	6	200 – 60e3	C
Johnson et al. [47]	Plate like prisms	62	0.1 - 1.6	C / V
Komar [30]	Cylinders	29	0.09 - 3	C / V
Lasso and Weidman [21]	Cylinders	66	0.05 - 1.5	C / V
List and Schemenauer [27]	Broad-branched crystal, cones, dendrite, disk, hexagonal plate, stellar crystal with plates, stellar crystal	340	0.03 - 875	V
McKay et al. [32]	Cylinder	66	9 – 5,700	C / V
Pettyjohn and Christiansen [15]	Cube, cube octahedron, octahedron, sphere, tetrahedron	635	2e-5 – 23e3	C
Data of Corey, Malaika, Wilde and Schulz through Schulz et al. [19], McNown et al. [29]	Cylinders, double cones, spheroid, square prism, natural sedimentary sands (ellipsoidal), sand grains from rock crusher fragments and gravels	421	1e-3 – 18e3	C/ V
Sharma and Chhabra [20]	Cones	8	0.5 - 292	V
Sheaffer [48]	Plate like prisms	40	0.07 - 0.4	C / V
Squires and Squires [24]	Thin disks, falling axially	50	0.002 - 5.4	V
Stringham et al. [14]	Cylinders, disks, oblate, prolate	186	6 – 94e3	C / V
Unnikrishnan and Chhabra [17]	Cylinders and sphere	11	0.2 - 180	C / V
Wang et al [28]	Hemisphere and spherical caps	72	26 – 13,390	V
Willmarth et al. [26]	Thin disks	54	0.4 - 6,300	C / V

* C = Correlation; V = Validation; N = Number of data.

4.3.2. Regression

In the present study, correlations are developed using the least squares regression method. Correlation constants are determined by minimizing the *sum of squares error*, *SSR*, defined as:

$$SSR = \sum_{i=1}^{N} \left(Y_{\exp} - Y_{cal} \right)^2 \tag{4.21}$$

where Y_{exp} is the experimentally measured value and Y_{cal} is the value calculated with a given correlation. The sum of squares error, *SSR*, for Stokes' and Newton's dynamic shape factors are defined linearly. For the drag coefficient data, *SSR* is defined logarithmically [12,13,34,39]:

$$SSR_{C_D} = \sum_{i=1}^{N} \left(\log\left(C^*_{D,\exp} \right) - \log\left(C^*_{D,cal} \right) \right)^2 \tag{4.22}$$

The goodness of fit is normally measured by the *root mean square* deviation, *RMS* [39,34]. The *RMS* deviation measures the average fractional displacement of the measured values, Y_{exp}, from the value calculated using the correlation, Y_{cal}. Mathematically, *RMS* is defined as:

$$RMS = \left(\frac{SSR}{N} \right)^{\frac{1}{2}} \tag{4.23}$$

where *N* is the number of data points used in the regression. The goodness of fit can also be assessed using absolute relative error:

$$\%E = \frac{\left| Y_{\exp} - Y_{cal} \right|}{Y_{\exp}} \times 100 \tag{4.24-a}$$

Here, we calculate two absolute relative errors, E_{Max} and E_{Ave}:

$$\%E_{Max} = \max(E_i), \;\; i = 1\, to\; N \tag{4.24-b}$$

$$\%E_{Ave} = \frac{\sum_{i=1}^{N} E_i}{N} \tag{4.24-c}$$

4.4. Results and discussion

4.4.1. Correlation development

4.4.1.1. Side view-Stokes' shape factor

The side view-Stokes' shape factors, K_{St_I}, are calculated using Eq. (4.17) and reported K_{St_V} in Chapter 3. Appendix 4.1 lists Stokes' shape factors, along with the corresponding geometrical shape factors and reported orientation, for nine different non-spherical particles. For applications where the particle volume cannot be measured, we propose an expression that correlates K_{St_I} with degree of roundness, ϕ:

$$\ln\left(\frac{1}{K_{St_I}} \right) = \frac{1}{\left(1.1523 + 33.695\, \phi^{6.3951}\right)} \tag{4.25}$$

This correlation is developed using 30 data points for nine different shapes with $\phi \geq 0.35$ reported in Appendix 4.1. Side view-Stokes' shape factors of highly non-isometric particles, including thin plates and disks settling in unstable orientations, are excluded in correlating K_{St_I}, since they do not correlate well with degree of roundness. The result is illustrated in Fig. 4.2. Except for the cube that has $K_{St_I} = 1.120$, the side view-Stokes' factors of other particles are distributed around the curve plotted using Eq. (4.25).

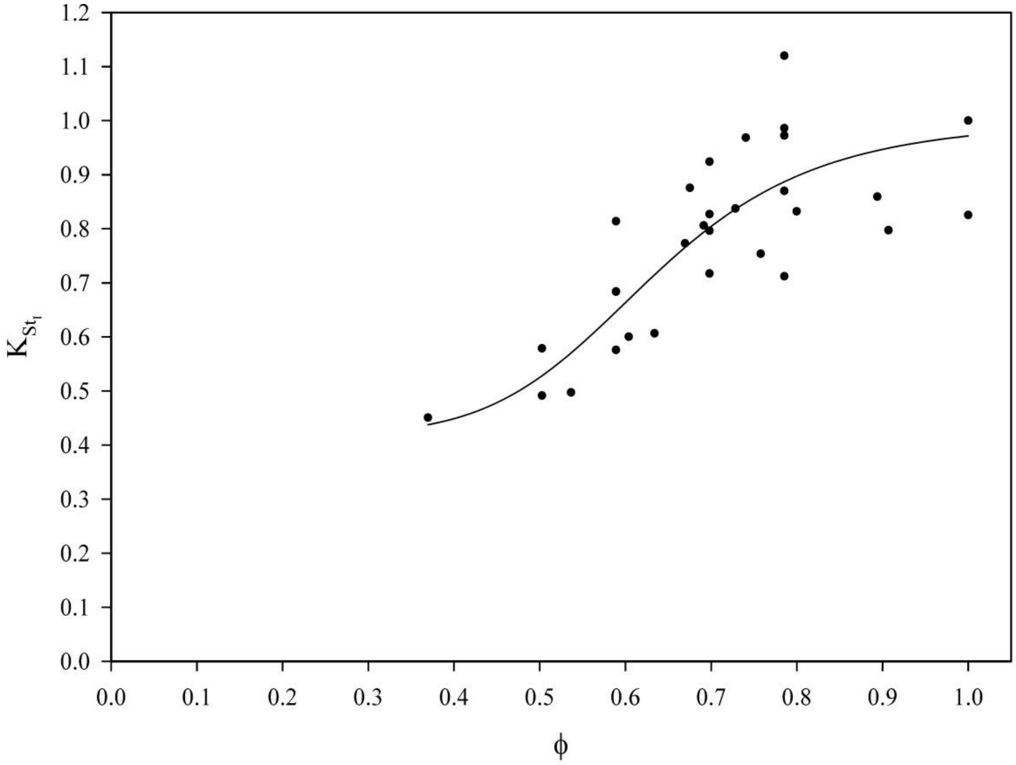

Fig. 4.2. Regression result for the side view-Stokes' shape factor data correlated with degree of roundness, ϕ, N = 30 points, 9 particles' shapes

Table 4.2 shows a comparison of the predictions of the present correlation and those from Leith [33] and Chapter 3. In general, there is reasonable agreement among the results. The correlation developed for the side view-Stokes' shape factor has higher *RMS* compared to the ones obtained for the volumetric Stokes' dynamic factor. It has an error band close to the prediction of the Leith expression. However, it does not provide a reasonable prediction for highly non-isometric bodies such as plates, disks and needle-like cylinders. This is due to their very low values of degree of roundness which cannot describe nonsphericities of these particles only using two-dimensional geometrical data. Also, for these types of particles there is a significant difference between Stokes' dynamic shape factors determined for two different orientations of axial-wise and round-wise settlings. For instance, a cylinder with aspect ratio of 4 has 23% difference in K_{St_I} for axial-wise and round-wise orientations. Therefore, we suggest to use Eq. (4.25) for shapes with $\phi \geq 0.35$. It is worth to remembering that degree of roundness cannot describe the orientation.

Table 4.2. Comparison of the correlations predicting Stokes' dynamic shape factors.

	Shape factor	R^2	*RMS*	% E_{Max}	% E_{Ave}
K_{St_I}, New correlation, Eq. (4.25), N = 30	ϕ	73.1	0.093	25.4	9.5
K_{St_V}, Chapter 3, Eq. (3.28-a), N = 69	ϕ	97.5	0.043	17.6	5.0
K_{St_V}, Leith expression [33,39], N = 69	ψ, $\frac{d_P}{d_V}$	-	0.060	30.8	7.8

4.4.1.2. Side view-Newton's shape factor

The side view-Newton's shape factors, K_{N_I}, are calculated using K_{N_V} reported in Chapter 3, Appendix 3.3 and Eq. (4.18). Appendix 4.2 summarizes Newton's shape factors along with the corresponding geometrical shape factors. The side view-Newton's dynamic shape factor, K_{N_I} is correlated with the degree of roundness, ϕ, using 37 data points for 12 different shapes:

$$\ln\left(K_{N_I}\right) = 1.1247 - 1.0858\phi + 1.1616\left(-\ln\phi\right)^{0.5} \tag{4.26}$$

All Newton's shape factor data used to develop the K_{N_V} correlation in Chapter 3 are used in Eq. (4.26) after converting to K_{N_I}. Figure 4.3 depicts the experimental K_{N_I} and the prediction of Eq. (4.26). It shows that K_{N_I} is well predicted by the developed expression.

Table 4.3 gives goodness of fit and regression result. The results are compared with the prediction of volumetric Newton's shape factor expressions proposed by Ganser [39] and in Chapter 3. Despite the fact that particle volume is not used to correlate side view-Newton's shape factor, the present expression predicts K_{N_I} more accurately than those correlations developed for K_{N_V} . Recall that in Chapter 3 the volumetric Newton's shape factor was correlated using degree of roundness, while Ganser [39] used sphericity. The present K_{N_I} expression has similar regression coefficient R^2, lower *RMS* deviation, E_{Max} and E_{Ave} compared to the correlations.

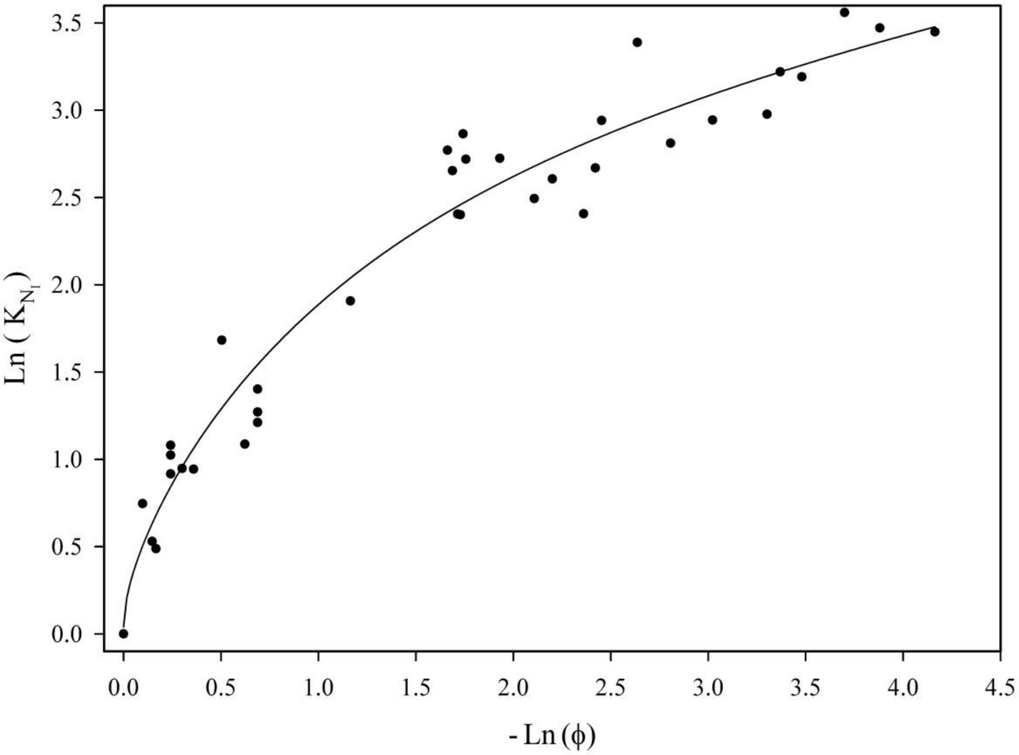

Fig. 4.3. Regression result for the side view-Newton's shape factor data correlated with degree of roundness, ϕ. N = 37 points; 12 particles shapes.

Table 4.3. Comparison of the correlations predicting Newton's dynamic shape factors, N=37

	Shape factor	R^2	*RMS*	% E_{Max}	% E_{Ave}
K_{N_I} , Eq. (4.26)	ϕ	95.2	3.169	49.2	18.5
K_{N_V} , Chapter 3, Eq. (3.29)	ϕ	96	6.149	84.4	22.5
K_{N_V} , Ganser [39]	ψ	-	7.571	53.0	20.4

4.4.1.3. Drag correlation

We developed the new correlation based on the form of the Ganser correlation, which is used in Chapter 3, Eq. (3.30). The correlation predicts that the normalized drag coefficient depends only on the normalized Reynolds number:

$$C_D^* = \frac{24}{Re^*}(1 + B_1\, Re^{*\,B_2}) + \frac{B_3}{\left(1 + \frac{B_4}{Re^*}\right)} \qquad (4.27)$$

where B$_1$ to B$_4$ are correlation constants.

As explained in Section 4.2.3. both Re^* and C_D^* are independent of the parameters used in their respective definitions. In other words, the $C_D^* - Re^*$ correlation is the same for both $C_{D_V} - Re_V$ and $C_{D_I} - Re_I$. This independency was double-checked through the determination of $C_D^* - Re^*$ data using both the volumetric and side view-dynamic shape. A comparison showed that they were identical. Therefore, we will use identical values of the universal drag correlation constants for B_1 to B_4 in Eq. (4.27), which were reported previously in Chapter 3 (see Table 3.6).

Our main interest is to obtain a universal drag coefficient applicable to any particle shape. Therefore, the regression was performed using 702 data points for nine different shapes (cube, cube octahedron, cylinders, double cones, octahedron, prism, sphere, spheroid and tetrahedron). Substitution of the overall constants into Eq. (4.27) yields the following universal drag expression:

$$C_D^* = \frac{24}{Re^*}(1 + 0.0998\, Re^{*\,0.6864}) + \frac{0.4025}{\left(1 + \frac{3210}{Re^*}\right)} \qquad (4.28)$$

Loth [41] proposed a simpler form of drag correlation which is a modified version of that given by Cheng [46]. The regression yields the following expression:

$$C_D^* = \frac{24}{Re^*} + 0.5 \qquad (4.29)$$

Fig. 4.4 illustrates a plot of $C_D^* - Re^*$ (log - log scale) for the 702 experimental data points used to develop the correlations, along with the correlation given by Eqs. (4.28) and (4.29) and the Ganser correlation, Eq. (4.12). The graph shows that experimental data are well predicted with these correlations.

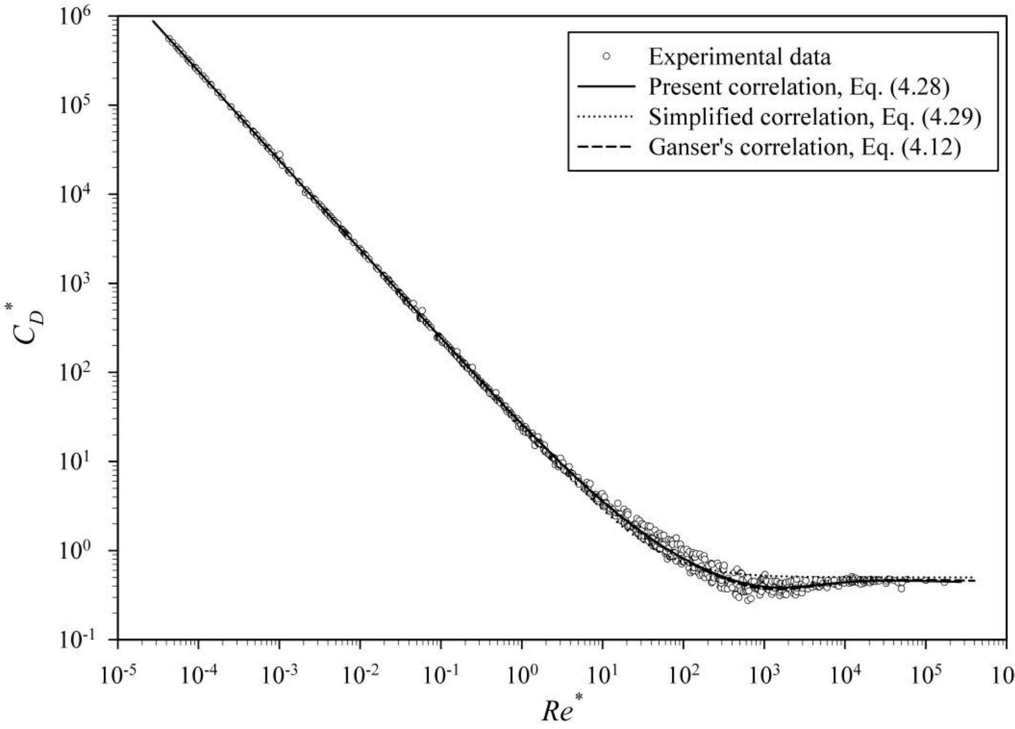

Fig. 4.4. Experimental normalized drag coefficient data along with Eqs. (4.28), (4.29) and Ganser correlation (Eq. 4.12).

Table 4.4 provides detailed statistical calculation results about the prediction performance of C_{D_I} using the present correlation and C_{D_V} using the Ganser correlation and the one proposed in Chapter 3. Comparison of the *RMS* deviations, E_{Max} and E_{Ave} associated with the prediction of the drag coefficients for different objects show that three correlations give similar results when the experimental Stokes' and Newton's dynamic shape factors are used. The mean absolute relative error, E_{Ave}, for this case is less than 10%. In contrast, C_{D_I} is predicted with less accuracy than C_{D_V} , when dynamic shape factors are determined using related correlations. The side view-drag coefficient has high

E_{Max} for a double cone with an aspect ratio of 4 and a disk with aspect ratio of 0.25. This means that the prediction of C_{D_I} for highly non-isometric objects can be erroneous. This is not surprising since the K_{St_I} correlation is developed after excluding the data for highly non-isometric particles (see Section 4.4.1.1.).

Comparison of volumetric drag coefficient predictions shows that the Ganser correlation has slightly better accuracy than the C_{D_V} correlation developed in Chapter 3, as indicated by lower *RMS* and E_{Max} values shown in Table 4.5. However, it is worth noting that the Ganser correlation requires two shape factors, ψ and d_P/d_V .

Table 4.4. Correlation performance for the data used to develop correlation. Overall constants used for all shapes, N = 702.

Object	Ref	N	Experimental Stokes' and Newton's dynamic shape factors									Stokes' and Newton's dynamic shape factors by correlations								
			C_{D_V} , Chapter 3, using ϕ			C_{D_V} , Ganser [39], using ψ , $\frac{d_P}{d_V}$			C_{D_I} , Eq. (4.28), using ϕ			C_{D_V} , Chapter 3, using ϕ			C_{D_V} , Ganser [39], using ψ , $\frac{d_P}{d_V}$			C_{D_I} , Eq. (4.28), using ϕ		
			RMS	E_{Max}	E_{Ave}	RMS	E_{Max}	E_{Ave}	RMS	E_{Max}	E_{Ave}	RMS	E_{Max}	E_{Ave}	RMS	E_{Max}	E_{Ave}	RMS	E_{Max}	E_{Ave}
Cube	[15]	179	0.051	53.2	8.9	0.047	45.6	8.3	0.050	53.1	8.6	0.047	28.5	7	0.041	40.2	7.2	0.097	41	23.7
Cube octahedron	[15]	170	0.019	18.8	3	0.019	15.1	3	0.019	18.9	3.1	0.033	23.5	5.4	0.019	16.7	3.3	0.086	32	17.3
Cylinder, E=0.25	[17,19,29]	12	0.049	17.1	10.8	0.054	21.3	11.5	0.057	22.3	12.9	0.039	18.9	7	0.069	33.9	9.1	0.309	164	100
cylinder, E=1	[17,19,21,29,32]	16	0.058	31.8	11.5	0.054	29.2	10.6	0.056	31.4	11.2	0.058	31	12	0.042	22.3	7.5	0.067	33.3	14.4
Cylinder, E=4	[17,19,23,29]	43	0.091	34.6	16.9	0.097	74.3	35.3	0.095	35.5	17.6	0.135	130.4	26.7	0.084	74.3	35.3	0.080	70.7	15.1
Double cone, E=1	[19,29]	11	0.036	14.9	6.7	0.045	18.9	8.3	0.032	14.9	5.3	0.074	28.7	10.8	0.119	40.9	16.8	0.084	32.2	12.6
Double cone, E=4	[19,29]	7	0.064	19.8	11.6	0.069	22.4	12.6	0.139	112.7	27	0.120	55.3	28.8	0.075	22.5	14.3	0.141	119.2	29.4
Octahedron	[15]	93	0.032	24	5.1	0.028	18.8	4.8	0.032	23.9	5.2	0.044	29.4	8.6	0.023	14.5	3.8	0.065	29	15.3
Prism, E=4	[19,29]	8	0.062	19.8	12.7	0.066	19.4	13.4	0.108	66.6	20.5	0.069	42.8	12.7	0.039	20.9	7.1	0.118	69.7	24.9
Sphere	[15,19]	68	0.065	28.4	9.6	0.069	30.5	10	0.064	26.3	9.5	0.061	27.4	9.5	0.069	30.5	10	0.056	23.7	8.9
Spheriod, E=4	[19,29]	14	0.085	27.1	13.3	0.094	30.7	14.3	0.160	100.5	33.7	0.091	82.3	16.2	0.053	18.2	10.4	0.120	74.7	24.1
Tetrahedron	[15]	81	0.035	18.6	6.1	0.038	20.7	6.4	0.035	18.6	6.1	0.044	29.7	6.1	0.034	19.2	6	0.096	45	14.5
All together		**702**	**0.048**	**53.2**	**9.7**	**0.049**	**45.6**	**7.5**	**0.054**	**112.7**	**8.1**	**0.058**	**130.4**	**8.8**	**0.046**	**74.3**	**6.8**	**0.095**	**164**	**19.0**

The performance of five different correlations is summarized in Table 4.5 along with their respective *RMS* deviations, E_{Max} and E_{Ave} values. Performance of correlations are shown separately for two cases of dynamic shape factors calculated using experimental data and those predicted using related correlations. The H & S correlation does not require the calculation of dynamic shape factors. The new correlation predicts C_{D_I} with similar performance to C_{D_V} when experimental dynamic Stokes' and Newton's shape factors are employed. The side view-drag coefficient prediction using correlations developed for K_{St_I} and K_{N_I} has higher *RMS* deviation, E_{Max} and E_{Ave} compared to C_{D_V} . High E_{Max} = 164% is calculated for a disk with thickness-to-diameter ratio of 0.25 reported by Unnikrishnan et al. [17] at Re_V = 0.23.

Table 4.5. Comparison of correlations performance in predicting 702 data points

Drag Correlation	Shape factor	Stokes' and Newton's dynamic shape factors	*RMS*	% E_{Max}	% E_{Ave}	% of data predicted within ±20 %
C_{D_I} , Eq. (4.28)	ϕ	Experimental K_{St_I} , K_{N_I}	0.054	113	8.1	91.7
		K_{St_I} , K_{N_I} by correlation	0.095	164	19.0	68.5
C_{D_I} ,Cheng-like fit, Eq. (4.29)	ϕ	Experimental K_{St_I} , K_{N_I}	0.085	113	13.7	78.8
		K_{St_I} , K_{N_I} by correlation	0.104	152	20	64.7
C_{D_V} ,Chapter 3, Eq. (3.31)	ϕ	Experimental K_{St_V} , K_{N_V}	0.048	53.2	9.7	92.7
		K_{St_V} , K_{N_V} by correlation	0.058	130	8.8	89.3
C_{D_V} ,Cheng-like fit (Eq. 3.32)	ϕ	Experimental K_{St_V} , K_{N_V}	0.081	95.6	12.9	79.8
		K_{St_V} , K_{N_V} by correlation	0.083	156	13.3	84.6
C_{D_V} ,Ganser, [39]	ψ , $\frac{d_P}{d_V}$	Experimental K_{St_V} , K_{N_V}	0.049	45.6	7.5	91.6
		K_{St_V} , K_{N_V} by correlation	0.046	74.3	6.8	92.3
C_{D_V} , H&S [42]	ψ , $\frac{d_P}{d_V}$	-	0.078	60	10.4	86.2

Overall performance of the C_{D_V} correlation developed in Chapter 3 using ϕ is comparable to the Ganser correlation using ψ and d_P/d_V . Both correlations have $E_{Ave} \leq 10\%$. The Ganser correlation has lower $E_{Max} = 74\%$ compared to correlation developed in Chapter 3 with $E_{Max} = 130\%$, both of which correspond to the case of a cylinder with an aspect ratio of 4 at $Re_V = 24{,}400$ having regular oscillatory and rotational motion around the vertical axis [14]. In terms of the standard statistical analysis of correlation accuracy, we can say that, for this set of data, the H&S correlation is less accurate than the Ganser correlation or the one proposed in Chapter 3. The maximum relative error for the H&S correlation ($E_{Max} = 60\%$) occurs for a cube octahedron at $Re_V = 348$ [15]. For the same data point, the correlation developed in Chapter 3 has $E_{Max} = 52\%$ and the Ganser correlation gives $E_{Max} = 13\%$.

Table 4.5 also provides the statistical percentage of the data predicted by different correlations within ± 20% of the experimental data. For C_{D_I}, the prediction with error less than $\pm 20\%$ covers 68.5% of the data bank. This is a reasonable performance considering the number of the geometrical parameters used to predict C_{D_I}. Overall, the Ganser correlation predicts 92.3% of the C_{D_V} data bank within ± 20% of experimental values while the correlation developed in Chapter 3 predicts 89.3% of the data. This means that the Ganser correlation has slightly lower error band than the correlation developed in Chapter 3. The H & S correlation does not provide any better prediction for this set of data, with 86.2% of data within ± 20% of the experimental C_{D_V} data.

From the preceding discussion, one can conclude that the simplified correlation (Eq. 4.29) is least accurate, as one would expect based on its formulation. The reality, though, is that its performance, on average, is not much worse than the other correlations (see Table 4.5).

4.4.2. Performance validation of new correlation

Performance of the new correlation is validated by predicting the drag coefficients of 1,080 experimental data points. It should be mentioned that these data points are not used to develop the correlation. Table 4.6 provides prediction comparison of correlations for C_{D_I} and C_{D_V}.

In general, the present correlation does not predict C_{D_I} as well as the C_{D_V} prediction using correlation developed in Chapter 3 and Ganser [39] correlation. As it is seen in Table 4.6, C_{D_I} is predicted with higher *RMS* deviations, E_{Max} and E_{Ave} than C_{D_V}. The error is more significant for highly non-isometric particles (dendrite, disk, hexagonal plate, plate-like prism and stellar crystals). However, considering the fact C_{D_I} is predicted with only a particle's two-dimensional geometrical data and particle volume is not used, the performance is reasonable. It predicts 1,080 drag data points with mean absolute relative error of 38.5%. The highest deviation from experimental data is for highly non-isometric particles including very thin bodies, such as disks, hexagonal plates and broad-branched crystals. The highest E_{Max} = 274% corresponds to a data point of a disk with an aspect ratio of 783 and $\phi = 0.004$ falling axially in Stokes' regime [24]. This high error band might be due to the error in the measurements; because under similar conditions, a disk with a higher aspect ratio than 783 had lower error. After excluding disks, hexagonal plates and broad-branched crystals data, reducing number of data points to 818, the correlation provides a reasonable estimate of C_{D_I} having E_{Max} = 76.5% and E_{Ave} = 31.8%. Note that for oblates, hemispheres and spherical caps, the prediction of C_{D_I} is better than C_{D_V}. Table 4.6 also reports the prediction capabilities of the Ganser correlation and the correlation introduced in Chapter 3 to predict C_{D_V}. As seen from this table, both correlations have similar performance. The detailed comparison was previously discussed in Chapter 3 (see Table 3.10).

Table 4.6. Summary of detailed statistical analysis of correlation performance for the data used to validate the new correlation, N =1,080.

Objects	E	ϕ	ψ	N	Re_V range	C_{D_I}, present correlation, using ϕ			C_{D_V}, Chapter 3, using ϕ			C_{D_V}, Ganser [39], using ψ, $\frac{d_P}{d_V}$		
						RMS	E_{Max}	E_{Ave}	*RMS*	E_{Max}	E_{Ave}	*RMS*	E_{Max}	E_{Ave}
Broad branched crystal [27]	25	0.12	0.28	41	0.08 - 46	0.082	27.5	19.9	0.035	15.7	7.4	0.027	16.0	4.9
Cone [37]; 90° cone-spherical segment; 70° cone-spherical segment; 90° cone-hemisphere segment; 90° tear drop[27]	0.9-2.1	0.52-0.75	0.78-0.98	69	0.5 - 875	0.140	57.4	35.2	0.144	76.0	34.8	0.146	64.0	19.5
Cylinders [14,17,21,23,32]	0.25-9.1	0.28-0.78	0.60-0.87	97	0.04 – 10,000	0.185	74.9	31.7	0.104	97.5	19.5	0.082	60.0	14.7
Dendrite [27]	25	0.12	0.27	50	0.03 - 93	0.256	49.1	44.4	0.075	20.4	15.8	0.107	28.0	21.6
Disk [14,24,26,27]	7.9-1602	0.002-0.31	0.019-0.53	180	0.002 – 25,000	0.263	274	74.5	0.139	123.4	26.9	0.136	89.7	21.7
Hemisphere and spherical caps [28]	1.09-2	0.75-0.98	0.84-0.99	72	26 – 13,390	0.198	76.8	34.3	0.214	69.8	35.5	0.238	63.3	38.2
Hexagonal plate [27]	25	0.12	0.30	41	0.06 - 38	0.120	39.7	31.3	0.036	16.6	8.0	0.029	14.7	4.9
Oblate [14]	0.5	0.86	0.94	38	13 – 41,500	0.055	21.3	10.7	0.104	31.8	19.5	0.178	44.9	30.7
Plate like prisms [47]	0.2-4	0.30-0.79	0.59-0.81	22	0.1 - 1.6	0.121	76.5	22.4	0.085	44.1	16.5	0.044	34.5	5.8
Prism [19]	0.25	0.50	0.64	4	11 - 92.4	0.127	36.1	34.0	0.019	5.5	3.9	0.005	5.0	3.5
Prolate [14]	0.5	0.84	0.95	34	14 – 94,000	0.124	36.1	22.9	0.075	38.6	14.4	0.131	40.3	23.4
Sands and gravel [19,31]	1.3-5.2	0.43-0.98	0.58-0.99	337	0.04 – 17,914	0.191	67.7	30.6	0.154	58.6	25.6	0.134	61.9	21.2
Steller crystal with plates, steller crystal [27]	25	0.12	0.28-0.30	48	0.02 - 96	0.271	63.9	39.2	0.079	31.5	15.0	0.129	36.4	23.9
Overall	**0.25-1602**	**0.002-0.98**	**0.019-0.99**	**1080**	**0.02 – 94,000**	**0.202**	**274**	**38.5**	**0.133**	**123.4**	**22.8**	**0.135**	**89.7**	**20.8**
overall, after excluding disk, hexagonal and broad branched crystal data	**0.25-25**	**0.12-0.98**	**0.27-0.99**	**818**	**0.02 – 94,000**	**0.195**	**76.5**	**31.8**	**0.137**	**97.5**	**23.4**	**0.141**	**64.0**	**22.2**

Table 4.7 summarizes the performance statistics of different correlations listed in Appendix 4.3 that are tested using the entire data bank comprised of 1,782 data points. Comparison of C_{D_I} and C_{D_V} predictions show that C_{D_I} is predicted with higher *RMS*, E_{Ave}, and E_{Max} than C_{D_V}. The mean absolute relative error of the C_{D_I} prediction is around E_{Ave} = 31%. The C_{D_I} correlation predicted around 85% of the experimental data within ± 45 %. This is a reasonably accurate considering the limited geometrical data used to predict C_{D_I}.

Table 4.7. Summary of statistical analysis comparison of drag coefficient correlations, N=1,782.

Data for validation	Shape factor	*RMS*	E_{Max}, %	E_{Ave}, %	Within ± 25 %	Within ± 40 %	Within ± 45 %
C_{D_I}, Eq. (4.28)	ϕ	0.168	274	30.8	55.6	78.3	84.6
C_{D_I}, Cheng-like, Eq. (4.29)	ϕ	0.177	271.5	31.7	54.2	75.4	79.7
C_{D_V}, Chapter 3	ϕ	0.109	130.4	17.3	77.5	92.0	94.1
C_{D_V}, Cheng-like, Chapter 3	ϕ	0.124	183.6	21.8	70.3	88.4	91.0
C_{D_V}, Ganser [39]	ψ, $\frac{d_P}{d_V}$	0.109	89.7	15.3	77.2	92.3	95.1
C_{D_V}, H&S [42]	ψ, $\frac{d_P}{d_V}$	0.109	85.4	15.5	80.4	92.5	94.6

Comparison of C_{D_V} predictions shows that all three C_{D_V} correlations have similar *RMS* deviation of 0.109. The correlation developed in Chapter 3 uses one shape factor and has slightly higher E_{Ave} than the H & S and Ganser correlations. Recall that the H & S and Ganser correlations require two shape factors which can be difficult to measure for many types of non-spherical particles. However, statistically speaking, three C_{D_V} correlations demonstrate similar accuracy, having a similar *RMS* deviation range, and E_{Ave} around 15.3 -17.3%. All three C_{D_V} correlations predict about 80% of the experimental data within ± 25 % and more than 95% of the experimental data within ± 45 %. The simplified Cheng-like fit, Eq. (4.29), performs poorly in comparison with Eq. (4.28) for both C_{D_I} and C_{D_V} owing to its simple form (see Chapter 3).

Cumulative absolute relative errors of various correlations are compared in Fig. 4.5. It can be seen that the cumulative distribution relative error for C_{D_I} prediction is higher than C_{D_V}. Part of the higher error of C_{D_I} prediction compared to C_{D_V} is caused by predicting drag data for very thin bodies such as disks, plates and needle-like cylinders. The graph shows that three C_{D_V} correlations, the Ganser and H & S correlations and the correlation developed in the chapter 3, have similar ability to predict C_{D_V}.

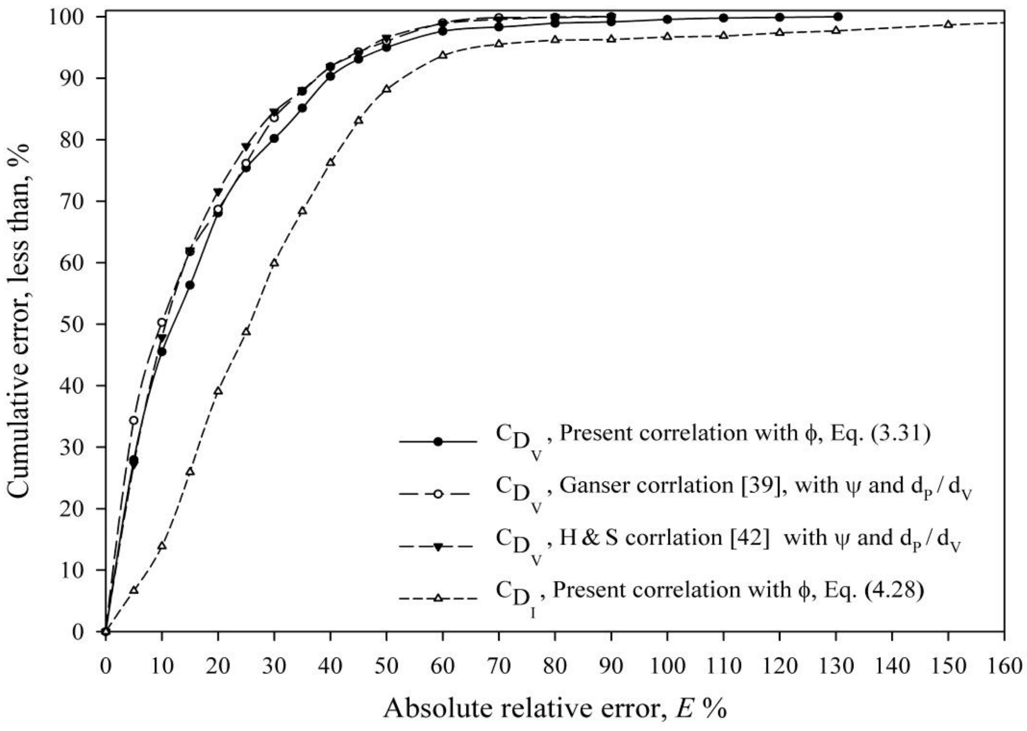

Fig. 4.5. Cumulative distribution of absolute relative error for four correlations

4.5. Summary

The present study presents a novel approach for predicting non-spherical drag coefficients using particle geometrical data obtained through online imaging measurements. Three important contributions are made:

- A new size descriptor, "side view-area equivalent sphere diameter" (d_I) is defined;
- New forms of drag coefficient (C_{D_I}) and Reynolds number (Re_I) are defined based on the new size descriptor; and
- A new correlation to estimate drag coefficient using only two-dimensional geometrical data is developed and validated.

The new size descriptor is defined based on the side view-projected area of the particle obtained from projection of the particle in a plane parallel to the particle's direction of motion. The same side view of the particle is used to calculate the degree of roundness. A combination of the new size descriptor and the degree of roundness is used to predict non-spherical particle drag coefficient.

The new universal drag coefficient correlation proposed here, based on side view-area equivalent sphere diameter and degree of roundness, is able to predict experimental drag data in the subcritical regime ($1.5 \times 10^{-5} < Re_v < 1.7 \times 10^{5}$) with reasonable accuracy. The main feature of the new correlation is that it provides, for the first time, a link between particle-fluid hydrodynamics and online imaging techniques where a moving particle is only viewed from the side. This approach has numerous advantages over the commonly used one in which the size and shape of a particle are described using particle volume and surface area. Particle volume and surface area are not available from typical online imaging measurements that are used frequently as a non-invasive method to monitor and control processes. Imaging techniques have gained a particular value to be used in the characterization of structures of highly irregular and fragile particles, and the present study can help improve the accuracy of their measurements. Another advantage of the new correlation is that it is based on a single shape factor (ϕ), while correlations proposed by Ganser [39], Hölzer and

Sommerfeld [42] require sphericity (ψ) and d_P/d_V as inputs. However, the new drag correlation is not as accurate as correlations developed by Ganser [39], Hölzer and Sommerfeld [42] and the one introduced in Chapter 3, particularly, for highly non-isometric particles such as very thin disks and plates.

4.6. Nomenclature

A	Particle characteristic projected area (L^2)
A_I	Side view-projected area of particle (L^2)
A_P	Normal view-projected area of particle (L^2)
C_D^*	Normalized drag coefficient
C_{D_I}	Side view-area equivalent sphere drag coefficient
C_{D_S}	Sphere drag coefficient
C_{D_V}	Volume equivalent sphere drag coefficient
D	Settling container diameter (L)
d_I	Side view-area equivalent sphere diameter (L)
d_V	Volume equivalent sphere diameter (L)
d_P	Normal view-projected area equivalent sphere diameter (L)
E	Particle aspect ratio
E_{Ave}	Percentage of average absolute relative error, %
E_{Max}	Percentage of maximum absolute relative error, %
F_D	Drag force ($M\ L\ T^{-2}$)
g	Gravitational acceleration ($L\ T^{-2}$)
K_{St_I}	Side view-Stokes' dynamic shape factor
K_{St_V}	Volumetric Stokes' dynamic shape factor
$K_{St_{I_m}}$	Measured side view-Stokes' dynamic shape factor
K_{N_I}	Side view-Newton's dynamic shape factor
K_{N_V}	Volumetric Newton's dynamic shape factor
N	Numbers of data points
P_I	Side view-projected perimeter (L)
Re^*	Normalized Reynolds number
Re_I	Side view-Reynolds number
Re_V	Volumetric Reynolds number
S	Particle surface area (L^2)
U	Particle settling velocity in infinite medium ($L\ T^{-1}$)
U_m	Measured particle settling velocity in a finite container ($L\ T^{-1}$)
V_P	Particle volume (L^3)
V_I	Volume of an imaginary sphere with diameter of d_I (L^3)
ϕ	Degree of roundness
μ_L	Liquid viscosity, ($M\ L^{-1}\ T^{-1}$)
ρ_L	Liquid density ($M\ L^{-3}$)
ρ_P	Particle density ($M\ L^{-3}$)
ψ	Wadell Sphericity

4.7. References

1. Yang, W., “Handbook of fluidization and fluid-particle systems”, Marcel Dekker Inc., NewYork, 2003.
2. Sin, K., Neethling, J.B., (1990). “Terminal settling characteristics of bio-particles”, Res. J. Water Pollut. Control Fed. 62(7), 901-906
3. Lee, D.J., Chen, G. W., Liao, Y. C., Hsieh, C. C. (1996). “On the free-settling test for estimating activated sludge floc density”, Water Research 30(3), 541-550.
4. Gregory, J. (1997). The density of particle aggregates. Water Science and Technology 36(4), 1-13.
5. Li, D., Ganczarczyk, J.J. (1992). “Advective Transport in Activated Sludge Flocs”, Water Environ. Res. 64(3), 236-240.
6. Tambo, N., Watanabe, Y. (1979). “Physical characteristics of flocs—I. The floc density function and aluminium floc”, Water Research 13(5), 409-419.
7. Nasser, M. S., James, A. E. (2007). ”Effect of polyacrylamide polymers on floc size and rheological behaviour of kaolinite suspensions”, Colloids and Surfaces A: Physicochemical and Engineering Aspects 301(1-3), 311-322.
8. Huang, H. (1993). “Porosity-size relationship of drilling mud flocs: fractal structure”, Clays and clay Minerals 41(3), 373-379.
9. Námer, J., Ganczarczyk, J.J. (1993). “Settling properties of digested sludge particle aggregates”, Water Res. 27(8), 1285-1294.
10. Vaezi G., F., Sanders, R.S., Masliyah, J.H., (2011). “Flocculation kinetics and aggregate structure of kaolinite mixtures in laminar tube flow”, J. Colloid and Interface Sci. 355, 96-105.
11. Clift, R., Grace, J.R., Weber, M.E., “Bubbles, drops and particles”, Academic press, New York, 1978.
12. Turton, R., Levenspiel, O., (1986). “A short note on the drag correlation for spheres”, Powder Tech. 47, 83-86.
13. Khan, A.R., Richardson, J.F., (1987). “The resistance to motion of a solid sphere in a fluid”, Chem. Eng. Commun. 62, 135-150.

14. Stringham, G.E., Simons, D.B., Guy, H.P. “The behavior of large particles falling in quiescent liquids”, US Geol. Surv. Prof. Pap., Vol. 562-C 1969.
15. Pettyjohn, E.S., Christiansen, E.B., (1948). “Effect of particle shape on free settling rates of isometric particles”, Chem. Eng. Prog. 44, 157–172.
16. Heiss, J.H., Coull, J., (1952). “The effect of orientation and shape on the settling velocity of non-isometric particles in a viscous medium”, Chem. Eng. Prog. 48, 133-140.
17. Unnikrishnan, A., Chhabra, R.P., (1991). “An experimental study of motion of cylinders in Newtonian fluids: wall effect and drag coefficient”, Can. J. Chem. Eng. 69, 729-735.
18. Madhav, G.V., Chhabra, R.P., (1995). “Drag on non-spherical particles in viscous fluids”, Int. J. Miner. Process. 43, 15–29.
19. Schulz, E.F., Wilde, R.H., Albertson, M.L., “Influence of shape on fall velocity of sedimentary particles”, Report prepared for the Missouri river division, Corps of Engineers, U.S. Army through Colorado, A&M research foundation, For Collins CO., 1954.
20. Sharma, M.K., Chhabra, R.P., (1991). “An experimental study of free fall of cone in Newtonian and non-Newtonian media: drag coefficient and wall effects”, Chem. Eng. Process. 30, 61-67.
21. Lasso, I.A., Weidman, P.D., (1986). “Stokes drag on hollow cylinders and conglomerates”, Phys. Fluids 29, 3921–3934.
22. N. Agarwal, N., R.P. Chhabra, R.P., (2007). “Settling velocity of cubes in Newtonian and power law liquids”, Powder Technol. 178, 17-21.
23. Komar, P.D., (1980). “Settling velocities of circular cylinders at low Reynolds numbers”, J. Geol. 88, 327-336.
24. Squires, L., Squires Jr., W., (1937). “The sedimentation of thin discs”, Trans. Am. Inst. Chem. Eng. 33 (1937) 1-12.
25. Isaacs, J.L., Thodos, G., (1967). “The free settling of solid cylindrical particles in the turbulent regime”, Can. J. Chem. Eng. 45, 150-155.
26. Willmarth, W.W., Hawk, N.E., Harvey, R.L., (1964). “Steady and unsteady motions and wakes of freely falling disks”, Phys. Fluids 7, 197–208.

27. List, R., Schemenauer, R.S., (1971). “Free – fall behaviour of planar snow crystals, conical graupel and small hail”, J. Atmos. Sci. 28, 110–115.
28. Wang, J., Qi, H., You, C., (2009). “Experimental study of sedimentation characteristics of spheroidal particles”, Particuology 7, 264-268.
29. McNown, J.S., Malaika, J., (1950). “Effect of particle shape on settling velocity at low Reynolds numbers”, Am. Geophys. Union, Trans. 31, 74-82.
30. Komar, P.D., Reimers, C.E., (1978). “Grain shape effects on settling rates”, J. Geol. 86, 193-209.
31. Baba, J., Komar, P.D., (1981). “Settling velocities of irregular grains at low Reynolds numbers”, J. Sediment. Petrol. 51, 121-128.
32. McKay, G., Murphy, W.R., Hillis, M., (1988). “Settling characteristics of discs and cylinders, Chem Eng. Res. Des. 66, 107-112.
33. Leith, D., (1987). “Drag on non-spherical objects”, Aerosol. Sci. Tech. 6, 153–161.
34. Haider, A., Levenspiel, O., (1989). “Drag coefficient and terminal velocity of spherical and non-spherical particles”, Powder Technol. 58, 63–70.
35. Swamee, P.K., Ojha, C.S.P., (1989). “Drag coefficient and fall velocity of non-spherical particles”, J. Hydraul. Eng. 117, 660-667.
36. Geldart, D., (1990). “Estimation of basic particle properties for use in fluid-particle process calculation”, Powder Technol. 60, 1-13.
37. Thompson, T.L., Clark, N.N., (1991). “A holistic approach to particle drag prediction”, Powder Technol. 67, 57–66.
38. Chien, S.F., (1994). “Settling velocity of irregularly shaped particles”, SPE Drilling and Completion, 9, 281-289.
39. Ganser, G.H., (1993). “A rational approach to drag prediction of spherical and non-spherical particles”, Powder Technol. 77, 143-152.
40. Chhabra, R.P., Agarwal, L., Sinha, N.K., (1991). “Drag on non-spherical particles: an evaluation of available methods”, Powder Technol. 101, 288–295.
41. Loth, E., (2008). “Drag of non-spherical solid particles of regular and irregular shape”, Powder Technol. 182, 342-353.

42. Hölzer, A., Sommerfeld, M., (2008). "New simple correlation formula for the drag coefficient of non-spherical particles", Powder Technol. 184, 361-365.
43. Bushell, G.C., Yan, Y.D., Woodfield, D., Raper, J., Amal, R., (2002). "On techniques for the measurement of the mass fractal dimension of aggregates", Adv. Colloid Interface Sci. 95, 1-50.
44. Bowen, B.D., Masliyah, J.H., (1973). "Drag force on isolated axisymmetric particles in Stokes flow", Can. J. Chem. Eng., 51, 8-15.
45. Chhabra, R.P., Agarwal, S., Chaudhary, K., (2003). "A note on wall effect on the terminal falling velocity of a sphere in quiescent Newtonian media in cylindrical tubes", Powder Technol. 129, 53-58.
46. Cheng, N.S., (1997). "Simplified settling velocity formula for sediment particle", J. Hydraul. Eng. 123, 149–152.
47. Johnson, D.L., Leith, D., Reist, P.C., (1987). "Drag on non-spherical, orthotropic aerosol particles", J. Aerosol. Sci. 18, 87-97.
48. Sheaffer, A., (1987). "Drag on modified rectangular prisms", J. Aerosol. Sci. 18, 11-16.

Appendix 4.1. Stokes’ dynamic shape factors for non-spherical particles, N = 30

Object	Orientation	E	$\frac{d_V}{d_I}$	$\frac{d_P}{d_V}$	ϕ	ψ	K_{St_V}	K_{St_I}	Data origin
Cube	-	1.0	1.100	0.910	0.785	0.806	0.926	1.120	[7]
Cube octahedron	-	1.2	0.908	1.102	0.907	0.905	0.969	0.797	[7]
Cylinder	Axial	1.0	1.015	0.874	0.785	0.874	0.958	0.986	[10, 21]
Cylinder	Axial	2.0	0.904	0.693	0.698	0.832	0.975	0.796	[10, 21]
Cylinder	Axial	3.0	0.845	0.606	0.589	0.779	0.958	0.684	[10, 21]
Cylinder	Round wise	0.5	0.909	0.878	1.000	0.826	0.961	0.826	[10]
Cylinder	Round wise	1.0	1.015	0.986	0.785	0.874	0.945	0.973	[10]
Cylinder	Round wise	2.0	0.904	1.106	0.698	0.832	0.878	0.717	[10]
Cylinder	Round wise	3.0	0.845	1.184	0.589	0.779	0.807	0.576	[10]
Cylinder	Round wise	4.0	0.805	1.242	0.503	0.734	0.758	0.503	[10]
Double cone	POA	1.0	0.995	1.260	0.785	0.891	0.879	0.870	[19]
Double cone	POA	4.0	0.790	1.267	0.370	0.770	0.723	0.451	[19]
Ellipsoidal sand	POA	3.2	0.841	1.274	0.634	0.804	0.858	0.607	[24]
Ellipsoidal sand	POA	2.6	0.979	1.251	0.728	0.899	0.873	0.837	[24]
Ellipsoidal sand	POA	1.7	0.973	1.132	0.894	0.962	0.907	0.859	[24]
Ellipsoidal sand	POA	2.8	0.932	1.420	0.691	0.735	0.928	0.806	[24]
Ellipsoidal sand	POA	2.9	0.995	1.275	0.675	0.895	0.884	0.876	[24]
Ellipsoidal sand	POA	2.2	0.970	1.283	0.800	0.842	0.885	0.832	[24]
Ellipsoidal sand	POA	3.0	0.921	1.216	0.670	0.908	0.912	0.773	[24]
Ellipsoidal sand	POA	2.4	0.893	1.253	0.758	0.836	0.946	0.754	[24]
Spheroid	POA	4.0	0.794	1.260	0.537	0.785	0.790	0.497	[19]
Octahedron	-	1.4	1.018	1.169	0.741	0.846	0.936	0.969	[7]
Prism	Given	2.0	0.873	0.810	0.785	0.762	0.935	0.712	[10]
Prism	Given	0.5	0.980	1.021	0.698	0.768	0.862	0.827	[10]
Prism	Given	0.33	0.916	1.092	0.589	0.719	0.816	0.684	[10]
Prism	Given	0.25	0.873	1.146	0.503	0.677	0.760	0.579	[10]
Prism	Given	2.0	0.980	0.722	0.698	0.768	0.963	0.924	[10]
Prism	Given	3.0	0.916	0.631	0.589	0.719	0.971	0.814	[10]
Sphere	-	1.0	1.000	1.000	1.000	1.000	1.000	1.000	[7]
Tetrahedron	-	1.2	0.844	1.222	0.604	0.671	0.843	0.600	[7]

[*] POA: Preferred Orientation Assumption

Appendix 4.2. Newton dynamic shape factors for various non-spherical objects

Object	E	Re^*	$\frac{d_V}{d_I}$	$\frac{d_P}{d_V}$	K_{N_V}	K_{N_I}	ϕ	ψ	Data origin
Cube	-	$6 - 36\times10^3$	1.100	0.910	3.062	2.784	0.785	0.806	[7]
Cube octahedron	-	$4 - 24\times10^3$	0.908	1.102	1.913	2.109	0.907	0.905	[7]
Cylinder	2	2×10^4	0.904	1.106	2.322	2.569	0.698	0.832	[52]
Cylinder	1	300	1.015	0.986	2.526	2.500	0.785	0.874	[19]
Cylinder	0.25	787	0.782	1.387	5.196	4.065	0.503	0.693	[19]
Cylinder	4	$2 - 21\times10^3$	0.805	1.242	2.704	3.358	0.503	0.734	[5,19,52]
Double cone	1	$1 - 2.1\times10^3$	1.005	1.260	2.933	2.947	0.785	0.891	[19]
Double cone	4	$1 - 1.7\times10^3$	0.789	1.267	2.898	3.671	0.370	0.770	[19]
Octahedron		$4 - 33\times10^3$	1.017	1.169	2.627	2.580	0.740	0.846	[7]
Oblate	2	$4 - 7.6\times10^4$	0.879		1.926	1.699	0.863	0.966	[5]
Prism	4	705	0.872	0.572	3.111	3.565	0.503	0.677	[19]
Prolate	2	$2 - 1.3\times10^5$	1.110		1.471	1.629	0.847	0.947	[5]
Sphere		$1 - 17\times10^4$	1.000	1.000	1.000	1.000	1.000	1.000	[7]
Spheroid	4	2,350	0.794	1.260	2.353	2.964	0.537	0.785	[19]
Tetrahedron	-	$5 - 51\times10^3$	0.844	1.221	4.540	5.378	0.604	0.671	[7]
Disk	7.9	13,631	1.433	1.743	9.649	6.734	0.312	0.526	[28]
Disk	14.5	7,927	1.584	2.130	25.303	15.974	0.190	0.387	[28]
Disk	14.9	3,028	1.592	2.151	22.617	14.208	0.185	0.382	[28]
Disk	15.4	22545	1.600	2.173	17.729	11.081	0.180	0.375	[28]
Disk	15.6	5,256	1.604	2.184	17.701	11.035	0.178	0.372	[28]
Disk	15.9	13,692	1.608	2.195	28.224	17.549	0.175	0.369	[28]
Disk	16.1	4,485	1.613	2.207	24.467	15.173	0.173	0.365	[28]
Disk	19.6	21,271	1.666	2.356	25.407	15.249	0.145	0.327	[28]
Disk	23.8	391	1.721	2.513	20.831	12.107	0.122	0.292	[28]
Disk	26.3	355	1.750	2.598	23.706	13.549	0.111	0.275	[28]
Disk	31.3	395	1.800	2.752	19.988	11.101	0.094	0.248	[28]
Disk	33.3	418	1.820	2.811	26.266	14.432	0.089	0.239	[28]
Disk	34.5	3,063	1.830	2.843	34.675	18.946	0.086	0.234	[28]
Disk	41.8	74,723	1.890	3.033	56.003	29.628	0.072	0.208	[28]
Disk	50	387	1.947	3.218	32.384	16.632	0.060	0.186	[28]
Disk	62.5	432	2.021	3.467	38.361	18.982	0.049	0.161	[28]
Disk	83.3	453	2.120	3.816	41.623	19.632	0.037	0.134	[28]
Disk	89.3	444	2.145	3.904	53.661	25.020	0.034	0.128	[28]
Disk	100	314	2.186	4.055	53.138	24.312	0.031	0.119	[28]
Disk	125	506	2.268	4.368	79.769	35.165	0.025	0.103	[28]
Disk	150	526	2.339	4.643	75.275	32.185	0.021	0.092	[28]
Disk	200	574	2.453	5.109	77.183	31.461	0.017	0.076	[28]

Appendix 4.3. Drag correlations

Reference	Drag correlations	Shape factor	Dynamic shape factors
C_{D_I}	$\frac{C_{D_I}}{K_{N_I}} = \frac{24}{\left(\mathrm{Re}_I \mathrm{K}_{\mathrm{St}_I} K_{N_I}\right)}\left(1+0.0998\left(\mathrm{Re}_I \mathrm{K}_{\mathrm{St}_I} K_{N_I}\right)^{0.6864}\right) + \frac{0.4025}{\left(1+\frac{3210}{\left(\mathrm{Re}_I \mathrm{K}_{\mathrm{St}_I} K_{N_I}\right)}\right)}$	(ϕ)	$\ln\left(\frac{1}{K_{St_I}}\right) = \frac{1}{\left(1.1523+33.695\,\phi^{6.3951}\right)}$ $\ln\left(K_{N_I}\right) = 1.1247 - 1.0858\phi + 1.1616\left(-\ln\phi\right)^{0.5}$
C_{D_I}, Cheng-like fit	$\frac{C_{D_I}}{K_{N_I}} = \frac{24}{\left(Re_I K_{St_I} K_{N_I}\right)} + 0.5$	(ϕ)	$\ln\left(\frac{1}{K_{St_I}}\right) = \frac{1}{\left(1.1523+33.695\,\phi^{6.3951}\right)}$ $\ln\left(K_{N_I}\right) = 1.1247 - 1.0858\phi + 1.1616\left(-\ln\phi\right)^{0.5}$
C_{D_V}, Ganser [39]	$\frac{C_{D_V}}{K_{N_V}} = \frac{24}{\left(Re_V K_{St_V} K_{N_V}\right)}\left(1+0.1118\left(Re_V K_{St_V} K_{N_V}\right)^{0.6567}\right) + \frac{0.4305}{\left(1+\frac{3305}{\left(Re_V K_{St_V} K_{N_V}\right)}\right)}$	(ψ) and $\frac{d_P}{d_V}$	For non-isometric particles: $K_{St_V} = \left(\frac{1}{3}\frac{d_P}{d_V} + \frac{2}{3}\frac{1}{\sqrt{\psi}}\right)^{-1}$ For isometric particles: $K_{St_V} = \left(\frac{1}{3} + \frac{2}{3}\frac{1}{\sqrt{\psi}}\right)^{-1}$ $K_{N_V}\ 10^{1.8148\left(-Log\psi\right)^{0.5743}}$
C_{D_V}	$\frac{C_{D_V}}{K_{N_V}} = \frac{24}{\left(Re_V K_{St_V} K_{N_V}\right)}\left(1+0.0998\left(Re_V K_{St_V} K_{N_V}\right)^{0.6864}\right) + \frac{0.4025}{\left(1+\frac{3210}{\left(Re_V K_{St_V} K_{N_V}\right)}\right)}$	(ϕ)	$K_{St_V} = \phi^{0.3291}$ $\ln\left(K_{N_V}\right) = 2.0214\left(-\ln\phi\right)^{0.5749}$
C_{D_V}, Cheng-like fit	$\frac{C_{D_V}}{K_{N_V}} = \frac{24}{\left(Re_V K_{St_V} K_{N_V}\right)} + 0.5$	(ϕ)	$K_{St_V} = \phi^{0.3291}$ $\ln\left(K_{N_V}\right) = 2.0214\left(-\ln\phi\right)^{0.5749}$
C_{D_V}, H & S [42]	$C_{D_V} = \frac{8}{Re_V}\frac{d_P}{d_V} + \frac{16}{Re_V}\frac{1}{\sqrt{\psi}} + \frac{3}{\sqrt{\mathrm{Re}_V}}\frac{1}{\psi^{0.75}} + 0.42\left(\frac{d_P}{d_V}\right)^2 10^{0.4\left(-\log\psi\right)^{0.2}}$	(ψ) and $\frac{d_P}{d_V}$	Does need dynamic shape factors

Chapter 5

Shear degradation and reflocculation of flocculated kaolinite mixtures in laminar tube flow

5.1. Introduction

The efficient solid-liquid separation of fine particles dispersed in water and/or wastewater streams is of importance to many chemical, environmental and mineral operations, such as chemical and biological wastewater treatment, and tailings treatment in the mining and oil sands industries. In the oil sands industry, water is used as an extraction agent to separate bitumen from oil sands. This process produces a suspension of clays as fine tailings. The main component of the fine solids in the oil sands tailings is kaolinite, whose particle size is in the colloidal range [1,2]. The small size and surface electric potential of fine clay particles cause difficulties in separating them from water using simple settling methods. The treatment of the fine solids suspension is one of the most important tailings management issues in the oil sands industry [1-3]. Recently, some oil sands operators have begun to utilize thickener technology, in which a polymer induces flocculation of fine particles. The thickening process produces clear water and a highly dense mixture that contains large, tenuous and porous aggregates [1-5]. The physical characteristics of the thickened mixtures change during and after the flocculation process, likely due to the changes in aggregate structures, depending on the physical and chemical conditions.

One of the sensitive and most important characteristics of a flocculated suspension is its rheological behavior, which affects transportation and disposal of the thickened tailings. The rheological behavior of the thickened tailings during and after flocculation depends on the hydrodynamic conditions to which the mixture is exposed. Flocculated slurries exhibit non-Newtonian fluid behavior where time-dependency and shear-thinning phenomena are common [6]. Schaan et al. [7] observed that the rheological behavior of a flocculated kaolinite slurry changes permanently upon shearing. This is an indication of aggregate structure sensitivity to shear. In other words, shearing can change the behavior of flocculated mixtures through the changes in the aggregate structure that occur. Therefore, a deeper understanding of the effect of shearing on the flocculated aggregate structure is needed.

5.1.1. Previous studies

Flocculation of small particles into larger aggregates is accomplished in a fluid shear field that provides good particle-flocculant dispersion and frequent collisions between particles. Initially, after adding flocculant in a shear field, the aggregation process is controlling, resulting in a rapid increase in the floc size. Breakage becomes more dominant as the floc size increases. Eventually, a dynamic equilibrium is established between aggregation and fragmentation that maintains a steady-state aggregate size [8,9]. Studies show that under similar physicochemical conditions, the limiting size depends on the applied shear. Serra et al. [10] studied coagulation of latex particles suspension with NaCl solution. They reported a shear threshold of $\bar{\gamma}$ = 30 s^{-1}: below this limit, an increasing average aggregate size with the shear rate was observed, whereas above the threshold limit a decreasing aggregate size with the shear rate was found. Similarly, Colomer et al. [11] observed an increasing average aggregate size with shear rate over a low shear rate range of 0.5 to 27 s^{-1}. Selomulya et al. [12] studied coagulation of latex particles in a mixed tank with a recirculation line using small-angle static light scattering technique. They observed aggregates restructuring in the average shear rate range of 40-80 s^{-1}, whereas above 100 s^{-1} the fragmentation of aggregates was more significant than aggregate compaction. They concluded that restructuring of aggregates probably was due to frequent exposure to the high shear impeller zone. Therefore, the magnitude of the shear rate during flocculation controls flocculated aggregate structure, which is defined in terms of size, density and fractal dimension.

Shearing after flocculation also influences the flocculated aggregate structure. Consequently, macroscopic characteristics of the flocculated suspension are affected by shearing [13]. Post-shearing normally occurs in subsequent processes after formation of aggregates. For instance, in thickening technology the thickened tailings is transported using a pipeline, where post-shearing occurs inside pipes and pumps [7]. There have been extensive studies on the effect of post-shearing on aggregate structure of different particles [14-38, 41-46].

Clark and Flora [14] reported significant changes in the structural properties of aggregate upon turbulent shearing in a mixed tank in average shear rate range of 150-1800 s^{-1}. They used image analysis and settling velocity measurements to measure the aggregate size and density. They hypothesized a multilevel floc structure, as was suggested in other studies [14,15]. They suggested two modes of breakage: large-scale fragmentation of flocs into “pieces” of comparable size and erosion of small segments from the exterior parts of the aggregates. Glasgow and Liu [17] found that kaolinite-polymer aggregates were denser after shearing. Sengupta et al. [18] reported that shearing in a mixed tank reduced the mean size and narrowed the size distribution of aggregates formed after flocculation of a kaolinite suspension with a cationic polymer. Spicer et al. [19,20] used small-angle light scattering method to study constant, cycled- , and tapered-shear flocculation of polystyrene-alum aggregates in a stirred tank. They found a significant increase in aggregate density and fractal dimension after exposure to high shearing. They postulated that aggregates broke preferentially at weak points and formed more compact fragments upon shearing. This is in agreement with conclusion of other studies [21]. Yuan and Farnood [22] studied breakage of activated sludge flocs under turbulent shear conditions using a Couette flow cell and attempted to quantify floc strength. They reported that under steady shear conditions, the larger flocs broke into smaller fragments that could resist further breakage. Wang et al. [23] studied evolution of aggregate size and fractal dimension in changing shear rate conditions for various coagulation mechanisms. They reported increasing aggregate fractal dimension and decreasing size upon shearing. Zhao et al. [24] used laser diffraction technique (Mastersizer) and a recirculation line from a stirred tank to the Mastersizer to study growth and breakage of aggregates formed during a water treatment process using Titanium tetrachloride ($TiCl_4$) and Polyaluminum chloride (PACl). They used a power law correlation for size and shear rate to quantify aggregate strength that was previously used by others, e.g. Tombo and Hozami [25] and Jarvis et al. [26]. Intense shearing produces fragments with less “stickiness” of the resulting smaller aggregates, meaning the collision efficiency of subsequent collisions is reduced. A reduction in collision efficiency of aggregates produces more compact and smaller structures compared to the case when collisions are more successful [12,14, 20-23]. Shearing of aggregates is likely to produce more compact particles even when fragmentation does not occur [12,20,27,28]. Numerical simulation supports this hypothesis [29].

There are a few studies related to regrowth and reflocculation of aggregates after exposure to high shearing. Once shear rate is reduced, two types of reversible and irreversible regrowth behaviors have been observed experimentally. In the reversible case, fragmented aggregates regain the initial size measured before shearing. The reversible behavior normally happens in coagulation where suspensions are destabilized with ionic salts, e.g. NaCl. These suspensions exhibit reversible behavior because floc fragmentation and re-aggregation do not affect particle interaction through van der Waals binding forces or electrostatic attraction [20,30-32]. In the irreversible type of behavior, the aggregates regrow partially, but the average size (and also the size distribution) before exposure to high shear rate and after cessation of shearing are different [14,20,23,24,33-38]. Francois [32] observed that aggregates regrew to some degree after cessation of shearing. Clark and Flora [14] observed partial and irreversible reflocculation of fragmented aggregates upon returning the shear rate to the same value before the fragmentation step. Yukselen and Gregory [33] used PDA to study the extent of reflocculation of aggregates formed during salt-induced coagulation and polymer-induced flocculation. They concluded that prolonged high shear reduced significantly the degree of recovery in the reflocculation period for flocs formed using coagulant and a low molecular weight cationic polymer. For a high molecular weight polymer, the degree of recovery in the reflocculation period did not depend on the duration of the shearing step and there was a high degree of reversibility. Yoon and Deng [34] used in-situ focused beam reflectance measurement (FBRM), also known as scanning laser microscopy, inserted in a stirred tank, to study the effect of shearing and extent of reflocculation. They compared the performance of different coagulants and flocculants. Their results show that the initial flocculation ability of the polymer is closely related to the polymer molecular weight, but the extent of reflocculation is dominated by the charge density of the polymer: the higher the charge density of the polymer, the greater degree of reflocculation.

High initial flocculation does not necessarily mean a high degree of reflocculation. For a dual polymer system consisting of cationic polymer followed by anionic polymer, the degree of reflocculation was higher when the final zeta potential of suspension was near to zero. Rasteiro et al. [35] used a light diffraction spectroscopy (Malvern Mastersizer 2000) instrument to study reflocculation of precipitated calcium carbonate aggregates. They used two different types of high molecular weight cationic polyacrylamides as flocculants, which had different charge densities and branching. They concluded that a straight chain polymer produced smaller flocs through a patching mechanism and resulted in a higher degree of reflocculation after shearing. Conversely, a chained high molecular weight polymer led to larger and stronger flocs through bridging/patching mechanisms, with less reflocculation due to polymer conformation or degradation after shearing. In other words, the degree of reflocculation depends on the polymer type. Indeed, flocs induced through a bridging mechanism are stronger than flocs induced by patching but the stronger the flocs are initially the more difficult is reflocculation when the aggregate breaks. Rasteiro et al. [35] also show that the extent of reflocculation increases as the shear stress during breaking increases, and flocs resulting from the reflocculation process are, in general, more compact than the ones formed before shearing.

In a recent study, Zhu et al. [36] used various polymers to flocculate kaolinite. Their results showed that polymers with high molecular weight induced formation of aggregates with larger size and relatively lower fractal dimension, no matter what charge type the polymer had. They reported that at a given molecular weight, flocs formed by cationic PAM showed greater resistance to shear and a higher degree of reflocculation than those of anionic PAM. Moreover, with the same charge type, higher molecular weight PAM gave stronger flocs. The results of Zhu et al. [36] differ from those of Yoon and Deng [34] results in terms of effect of charge density and polymer molecular weight on flocs strength and extent of reflocculation. Xu et al. [37] studied the effect of shear force and pH on the breakage and re-growth of flocs made from humic acid and two different types of aluminum salt polymers. They reported some degree of reflocculation depending on pH and type of coagulants; in other words, depending on the mechanism of coagulation. Xiao et al. [38] studied coagulation of kaolinite suspensions containing humic acid. The effect of shearing and the extent of reflocculation were evaluated using PIV and image analysis techniques. They stated that the irreversibility of aggregate reflocculation during cycled shear was most likely a result of particle-flocculant bond breakage during fragmentation; hence, both reorganization and restructuring could occur.

In summary, under high shear conditions, flocculated aggregates are broken either by disruption of the attachment points on the particle surface or by the scission of covalent bonds within the bridging polymer chains. This mean that the breakage process is likely irreversible and the adsorbed polymer cannot adopt another configuration during the breakage phase. In this condition, the degree of reflocculation is low. However, in charge neutralization or “electrostatic patch” mechanisms, polymer chain disruption is less likely and there is a high degree of reversibility after breakage [33,34,39]. Owen et al. [40] reviewed the effect of applied shear on an aqueous solution of polymeric flocculant. It appears that shearing leads to a mixture of chain scission (irreversible) and entanglement (reversible) of polymeric flocculant. This can explain partial recovery of aggregate structure in the reflocculation stage after cessation of shearing [39,40].

It should be noted that in most of the aforementioned studies, the shearing period is 5-10 min and the reflocculation period is 5-30min. However, in continuous processes shearing and reflocculation periods can be much shorter than this.

Francois [31,32] defined strength factor, *SF*, and recovery factor, *RF*, to quantify effect of shear and extent of reflocculation, respectively:

$$SF = \frac{d_S}{d_F} \tag{5.1-a}$$

$$RF = \frac{(d_R - d_S)}{(d_F - d_S)} \tag{5.1-b}$$

where d_F, d_S and d_R are mean diameters of flocculated, sheared and reflocculated aggregates, respectively. The strength factor is an indication of floc strength, which refers to the ability to resist rupture by a velocity gradient. Larger values of the strength factor indicate that the flocs are stronger than those with lower factors. This factor is used as a comparative measure of aggregate strength [26, 31-38]. Flocs with larger recovery factors show better recovery ability after shear degradation, which means better regrowth after breakage [31-38].

5.1.2. Shearing devices

Various types of shearing devices are used to study flocculation process, the effects of post-shearing and extent of reflocculation. Serra et al. [10] compared efficiency of an oscillating grid, a stirred tank with a paddle mixer and a Couette flow device as flocculators in a shear rate range of 4 to 102 s^{-1} using a range of initial primary particle concentrations. They did not observe any differences in average aggregate size at different initial primary particle concentration using the stirred tank and the oscillating grid. However, using a Couette flow device, they saw an increasing average aggregate size with initial primary particle concentration. The difference in the results is mainly due to differences in hydrodynamics of the flow in each apparatus. Aggregates are exposed to different shear rates in a stirred tank due to the random nature of the shear field therein. The exposure time of a given particle to different shear regions is also variable. Similarly, Spicer et al. [41] found only slight differences between steady state structures of polystyrene-alum aggregates formed using three different types of impellers. The results of Serra et al. [10] Spicer et al. [41] show that the sensitivity of the results to the experimental conditions using a stirred tank are less those of a Couette flow device. The stirred tank and Couette flow device are extensively used in various studies [27-39, 41-47].

Recently, Vaezi et al. [9] discussed drawbacks associated with the stirred tank as well as Couette flow device compared to a laminar tube device (see also Chapter 2). They concluded that the laminar tube flow device is a better alternative to the stirred tank or Couette flow device in terms of uniformity of shear field, accurate estimation of the shear rate and direct aggregate sampling. Samples are taken directly from tube outlet which minimizes the effect of sampling on the aggregate structure.

There are few recent studies using turbulent pipe flow [48-52]. Turbulent pipe flow offers the advantages of relatively homogeneous turbulence compared to a stirred tank and a well-controlled flocculation time due to the plug flow nature of the turbulent flow. However, the mean shear rate that aggregates are exposed to is typically estimated using correlations and turbulence models that are not very accurate. Furthermore, online sampling of aggregates from turbulent pipe outlet can inevitably lead to some degree of rupture and structural change before measurement.

Gregory [53-55] used laminar tube flow for qualitative monitoring of size evolution in developing the Photometric Dispersion Analyzer (PDA). Vaezi et al. [9] studied flocculation kinetics and evolution of aggregate size, density and fractal dimension using a laminar tube flow device. In the Newtonian laminar flow inside a straight tube, the shear rate varies linearly with the tube radius. Longer residence time in laminar tube flow device requires a very long tube length. Therefore, experimental works are normally carried out using a coiled tube configuration [9]. The equation required to determine the average shear rate for the laminar flow inside a coiled tube is [9,56,57]:

$$\bar{\dot{\gamma}}_{Curved} = \frac{64Q}{3\pi\left[1-\left(1-\left(\frac{11.6}{De}\right)^{n}\right)^{\frac{1}{n}}\right]D_t^3} \qquad (5.2\text{-a})$$

where D_t is the tube internal diameter, Q is the volumetric flow rate and De is the Dean number, which is defined as:

$$De = \left(\frac{D_t}{D_C} \right)^{0.5} Re_t \tag{5.2-b}$$

McConalogue [55] gives the exponent of n = 0.45, for $11.6 < De < 3000$. In Eq. 5.2-b, D_t is tube internal diameter, D_C is diameter of tube curvature (diameter of the cylinder that the tube is coiled around) and Re_t is the tube flow Reynolds number, given by:

$$Re_t = \frac{4 \rho_L Q}{\pi \mu_L D_t} \tag{5.2-c}$$

where ρ_L and μ_L are liquid density and viscosity, respectively.

The objective of this chapter is to investigate shear degradation and reflocculation of flocculated suspensions using a well-defined shear field. Laminar tube flow is used to establish a uniform shear field. A flocculated suspension of model fine clay particles is prepared under physicochemical conditions similar to those of oil sand tailings. A detailed statistical analysis was undertaken to investigate the reproducibility of the formation of flocculated aggregate structure. This ensures that a similar aggregate structure is prepared for every experiment. The effect of magnitude of shear rate and shearing time on the structure of flocculated aggregates is studied. Furthermore, the extent of reflocculation after cessation of shearing is investigated. The three main aggregate structural parameters (size, shape and density) are monitored from analysis of aggregate settling velocity measurements and image analysis. The aggregate fractal dimension is determined using aggregate size and density data. The effects of the aggregate shape and Reynolds number on the aggregate drag coefficient, along with the effect of advective flow through the aggregate porous structure, are considered while estimating the aggregate density.

5.2. Aggregate structure monitoring

Aggregate size and density are the main parameters needed to describe an aggregate's structure. Many studies have shown that these two parameters can be related using fractal theory. In a fractal model, aggregate density, ρ_a, and size, *L*, are related with a power-law relationship of the form [58-63]:

$$\rho_{Eff} = (\rho_a - \rho_L) \propto L^{(D_F - 3)} \tag{5.3}$$

where D_F is the mass fractal dimension that varies in range of 1-3. Larger values of D_F suggest more densely packed aggregates [62,63].

Bushell et al. [62] suggest using the aggregate maximum length in Eq. 5.3, while Gregory [61] states the choice of L does not matter as long as the choice is consistent. Our observation also indicates that the choice of size L does not affect the fractal dimension significantly [9]. Here, the maximum aggregate diameter of, d_{max}, determined as the minimum diameter of a circle that circumscribes the projected image of the aggregate, is used in Eq. 5.3.

5.2.1. Size

In the present study, aggregate size is described using area-based aggregate diameter, d_a, which is calculated after measuring the projected area of an aggregate's image on a plane parallel to the settling direction of the aggregate, A_I, i.e.

$$d_a = \left(\frac{4A_I}{\pi}\right)^{0.5} \tag{5.4}$$

This measure of aggregate size is used in many studies [9,14,38,45-47,62].

5.2.2. Shape

Another important structural parameter is aggregate shape. The highly irregular three-dimensional structure of an aggregate and its inherent frangible nature make it difficult to quantify its morphology using any standard shape factor. The common shape factors used for non-spherical particles, such as sphericity, cannot be determined for a fragile aggregate. In Chapters 3 and 4, aggregate shape is described using a two-dimensional shape factor, denoted as degree of roundness, ϕ:

$$\phi = \frac{4\pi A_I}{P_I^2} \tag{5.5-a}$$

Substituting $A_I = {\pi d_a^2}/{4}$ into Eq. 5.5-a yields

$$\phi = \frac{\pi^2 d_a^2}{P_\mathrm{I}^2} \tag{5.5-b}$$

where P_I is the side view-projected perimeter of the particle that is obtained from image analysis. For a sphere, the degree of roundness is unity and for a non-spherical object it is less than one.

5.2.3. Measurement of aggregate density and fractal dimension

There are several simple techniques that can be used to measure aggregate size; however, density and fractal dimension cannot be measured easily. Gregory [61] has summarized different methods of aggregate density and fractal dimension measurement. Bushell et al. [62] have also reviewed different methods of fractal dimension measurement. Among the techniques that are typically employed, measurement of aggregate sedimentation velocity is a direct and less invasive method for determining aggregate density and fractal dimension. It is worth noting that in most light scattering and diffraction techniques used to determine aggregate structural parameters, including size and fractal dimension, particles are assumed to be spherical [21]. This contradicts directly with the assumption that an aggregate has a fractal structure.

Aggregate size, shape and sedimentation rate can be measured by direct visualization followed by image analysis. This technique has been used to estimate the aggregate density in many studies [60,64-68]. In Chapter 2, this technique was successfully applied to study the kinetics of flocculation. In general, a force balance on a non-spherical porous aggregate settling steadily in an infinite medium leads to the general equation [62,66,67,69]:

$$\frac{\rho_a-\rho_L}{\rho_P-\rho_L}=1-\varepsilon=\frac{\rho_L A\Omega C_D}{2g(\rho_P-\rho_L)V}U_a^2 \tag{5.6-a}$$

where ρ_a is aggregate density, ρ_L liquid density, ρ_P is primary particle density, ε is aggregate porosity, *A* is aggregate characteristic projected area, Ω is correction factor for advective flow through the aggregate interior, C_D is drag coefficient, g is gravitational acceleration, *V* is the aggregate volume and U_a is the aggregate's terminal settling velocity.

For a particle with an arbitrary shape, most of the drag correlations found in literature are defined based on assuming the characteristic projected area of $A=A_V={\pi d_V^2}/{4}$ where d_V is an equivalent sphere diameter having the same volume as the particle. Substitution of A_V into Eq. 5.6 requires that a volumetric drag coefficient, C_{D_V}, be defined using particle volume, which is commonly encountered in the particle-fluid dynamics literature (see Section 3.2.2. in Chapter 3). However, measuring the volume of a highly irregular and fragile aggregate is almost impossible. The readily available measure of the aggregate size using an image analysis technique is the area-based aggregate diameter, d_a, (see Eq. 5.4). An imaginary equivalent spherical particle is assumed having a diameter of d_a [9,62]. Substitution of *V* and *A* with $V_I={\pi d_a^3}/{6}$ and $A_I={\pi d_a^2}/{4}$, respectively in Eq. 5.6-a leads to:

$$\frac{\rho_a-\rho_L}{\rho_P-\rho_L}=1-\varepsilon=\frac{3\rho_L\Omega C_{D_I}}{4g(\rho_P-\rho_L)d_a}U_a^2 \tag{5.6-b}$$

where C_{D_I} is denoted as side view-area equivalent sphere drag coefficient (see Chapter 4).

The main feature of this C_{D_I} definition is that it uses only two-dimensional geometrical data obtained using image analysis of the projection of the particle in a plane parallel to its direction of motion. It is obvious that numerical values of

C_{D_V} and C_{D_I} are not identical, but they are related easily, as explained in Chapter 4. Section 5.2.4 describes the C_{D_I} correlation in detail.

The difference between aggregate density, ρ_a, and liquid density, ρ_L, in Eqs. 5.6 is known as the aggregate effective density, ρ_{Eff}. Other than aggregate equivalent diameter, d_a, aggregate shape, ϕ, and settling velocity, U_a, which are measured in a free-settling test, three unknowns are encountered in the Eq. 5.6-b: ρ_P, primary particle density; C_{D_I}, side-view drag coefficient; and Ω, the correction factor for advective flow through the aggregate interior. In the subsequent sections, approaches taken to estimate these three unknowns (ρ_P, Ω and C_{D_I}) are described.

5.2.4. Primary particle density

In Eq. 5.6-b, ρ_P is the density of the primary structural units that form the aggregate. The aggregate is comprised of micro-flocs that have some internal water as part of their structure. This structure has been confirmed experimentally by Michaels and Bolger [15] and Li and Logan [70], and by Woodfield and Bickert [71] using simulations. In the present study, a two-stage aggregation process is used, which involves the destabilization of dispersed primary particles by a coagulation step, which produces primary flocs, followed by the aggregation of primary flocs into large aggregates using polymer flocculation [9]. The primary floc density can be estimated using the fractal model. Vaezi et al. [9] describe the method used to determine the primary floc density, ρ_P, using the model given by Gmachowski [72]. For the experimental conditions studied here, the primary floc density is estimated to be $\rho_P = 1625 kg/m^3$, using measurements of primary particle and primary floc size [9].

5.2.5. Internal advective flow correction factor

The correction factor, Ω, takes account of advective flow through the aggregate interior. The correction factor is unity for an impermeable spherical aggregate and less than unity for a porous aggregate. Neale et al. [73] solved the general form of the Brinkman equation to obtain Ω for a highly porous sphere made of porous sub-clusters. We assume the same solution is valid for a non-spherical aggregate:

$$\Omega = \frac{2\beta^2\left[1-(\tanh\beta)/\beta\right]}{2\beta^2+3\left[1-(\tanh\beta)/\beta\right]} \tag{5.7-a}$$

where β is known as the normalized aggregate equivalent diameter, or the permeability factor, and is expressed by:

$$\beta = \frac{d_a}{2\sqrt{k}} \tag{5.7-b}$$

where d_a is the aggregate equivalent diameter and k is the aggregate permeability (m^2).

Calculation of Ω requires knowledge of aggregate permeability, k, whose evaluation is usually based on permeability models. For a given aggregate size, the permeability controls the extent of the advective flow. In this study, the Brinkman permeability model corrected with a shielding coefficient introduced by Vanni [74] is used:

$$k = \frac{d_P^2}{72}\left[3+\frac{4}{(1-\varepsilon)}-3.\sqrt{\frac{8}{(1-\varepsilon)}-3}\right].\frac{1}{\xi} \tag{5.7-c}$$

where

$$\xi = 1-0.6e^{-10(1-\varepsilon)} \tag{5.7-d}$$

Details of the model explained above are given in Chapter 2.

5.2.6. Aggregate shape and drag coefficient

There is no generally valid model or correlation to obtain the drag coefficient for a non-spherical permeable object [62,67]. In most studies aggregates are assumed to be spherical, despite the fact that it very rarely is true. There are two main approaches used to calculate C_D for a spherical permeable aggregate. In the first approach, Stokes' law is applied even though $Re_a > 0.1$, and the aggregate diameter was known to be around 1mm [64,66,68]. One should expect that under these conditions, Stokes' law is not valid. In the second approach, a $C_{D_V} - \mathrm{Re}$ correlation for spheres is employed [62]. Huang [60] used Stokes' law for $Re_a < 1$ and a correlation for $Re_a > 1$. Johnson et al. [69] reported a correlation for the drag coefficient of a permeable aggregate, but it deviates considerably from many of the results reported in literature [62,75]. Vaezi et al. [9] used the correction proposed by Masliyah and Polikar [76] for a falling permeable sphere with a permeability factor of $\beta > 15$ and $Re < 120$.

The correlations described above are, strictly speaking, valid only for spherical particles or aggregates. The drag coefficient of a non-spherical particle deviates considerably from that of spherical particle having same size and density. In theory, non-spherical drag coefficients can be estimated using the Reynolds number and an appropriate shape factor. However, the fragile and non-isometric structure of an aggregate restricts attempts to measure the shape factors used in most standard drag correlations, e.g. sphericity (see Chapter 4). In previous published studies, the aggregate is either assumed to be spherical or a constant shape factor is used to estimate the drag coefficient. Tambo and Watanbe [64] and Nasser and James [68] assumed a constant factor of 0.8 to account for the effect of shape. Li and Ganczarczyk [66] assumed aggregates could be described as ellipsoids and applied shape factors of 0.8 and 0.9 for any aggregate regardless of its real shape. Farrow et al. [77] assumed an ellipsoidal shape in describing the non-sphericity of the aggregate and used an equivalent sphere having the same Stokes' settling velocity as an aggregate for $Re < 0.2$. Námer and Ganczarczyk [78] defined a two dimensional shape factor using image analysis data (similar to ϕ , defined previously) and assumed it was equal to sphericity. They applied this approximation for $Re < 5.0$ to calculate the drag coefficient. However, their method was not based on any background or supportive experimental evidence and substituting ϕ for sphericity is not appropriate. There have been other attempts to develop non-spherical drag coefficient using two-dimensional imaging data. However, they are system-specific rather than being general correlations. Also, some of the assumptions made to develop the correlations are questionable [79,80].

In Chapter 4, a universal non-spherical drag coefficient was developed, which was suitable for image analysis applications valid for 1.5 × 10^{-5} < Re < 1.7 × 10^{5}. The correlation provides an estimation of side-view drag coefficient, C_{D_I} :

$$\frac{C_{D_I}}{K_{N_I}} = \frac{24}{\left(\mathrm{Re}_a\ \mathrm{K}_{\mathrm{St}_\mathrm{I}} K_{N_I}\right)}\left(1+0.0998\left(\mathrm{Re}_a\ \mathrm{K}_{\mathrm{St}_\mathrm{I}} K_{N_I}\right)^{0.6864}\right)+\frac{0.4025}{\left(1+\frac{3210}{\left(\mathrm{Re}_a\ \mathrm{K}_{\mathrm{St}_\mathrm{I}} K_{N_I}\right)}\right)} \tag{5.8-a}$$

where K_{St_I} is the side view-Stokes' dynamic shape factor, K_{N_I} is the side view-Newton's dynamic shape factor and Re_a is the side view-Reynolds number. The Reynolds number is defined using data obtained from image analysis and settling velocity measurements:

$$\mathrm{Re}_a = \frac{\rho_L U_a d_a}{\mu_L} \tag{5.8-b}$$

The equations that define K_{St_I} and K_{N_I} as a function of the degree of roundness, ϕ are presented in the Chapter 4 but are shown again here for convenience:

$$\ln\left(\frac{1}{K_{St_I}}\right) = \frac{1}{\left(1.1523+33.695\ \phi^{6.3951}\right)} \tag{5.8-c}$$

$$\ln\left(K_{N_I}\right) = 1.1247-1.0858\phi+1.1616\left(-\ln\phi\right)^{0.5} \tag{5.8-d}$$

5.3. Experimental method

5.3.1. Materials

- **Concentrated clay slurry**

A mass of 125 g of kaolinite (Dry Branch Kaolin Co., Georgia, US) is dispersed in 900 mL deionised water. The inherent density of kaolinite is 2560 kg/m^3 (reported by the supplier) with a moisture content of 4.6 % (w/w) measured by drying at 120°C. To fully disperse the clay, the pH of the slurry is adjusted to 8.70 using a 0.25N NaOH solution. The total mixture volume is then adjusted to 1

L. After the suspension is left to settle overnight, the top 800 mL is decanted. The dispersion followed by settling provides a narrow size distribution for the dispersed fine clay. The mean primary particle size is 0.64±0.02 μm, as measured with a Malvern Mastersizer (Hydro 2000SM series). The solids content of the dispersed kaolinite mixture is measured using a Pycnometer. A typical solids concentration is 50-60 g/L. This stock suspension is used to prepare 3.57 g/L slurry of primary particles through the addition of deionised water. Calcium chloride (0.1 M solution) is added to the prepared clay suspension to obtain 0.325 mM of Ca^{+2} in the suspension. The suspension pH is adjusted to 8.0. The calcium ions destabilize the dispersed primary clay particles, possibly through a charge neutralization mechanism, and prompt the formation of primary flocs. The average primary floc size was found to be 2.7±0.3 μm through Zetasizer (Malvern, Nano-ZS series) measurements and was confirmed to be 2.1±0.3 μm using an optical sizing technique (Sysmex, FPIA-3000). The difference in floc diameter is likely due to the settling of some flocs in the Zetasizer's measuring cell.

- **Polymer flocculant solution**

MAGNAFLOC 1011 polymer flocculant (CIBA Specialty Chemicals) was used for this study. It is a high molecular weight polyacrylamide with approximately 30% degree of anionicity. A concentrated polymer solution of 2 g/L is prepared by dissolving 0.2 g of dry polymer in 100 ml of de-ionized water. The polymer stock solution is used within two days of preparation. For flocculation experiments, a fresh dilute polymer solution of 6.25 mg/L is prepared by diluting the concentrated stock solution.

- **Settling medium solution**

A portion of the 3.57 g/L suspension is flocculated separately in a mixed tank, with the same procedure used for the experiments. The flocculated slurry is filtered using 2 μm filter paper. The filtrate solution is used to fill the settling chamber. This provides identical water chemistry for the flocculated slurry and the liquid in the settling chamber, thus preventing any change in the aggregate structure during the settling velocity experiments. The filtrate was found to behave as a Newtonian fluid with a viscosity of 1.04 mPa.s at 22°C (AR G2 Rheometer, TA Instruments). The temperature of the settling media and clay slurry are checked before each experiment to ensure they are nearly identical. This ensures that free convection caused by a temperature gradient and fluid viscosity changes does not affect the settling velocity measurements and hence the calculation of aggregate density.

5.3.2. Experimental apparatus

A drawing of the experimental apparatus is shown as Fig. 5.1. The apparatus includes 5 zones:

- Feed zone,
- Flocculation zone,
- Shearing Zone,
- Reflocculation zone, and
- Sampling and measurement zone

The following sections describe these zones. Appendix 5.1 provides the details of experimental set-up and flow rates for flocculation, shearing and reflocculation zones.

- **Feed zone**

The feed zone supplies the required clay suspension and polymer solution, which are prepared in separate mixed tanks. The clay suspension and polymer solution are delivered using two peristaltic pumps. A rotameter measures the flow rate of each feed stream. The flow meters were calibrated with the same mixtures used during experiments. A T-valve combines the clay suspension and polymer solution. An in-line mixer is situated downstream of the T-valve. An in-line mixer (Kenics with L/D=1), with 24 elements and OD of 3/16 inches fitted tightly inside Tygon tubing, is situated upstream of the flocculation tube It promotes mixing of the polymer solution and clay suspension feed streams.

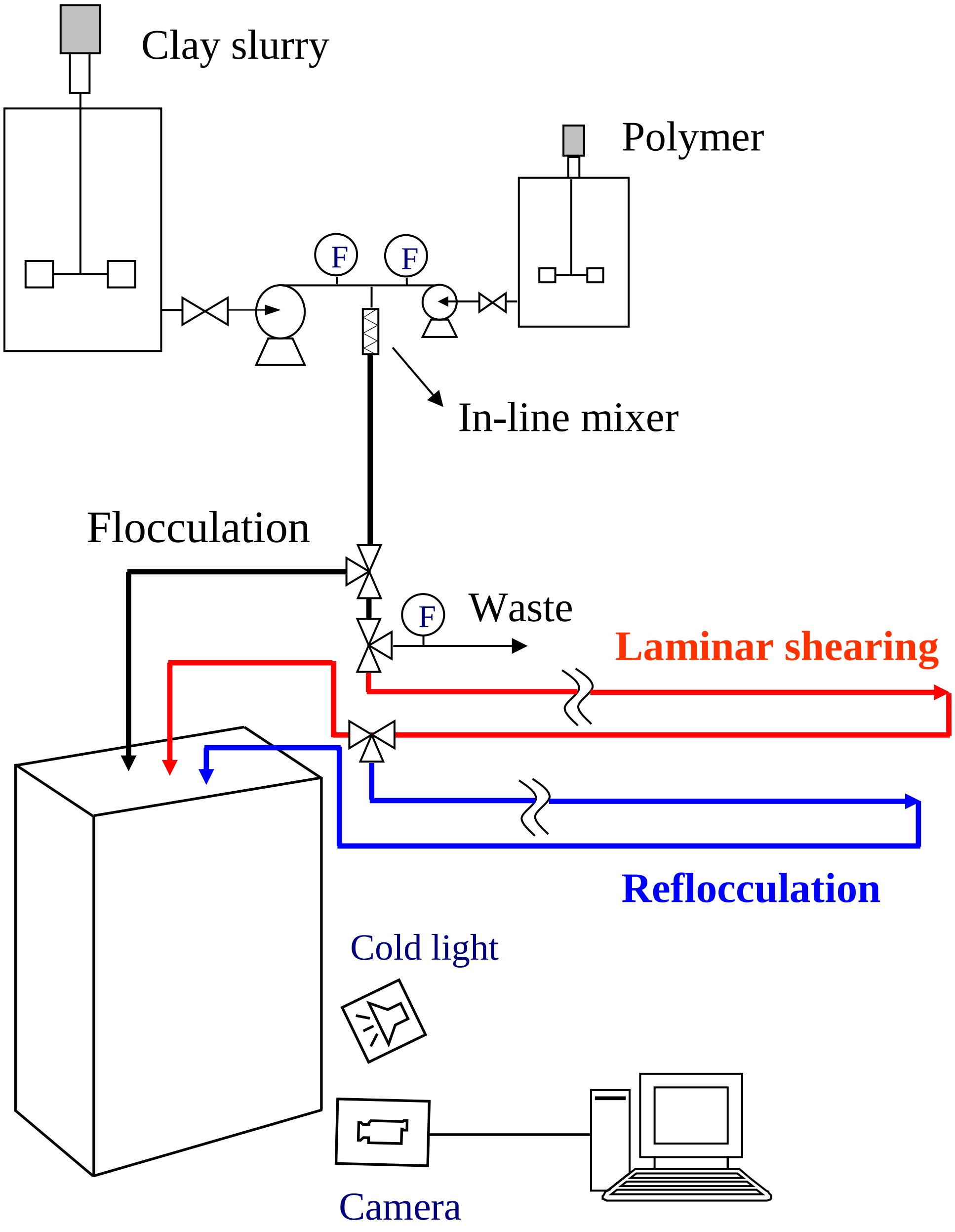
Clay slurry
Polymer
F
F
In-line mixer
Flocculation
F
Waste
Laminar shearing
Reflocculation
Cold light
Camera

Fig. 5.1. Experimental set-up

- **Flocculation zone**

The flocculation zone consists of a transparent Tygon tube which provides a laminar flow region where polymer-induced flocculation proceeds. The low shear field inside the tube provides the conditions required for orthokinetic flocculation and the formation of large and tenuous aggregates. The ratio of the clay suspension to polymer solution flow rate is set at 7/3 to provide final solids and polymer solutions concentrations of 2.5 g/L and 1.875 mg/L, respectively. For all experiments, tubes are coiled around a 166 mm diameter cylinder. The flow rate in the flocculation zone is held constant at 200±5 mL/min inside a tube with an ID of 6.4 mm. This is the minimum flow rate required to prevent the sedimentation of aggregates inside the flocculation tube. The given flow rate results in an average shear rate of $\bar{\gamma}_F$ =145 ± 3 s^{-1} inside the coiled tube. The tube length was sufficient to provide a flocculation time of τ_F = 120s. A T-valve provides an option to discharge samples of the flocculated suspension to the settling chamber or to feed the shearing zone. Over 25 experiments, the shear rate and flocculation time were varied in the range of $\bar{\gamma}_F$ = 146.3 ± 0.9 s^{-1} and τ_F = 117.3 ± 0.5 s, respectively.

- **Shearing Zone**

The shearing zone consists of a transparent Tygon tube with an ID of 3.2 mm coiled around a 166 mm diameter cylinder. The outlet stream of the flocculation zone is fed to the shearing zone through a T-valve. A side stream equipped with a rotameter controls the flow rate in the shearing zone. A range of flow rates in the shearing zone were tested to provide different shear rates over the range $\bar{\gamma}_S$ = 200-1400 s^{-1}.Tube lengths are varied to have different shearing times (See Appendix 5.1).

- **Reflocculation**

Transparent Tygon tubes with different inner diameters of 4, 4.8 and 6.3 mm, depending on the flow rate, are used to keep the shear rate constant around 145 s^{-1}

for all reflocculation experiments. The tubes are coiled around the 166 mm diameter cylinder. The outlet stream of the shearing zone is fed to the reflocculation zone through a T-valve. The tube length in the reflocculation zone varies to keep the reflocculation time constant around τ_R = 120 s. During 11 experiments the shear rate and reflocculation time were approximately $\bar{\gamma}_R$ = 123.1 ± 10.8 s^{-1} and τ_R = 114 ± 3.7 s, respectively (See Appendix 5.1).

- **Sampling and measurement zone**

This zone consists of a glass settling chamber and digital camera to record images of the settling aggregates. The settling chamber is filled with the settling medium solution. A CCD camera (QICAM Fast 1394 CCD, QImaging designs, Canada), equipped with a macro video zoom lens (Edmund optics Inc.), is mounted on the front face of the settling chamber. The pixel size of the camera is 6.5 μm. The camera is connected to a personal computer which is used to record digital videos of settling aggregates. A cold light illuminates the field of view. A black piece of paper is placed on the back side of the settling chamber to provide the required contrast between aggregates and the surroundings.

Sampling is done by diverting the outlet streams of the different zones to the settling chamber and the camera is used to capture videos of the falling aggregates. For each experiment, 5-8 samples are directed periodically from the tube outlet, thereby providing random samples of aggregates to prevent biased sampling. To minimize errors in settling velocity measurement, the sample volume is adjusted so that samples do not disturb the stagnant settling media significantly.

A software package, ImagePro Plus 6.1 (Media Cybernetics, USA), is used to control the CCD camera, to capture and to analyze the images. The error associated with the measurement of aggregate diameter is determined by the optical resolution of the camera, which is estimated to be within 10 μm. During the experiments, we found that two different persons could analyze images with less than 5% difference in diameter. Thus, the ultimate error in area-based aggregate diameter would be less than 20-50 μm, for aggregates that are 100-1200 μm in size.

The terminal settling velocity of an aggregate is evaluated by image analysis. The trajectory of a settling aggregate is tracked and the number of frames in which the aggregate is visible in the field is determined. The settling time is calculated using the number of frames and the recording speed of the camera (in frames per second). The setting velocity is calculated as $U_t = \Delta x / \Delta t$, where Δx is the distance that the aggregate settling distance and Δt is the settling time. Only terminal velocities of falling aggregates with vertical trajectories are measured.

5.4. Results and discussion

5.4.1. Flocculation of dispersed slurry

In a previous study, we investigated kinetics of the flocculation process in terms of the evolution of aggregate size, density and fractal dimension [10]. The results show that aggregates grow quickly to become relatively tenuous with an open structure in the early stages of the flocculation process (See Figs. 2.7, 2.8 and 2.9). A dynamic steady state condition appeared after 90 s of flocculation time, for the experimental conditions introduced earlier in this chapter (see Section 5.3). A detailed statistical analysis proved the establishment of a steady state condition (see Section 2.4 in Chapter 2). Based on these findings, in the present study the flocculation time was set τ_F = 120 s and the average shear rate of the flocculation zone was set to 145 s^{-1}. These conditions ensured that a steady state condition was established in the flocculation zone and that large and tenuous aggregates were formed without any aging, i.e. structural conformation occurred. Figures 5.2 show the cumulative population of aggregate size and density for seven flocculation runs conducted at similar conditions. It is clear from Figs. 5.2 that the aggregates formed in the flocculation zone are reproducible. One should note that the aggregate density is calculated considering that the aggregates are non-spherical. In Chapter 2, however, aggregates were assumed to be spherical for the study of flocculation kinetics and the evolution of aggregate structure.

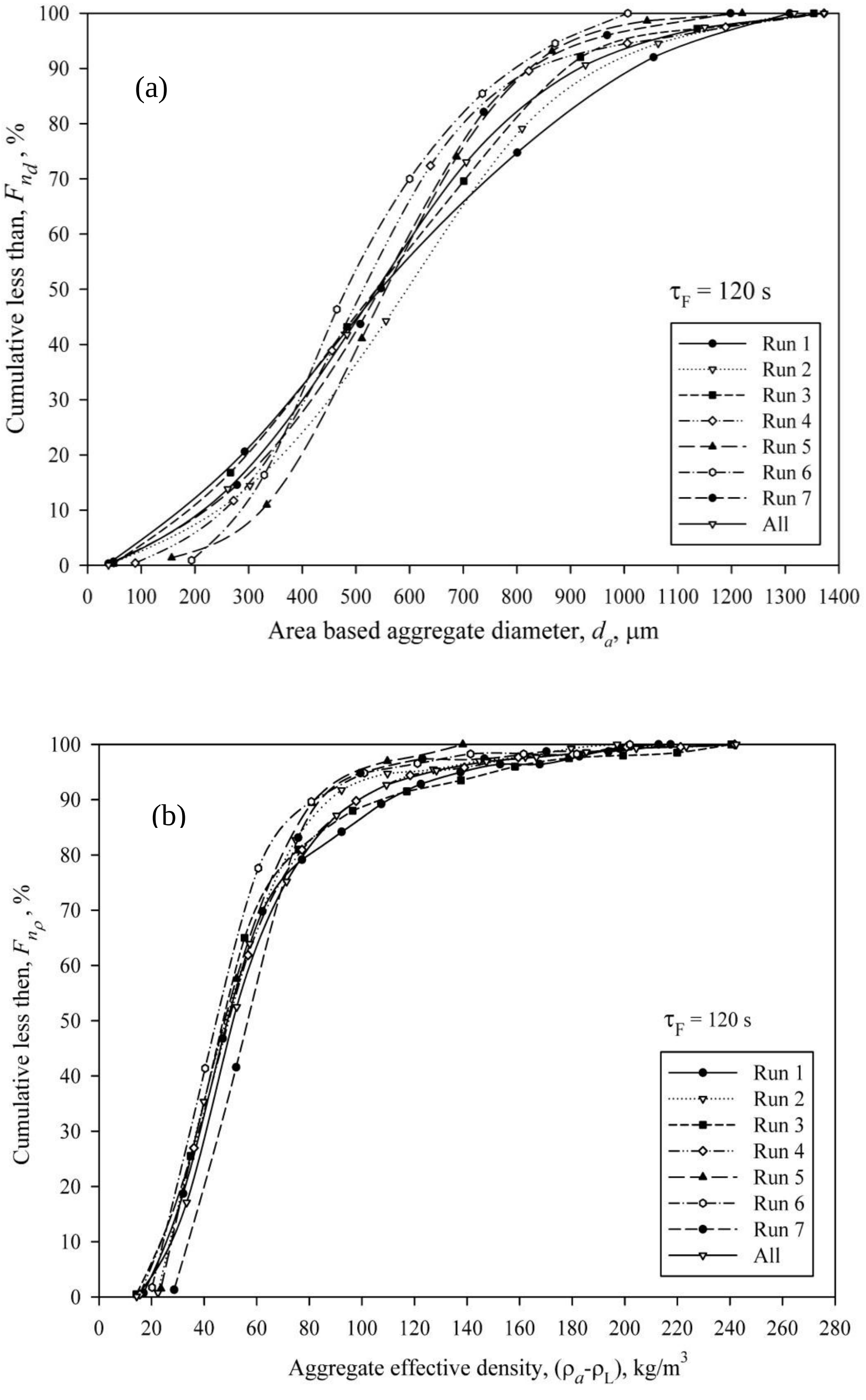

Figure 5.2. Aggregate (a) size and (b) density cumulative distribution for seven flocculation runs at similar conditions to prove reproducibility of flocculation process

Table 5.1 summarizes the structural properties of the aggregates formed for seven flocculation runs and average of all seven runs, including: mean diameter, d_{10}, Sauter mean diameter, d_{32}, average degree of roundness, ϕ, harmonic mean effective density, $\bar{\rho}_{Eff}$, fractal dimension, D_{F_F} ,and their 95% confidence intervals. Table 5.1 show that the structural parameters determined for different runs are statistically same and supports the distribution shown in Figs 5.2. The number of aggregates used to calculate the mean diameters and the degree of roundness, N_d, is greater than the number of aggregates used to calculate harmonic effective density and fractal dimension, N_ρ. The reason was that the aggregates did not settle vertically in the settling chamber and data points with $\varepsilon \leq 0.6$ were excluded from the density calculation.

Table 5.1. Structural properties of aggregates formed in the flocculation zone

	Run 1	Run 2	Run 3	Run 4	Run 5	Run 6	Run 7	All
N_d	301	201	250	239	73	110	151	1324
d_{10}, μm	566	599	546	540	563	520	531	555
d_{32}, μm	863	812	785	764	704	650	726	787
$(C.I.)_d$	37	39	34	31	48	35	41	15
ϕ	0.57	0.53	0.63	0.67	0.61	0.61	0.54	0.60
$(C.I.)_\phi$	0.02	0.02	0.02	0.02	0.03	0.03	0.03	0.01
$\bar{\rho}_{Eff}$, kg/m^3	58.7	55.4	56.5	56.5	50.2	51.6	60.6	58.4
N_ρ	139	133	200	215	66	58	77	995
$(C.I.)_\rho$	6.3	5.1	5.6	4.7	5.2	7.6	6.3	2.1
D_{F_F}	2.32	2.21	2.16	2.22	2.38	2.25	2.34	2.27
$(C.I.)_{DF}$	0.10	0.10	0.09	0.09	0.11	0.13	0.14	0.05

The repeatability of the flocculation steady state conditions at $\tau_F = 120$ s was checked using a detailed statistical analysis. For this purpose, we conducted the *F*-test, *t*-test and analysis of variances test (ANOVA) for the aggregate populations produced in seven flocculation runs conducted at similar conditions. The *F*-test showed that the seven populations produced in the experimental runs had equal variances. The *t*-test and ANOVA test showed that the arithmetic means of the aggregate size data were similar. The similar statistical tests were conducted for the aggregate density data and a similar result was obtained. This implies that the flocculation conditions tested here can produce aggregates with well-defined and statistically reproducible structure. The immediate application of this result is to have constant and reproducible aggregate structural properties for the shearing tests.

When the aggregate drag coefficients were estimated through the characterization of each aggregate's shape factor, larger values of aggregate density were obtained than when the aggregates were assumed to be spherical. Under similar conditions, a non-spherical particle experiences a greater drag force and thus will have a greater drag coefficient. In other words, a non-spherical aggregate with a volume equal to a spherical particle must be denser to settle with a same settling velocity as of the spherical particle (See Eqs. 5.6). Furthermore, due to the aggregate shape distribution, the density population determined for the non-spherical aggregates is more broadly distributed compared to the spherical aggregates. In the same way, the aggregate fractal dimension calculated using the non-spherical density-size data gives a larger fractal dimension and a lower regression coefficient compared to the spherical aggregate assumption. In other words, assuming an aggregate to be spherical leads to an underestimation of both the aggregate density and fractal dimension. This explains why density and fractal dimension determined in the present study are somewhat greater than values we presented previously [9]. Table 5.2 compares fractal dimensions calculated when the different assumptions are employed. As noted before, data points with $\varepsilon \leq 0.6$ were excluded from the density and fractal dimension calculations.

Table 5.2. Fractal dimension, D_{F_F}, of flocculated suspension

Assumption	Size-Density	D_{F_F}	$(C.I.)_{DF}$	R^2	N
Spherical	d_{max} - ρ	2.09	0.04	0.61	1157
Spherical	d_a - ρ	2.01	0.04	0.63	1157
Non-spherical	d_{max} - ρ	2.27	0.05	0.43	995
Non-spherical	d_a - ρ	2.18	0.05	0.50	995

As given in Table 5.2., application of non-spherical drag coefficients to density calculations results to greater value of fractal dimension and slightly higher value of confidence interval (C.I.) and lower regression factor, R^2, compared to the case in which aggregates are assumed spherical. Fractal dimensions calculated using maximum diameter, d_{max}, are slightly greater than the case that is calculated using area-based aggregate diameter, d_a, but the confidence intervals (C.I.), are identical. The regression factor, R^2, is slightly improved when the area-based aggregate diameter, d_a, is used.

5.4.2. Shearing Zone

- **Aggregate size**

The shearing zone experiments were conducted at different shear rates ranging from $\bar{\gamma}_S = 216$ to 1379 s^{-1} (by varying the flow rates) and at four different shearing times of τ_S = 15, 30, 60 and 120 s (by varying the flow rate and tube length). Figure 5.3a illustrates the aggregate size distribution measured after the flocculated mixture was exposed to selected shearing rate (in the range of 224 to 1331 s^{-1}) for a constant shearing time of τ_S = 60 s. Each curve shown in this figure involves the analysis of 350-600 aggregates. The aggregate size distribution of the feed mixture, which is the flocculated suspension stream produced in the flocculation zone, is also given ($\bar{\gamma}_F = 145$ s^{-1} and τ_F = 120 s).

When the flocculated suspension is sheared, the aggregate size distribution shifts toward smaller aggregate sizes. The magnitude of this shift increases with increasing the shear rate, meaning that aggregates break down as the shear rate is increased. The flocculated mixture has a normal distribution; however, after shearing the distribution is right-skewed, indicating that most of the remaining aggregates are small and only few large aggregates remain. Another finding is that as the shear rate increases the aggregate size distribution becomes narrower and at the same time again approaches to a normal distribution. At shearing times of 60 and 120 s, the aggregate size decreases as shear rate increases, which is in agreement with previous studies [14,18,20,48,52].

The change in the shape and the mode of the size distribution curves is likely caused by the fact that the number of aggregate-aggregate and aggregate-tube wall collisions increases with increasing shear rate. As a result, fragmentation dominates aggregation and aggregates decrease in size. While larger aggregates formed in the flocculation zone degrade significantly upon shearing, they do not completely break down to form primary particles or even primary flocs [9] as there is little increase in the number of particles that are 50 μm or less in size. This suggests that the main degradation mechanism is aggregate breakage rather than aggregate erosion, even though there is slight aggregate erosion.

A similar trend in the change of the aggregate size distribution with increasing shear rate is observed for a shearing time of τ_S = 120 s, as shown in Figure 5.3b. Experiments at τ_S =120 s could not be conducted at shear rates higher than $\bar{\gamma}_S = 800$ s^{-1} as a very long tube was required at high flow rates to maintain a residence time of 120 s.

The change in the size distribution with shear rate does not follow the same behavior at the lowest shearing duration, τ_S = 15 s. Figure 5.3c shows how aggregate size distribution changes upon shearing for τ_S = 15 s. There is not any significant difference in the aggregate size distribution at different shear rates. The statistical analysis confirmed that the shearing zone aggregate populations are likely identical at different shearing rates for τ_S = 15 s. This behavior was checked by repeating two set of experiments at $\bar{\gamma}_S$ = 680 and 1350 s^{-1}. The repeated experiments gave similar results. The results imply that the early stages of the fragmentation process are independent of shear rate. Clearly, though, shear rate plays a critical role in determining the aggregate size for longer exposure times that if the hydrodynamic conditions change after completion of the flocculation process.

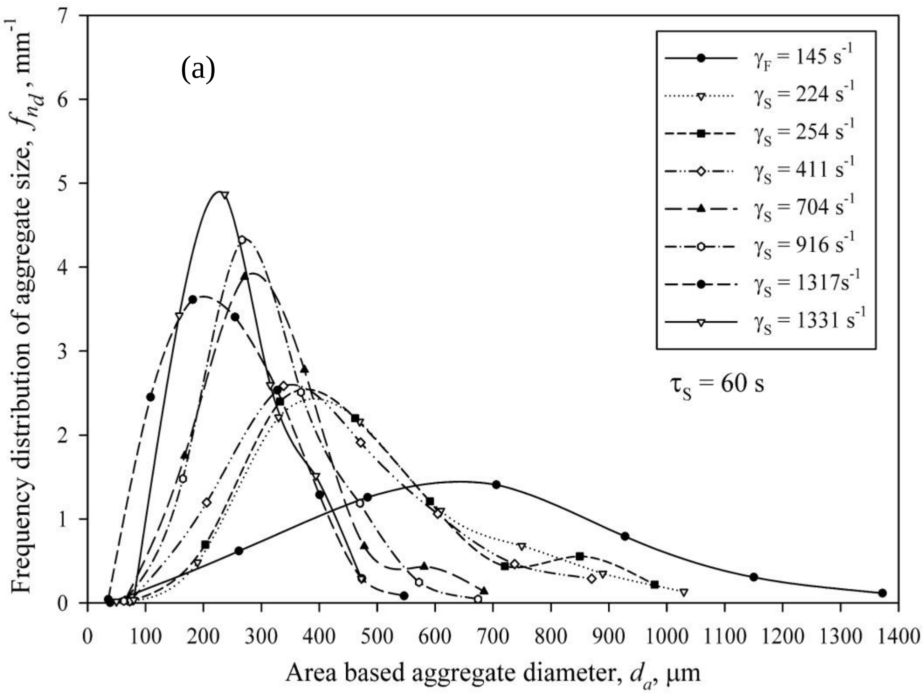
(a)
Frequency distribution of aggregate size, f_{n_d}, mm^{-1}
Area based aggregate diameter, d_a, µm
γ_F = 145 s^{-1}
γ_S = 224 s^{-1}
γ_S = 254 s^{-1}
γ_S = 411 s^{-1}
γ_S = 704 s^{-1}
γ_S = 916 s^{-1}
γ_S = 1317s^{-1}
γ_S = 1331 s^{-1}
τ_S = 60 s
0
1
2
3
4
5
6
7
0
100
200
300
400
500
600
700
800
900
1000
1100
1200
1300
1400

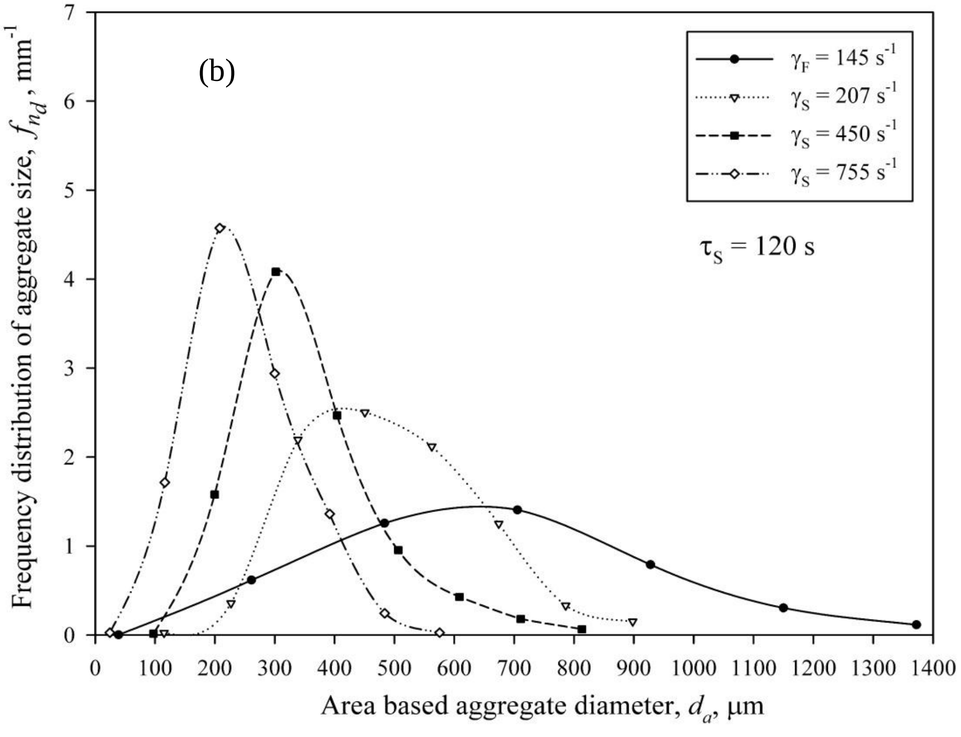
(b)
Frequency distribution of aggregate size, f_{n_d}, mm^{-1}
Area based aggregate diameter, d_a, µm
γ_F = 145 s^{-1}
γ_S = 207 s^{-1}
γ_S = 450 s^{-1}
γ_S = 755 s^{-1}
τ_S = 120 s
0
1
2
3
4
5
6
7
0
100
200
300
400
500
600
700
800
900
1000
1100
1200
1300
1400

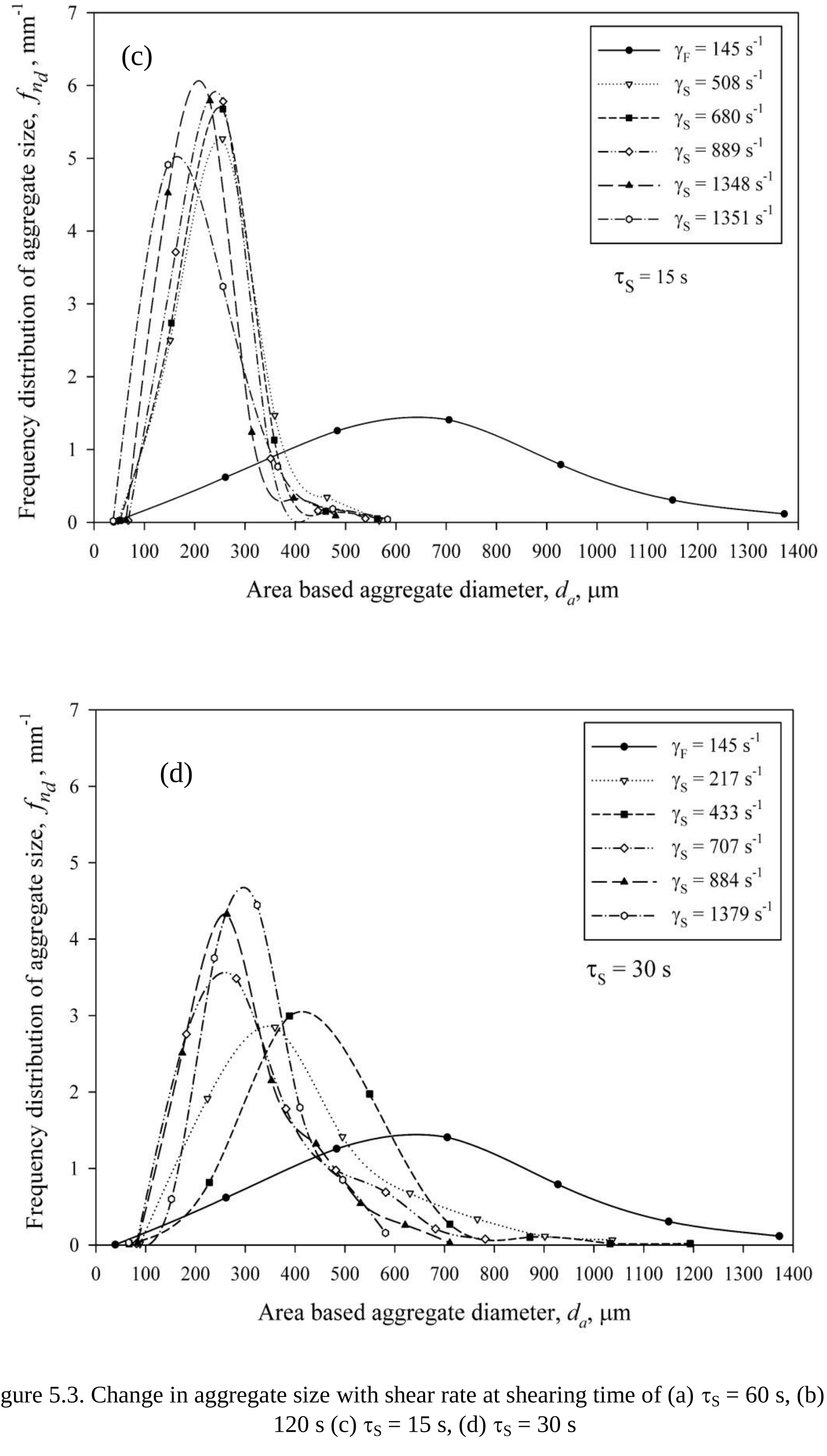

Figure 5.3. Change in aggregate size with shear rate at shearing time of (a) $\tau_S = 60$ s, (b) $\tau_S = 120$ s (c) $\tau_S = 15$ s, (d) $\tau_S = 30$ s

The sensitivity of the aggregates to any change in hydrodynamic conditions shows that aggregates fed to the shearing zone are very fragile. We hypothesize that the main reason for this observation is that the shearing time of 15 s is not sufficient to produce a dynamic steady state condition. In other words, a steady state condition cannot be established between the fragmentation and aggregation processes in 15 s. In the early stages of shearing, the fragmentation process dominates and fragile aggregates are broken down easily. The result implies that in early stages of shearing process the change in the hydrodynamic conditions is likely more important than magnitude of the change. If this hypothesis is valid, at longer residence time in the shearing zone aggregation process becomes comparable to fragmentation, unlike the shorter shearing time that fragmentation dominates. This hypothesis is confirmed through analysis of the results for τ_S = 30 s. Figure 5.3d depicts how the aggregate size distribution changes upon shearing at τ_S = 30 s. The changes in the aggregate size distribution at τ_S = 30 s are somewhat between those of at τ_S = 15 s and τ_S = 60 s. This transitional behavior can be explained as follows. In comparison to τ_S = 15 s, at lower shear rates the residence time of τ_S = 30 s provides some time for a transitional balance between aggregation and fragmentation processes at $\bar{\gamma}_S$ = 433 s^{-1}. The collision between aggregates at $\bar{\gamma}_S$ = 433 s^{-1} and τ_S = 30 s is likely enough that aggregation competes with the fragmentation. However, as the shear rate increases beyond 433 s^{-1}, the magnitude of shear rate becomes important. It is likely that at higher shear rates, e.g. $\bar{\gamma}_S$ = 707 s^{-1}, the effect of shear rate and fragmentation become dominant. Comparison of Figs. 5.3a with 5.3c and 5.3d shows that the residence time of the τ_S = 60 s provides enough time to reach a dynamic balance between the fragmentation and aggregation processes at any shear rate. These results suggest that aggregate reflocculation may become important in longer shearing times, which is discussed further in subsequent sections. There might be other reasons for this behavior and further investigation is required.

The aggregate size dependency on the shear rate and shearing time is summarized in Fig. 5.4a, in which the Sauter mean diameter, d_{32}, (or volume –

surface mean diameter) is plotted against the shear rate at shearing times of 15, 30, 60 and 120 s. The Sauter mean diameter is defined as:

$$d_{32} = \frac{\sum_{i=1}^{n} N_i.d_i^3}{\sum_{i=1}^{n} N_i.d_i^2} \tag{5.9}$$

where N_i is the number of aggregates with a diameter of d_i.

The overall trend shows that aggregate size reduces with increasing shear rate. However, at the shortest shearing time tested, $\tau_S = 15$ s, aggregate breakage does not depend on the magnitude of the shear rate. As explained before, this is due to the fragile nature of the aggregates and the fact that insufficient residence time in the shearing zone does not provide a balance between aggregate breakage and regrowth. As residence time increases to $\tau_S = 30$ s, a dynamic balance between aggregation and fragmentation is at least partially established, especially at shear rates higher than 433 s^{-1}. In most of the previous studies in this area, the shearing time is long enough, e.g. around 5-10 minutes, that the transitional competition of fragmentation and aggregation is not observed. Another distinction is that in most of previous studies, shearing took place in a stirred tank under turbulent conditions, meaning that aggregates were exposed to a broad range of shear rates and shear exposure times. It is also worth noting that in those studies, sampling has some effect on the aggregate structure [19,27,28,33,35-38]. This is not the case in the present study.

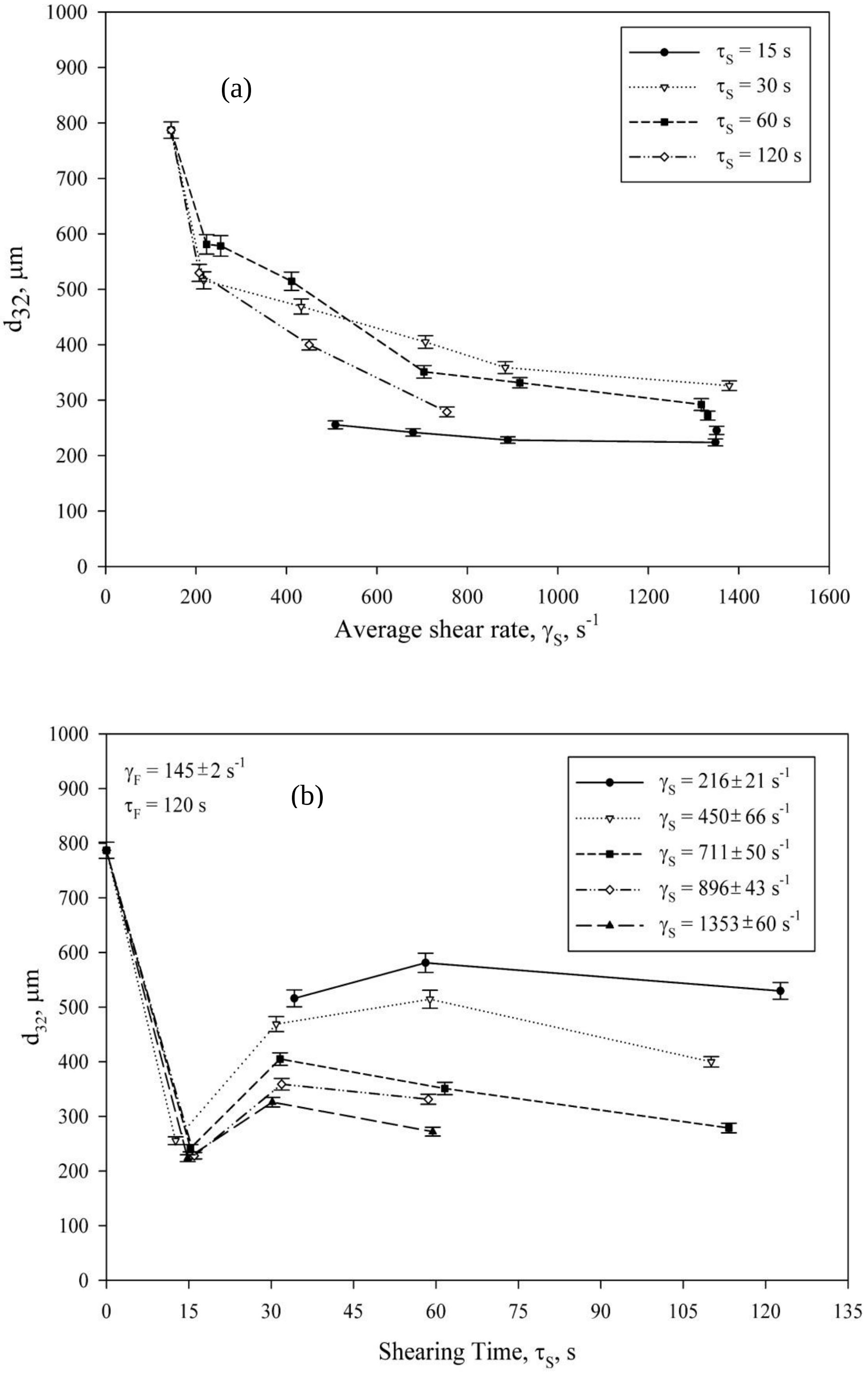

Figure 5.4. Effect of shear rate and shearing time on aggregate mean diameter at constant (a) shearing time and (b) constant shear rate

Figure 5.4b shows similar results, where d_{32} is plotted against residence time in the shearing zone at average constant shear rates. At short exposure times, the aggregates are fragmented and the extent of the effect is independent of shear rate. As residence time increases, aggregation competes with fragmentation and there is an increase in aggregate mean size. Longer exposure times reduce aggregate size even further. It appears that after 60 s a dynamic condition appears, in which a balance between aggregation and fragmentation is maintained and the final aggregate mean diameter depends on the magnitude of the shear rate. Higher shear rates produce smaller aggregates. A similar behavior is observed for τ_S =120 s. The experiments are done at constant shearing times and thus it was not straightforward to control the flow rate, which explains 4 to 15% variation in the shear rates.

Aggregate strength is examined using the Strength Factor, *SF*, defined by Eq. 5.1-a. As shown in Fig. 5.5, the aggregate strength decreases with increasing shear rate and shearing time. This is in agreement with previous studies [24].

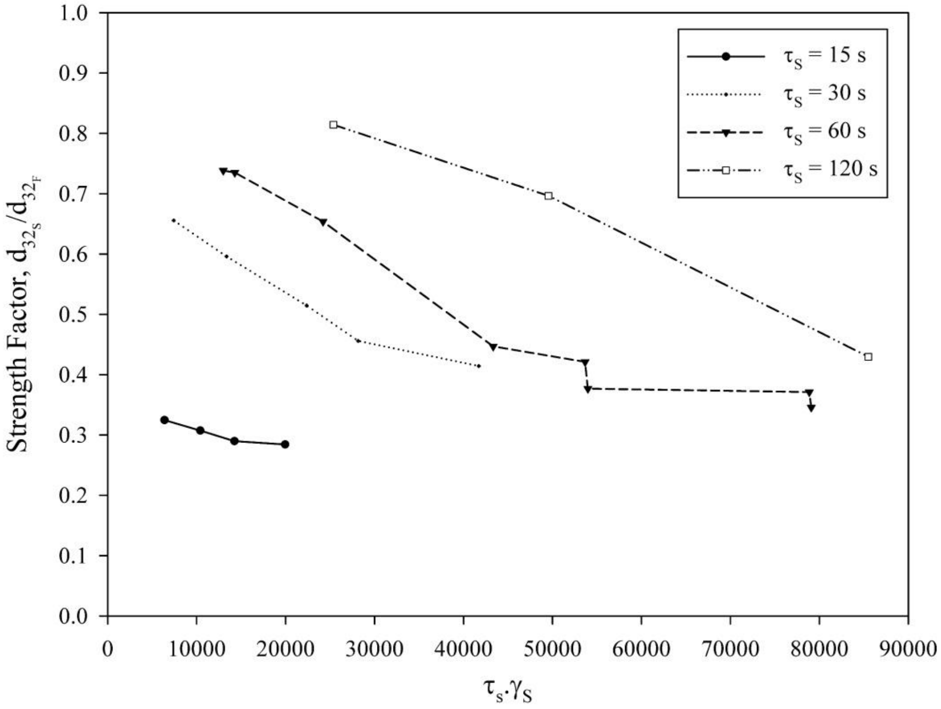

Fig. 5.5. Strength factor at four different shearing times of 15 to 120s

- **Aggregate shape**

In the present study, aggregate shape is described using degree of roundness, ϕ. Figure 5.6 shows the effect of shear rate on the measured degree of roundness at different shearing times of τ_S = 15 to 120s. The cumulative frequency distribution of the degree of roundness of the flocculated suspension, that is the feed to the shearing zone, is also shown. The degree of roundness increases as flocculated suspension is sheared. Figure 5.6c shows that the increasing degree of roundness does not depend significantly on shear rate, when the flocculated suspension is sheared for τ_S = 15 s, which is similar to the behavior seen for aggregate size. However, Figs. 5.6.a,b and d show how the degree of roundness population shifts toward larger values with increasing shear rate, when the flocculated suspension is sheared for τ_S = 30,60 and 120 s.

Comparison of the effect of shearing on the degree of roundness populations with the aggregate size populations, shown in Figs. 5.4 and 5.5, reveal that on average, smaller aggregates have larger degree of roundness values. In other words, the larger aggregates are more non-spherical than smaller aggregates. There are two possible reasons for this: the way aggregates grow and the effect of external forces. In a flocculated suspension, less irregularly shaped flocs and smaller aggregates collide continuously. If the attractive forces are strong enough and collision is effective, a larger aggregate will form. Such a growth process will result in a larger aggregate with more irregularity in the geometry and further deviation from spherical compared to its nuclei. The second reason is the effect of external forces and aggregate fragmentation. Elongated shapes and large aggregates are more likely to break down to smaller fragments. The reasons are likely pressure gradient across the aggregate, aggregate-aggregate and aggregate-wall contacts and the aggregate surface erosion by the shear forces. The result is smaller aggregates that are less non-spherical. For shearing times of 30 s and 120 s, similar behavior is seen for the degree of roundness populations, as shown in Figs. 5.6b and d.

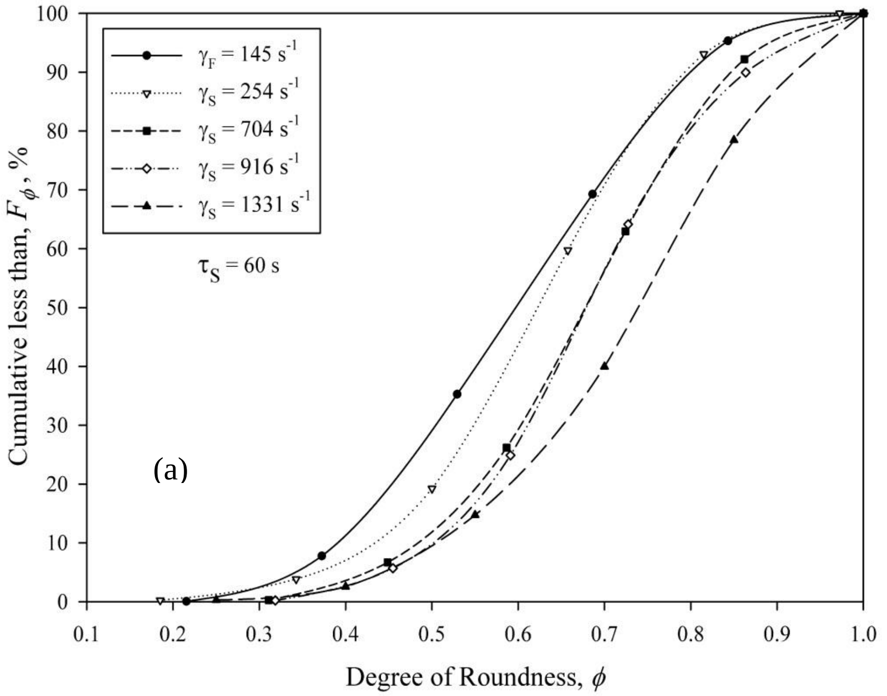

γ_F = 145 s^{-1}
γ_S = 254 s^{-1}
γ_S = 704 s^{-1}
γ_S = 916 s^{-1}
γ_S = 1331 s^{-1}
τ_S = 60 s
(a)
Cumulative less than, F_ϕ, %
0
10
20
30
40
50
60
70
80
90
100
0.1
0.2
0.3
0.4
0.5
0.6
0.7
0.8
0.9
1.0
Degree of Roundness, ϕ

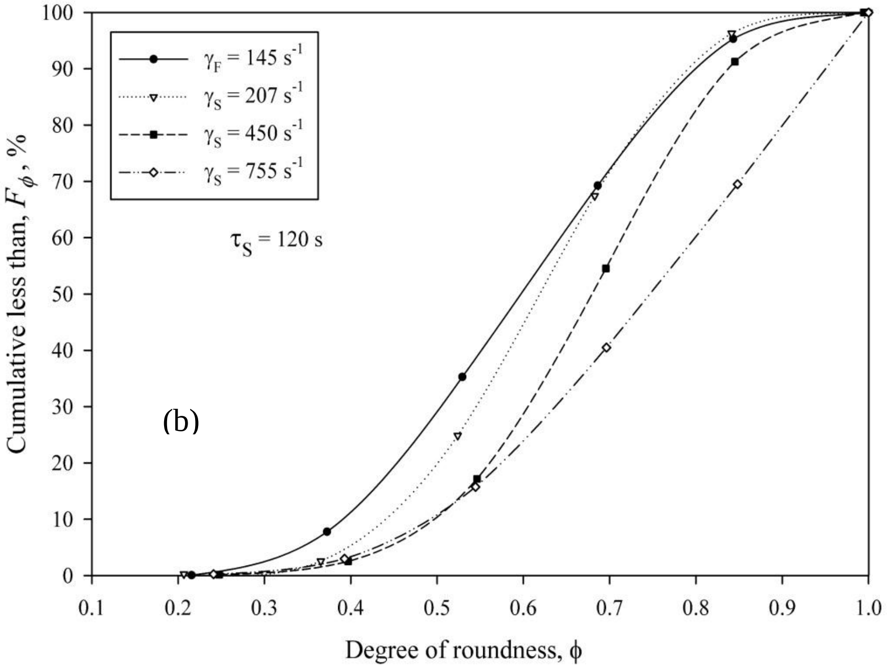

γ_F = 145 s^{-1}
γ_S = 207 s^{-1}
γ_S = 450 s^{-1}
γ_S = 755 s^{-1}
τ_S = 120 s
(b)
Cumulative less than, F_ϕ, %
0
10
20
30
40
50
60
70
80
90
100
0.1
0.2
0.3
0.4
0.5
0.6
0.7
0.8
0.9
1.0
Degree of roundness, ϕ

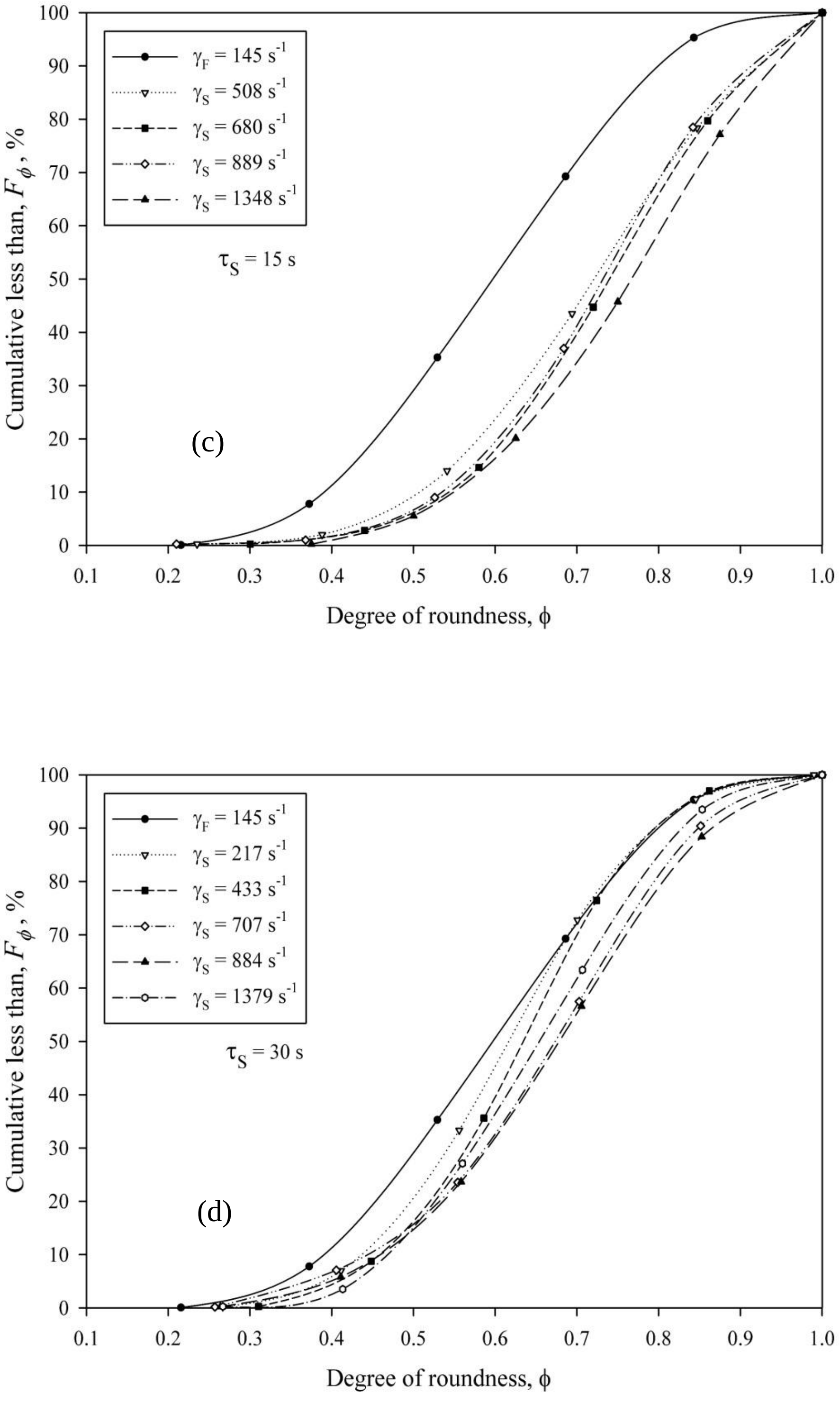

Figure 5.6. Effect of shear rate and shearing time on degree of roundness (a) τ_S = 60 s, (b) τ_S = 120 s, (c) τ_S = 15 s and (d) τ_S = 30 s

The effects of shearing time and magnitude of the shear rate on the arithmetic mean degree of roundness are shown in Fig. 5.7.

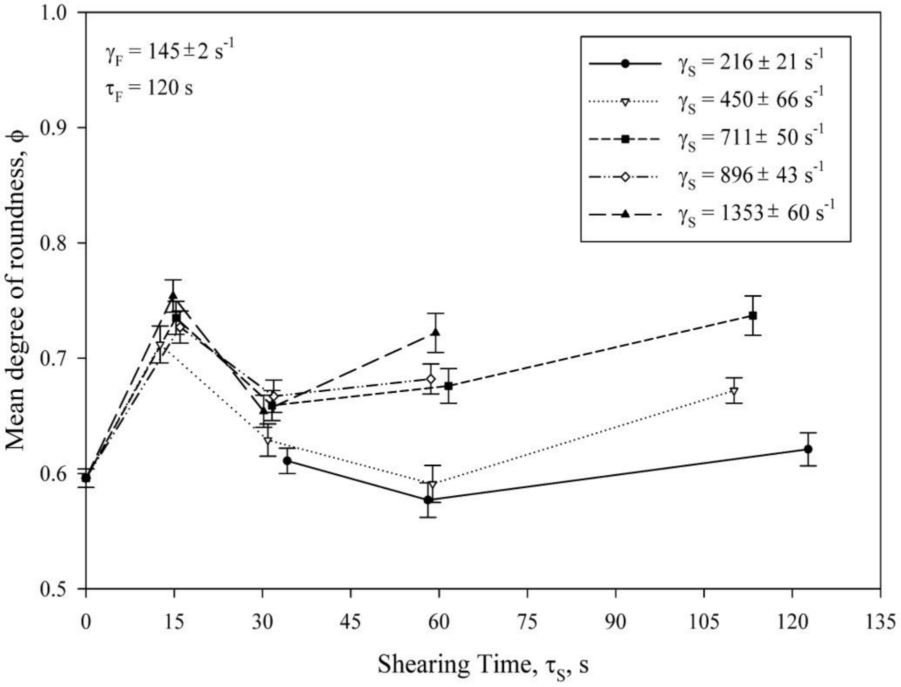

Figure 5.7. Effect of shear rate and shearing time on mean degree of roundness

This figure shows that higher shear rates and longer shearing times can increase the degree of roundness. It appears that the degree of roundness correlates with the aggregate size. Comparison of Figs. 5.5 and 5.7 reveals that when the flocculated suspension is exposed to a change in hydrodynamic conditions, the fragmentation process becomes dominant. This leads to a significant decrease in the aggregate size and a significant increase in the aggregate degree of roundness. The change in the size and shape is almost independent of magnitude of shear rate at short exposure times. As shearing continues, the aggregation process competes with fragmentations, causing aggregate growth to some extent, and the degree of roundness decreases. Longer exposure times tend to lead a decrease in the aggregate size and an increase in the degree of roundness. At this stage magnitude of shear rate becomes important, meaning that as the shear rate increases the change in the aggregate size and shape become larger.

- **Aggregate density**

To determine the densities of the aggregates using Eq. 5.6, the primary floc density of ρ_P = 1625 kg/m^3 was used. Estimation of the primary floc density is described in Chapter 2.

Measured aggregate size and settling velocity data and corresponding Reynolds numbers indicate that we cannot apply Stokes' law for the entire range of aggregate size-velocity data. In other words, a drag coefficient correlation to account for the effect of Reynolds number is required. In addition, visual observation of aggregate morphology reveals that aggregates are quite non-spherical (see Figs 5.6 and 5.7). Consequently, Eqs. 5.8 are used to calculate aggregate drag coefficient so that effects of transition flow regime and the non-sphericity of the aggregates are included.

The aggregate effective porosity and subsequently aggregate effective density were calculated using Eqs. 5.6 to 5.8. These equations were solved numerically using Matlab. The complete set of equations and methodology used to calculate the effective aggregate density is described in detail in Chapter 2. The result indicates that aggregate effective density is typically around 10-300 kg/m^3, meaning the aggregate density is near the liquid density. The results of the aggregate effective porosity calculations indicate that only about 5% of an aggregate is comprised of solids. The density-diameter trend shows that the aggregate effective density decreases as aggregate size increases in a power law form. This is a characteristics of a fractal-like object and the result is in good agreement with previously reported results for aggregates of various particles [9,45-47,60-65,67-69].

One of the features of the present study is to include the aggregate shape, expressed by the degree of roundness, in calculating the aggregate density. We apply a state-of-the-art non-spherical drag coefficient correlation described in

Chapter 4. It is worth noting that it will lead to a greater variation in the estimated aggregate density. Imagine two aggregates with identical area based average diameters, d_a, and settling velocities, U_a, but having different shape factors, ϕ. Due to the shape differences, these two aggregates will experience different drag forces. Consequently, two different densities for two aggregates having identical sizes and settling velocities will be calculated. If aggregates are assumed to be spherical, this effect disappears and identical values of aggregate effective density will be calculated for the two aggregates. In most of the previous studies aggregate is either assumed spherical [64,67,68] or a questionable assumption was made to include non-sphericity of aggregate [78].

Figure 5.8a shows number frequency plots of the aggregate effective density of a sheared suspension for τ_S = 60 s at different shear rates. The number frequency of the flocculated suspension prior to the shearing is also shown. It is clearly seen that the aggregate density distribution shifts toward greater values of aggregate density upon shearing. For instance, when the flocculated suspension is exposed to a high shear rate of $\bar{\gamma}_S$ =1317 s^{-1} for τ_S = 60 s, the aggregate density more than doubles, on average. Another aspect shown in Fig. 5.8a is that the aggregate density distribution becomes somewhat broader upon shearing. This is also clearly depicted in Fig. 5.8b, which illustrates how the aggregate effective density changes when the flocculated suspension is sheared for 120s at different shear rates. The increase in aggregate effective density and the tendency for the density to become more broadly distributed with shearing are most probably related to aggregate breakage and compaction. Aggregate breakage was described previously and is shown in Figs. 5.4 and 5.5. The fractal nature of the aggregate (See Eq. 5.3) suggests a power-law relationship between the aggregate density and size. Therefore, at a constant fractal dimension, a small aggregate has a higher density than a large aggregate [9,61]. The second phenomenon is the compaction of the aggregates. If compaction occurs, the aggregate fractal dimension will increase, meaning the compacted aggregate should have a higher density than an un-compacted aggregate having the same size. This is investigated in the subsequent sections. The size reduction and compaction increase the aggregate effective density. That is why the number of frequency of aggregates with lower density is reduced upon shearing.

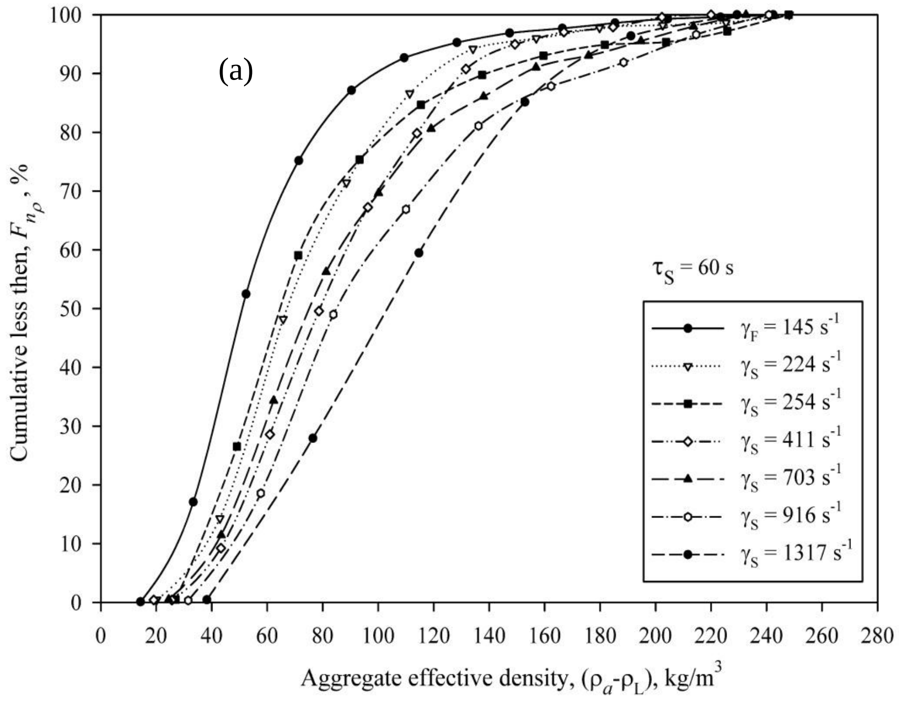

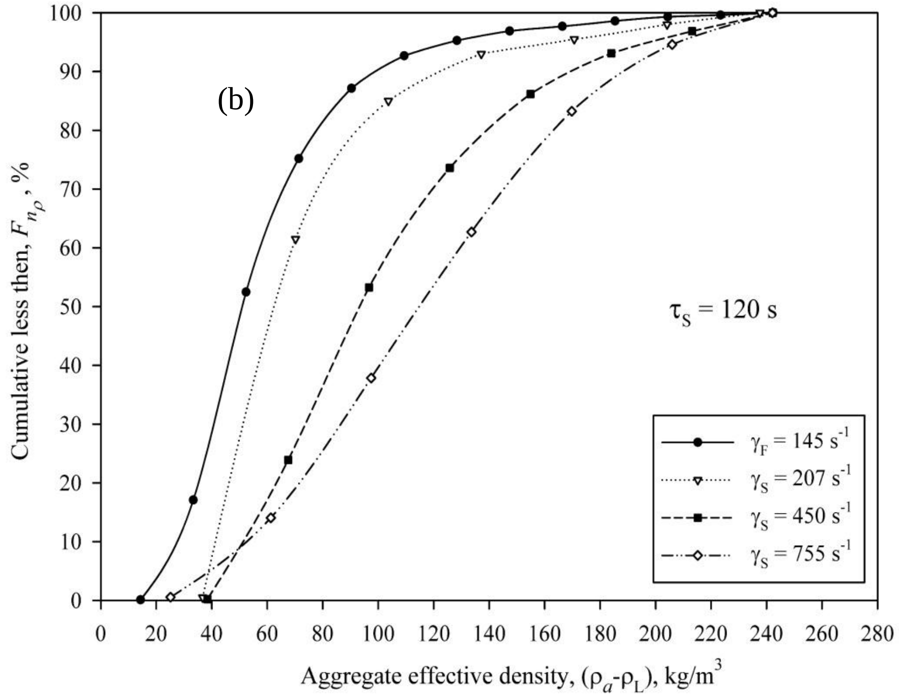

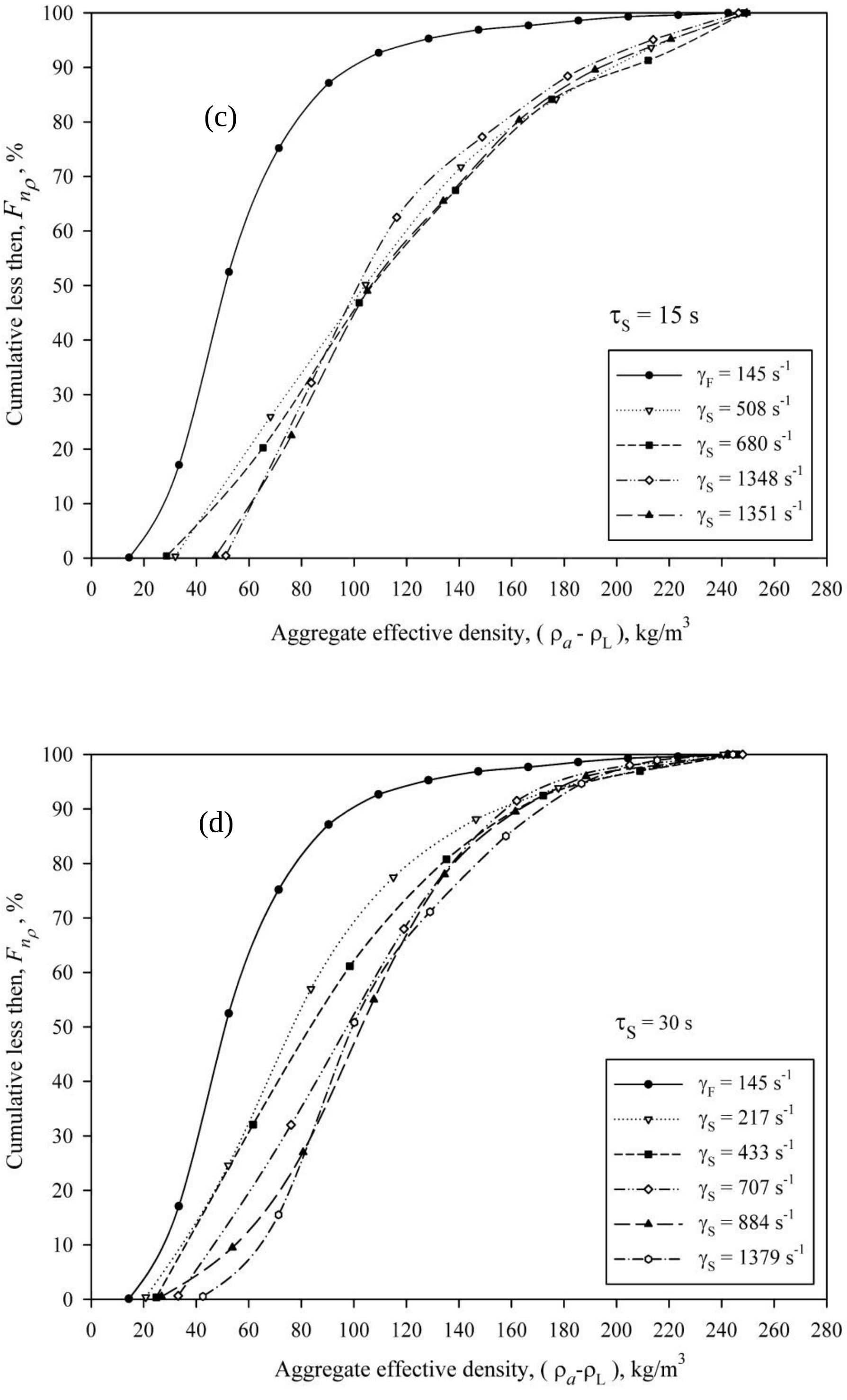

Figure 5.8. Effect of shear rate and shearing time on aggregate density distribution at (a) τ_S = 60 s, (b) τ_S = 120 s, (c) τ_S = 15 s and (d) τ_S = 30 s

The estimation of aggregate density using settling velocity, size and shape data depend on the accuracy of the measurements and the accuracy of the drag coefficient prediction. The higher variance in aggregate density is at least partly due to drag force and density estimation errors. Meanwhile, shearing increases aggregate degree of roundness, which affects calculation of aggregate density. The importance and extent of the calculation errors and shape factor affecting the aggregate density needs more investigation.

Similar trends are seen for shearing times of τ_S = 15 and 30 s, as shown in Figs. 5.8c and 5.8d.

The harmonic mean aggregate density is calculated using Eq. 5.9:

$$\overline{\rho}_a - \rho_L = \left(\frac{1}{N_T} \sum_{i=1}^{N_T} \frac{N_i}{\rho_{a_i}} \right)^{-1} - \rho_L \qquad (5.10)$$

and is plotted in Fig. 5.9 as a function of shearing time at different shear rates. The harmonic mean aggregate effective density of the flocculated suspension, which is the outlet stream from the flocculation zone, is ρ_{Eff} = 58.4 ± 2.14 kg/m^3 (see Table 5.1)

As shown in Fig. 5.9., the harmonic mean aggregate effective density increases at early shearing times (τ_S <15s), followed by a decrease (15s <τ_S< 60 s) and a secondary increase at longer shearing times (>60 s). At short shearing time (τ_S <15s), the increase in the average effective density is independent of the magnitude of the shear rate, which is similar to the effect of shear rate on the aggregate size at τ_S = 15 s (see Fig. 5.3c).At longer shearing times, the aggregate effective density decreases gradually, as seen at 15s <τ_S< 60 s. This is likely due to competition between aggregation and fragmentation and aggregate size growth, which occurs with simultaneous decrease in the effective density governed by aggregate fractal characteristics. At this stage, the decrease in the aggregate effective density depends on the magnitude of the shear rate. At longer shearing times than 60 s, the trend changes and the aggregate mean effective density increases again. The later increase in the aggregate effective density is more significant in larger magnitude of shear rate, as the slope of lines show. The secondary increase in the aggregate effective density is likely due to restructuring. As described previously about the changes in the aggregate density populations, the initial increase followed by a decrease is caused by the breakage and the reflocculation and later increase is likely caused by compaction which is investigated further in Section 5.4.2.4.

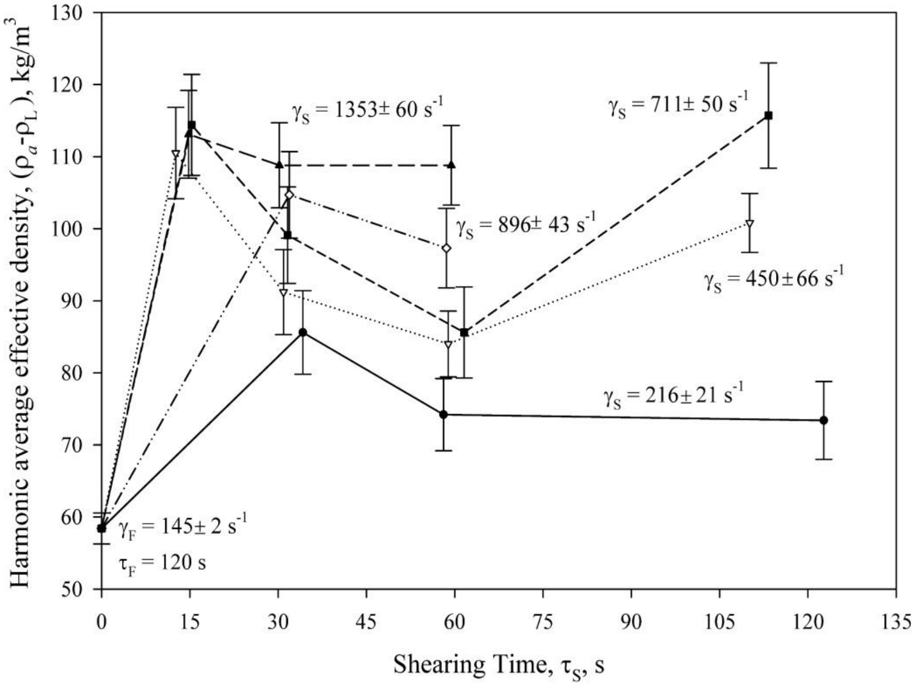

Figure 5.9. Changes in harmonic average effective density after shearing

At the highest high shear rate tested, $\overline{\gamma_S}$ =1353 s^{-1}no reduction of the aggregate effective density at τ_S > 15 s is observed because the very large shear forces prevent aggregation and regrowth.

- **Aggregate structure, Fractal dimension**

Average aggregate mass fractal dimension was calculated by regression of the aggregate effective density and aggregate maximum diameter, d_{max}, data using Eq. 5.3. A similar result was obtained by regression of aggregate effective density and area-based diameter. The only difference is that using the maximum diameter results in a larger fractal dimension than using the area-based diameter. This is in agreement with previous studies [9,61].

Effects of shearing time and shear rate on the fractal dimension of aggregates are shown in Fig. 5.10. The validity of the fractal dimension calculation was checked elsewhere by using two different methods to calculate the fractal dimension [9]. The fractal dimension of a primary floc was assumed to be 2.5, which was used to calculate the primary floc effective density. The average fractal dimension of the flocculated aggregates is given in Table 5.2, that is, D_{F_F}= 2.27 ± 0.05, calculated using the aggregate maximum diameter and the effective density determined assuming the aggregates are non-spherical.

Fig. 5.10 shows that the fractal dimension increases when the flocculated suspension is exposed to high shear rates for more than 15 s. Shearing at lower shear rates and/or short shearing times does not change the fractal dimension significantly. It appears that longer periods of shearing also affect the aggregate structure. Comparison of the change in aggregate size, density and fractal dimension, depicted in Figs. 5.5, 5.9 and 5.10, respectively, shows that in the early stages of shearing, the aggregate fractal dimension is essentially constant. In other words, the increasing effective density with decreasing aggregate size is expected because of the power law relationship between the size and density for aggregates having a constant fractal dimension. However, as shearing continues, the fractal dimension increases, which implies that aggregates are compacted. Higher shear rates appears to be responsible for the compaction and the structural conformation phenomena. For example, when the flocculated suspension ($D_{F_F} = 2.27$) is exposed to a shear rate of $\bar{\gamma}_S$ =1353 s^{-1} for 60 s, the fractal dimension increases ($D_{F_S} = 2.62$).

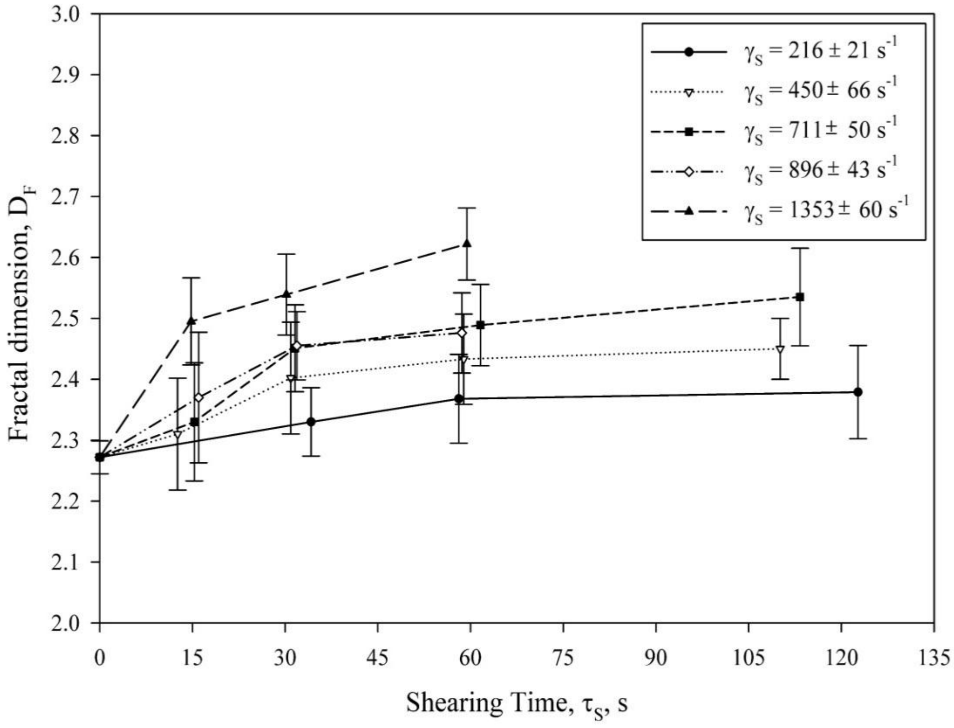

Fig. 5.10 Changes in Fractal dimension with shear rate and shearing time

As Fig. 5.10 shows, the confidence level of the calculated fractal dimensions is around 0.05-0.19 (2.3-7.8% of the fractal dimension). This relatively high deviation is caused by the wide distribution of the aggregate density, which in turns is related to the distribution of aggregate nonsphericity, error associated with the estimation of the non-spherical drag coefficient and error associated with the regression of density and size data. Nevertheless, we can conclude that shearing leads to an increase in the fractal dimension. This is shown in Fig. 5.11, which depicts the fractal dimension ratio of the suspension after and prior to shearing, D_{F_S}/D_{F_F}. This figure clearly illustrates that the fractal dimension increases upon shearing. The increase is significant at higher shear rates and longer shearing times.

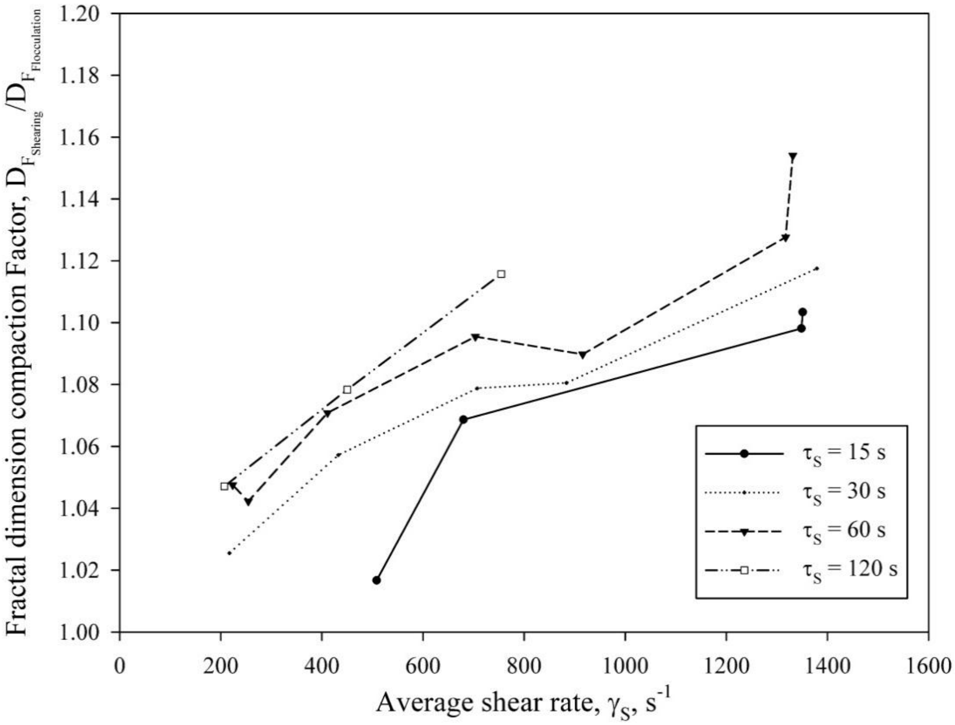

Fig. 5.11. Fractal dimension ratio D_{F_S}/D_{F_F}

5.4.3. Reflocculation zone

- **Aggregate size**

The reflocculation zone experiments were conducted by conditioning the sheared suspension at a lower shear rate of $\bar{\gamma}_R$ = 126 ± 11 s^{-1} for 112 ± 6 s. Three tube sizes of 4, 4.8 and 6.3 mm were used at different suspension flow rates to keep the shear rate constant in the reflocculation zone. Reflocculation zone experiments could not be run for all shearing zone conditions. The reason was that the tubes were available only in specific sizes and the shear rate at the reflocculation zone could not be maintained for all the flow rates (or shear rates) of the shearing zone.

Figures 5.12a to c illustrate the changes in aggregate size distribution upon shearing for τ_S = 60s at three different shear rates of 224, 411 and 1331 s^{-1} following reflocculation for τ_R = 120s. A general trend is observed: when the flocculated suspension is sheared, the aggregate size distribution curve shifts toward smaller aggregate sizes and the distribution narrows. However, when the sheared suspension is conditioned in a lower shear rate in the reflocculation zone, the aggregate size distribution curve shifts back toward larger aggregate sizes and the distribution curve again becomes broader. This behavior indicates that the aggregates regrow, meaning reflocculation occurs. When the shear rate is very high in the shearing zone, $\bar{\gamma}_S$ = 1331 s^{-1} (See Fig. 5.12c), the change in the mode and variance of the size distribution curve is very significant. Nevertheless, when the sheared suspension is exposed to the lower shear rate in the reflocculation zone, the aggregates grow and the size distribution curve becomes similar to that of the suspension before it was exposed to the high shear rate. A similar behavior was observed when the flocculated suspension was sheared at different shear rates and shearing times of τ_S = 30 and 120s followed by conditioning in the reflocculation zone for τ_R = 120s. However, Fig. 5.12d illustrates that when the shearing time is short and a steady state condition in terms of aggregate structural properties is not yet developed, the final aggregate size distribution does not match the original size distribution measured prior to shearing (compare the curves for $\bar{\gamma}_F$ and $\bar{\gamma}_R$ in Fig. 5.12d).

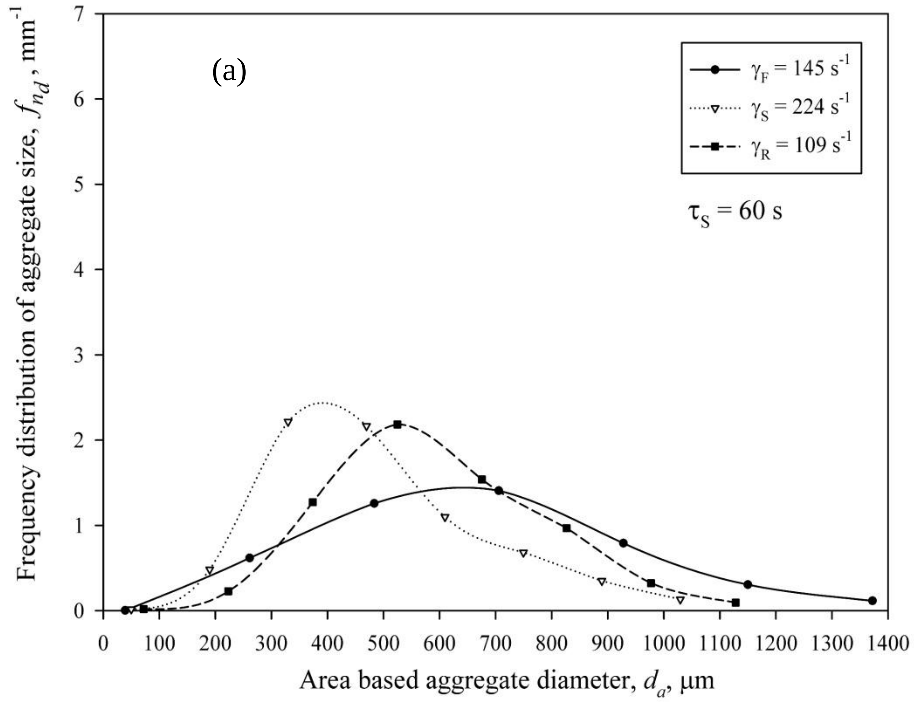
(a)
γF = 145 s-1
γS = 224 s-1
γR = 109 s-1
τS = 60 s
Frequency distribution of aggregate size, fnd, mm-1
Area based aggregate diameter, da, µm
0
1
2
3
4
5
6
7
0
100
200
300
400
500
600
700
800
900
1000
1100
1200
1300
1400

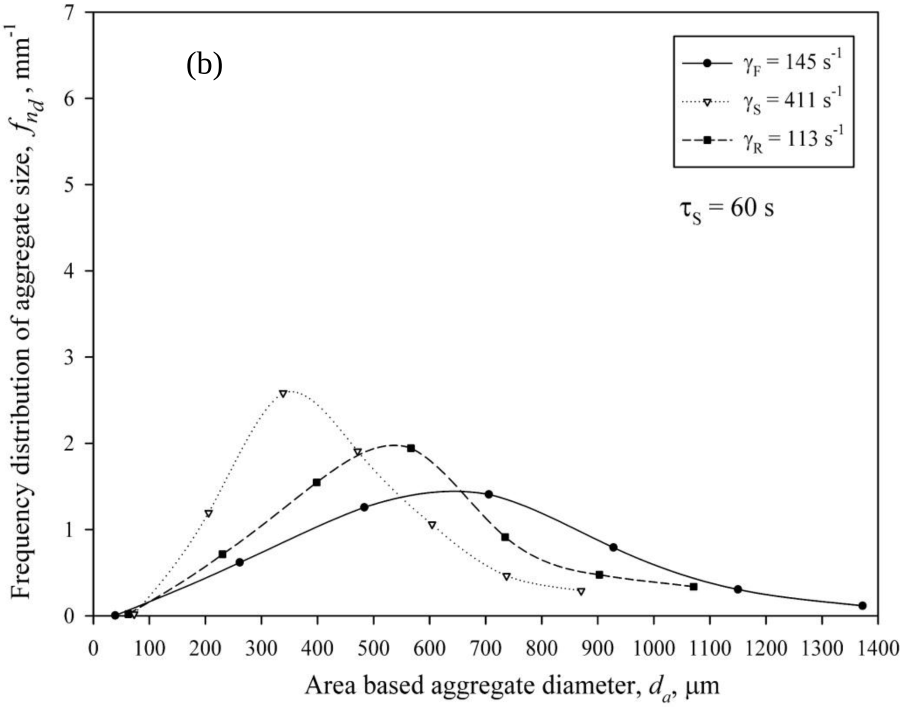
(b)
γF = 145 s-1
γS = 411 s-1
γR = 113 s-1
τS = 60 s
Frequency distribution of aggregate size, fnd, mm-1
Area based aggregate diameter, da, µm
0
1
2
3
4
5
6
7
0
100
200
300
400
500
600
700
800
900
1000
1100
1200
1300
1400

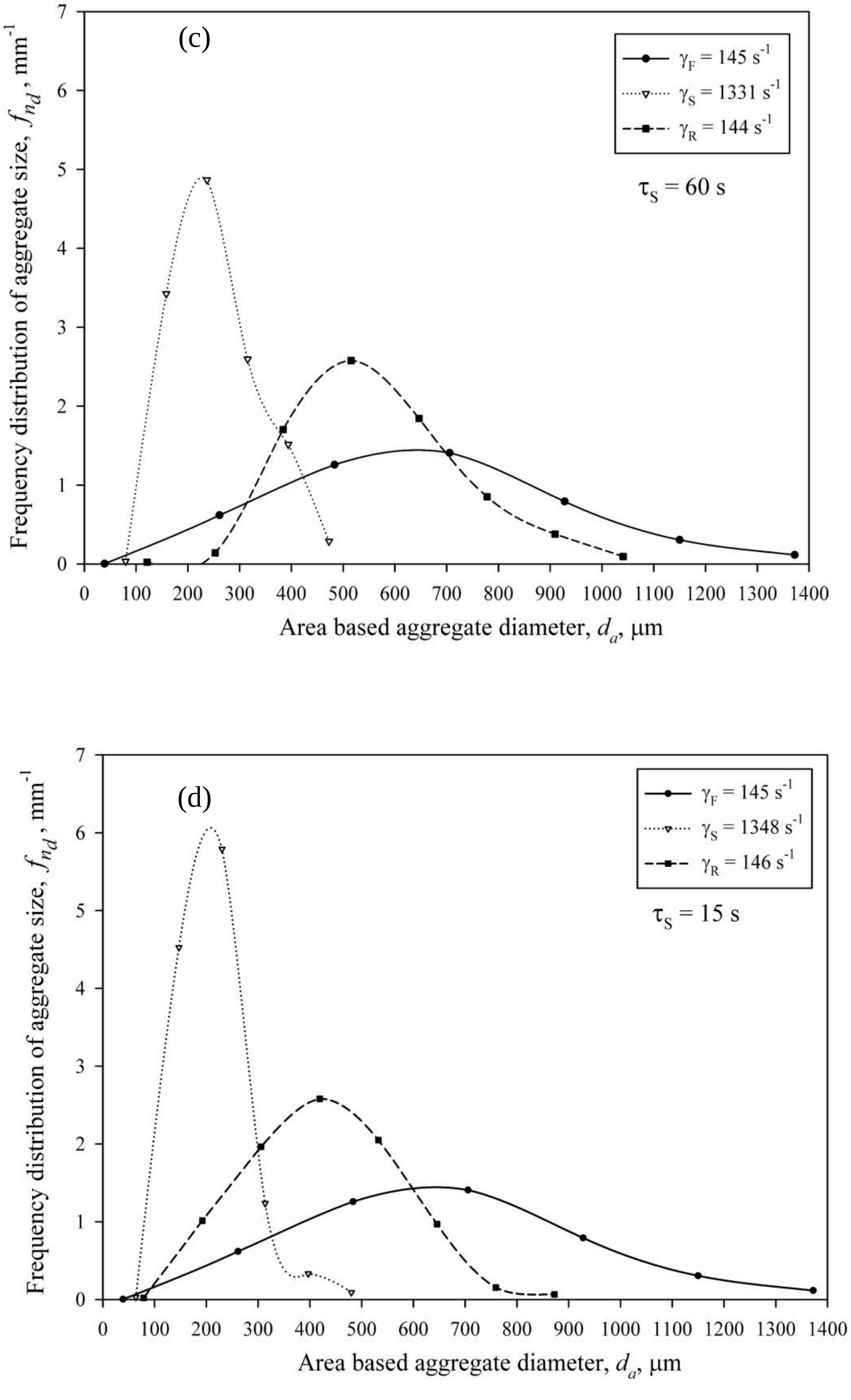

Fig. 5.12. Change in aggregate size distribution upon shearing followed by reflocculation at (a) τ_S = 60 s and $\bar{\gamma}_S$ = 224 s^{-1}, (b) τ_S = 60 s and $\bar{\gamma}_S$ = 411 s^{-1}, (c) τ_S = 60 s and $\bar{\gamma}_S$ = 1331 s^{-1}, (d) τ_S = 15 s and $\bar{\gamma}_S$ = 1348 s^{-1}

Figures 5.13 show how the Sauter mean diameter, d_{32}, changes upon shearing at different shear rates and shearing times followed by reflocculation. At all shear rates and shearing times, the trends are similar; that is, shearing the flocculated suspension at high shear rates reduces the Sauter mean diameter, d_{32}. The decrease in d_{32} depends on the magnitude of the shear rate and the shearing time, as previously explained. When the shear rate is decreased, aggregates reflocculate and d_{32} increases. An interesting feature shown in Figs. 5.13 is that the d_{32} of the reflocculated suspension is almost independent of the shearing history of the suspension the shearing zone.

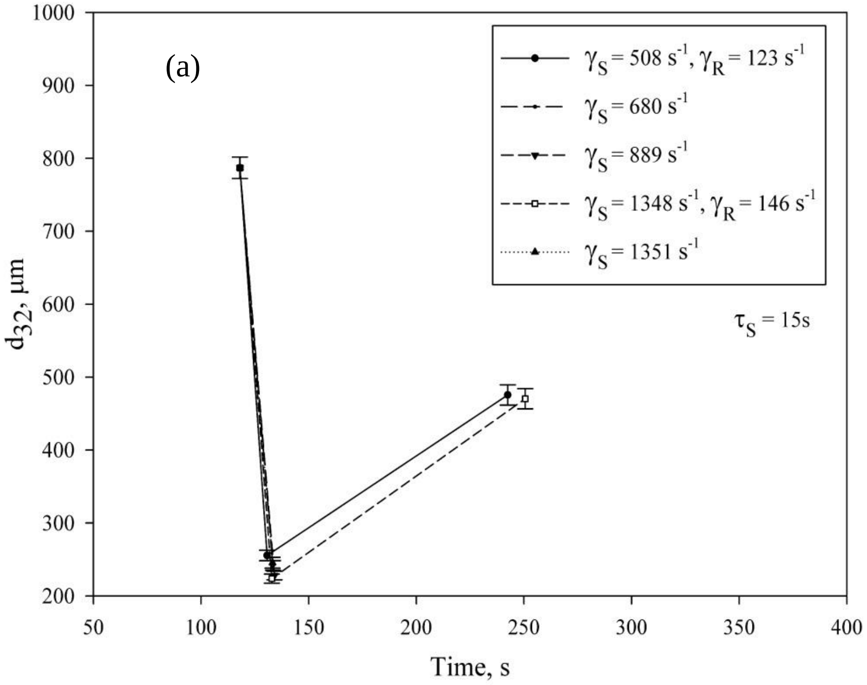
(a)
d_{32}, μm
Time, s
τ_S = 15s
γ_S = 508 s^{-1}, γ_R = 123 s^{-1}
γ_S = 680 s^{-1}
γ_S = 889 s^{-1}
γ_S = 1348 s^{-1}, γ_R = 146 s^{-1}
γ_S = 1351 s^{-1}
1000
900
800
700
600
500
400
300
200
50
100
150
200
250
300
350
400

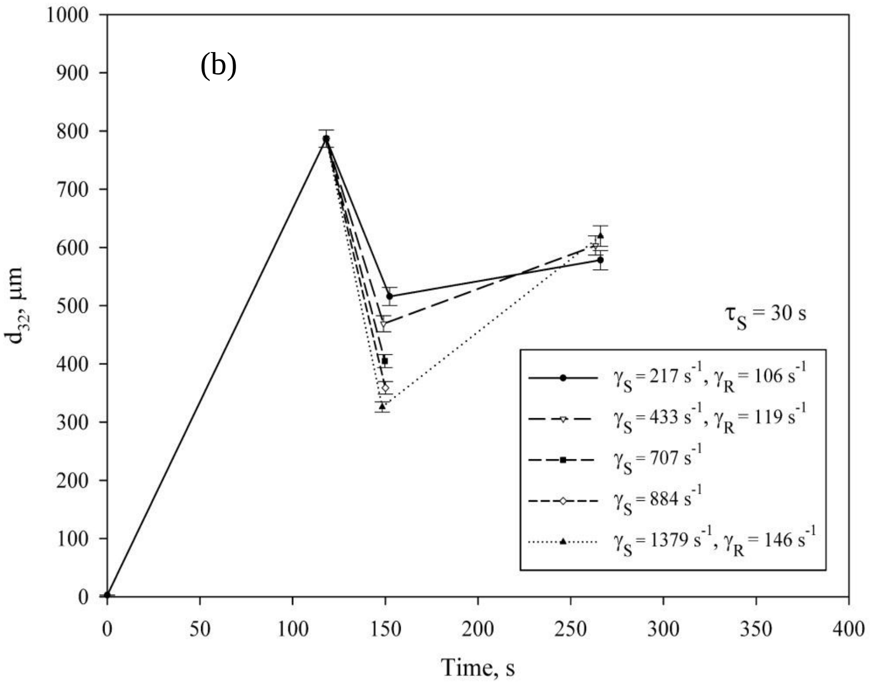
(b)
d_{32}, μm
Time, s
τ_S = 30 s
γ_S = 217 s^{-1}, γ_R = 106 s^{-1}
γ_S = 433 s^{-1}, γ_R = 119 s^{-1}
γ_S = 707 s^{-1}
γ_S = 884 s^{-1}
γ_S = 1379 s^{-1}, γ_R = 146 s^{-1}
1000
900
800
700
600
500
400
300
200
100
0
0
50
100
150
200
250
300
350
400

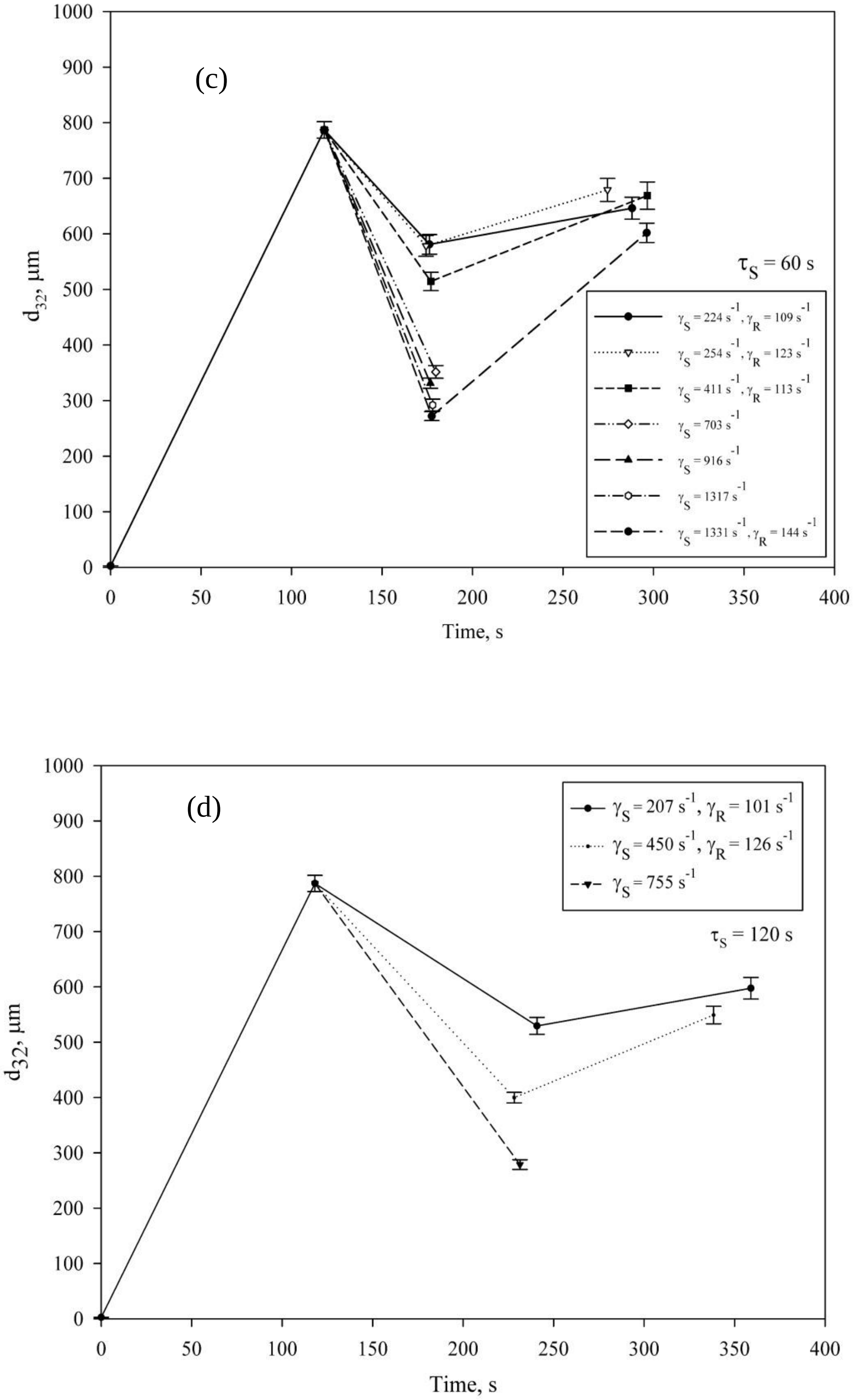

Fig. 5.13. Change in aggregate Sauter mean diameter, d32, upon shearing followed by reflocculation at shearing times of (a) τ$_S$ = 15 s, (b) τ$_S$ = 30 s, (c) τ$_S$ = 60 s and (d) τ$_S$ = 120 s

The extent of reflocculation can be examined using the reflocculation recovery factor, *RF*, defined by Eq. 5.1-b. As shown in Fig 5.14, at a constant shearing time, the degree of reflocculation increases with shear rate and then reaches a plateau at very high shear rates. This is in agreement with previous studies [35]. This is likely due to the high molecular weight of the polymer used in the present study. In other words, exposure to higher shear rates causes a more substantial break down of aggregates; however, these broken down aggregates can reflocculate to a greater extent when the shear rate is lowered.

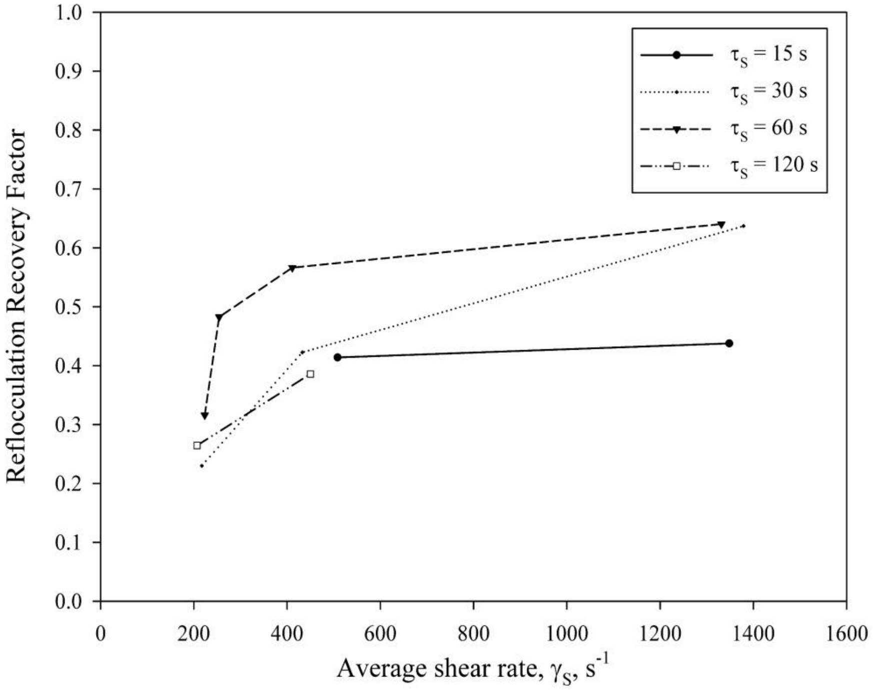

Fig. 5.14. Degree of reflocculation at shearing times of τ_S = 15,30, 60, 120 s

This is an indication of an increase in aggregate strength at higher shear rate. The results of Fig 5.14 also shows that longer exposure times at higher shear rates facilitates reflocculation, at least for the range of shear rates and exposure times studied here. This is not in agreement with the results of Yukselen and Gregory [33], where the degree of reflocculation for high molecular weight flocculants did not depend on the shearing time. However, our experimental conditions, in terms of suspension concentration and shearing and reflocculation times, are different from those of Yukselen and Gregory [33]. As can be seen in Fig. 5.14, the degree of reflocculation is greatest when the suspension is sheared for τ_S =60 s.

- **Aggregate degree of roundness**

As shown in Section 5.4.2., shearing produces aggregates that are more spherical in shape than the aggregates prior to shearing. Since reflocculation changes aggregate size distribution, it is expected that aggregate shape will change as well. The image analysis results confirm this hypothesis. Figures 5.15 show the evolution of the cumulative distribution of the degree of roundness after flocculation, shearing and reflocculation. Three cases of shearing at $\bar{\gamma}_S$ =1348 s^{-1} for τ_S = 15 s, $\bar{\gamma}_S$ = 1331 s^{-1} for τ_S = 60 s, and $\bar{\gamma}_S$ = 450 s^{-1} for τ_S = 120 s are shown in these figures.

As shown in Figs. 5.15, exposure to high shear rates shifts the degree of roundness distribution toward the right side, i.e. the aggregates, on average, become more spherical. Then, upon lowering the shear rate in the reflocculation zone, the degree of roundness shifts back toward left side. It has already been discussed that reflocculation prompts regrowth of aggregates. This means that few smaller aggregates can bond to each other and form a larger aggregate in the reflocculation zone. The regrowth process changes the morphology of aggregates, as seen in Figs. 5.15. Aggregation of smaller aggregates results in larger aggregates that are more non-spherical than their building blocks, i.e. the small aggregates. Reflocculation of sheared suspensions at different shear rates and shearing times than those shown in Figs. 5.15 follows a similar trend to those shown in Figs. 5.15.

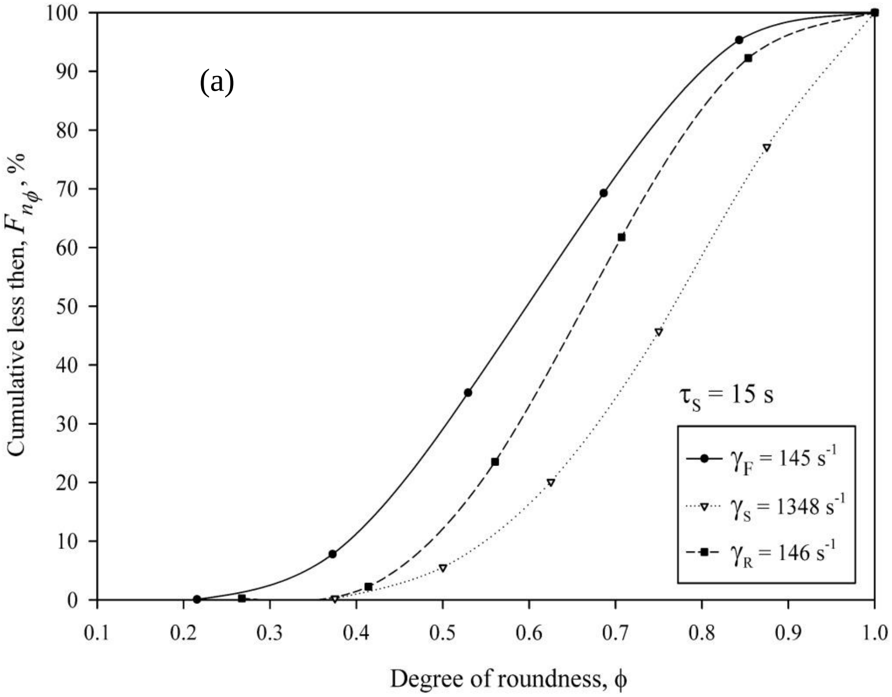
(a)
τ_S = 15 s
γ_F = 145 s^{-1}
γ_S = 1348 s^{-1}
γ_R = 146 s^{-1}
Cumulative less then, $F_{n\phi}$, %
Degree of roundness, ϕ
0
10
20
30
40
50
60
70
80
90
100
0.1
0.2
0.3
0.4
0.5
0.6
0.7
0.8
0.9
1.0

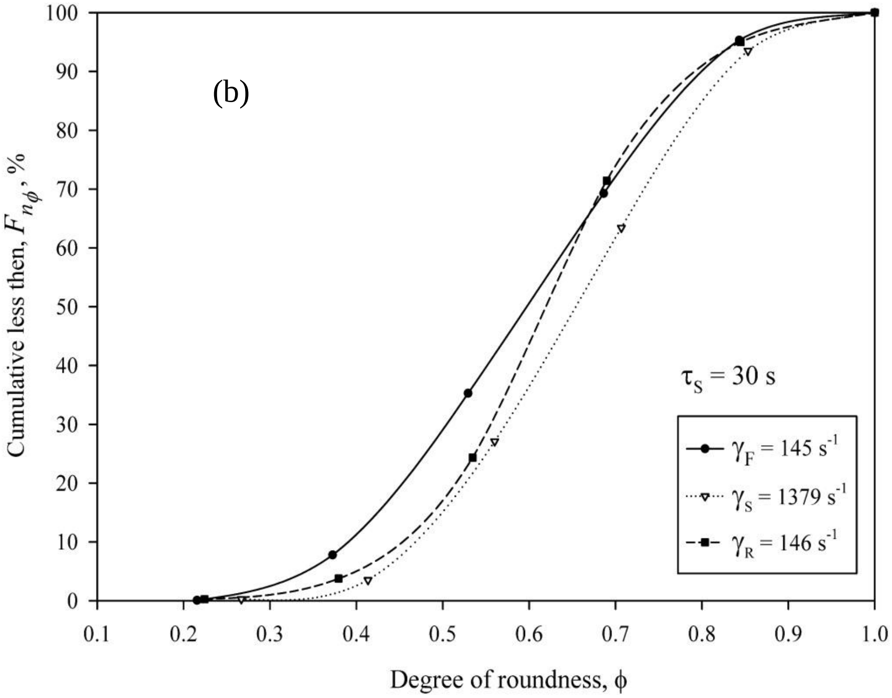
(b)
τ_S = 30 s
γ_F = 145 s^{-1}
γ_S = 1379 s^{-1}
γ_R = 146 s^{-1}
Cumulative less then, $F_{n\phi}$, %
Degree of roundness, ϕ
0
10
20
30
40
50
60
70
80
90
100
0.1
0.2
0.3
0.4
0.5
0.6
0.7
0.8
0.9
1.0

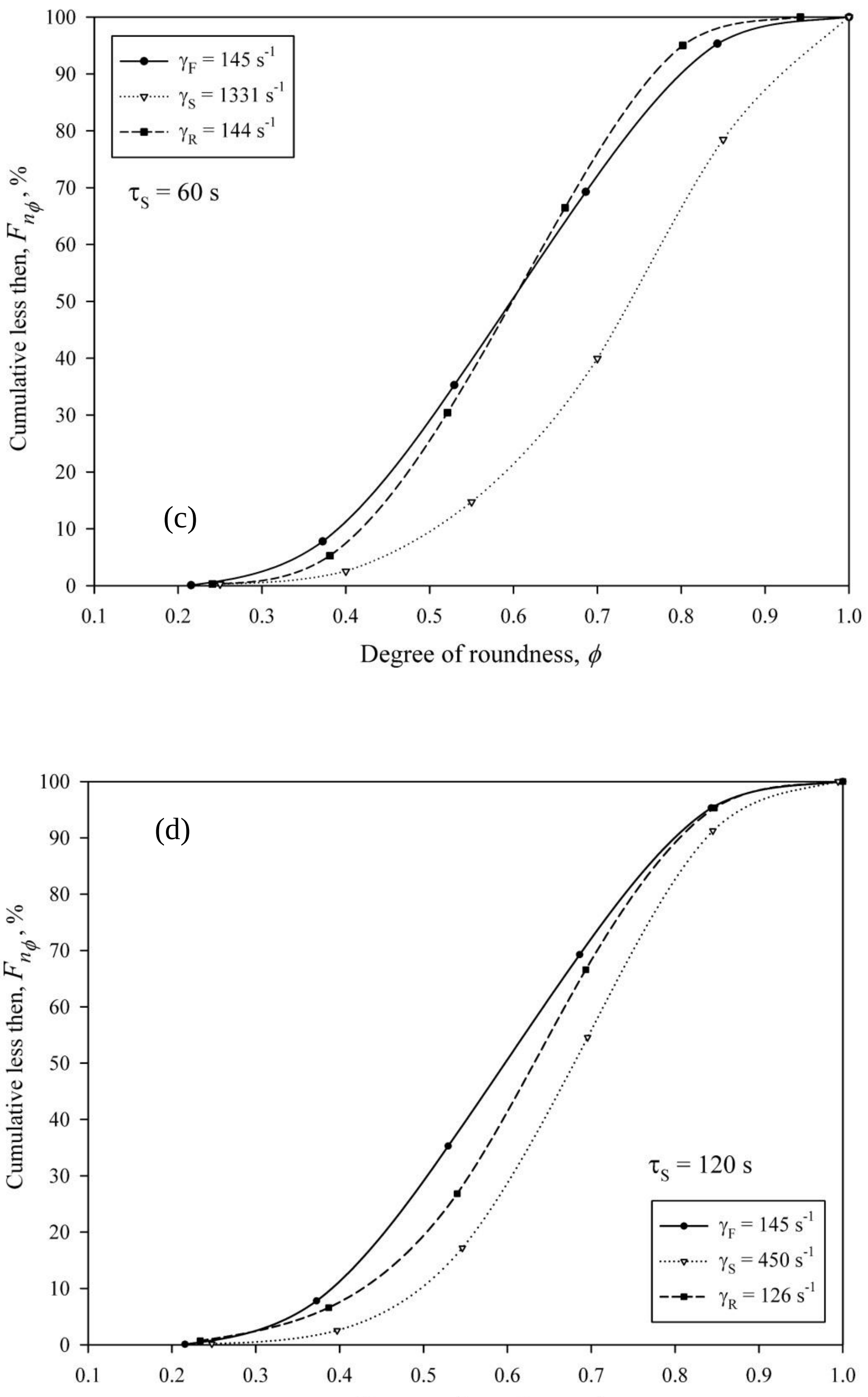

Fig. 5.15. Change in cumulative distributions of degree of roundness upon shearing followed by reflocculation at three different shearing condition of (a) τ_S = 15 s, $\bar{\gamma}_S$ = 1348 s^{-1}, (b) τ_S = 30 s, $\bar{\gamma}_S$ = 1379 s^{-1} (c) τ_S = 60 s, $\bar{\gamma}_S$ = 1331 s^{-1} and (d) τ_S = 120 s, $\bar{\gamma}_S$ = 450 s^{-1}

The average degree of roundness after flocculation, shearing and reflocculation are shown in Figs. 5.16 at constant shearing times. At all shearing times, the average degree of roundness increases after the flocculated suspension is exposed to high shear rates. In the reflocculation zone, the average degree of roundness decreases. Flocculation and reflocculation at low shear rates generates aggregates that are more non-spherical than those exposed to high shear rates. However, changes in the average degree of roundness are not very significant. Comparison of Figs. 5.3, 5.4, 5.6, 5.13 and 5.16 implies that there may be a correlation between aggregate size and shape.

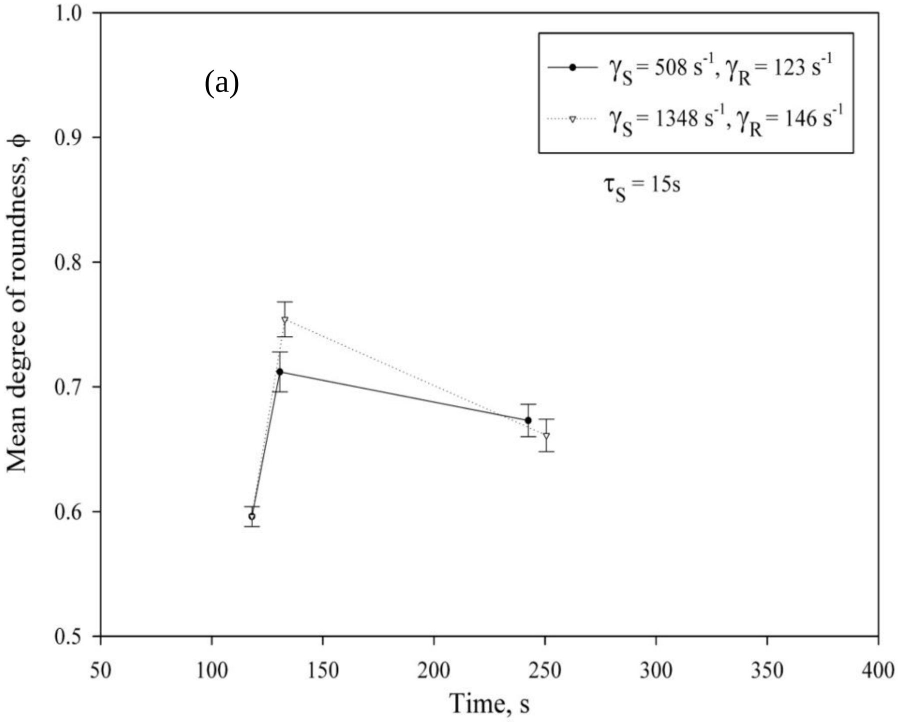
(a)
$\gamma_S = 508\ s^{-1}, \gamma_R = 123\ s^{-1}$
$\gamma_S = 1348\ s^{-1}, \gamma_R = 146\ s^{-1}$
$\tau_S = 15s$
Mean degree of roundness, ϕ
Time, s
1.0
0.9
0.8
0.7
0.6
0.5
50
100
150
200
250
300
350
400

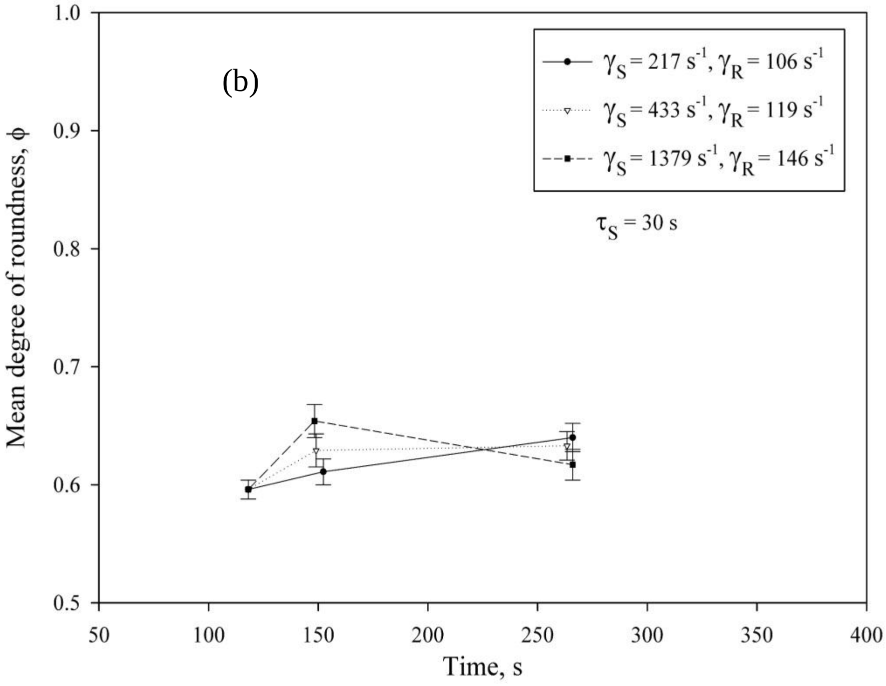
(b)
$\gamma_S = 217\ s^{-1}, \gamma_R = 106\ s^{-1}$
$\gamma_S = 433\ s^{-1}, \gamma_R = 119\ s^{-1}$
$\gamma_S = 1379\ s^{-1}, \gamma_R = 146\ s^{-1}$
$\tau_S = 30\ s$
Mean degree of roundness, ϕ
Time, s
1.0
0.9
0.8
0.7
0.6
0.5
50
100
150
200
250
300
350
400

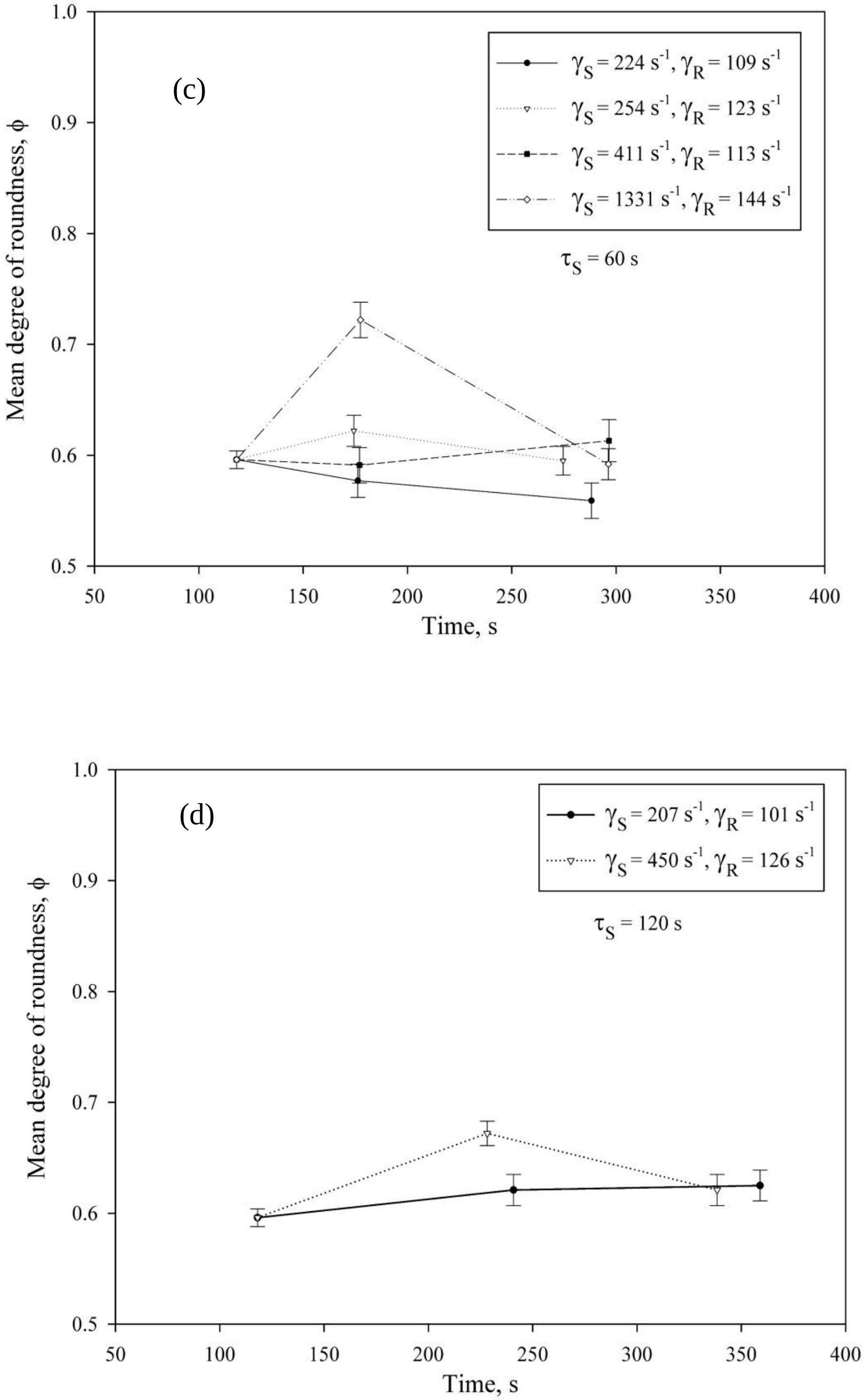

Fig. 5.16. Change in the degree of roundness after flocculation, shearing and reflocculation at different shearing times of (a) τ_S = 15 s, (b) τ_S = 30 s, (c) τ_S = 60 s and (d) τ_S = 120s

- **Aggregate density**

The method used to determine the aggregate effective density was described in Section 5.4.2. The same method is applied to the size, shape and settling velocity data collected from the reflocculation zone experiments to determine the aggregate density of the reflocculated suspensions.

Figures 5.17 show changes in the cumulative distribution of the aggregate effective density after flocculation, followed by shearing at highest shear rates for different shearing times, and then ending with the reflocculation step. It is clearly seen that exposure of the flocculated suspension to high shear rates shifts the aggregate density distribution to the right side, i.e. higher aggregate densities. This trend was discussed in Section 5.4.2. After reduction of the shear rate in the reflocculation zone, the aggregate density distribution curve shifts back toward lower densities. For instance, when the flocculated suspension is exposed to a high shear rate of 1331 s^{-1} for τ_S = 60 s, the aggregate density increases more than 2 times on average. Later, when the sheared suspension is conditioned by lowering the shear rate in the reflocculation zone to $\bar{\gamma}_R$ = 144 s^{-1}, the aggregate density decreases to an average value between that of the aggregates in the flocculation and shearing zones. The trend shown in Figs. 5.17 is observed upon reflocculation for all shearing times between 15 and 120s.

Another aspect of Figs. 5.17 is that the variances of the density distribution curves are different in the flocculation, shearing and reflocculation zones. Aggregate destiny distributions in the shearing zone have higher variances than the density distribution curves in the flocculation and reflocculation zones. The possible reasons for a broader density distribution curve are described in Section 5.4.2. Briefly, they include distribution of aggregate shape factor after shearing, relative compaction of aggregate, and errors associated with estimation of drag coefficient and density.

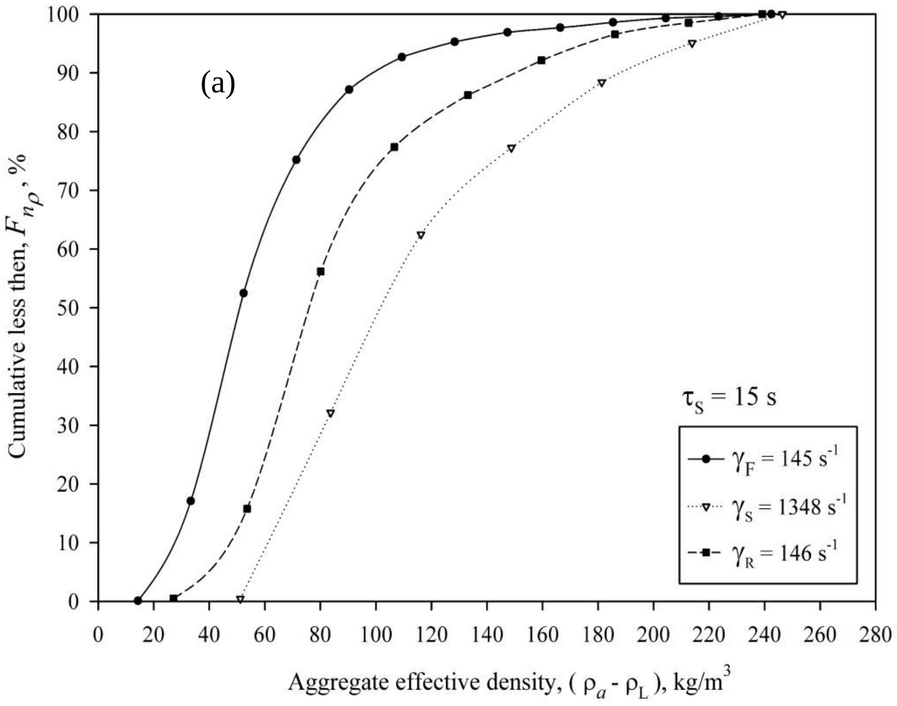
(a)
Cumulative less then, F_{n_ρ}, %
0
10
20
30
40
50
60
70
80
90
100
Aggregate effective density, (ρ_a - ρ_L), kg/m^3
0
20
40
60
80
100
120
140
160
180
200
220
240
260
280
τ_S = 15 s
γ_F = 145 s^{-1}
γ_S = 1348 s^{-1}
γ_R = 146 s^{-1}

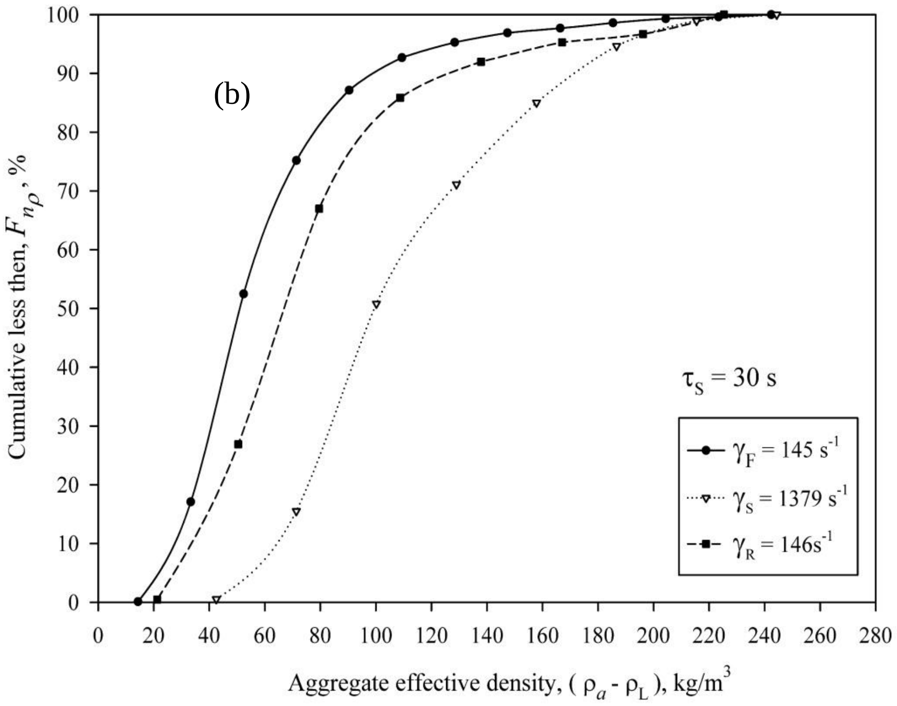
(b)
Cumulative less then, F_{n_ρ}, %
0
10
20
30
40
50
60
70
80
90
100
Aggregate effective density, (ρ_a - ρ_L), kg/m^3
0
20
40
60
80
100
120
140
160
180
200
220
240
260
280
τ_S = 30 s
γ_F = 145 s^{-1}
γ_S = 1379 s^{-1}
γ_R = 146s^{-1}

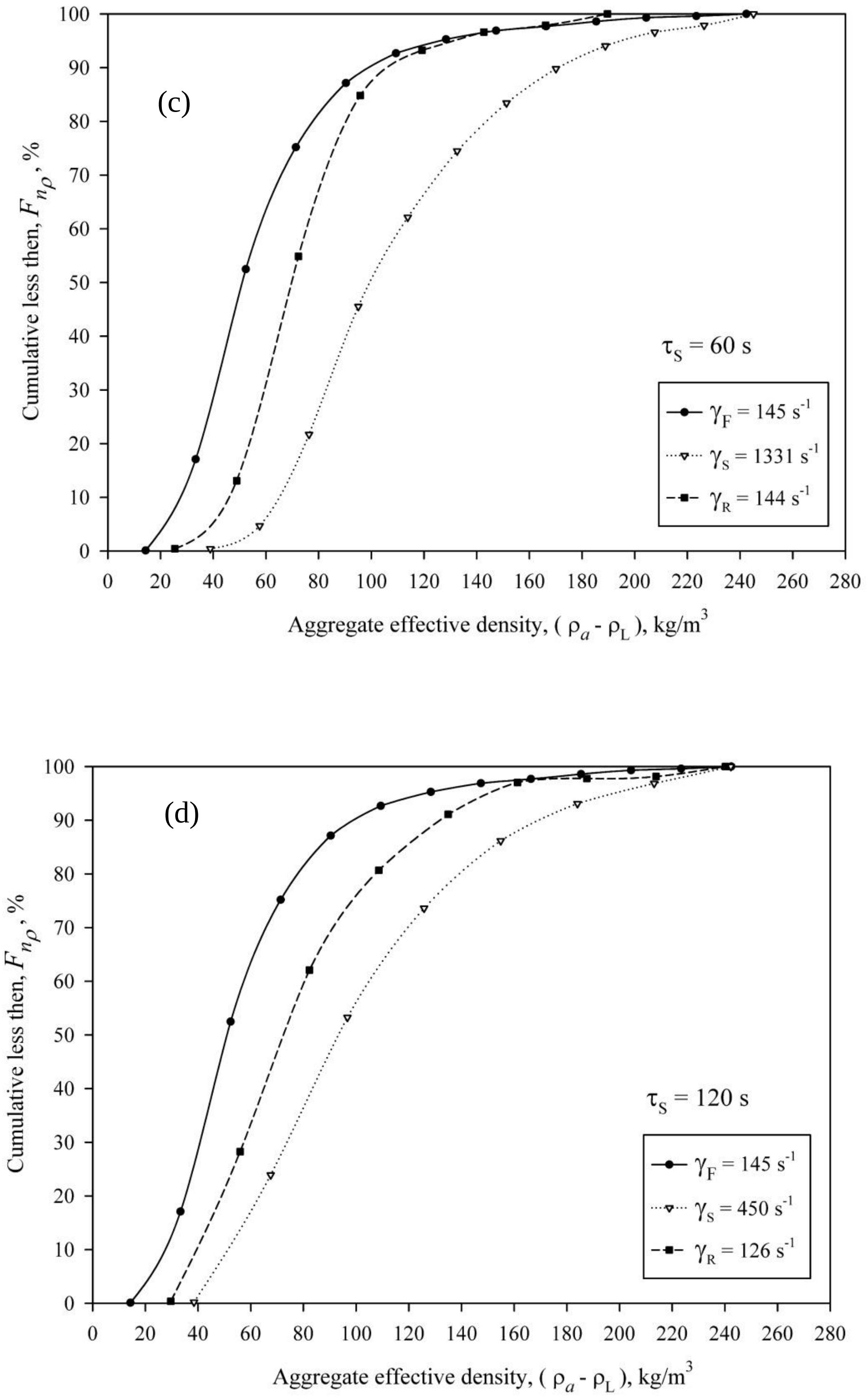

Fig. 5.17. Change in cumulative distributions of aggregate effective density after flocculation, shearing and reflocculation at four different shearing condition of (a) τ_S = 15 s, $\bar{\gamma}_S$ = 1348 s^{-1}, (b) τ_S = 30 s, $\bar{\gamma}_S$ = 1379 s^{-1} and (c) τ_S = 60 s, $\bar{\gamma}_S$ = 1331 s^{-1} and (d) τ_S = 120 s, $\bar{\gamma}_S$ = 450 s^{-1}

The harmonic mean aggregate density is calculated using Eq. 5.9 and is illustrated in Figs. 5.18 for different experimental conditions. The harmonic mean effective density of the flocculated suspension, which is the outlet stream from the flocculation zone, is $\rho_{Eff} = 58.4 \pm 2.14$ kg/m^3 (see Table 5.1). For all conditions, it is clearly seen that shearing increases the average effective density to about 80-120 kg/m^3, depending on the shear rate and shearing time, and reflocculation decreases the average effective density to 70-85 kg/m^3. The ultimate average density after reflocculation is between the average densities of aggregates in the flocculated and sheared suspensions.

As discussed in Section 5.4.2 and shown in Fig 5.18a, the increase in the average effective density for a short shearing time of $\tau_S = 15$s is independent of the magnitude of the shear rate, which is similar to the effect of short exposure times on the aggregate size (See Fig. 5.13). After reduction of the shearing in the reflocculation zone, the aggregate average density decreases to about 80 kg/m^3.

For longer shearing times, i.e. $\tau_S = 30$, 60 and 120s, the aggregate effective density increases upon shearing. However, for these shearing times, the increase in the average effective density of the sheared suspension depends on the magnitude of the shear rate. In addition, the increases in the average effective densities for the longer shearing times are not as great as at the shearing time of 15 s. As shown in Figs 5.18 for each shearing time and considering the error bound, the ultimate average effective density of the reflocculated suspension reaches to a about same values. This means that the effective density of the reflocculated suspension is independent of the aggregate shearing history at a given shearing time.

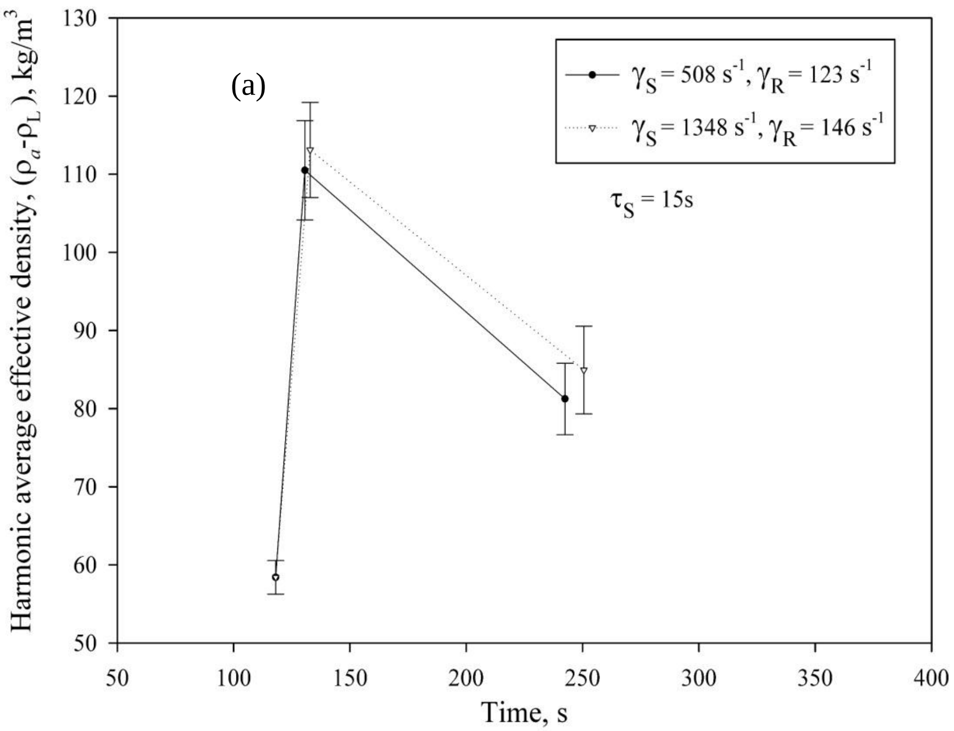
(a)
γ_S = 508 s^{-1}, γ_R = 123 s^{-1}
γ_S = 1348 s^{-1}, γ_R = 146 s^{-1}
τ_S = 15s
Harmonic average effective density, (ρ_a-ρ_L), kg/m^3
Time, s
50
60
70
80
90
100
110
120
130
50
100
150
200
250
300
350
400

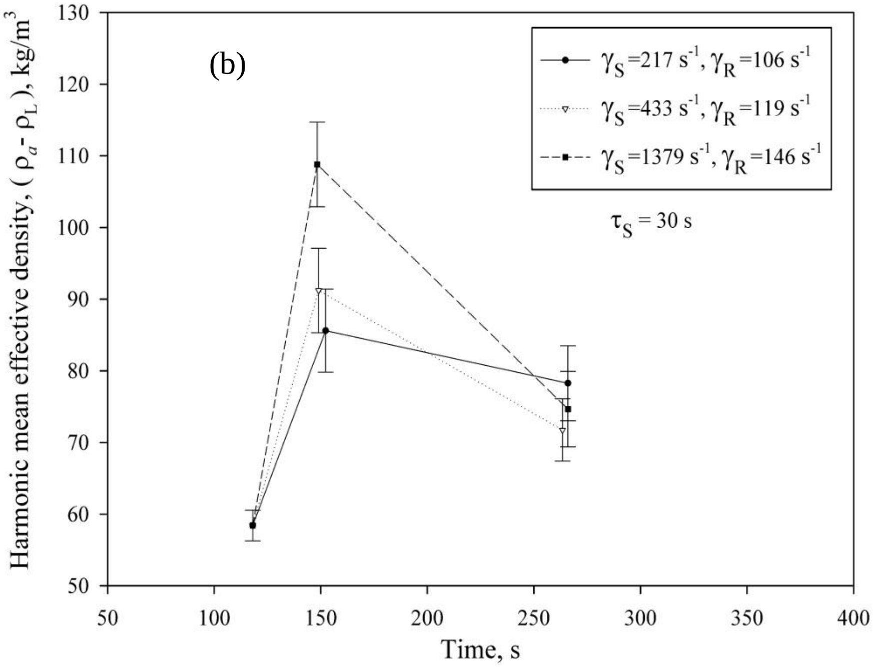
(b)
γ_S=217 s^{-1}, γ_R=106 s^{-1}
γ_S=433 s^{-1}, γ_R=119 s^{-1}
γ_S=1379 s^{-1}, γ_R=146 s^{-1}
τ_S = 30 s
Harmonic mean effective density, (ρ_a- ρ_L), kg/m^3
Time, s
50
60
70
80
90
100
110
120
130
50
100
150
200
250
300
350
400

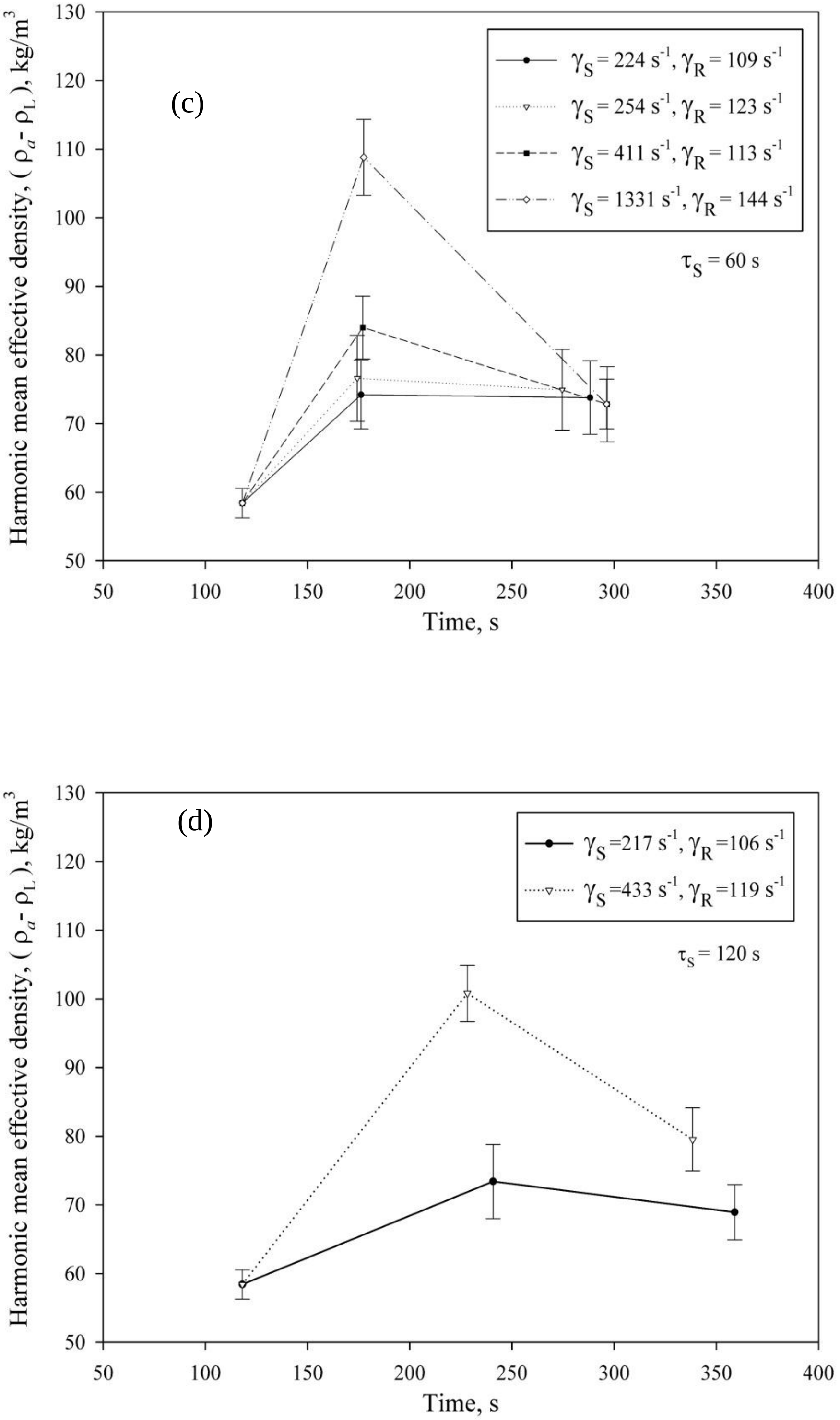

Figure 5.18. Changes in the harmonic mean effective density after flocculation shearing and reflocculation at shearing times of (a) τ_S = 15 s, (b) τ_S = 30 s, (c) τ_S = 60 s and (d) τ_S = 120 s.

- **Fractal dimension**

The average aggregate fractal dimension was calculated by regression of the aggregate effective density and aggregate maximum diameter using Eq. 5.3. Fractal dimensions of the flocculated (D_{F_F}) sheared (D_{F_S}) and reflocculated (D_{F_R}) suspensions are shown graphically in Figs. 5.19. This figures show evolution of the fractal dimension. The fractal dimension increases when the flocculated suspension is exposed to high shear rates. However, upon reflocculation, the fractal dimension decreases. Table 5.3 summarizes the fractal dimension data for different shearing experiments followed by reflocculation step.

Table 5.3. Fractal dimension of aggregates in shearing and reflocculation zones

Shearing zone				Reflocculation zone, τ_R = 114 ± 3.7 s, $\bar{\gamma}_R$ = 123.1 ± 10.8 s^{-1}			
τ_S, s	$\bar{\gamma}_S$, s^{-1}	$(d_{32})_S$, μm	D_{F_S}	τ_R, s	$\bar{\gamma}_R$, s^{-1}	$(d_{32})_R$, μm	D_{F_R}
12.6	508	256±7	2.38±0.18	112	123	476±14	2.33±0.13
14.8	1348	224±6	2.50±0.14	118	146	470±14	2.36±0.09
34.2	217	518±16	2.33±0.11	114	106	578±17	2.31±0.18
30.9	433	469±14	2.40±0.18	114	119	603±16	2.33±0.14
30.2	1379	326±9	2.54±0.13	118	146	620±18	2.37±0.17
58.1	224	581±18	2.38±0.13	112	109	646±20	2.34±0.15
56.2	254	578±19	2.37±0.14	100	123	679±21	2.36±0.19
58.9	411	514±17	2.43±0.15	120	113	669±25	2.36±0.14
59.4	1331	272±8	2.62±0.11	119	144	602±17	2.39±0.12
122.7	207	530±15	2.38±0.15	118	101	598±20	2.30±0.13
110.1	450	400±10	2.45±0.10	110	126	549±16	2.33±0.12

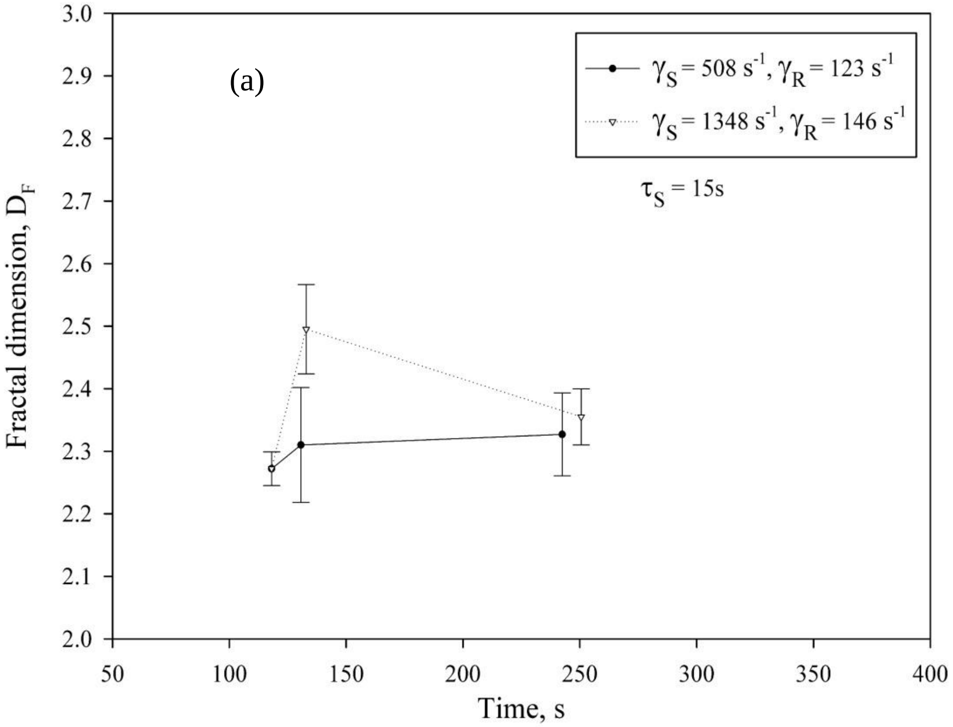
(a)
$\gamma_S = 508\ s^{-1}$, $\gamma_R = 123\ s^{-1}$
$\gamma_S = 1348\ s^{-1}$, $\gamma_R = 146\ s^{-1}$
$\tau_S = 15s$
Fractal dimension, D_F
Time, s
3.0
2.9
2.8
2.7
2.6
2.5
2.4
2.3
2.2
2.1
2.0
50
100
150
200
250
300
350
400

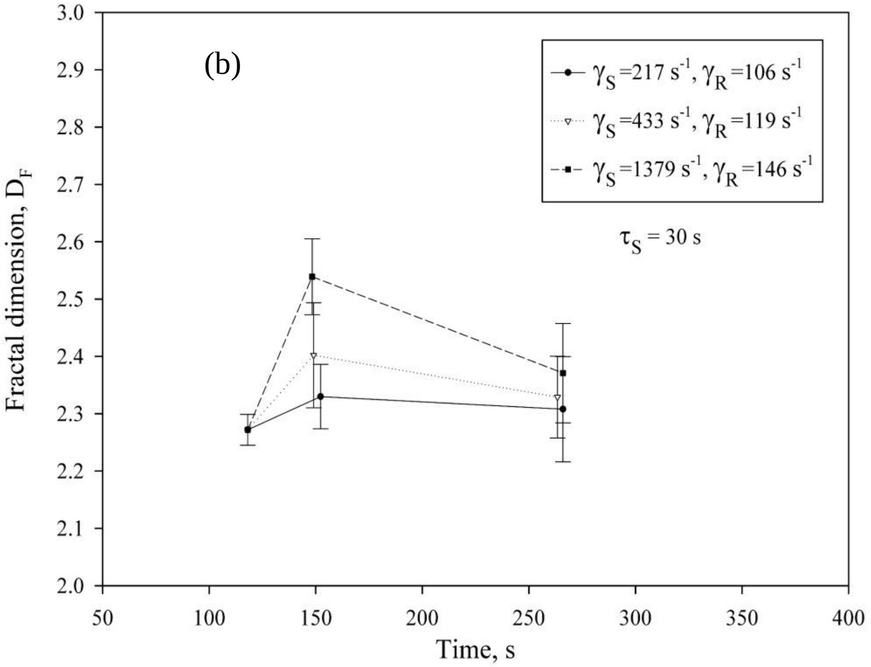
(b)
$\gamma_S = 217\ s^{-1}$, $\gamma_R = 106\ s^{-1}$
$\gamma_S = 433\ s^{-1}$, $\gamma_R = 119\ s^{-1}$
$\gamma_S = 1379\ s^{-1}$, $\gamma_R = 146\ s^{-1}$
$\tau_S = 30\ s$
Fractal dimension, D_F
Time, s
3.0
2.9
2.8
2.7
2.6
2.5
2.4
2.3
2.2
2.1
2.0
50
100
150
200
250
300
350
400

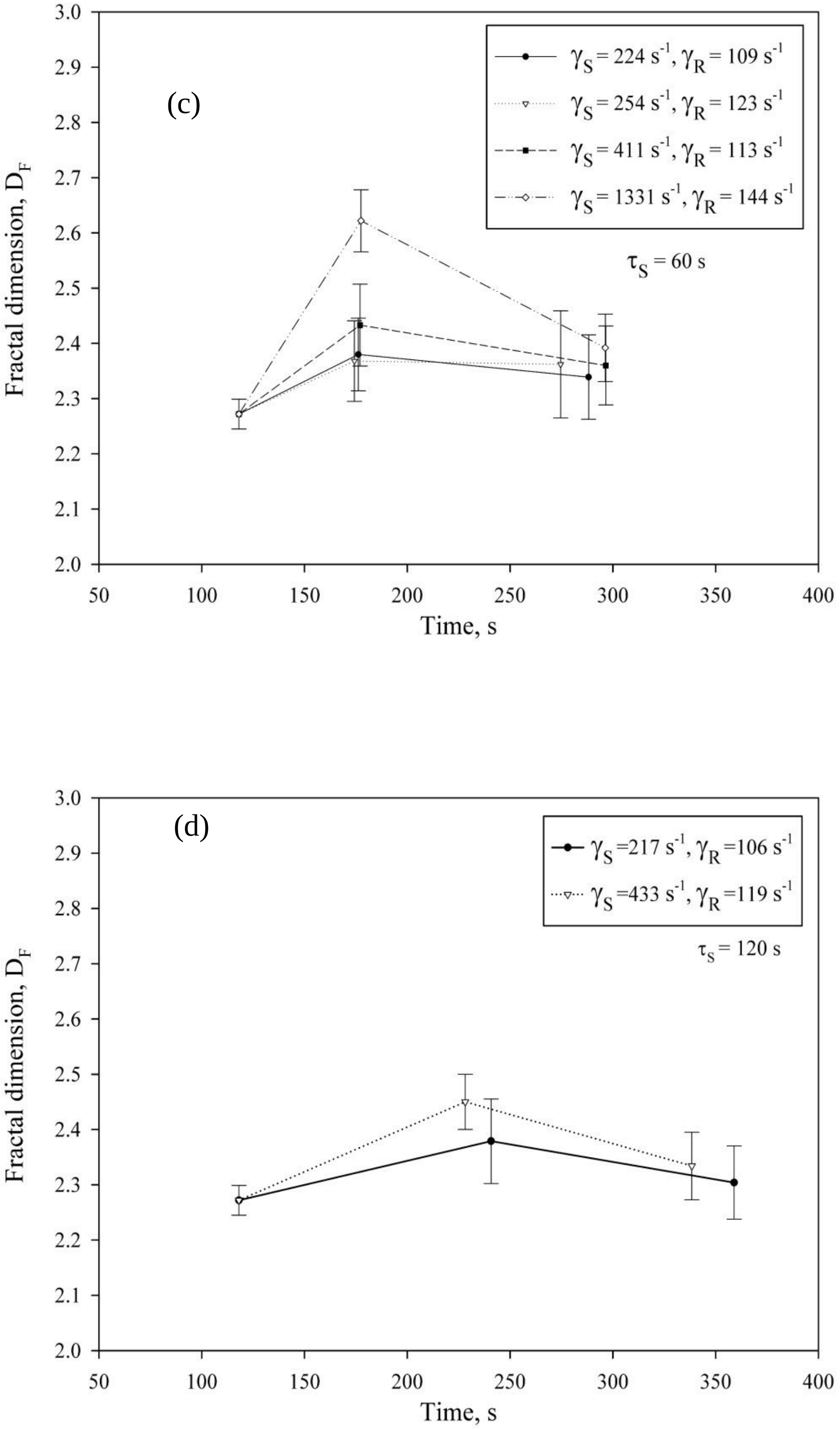

Fig. 5.19. Changes in fractal dimension after flocculation, shearing and reflocculation at shearing times of (a) τ_S = 15s, (b) τ_S = 30s, (c) τ_S = 60 s and (d) τ_S = 120 s

The increase in the fractal dimension indicates that shearing restructures the aggregates, leading to more compact aggregates than those found prior to shearing. At shorter shearing times, shearing does not change the fractal dimension significantly. However, at longer shearing time, increasing the fragmentation rate by increasing the shear rate produces more compact structures relative to aggregates produced at lower shear rates. For instance, Fig. 5.19b,c and Table 5.3 show that at τ_S = 30 s the fractal dimension changes from D_{F_S} = 2.33 ± 0.11 at $\bar{\gamma}_S$ =217 s^{-1} to D_{F_S} = 2.54 ± 0.13 at $\bar{\gamma}_S$ =1379 s^{-1} , but at τ_S = 60 s the fractal dimension changes from D_{F_S} = 2.38 ± 0.13 at $\bar{\gamma}_S$ =224 s^{-1} to D_{F_S} = 2.62 ± 0.11 at $\bar{\gamma}_S$ =1331 s^{-1} . It appears that at higher shear rates and longer exposure time to shear, the increase in fractal dimension is more significant.

After reduction of the shear rate in the reflocculation zone, a new steady state fractal dimension, D_{F_R}, is reached that is lower than the fractal dimension of the sheared suspension. The results of Table 5.3 and Figs 5.19 show that the average fractal dimensions of reflocculated aggregates are statistically similar considering the error bands. This is the case for any given value of residence time in the shearing zone. In other words, conditioning of the sheared suspension in the reflocculation zone produces regrown and restructured aggregates with structural properties that are independent of the shearing history prior to reflocculation.

The average fractal dimension of reflocculated suspensions is about D_{F_R} = 2.34 ± 0.02 for 11 reflocculation runs using D_{F_R} given in Table 5.3. The slight increase in the fractal dimension after reflocculation compared to that of the flocculated suspension, D_{F_F} = 2.27 ± 0.05, is in agreement with previous studies [35]. These results are also in agreement with those of Spicer et al. [19] to some extent. They reported similar behavior upon shearing and reflocculation in of a polystyrene-alum system. However, in their results, the ultimate fractal dimension of the reflocculated suspension depended on shearing history.

The relatively large error bars for the calculated fractal dimensions are caused by the wide aggregate density distribution, which, as described previously, is related to the shape factor distribution (degree of roundness), error associated with the estimation of the non-spherical drag coefficient and error associated with the regression of the density and size data.

5.5. Summary

In this chapter, the results of an experimental study on the effect of shear degradation and reflocculation of flocculated aggregates in a laminar tube flow device were presented. Laminar tube flow was shown to be a uniform and well-characterized shear field in which to monitor the flocculation process, especially compared with more conventional geometries, such as stirred tanks that have turbulent hydrodynamics with a random nature. It also allowed for direct aggregate sampling, which minimizes alteration of aggregate structure compared to other sampling methods described in the literature.

The main aggregate structural parameters; namely, aggregate size, shape, density and fractal dimension were determined from image analysis and settling velocity measurements. Large numbers of aggregates were analyzed to ensure that the results were consistent and statistically representative. One of the features of the present study is that it takes into consideration the effect of aggregate shape and Reynolds number on aggregate density. A state-of-the-art non-spherical drag correlation was used for this purpose.

The effect of shear rate and shearing time on aggregate size, shape, density and fractal dimension of a flocculated suspension were investigated. Results showed that the changes in the aggregate structural properties do not depend on the magnitude of the shear rate when the shearing time is very short. However, at longer shearing times, the magnitude of the shear rate becomes important. Shearing changes aggregate structure through breakage and compaction, which leads to a decreasing aggregate size and an increasing aggregate density and fractal dimension. This implies that aggregates undergo a structural change upon shearing.

A step change reduction in shear rate leads to a secondary structural conformation through reflocculating of the degraded aggregates. The results confirm that reflocculation occurs and that there is a significant degree of reversibility in regaining aggregate structural properties. There is a slight increase in fractal dimension of the reflocculated suspension compared to that of the flocculated suspension prior to shearing. An interesting result is that the extent of the reflocculation does not depend on the shearing history of the suspension, for the conditions studied here.

5.6. Nomenclature

A	Projected area of a particle (l^2)
A_i	Projected area of aggregate on a plane parallel to direction of motion (l^2)
A_V	Projected area of volume equivalent sphere (l^2)
C_D	Drag coefficient
C_{D_I}	Side view-area equivalent sphere drag coefficient
C_{D_V}	Volume equivalent sphere drag coefficient
d_{32}	Sauter mean diameter (l)
d_a	Aggregate area-based equivalent diameter (l)
$\bar{d}_i$	Arithmetic mean of aggregate size population at time *i* (l)
d_i	Aggregate size at size interval of *i* (l)
d_{max}	Maximum diameter of an aggregate (l)
d_V	Volume equivalent sphere diameter (l)
D_C	Curvature diameter for a coiled tube, diameter of cylinder tube coiled around (l)
D_e	Dean number for a curved tube
D_F	Mass fractal dimension
D_{F_F}	Fractal dimension of flocculated aggregate
D_{F_S}	Fractal dimension of sheared aggregate
D_{F_R}	Fractal dimension of reflocculated aggregate
D_i	Image fractal dimension
d_K	Dispersed Kaolinite diameter (l)
d_P	Primary floc diameter (l)
D_{PF}	Mass fractal dimension of primary flocs
D_t	Tube internal diameter (l)
f_{n_d}	Frequency distribution of size, mm^{-1}
F_{n_d}	Cumulative aggregate size distribution, less than %
f_{n_ρ}	Aggregate density number frequency, m^3/kg
F_{n_ρ}	Cumulative aggregate density distribution, less than %
g	Gravitational acceleration ($l\ T^{-2}$)
k	Aggregate permeability (l^2)
K_{N_I}	Side view-Newton's dynamic shape factor
K_{St_I}	Side view-Stokes' dynamic shape factor
L	Aggregate size (l)
N_i	Number of aggregate with size d_i
N_T	Total number of aggregates
P_I	Side view-projected perimeter of aggregate

Q	volumetric flow rate (l^3T^{-1})
Re_a	Area-based aggregate Reynolds number, $\mathrm{Re}_a = \frac{\rho_L U_a d_a}{\mu_L}$
Re_t	Reynolds number inside a tube $\mathrm{Re}_t = \frac{4\rho_L Q}{\pi \mu_L D_t}$
RF	Recovery factor
S	Structural pre factor
SF	Strength factor
t	Flocculation time (T)
U_a	Aggregate settling velocity ($l\ T^{-1}$)
V	Actual volume of aggregate (l^3)
V_I	Imaginary equivalent sphere volume having a diameter of d_a (l^3)
α	Significance level
β	Permeability factor
ε	Aggregate overall porosity
ϕ	Degree of roundness shape factor
$\bar{\dot{\gamma}}_{Curved}$	Average shear rate in a coiled tube (T^{-1})
$\bar{\gamma}_F$	Average shear rate in flocculation zone (T^{-1})
$\bar{\gamma}_R$	Average shear rate in reflocculation zone (T^{-1})
$\bar{\gamma}_S$	Average shear rate in shearing zone (T^{-1})
$\bar{\dot{\gamma}}_{Straight}$	Average shear rate in a straight tube (T^{-1})
μ_L	Liquid viscosity, ($M\ l^{-1}T^{-1}$)
ρ_a	Aggregate density ($M\ l^{-3}$)
ρ_{Eff}	Aggregate effective density, ($M\ l^{-3}$)
ρ_K	Kaolinite density ($M\ l^{-3}$)
ρ_L	Liquid density ($M\ l^{-3}$)
ρ_P	Primary floc density ($M\ l^{-3}$)
$\bar{\rho}_i$	Arithmetic mean of effective density population at time i ($M\ l^{-3}$)
τ_F	Flocculation time (T)
τ_R	Reflocculation time (T)
τ_S	Shearing time (T)
ξ	Shielding coefficient of particles interaction
Ω	Advective flow correction factor
Δx	Aggregate settling distance (l)
Δt	Aggregate settling time (T)

5.7. References

1. Cymerman, G., Kwong, T., Lord, E., Hamza, H.A., Xu, Y., “Thickening and disposal of fine tails from oil sand processing”, In: Polymer in Mineral Processing-Proc. 3rd UBC-McGill Int. Symp., (Ed. By) Laskowski, J.S., Metallurgical Society of CIM, Quebec City, 1999, 605-619.
2. Scott, J.D., Cymerman, G., “Prediction of viable tailings disposal methods”, Symposium on Sedimentation Consolidation Models, ASCE, San Francisco, 1984, 522-544.
3. Xu, Y., Cymerman, G., “Flocculation of fine oil sand tails”, In: Polymer in Mineral processing-Proc. 3rd UBC-McGill Int. Symp., (Ed. By) Laskowski, J.S., Metallurgical Society of CIM, Quebec City, 1999, 591-604.
4. Hamza, H.A., Stanonik, D. J., Kessick, M.A., (1996). “Flocculation of lime-treated oil sands tailings”, Fuel, 75, 280-284.
5. Lord, E.R., Liu, Y., “Depositional and geotechnical characteristics of paste produced from oil sand tailings”, Tailings and Mine Waste “98” Proceeding of the Fifth Int. Confer. On Tailings and Mine Waste “98”/Colorado, USA, 1998, 26-28 Jan, 147-157.
6. Mills, P.D.A., Goodwin, J.W., Grover, B.W., (1991). “Shear field modification of strongly flocculated suspensions-Aggregate morphology”, Colloid Poly. Sci., 269, 949-963.
7. Schaan, J., Sanders, R.S., Gillies, R.G., McKibben, M.J., Litzenberger, C., Sun, R-J., Shook, C.A., “Effect of shear history on the flow properties of flocculant-dosed thickened tailings slurries”, 6th International Conference on Hydrotransport, Vol. II, Santiago, Chile, 2004, 26-28 April, 403-414.
8. Hogg, R., (2000). “Flocculation and dewatering”, Int. J. Miner. Proc., 58, 223-236.
9. Vaezi G., F., Sanders, R.S., Masliyah, J.H., (2011). “Flocculation kinetics and aggregate structure of kaolinite mixtures in laminar tube flow”, J. of Colloid and Interface Sci., 355, 96-105.
10. Serra, T., Colmer, J., Logan, B.E., (2008). “Efficiency of different shear devices on flocculation”, Water Res., 42, 1113-1121.

11. Colomer, J., Peters, F., Marrase, C., (2005). “Experimental analysis of coagulation of particles under low-shear flow”, Water Res., 39, 2994–3000.
12. Selomulya, C., Amal, R., Bushell, G., Waite, D., (2011). “Evidence of shear rate dependence of restructuring and breakup of latex aggregates”, J. Colloid Interface Sci., 236, 67-77.
13. Michaels, A.S., Bolger, C.B., (1962). “The plastic flow behavior of flocculated kaolin suspensions”, I & EC Fundamen., 1, 153-162.
14. Clark, M.M., Flora, J.R.V., (1991). “Floc restructuring in varied turbulent mixing”, J. of Colloid and Inter. Sci., 147, 407-421.
15. Michaels, A.S., Bolger, J.C., (1962). “Settling rate and sedimentation volumes of flocculated kaolin suspensions”, I & EC Fundamen., 1, 24–33.
16. Lagvankar, A.L., Gemmell, R.S., (1968). “A size-density relationship for flocs”, J. AWWA, 60, 1040-1046.
17. Glasgow, L.A., Liu, S.X., (1995). “Effects of dosing regimen and agitation profile upon floc characteristics”, Chem. Eng. Commun. 132, 223-237.
18. Sengupta, D.K., Kan, J., Al Taweel, A.M., Hamza, H.A., (1997). “Dependence of separation properties on flocculation dynamics of kaolinite suspension”, Int. J. Miner. Process. 49, 73-85.
19. Spicer, P.T., Pratsinis, S.E., (1996). “Shear-Induced flocculation: the evolution of floc structure and shape of the size distribution at steady state”, Water Res., 30, 1049-1056.
20. Spicer, P.T., Pratsinis, S.E., Raper, J., Amal, R., Bushell, G., (1998). “Effect of shear schedule on particle size, density, and structure during flocculation in stirred tank”, Powder Technol., 97, 26-34.
21. Thomas, D.G., (1964). “Turbulent disruption of flocs in small particle size suspensions”, AIChE J. 10, 517-523.
22. Yuan, Y., Farnood, R.R., (2010). “Strength and breakage of activated sludge flocs”, Powder Tech., 199, 111-119.
23. Wang, D., Wu, R., Jiang, Y., Chow, C.W.K. (2011). “Characterization of floc structure and strength: Role of changing shear rates under various coagulation mechanisms”, Colloids Surf. A Physicochem. Eng. Aspects, 379, 36-42.

24. Zhao, Y.X., Gao, B.Y., Shon, H.K., Kim, J-H., Yue, Q.Y., (2011). “Effect of shear force, solution pH and breakage period on characteristics of flocs formed by Titanium tetrachloride ($TiCl_4$) and Polyaluminum chloride (PACl) with surface water treatment”, J. Hazardous Mat., 187, 495-501.
25. Tambo, N., Hozumi, H., (1979). “Physical characteristics of flocs-II. Strength of floc”, Water Res., 13, 421-427.
26. Jarvis, P., Jefferson, B., Gregory, J., Parsons, S.A., (2005). “A review of floc strength and breakage”, Water Res., 39, 3121–3137.
27. Serra, T., Colomer, J., Casamitjana, X., (1997). “Aggregation and breakup of particles in a shear flow”, J. Colloid and Interface Sci., 187, 466-73.
28. Serra, T., Casamitjana, X., (1998). “Effect of the shear and volume fraction on the aggregation and breakup of particles”, AIChE J., 44, 1724-1730.
29. Kusters, K.A., Wijers, J.G., Thoenes, D., (1997). “Aggregation kinetics of small particles in agitated vessels”, Chem. Eng. Sci., 52, 107-121.
30. Chen, W., Fisher, R.R., Berg, J.C., (1990). “Simulation of particle size distribution in an aggregation-breakup process”, Chem. Eng. Sci., 45, 3003-3005.
31. Francois, R.J., (1987)a. “Ageing of aluminium hydroxide flocs”, Water Res. 21, 523-531.
32. Francois, R.J., (1987)b. “Strength of aluminium hydroxide flocs”, Water Res. 21, 1023-1030.
33. Yukselon, A., Gregory, J., (2004). “The reversibility of floc breakage”, Int. J. Miner. Process, 73, 251-259.
34. Yoon, S.Y., Deng, Y., (2004). “Flocculation and reflocculation of clay suspension by different polymer systems under turbulent conditions”, J. Colloid Interface Sci., 278, 139-145.
35. Rasteiro, M.G., Garcia, F.A.P., Ferreira, P., Blanco, A., Negro, C., Antunes, E., (2008). “Evaluation of flocs resistance and reflocculation capacity using LDS technique”, Powder Technol., 183, 231-238.

36. Zhu, Z., Li, T., Lu, J., Wang, D., Yao, C., (2009). "Characterization of kaolin flocs formed by polyacrylamide as flocculation aids", Int. J. Miner. Process., 91, 94-99.
37. Xu, W., Gao, B., Yue, Q., Wang, Y., (2010). "Effect of shear force and solution pH on flocs breakage and regrowth formed by nano-Al_{13} polymer", Water Res., 44, 1893-1899.
38. Xiao, F., Lam, K.M., Li, X.Y., Zhong, R.S., Zhang, X.H., (2011). "PIV characterization of flocculation dynamics and floc structure in water treatment", Colloids and Surfaces A: Physicochem. Eng. aspects, 379, 27-35.
39. Horn, A.F., Merrill, E.W., (1984). "Midpoint scission of macromolecules in dilute solution in turbulent flow", Nature 312, 140–141.
40. Owen, A.T., Nguyen, T.V., Fawell, P.D., (2009). "The effect of flocculant solution transport and addition conditions on feed-well performance in gravity thickeners", Int. J. Miner. Process. 93, 115-127.
41. Spicer, P.T., Keller, W., Pratsinis, S.E., (1996). "The effect of impeller type on floc size and structure during shear-induced flocculation", J. Colloid Interface Sci. 184, 112–122.
42. Bouyer, D., Liné, A., Do-Quang, Z., (2004). "Experimental analysis of floc size distribution under different hydrodynamics in a mixing tank", AICHE J. 50, 2064-2081.
43. Coufort, C., Bouyer, D., Line, A., (2005). "Flocculation related to local hydrodynamics in a Taylor-Couette reactor and in a jar", Chem. Eng. Sci., 60, 2179-2192.
44. Bouyer, D., Coufort, C., Live, A., Do-Quang, Z., (2005). "Experimental analysis of floc size distribution in a 1-L jar under different hydrodynamics and physiochemical conditions", J. of Colloid and Interface Sci., 292, 413-428.
45. Rahmani, N.H.G., Masliyah, J.H., Dabros, T., (2003). "Characterization of asphaltene aggregation and fragmentation in a shear field", AIChE J., 49, 1645-1655.

46. Rahmani, N.H.G., Dabros, T., Masliyah, J.H., (2004). “Evolution of Asphaltene Floc Size Distribution in Organic Solvents Under shear”, Chem. Eng. Sci., 59, 685-697.
47. Rahmani, N.H.G., Dabros, T., Masliyah, J.H., (2005). “Online Optical Monitoring of Asphaltene Aggregation”, Ind. Eng. Chem. Res., 44, 75-84.
48. Swift, J.D., Simic, K., Johnston, R.R.M., Fawell, P.D., Farrow, J.B., (2004). “A study of the polymer flocculation reaction in a linear pipe with a focused beam reflectance measurement probe”, Int. J. Miner. Process. 73, 103–118.
49. Carissimi, E., Rubio, J., (2005). “The flocs generator reactor - FGR: a new basis for flocculation and solid–liquid separation”. Int. J. Miner. Process. 75, 237–247.
50. Zumaeta, N., Byrne, E., Fitzpatrick, J.J., (2006). “Predicting precipitate particle breakage in a pipeline: effect of agitation intensity during precipitate formation”, Chem. Eng. Sci. 61, 7991–8003.
51. Carissimi, E., Miller, J.D., Rubio, J., (2007). “Characterization of the high kinetic energy dissipation of the flocs generator reactor”, Int. J. Miner. Process. 85, 41-49.
52. Owen, A.T., Fawell, P.D., Swift, D.M., Benn, F.A., Farrow, J.B., (2008). “Using turbulent pipe flow to study the factors affecting polymer-bridging flocculation of mineral systems”, Int. J. Miner. Process. 87, 90-99.
53. Gregory, J. (1981). “Flocculation in laminar tube flow”, Chem. Eng. Sci. 36, 1789-1794.
54. Gregory, J., Nelson, D.W., (1986). “Monitoring of Aggregates in Flowing Suspensions”, Colloids Surf., 18, 175–188.
55. Gregory, J., (1987). “Laminar dispersion and the monitoring of flocculation processes”. J. of Colloid and Interface Science 118, 397-409.
56. McConalogue, D.J., “The effect of secondary flow on the laminar dispersion of an injected substance in a curved tube”, Proc. Roy. Soc. Lond. A., 315 (1970) 99-113.
57. Berger, S.A., Talbot, L., Yao, L.S., (1983). “Flow in curved pipes”. Ann. Rev. of Fluid Mech., 15, 461-512.

58. Li, D.H., Ganczarczyk, J.J., (1989). “Fractal geometry of particle aggregates generated in water and wastewater treatment processes”, Envir. Sci. & Technol., 23, 1385-1389.
59. Jiang, Q., Logan, E.B., (1991). “Fractal dimension of aggregates determined from steady-state size distribution”, Envir. Sci. Tech., 25, 2031-2038.
60. Huang, H., (1993). “Porosity-size relationship of drilling mud flocs: fractal structure”, Clays and Clay Minerals, 41, 373-379.
61. Gregory, J., (1997). “The Density of Particle Aggregates”, Water Sci. Technol., 36, 1-13.
62. Bushell, G.C., Yan, Y.D., Woodfield, D., Raper, J., Amal, R., (2002). “On techniques for the measurement of the mass fractal dimension of aggregates”, Adv. Colloid Interface Sci. 95, 1-50.
63. Jarvis, P., Jefferson, B., Parsons, S. A., (2005). “Measuring floc structural characteristics” Reviews in Environ. Sci. Biotechnol. 4, 1-18.
64. Tambo, N., Watanabe, Y., (1979). “Physical characteristics of flocs-I The floc density function and aluminum floc”, Water Res., 13, 409-419.
65. Klimpel, R.C., Hogg, R., (1991). “Evaluation of floc structures”, Colloids Surf., 55, 279-288.
66. Li, D., Ganczarczyk, J., (1992). “Advective transport in activated sludge flocs”, Water Environ. Res., 64, 236-240.
67. Lee, D.J., Chen, G.W., Liao, Y.C., Hsieh, C.C., (1996). “On the free-settling test for estimating activated sludge floc density”, Water Res., 30, 541-550.
68. Nasser, M.S., James, A.E., (2007). “Effect of polyacrylamide polymers on floc size and rheological behavior of kaolinite suspensions”, Colloids Surf. A PhysicoChem. Eng. Aspects, 301, 311–322.
69. Johnson, C.P., Li, X., Logan, B.E., (1996). “Settling velocities of fractal aggregates”, Environ. Sci. Technol., 30, 1911-1918.
70. Li, X.Y., Logan, B.E., (1997). “Collision frequencies between fractal aggregates and small particles in a turbulent sheared fluid”, Environ. Sci. Technol., 31, 1237-1242.

71. Woodfield, D., Bickert, G., (2001). “An improved permeability model for fractal aggregates settling in creeping flow”, Water Res., 35, 3801-3806.
72. Gmachowski, L., (2000). “Estimation of the dynamic size of fractal aggregates” Colloids Surf. A Physicochem. Eng. Aspects, 170, 209-216.
73. Neale, G., Epstein, N., Nader, W., (1973). “Creeping flow relative to permeable spheres”, Chem. Eng. Sci., 28, 1865-1874.
74. Vanni, M., (2000). “Creeping flow over spherical permeable aggregates”, Chem. Eng. Sci., 55, 685-698.
75. Gruy, F., Cugniet, P., (2004). “Experimental study of small aggregate settling”, J. Colloid Interface Sci., 272, 465-471.
76. Masliyah, J.H., Polikar, M., (1980). “Terminal velocity of porous spheres”, Can. J. Chem. Eng., 58, 299-302.
77. Farrow, J.B., Warren, L.J., “Measurements of the size of aggregates in suspension“ in: Dobias, B. (Ed.), “Coagulation and flocculation-Theory and application”, Marcel Dekker, NewYork, 1993, Chapter 9, 391-426.
78. Námer, J., Ganczarczyk, J.J., (1993). “Settling properties of digested sludge particle aggregates”, Water Res. 27, 1285-1294.
79. Ro, K.S., Neethling, J. B., (1990). “Terminal settling characteristics of bio-particles”, Res. J. Water Pollut. Control Fed., 62, 901-906.
80. Mu, Y., Ren, T-T., Yu, H.Q., (2008). “Drag coefficient of porous and permeable microbial granules”, Envir. Sci. Technol., 42, 1718-1723.

Appendix 5.1. Details of experimental setup and conditions for shearing and reflocculation tests

	Flocculation zone (L_F=12.4m, tube ID_F=6.4mm)					Shearing zone (tube ID_S=3.2mm)					Reflocculation zone (τ_R =120s)					
Test parameters	gr polymer/ tonnes clay	Q_{Fmean} [ml/min]	C.I. Q_{Fmean} [ml/min]	$\bar{\dot{\gamma}}_{Curved})_F$ [s^{-1}]	τ_F ,[s]	Q_{Smean} [ml/min]	C.I. Q_{Smean} [ml/min]	$\bar{\dot{\gamma}}_{Curved})_S$ [s^{-1}]	L_S, [m]	τ_S ,[s]	Q_{Rmean} [ml/min]	C.I. Q_{Rmean} [ml/min]	ID_R, [mm]	$\bar{\dot{\gamma}}_{Curved})_R$ [s^{-1}]	L_R, [m]	τ_R ,[s]
τ_S =15 s	788	203.0	-	144.8	118.2	98.3	-	508	2.6	12.6	98.3	-	4.8	142	9.2	100
	786	203.4	3.4	145.2	118	122.5	1.7	680	4.0	15.3	-	-	-	-	-	-
	745	207.9	1.4	149.5	115.4	149.8	2.4	890	5.1	16	-	-	-	-	-	-
	738	203.9	1.0	145.7	117.7	203.9	1.0	1348	6.4	14.8	203.9	1.0	6.4	146	12.4	118
	736	204.2	3.9	146	117.5	204.2	1.3	1351	6.5	15.1	-	-	-	-	-	-
τ_S =30 s	748	205.2	0.5	146.9	117	50.7	0.7	217	3.7	34.2	50.7	3.0	4.0	106	7.7	114
	783	205.1	2.0	146.8	117	86.9	1.2	433	5.7	30.9	86.9	1.4	4.8	121	9.2	113
	758	205.8	1.1	147.5	116.3	126.2	1.6	707	8.4	31.6	-	-	-	-	-	-
	754	204.8	1.5	146.6	117.1	149.1	2.2	884	10.0	31.9	-	-	-	-	-	-
	793	207.3	1.3	149.0	117.9	207.3	1.8	1379	13.2	30.2	207.3	1.3	6.4	149	12.4	116
τ_S =60 s	650	210.3	1.7	151.9	114.1	51.9	3.2	224	6.4	58.1	51.9	2.6	4	109	7.7	112
	774	206.6	0.6	148.3	116.1	57.7	1.3	254	6.8	56.2	57.5	1.3	4	123	7.7	100
	711	202.3	1.3	144.2	118.6	83.9	3.9	411	10.4	58.9	83.6	7.2	4.8	115	9.2	118
	757	203.5	1.3	145.3	117.9	125.7	2.9	704	16.3	61.6	-	-	-	-	-	
	760	203.9	2.4	145.7	117.8	153.1	2.1	916	18.9	58.6	-	-	-	-	-	
	722	200.4	1.8	142.4	119.7	200.4	5.4	1317	25.3	59.9	-	-	-	-	-	
	734	202.0	1.5	143.9	118.8	202.0	1.5	1331	25.3	59.4	202	1.5	6.4	144	12.4	119
τ_S =120 s	745	203.4	1.9	145.2	118	48.8	1.3	207	12.6	123	48.8	1.3	4	101	7.7	118
	735	204	1.6	145.8	117.6	89.6	4.4	450	20.8	110	89.6	4.4	4.8	126	9.3	110
	747	205.5	1.3	147.2	116.8	132.5	3.3	755	31.6	113	-	-	-	-	-	-

Chapter 6

Conclusions and Recommendations

6.1. General summary

The research described in this dissertation explores different aspects of the aggregation and fragmentation of a clay suspension dosed with polymer flocculant. The major contribution of the present study is to provide a fundamental understanding of the flocculation process, and of aggregate structure, based on experimental observations. The specific focus is on the effect of shearing on the structure of the flocculated kaolinite aggregates. The complexity associated with the oil sands tailings, due to the diversity of and complexity of interactions among constituents, is simplified by choosing a kaolinite particle suspension as a model system. The physicochemical conditions were similar to that of oil sand tailings.

This research also provides new insight into fluid-particle dynamics and the interaction of highly irregular, non-spherical particles and/or fragile, non-spherical objects with the surrounding fluid. Two new drag coefficient expressions for non-spherical particles are introduced; one of them is specifically useful to estimate drag coefficients of fragile objects similar to the flocculated aggregates encountered in this study.

The second chapter described the flocculation of a dispersed kaolinite suspension using a high molecular weight anionic polymer. The required steps were taken to study the kinetics of a two-stage coagulation-flocculation process. An experimental technique was developed to prepare flocculated aggregates and to measure aggregate structural parameters; namely, size, density and fractal dimension. The experimental device was based on using a laminar shear field, which allowed for direct aggregate sampling where their structures were less likely to be altered during sampling, especially compared to other sampling methods found in the literature.

The aggregate size and density were determined from image analysis and settling velocity measurements, and aggregate fractal diameter was calculated using the size and density data. The kinetics of the flocculation process, in terms of the evolution of the aggregate size, density and fractal dimension, were investigated. Results showed that aggregates grew quickly to become relatively tenuous with open structures in the early stages of the flocculation process. A detailed statistical analysis confirmed establishment of a steady state condition in terms of aggregate structural parameters. The statistical analysis did not show any ageing or structural conformation occurring for the range of flocculation times studied here. One of the most important results described in the second chapter was the definition of a set of conditions, in terms of a flocculation procedure and process conditions, to produce aggregates with defined and reproducible structures. The reproducibility was validated by repeating the flocculation tests and conducting a detailed statistical analysis. The reproducible formation of aggregate structure prevented random and/or biased structural properties of the flocculated aggregates, which was an essential requirement for the shear degradation experiments that was the main focus of this research.

For the flocculation kinetics study described in the second chapter, aggregates were assumed to be spherical and the aggregate density was calculated using this assumption. However, published studies in the literature and the visual observations made during the experiments did not support this assumption, meaning aggregates were highly non-spherical and irregular in their geometry. It is worth noting that aggregate non-sphericity influences the calculation of drag coefficient and consequently, aggregate density.

A detailed literature review was conducted and no correlation was found suitable for determination of aggregate drag coefficient. The non-spherical drag correlations found in the literature require particle geometrical parameters, such as volume, surface area and projected area, to describe the non-sphericity of a particle. However, most of these parameters, especially particle volume and surface area, cannot be measured for an aggregate due to its fragile nature and highly irregular morphology. Also, accurate experimental measurement of drag coefficient of an aggregate is unlikely to be done, for the same reasons.

The third and fourth chapters dealt with the development of a new non-spherical drag coefficient correlation. In Chapter 3, a modified universal correlation was developed using experimental drag coefficient data reported in the literature. The modified universal correlation allows for determination of the drag coefficient for a non-spherical particle using only particle volume and a new shape factor, denoted as “degree of roundness”.

The modified universal drag coefficient correlation is very useful for highly irregular particles. Nevertheless, the fragile nature of the aggregates made it impossible to measure aggregate volume and thus a different approach was required. The dilemma was resolved by defining a new form of drag coefficient in Chapter 4, based on only two dimensional geometrical data accessible through imaging measurements. In other words, the new form of the drag coefficient correlation does not require particle volume, unlike the most commonly used drag coefficient expressions found in the literature. The novel correlation presented in Chapter 4 provides a more accurate estimation of the aggregate drag coefficient compared to the case where aggregates are assumed to be spherical.

Chapter 5 details the core objective of the thesis; specifically, how shear affects the structure of flocculated aggregates. Flocculated aggregates were produced using the experimental procedure described in Chapter 2. The reproducibility was validated by repeating the flocculation tests and conducting a detailed statistical analysis. Aggregates were exposed to various shear rates for different periods of time and degraded aggregates were then conditioned in reflocculation experiments. The main aggregate structural parameters, aggregate size, shape, density and fractal dimension, were monitored through the image analysis and settling velocity measurements. Large numbers of aggregates were analyzed to ensure that the results were consistent and statistically representative.

In Chapter 5, the aggregate non-sphericity was considered in the calculation of aggregate drag coefficient and this in estimating aggregate density. The non-spherical drag correlation developed in Chapter 4 was used for this purpose.

Results of shearing experiments showed that the changes in the aggregate structural parameters did not depend on the magnitude of shear rate when the shearing period was very short. However, at longer shearing times (t> 15 s), the magnitude of the shear rate became important. Shearing reduced aggregate size and simultaneously increased aggregate density and fractal dimension. In other words, shearing changed aggregate structure through breakage and compaction, and structural conformation occurred.

Conditioning of sheared aggregates at a lower shear rates led to a secondary structural conformation through reflocculation of the degraded aggregates. The results confirmed that there was a significant degree of both reflocculation and recovery of aggregate structural parameters. The extent of the reflocculation did not depend on shearing history, for the conditions studied here.

Even though the results of the present research are not directly applicable to thickening of fine tailings, they provide fundamental knowledge and insight into the effect of hydrodynamic conditioning on aggregate structure. This knowledge is essential for developing a better understanding of the non-Newtonian rheological characteristics of the thickened fine tailings, which in turn will lead to improvements in thickening processes [1-3].

6.2. Novel contributions

6.2.1. An experimental technique to monitor structure of aggregates

An experimental technique was developed to prepare flocculated aggregates, to degrade the aggregates at high shear rates for different shearing periods and to reflocculate them by conditioning the degraded aggregates at lower shear rates. The experimental technique that was developed combined a laminar shear field device, a sampling method, a sedimentation chamber and an imaging technique. The laminar tube flow was shown to be an excellent, well-characterized shear field with numerous advantages in terms of controlling and estimating the shear rate, especially compared with more conventional geometries, such as stirred tanks, which are typically used for these types of studies. It also allowed for direct aggregate sampling where their structures are less altered by the sampling as compared to other sampling methods. The samples from the laminar flow device were directed to a settling chamber where images of settling aggregates were taken. The subsequent image analysis provided aggregate geometrical parameters and aggregate settling velocities.

6.2.2. An improved drag correlation for non-spherical particles

An important contribution to the field of fluid-particle dynamics was made by developing a modified universal volumetric drag correlation for non-spherical particles that only used particle volume and a new shape factor, denoted “degree of roundness”. This shape factor used only particle geometrical information obtained from a side view-projection of the particle in a plane parallel to the particle’s direction of motion.

Application of the degree of roundness parameter has numerous advantages compared to common shape factors used to define particle shape, such as sphericity, which requires measurement of particle surface area. Particle surface area is difficult to measure for non-spherical particles, especially for highly irregular geometries or particles with rough surfaces. The side view of the particle on a plane parallel to direction of particle motion is easily accessible using online/offline imaging techniques. Also, two-dimensional geometrical parameters used to define the degree of roundness can be determined easily and with a higher accuracy compared to particle surface area.

The modified universal drag coefficient correlation predicted experimental drag data in the subcritical regime ($1.5 \times 10^{-5} < Re_v < 1.7 \times 10^5$) with a degree of accuracy similar to that associated with the most accurate correlations available in the literature. The correlations in the literature normally use two shape factors, which require three geometrical parameters: volume, surface area and projected area on a plane normal to the direction of particle motion. These geometrical parameters are not readily available in most practical cases. The correlation developed in this research needs only one shape factor that is readily available from the projection of particle shape on a plane parallel to the direction of particle motion. The difficulties inherent in measuring sphericity for non-isometric and highly irregular particles are avoided in the use of the new drag coefficient correlation.

6.2.3. A novel drag coefficient correlation for fragile non-spherical objects

A state-of-the-art drag coefficient correlation for non-spherical particles was developed that provides, for the first time, a link between fluid-particle dynamics and online imaging techniques where a moving particle is viewed only from the side. An important feature of the new correlation is that it does not need particle volume. The correlation uses a new form of drag coefficient, denoted as side view- drag coefficient, which is defined using two- dimensional side view geometrical parameters.

The side view-drag correlation can be used to predict experimental drag data in the subcritical regime ($1.5 \times 10^{-5} < Re_v < 1.7 \times 10^{5}$) with a reasonable degree of accuracy for objects with degree of roundness, $\phi > 0.4$. It is not as accurate as the commonly used form of the drag coefficient, i.e. volumetric drag coefficient and it is not appropriate for highly isometric objects such as needles and thin disks. However, it uses only two-dimensional geometrical parameters accessible through the imaging measurements and does not require particle volume. This is advantageous for applications with limited access to particle geometrical data, such as fragile objects. The application of the side view drag coefficient correlation is well demonstrated in the present research. A potential application for the new correlation is online measurements coupled with imaging techniques that are frequently used as a non-invasive method to study fluid-particle dynamics.

6.2.4. Improved determination of a complete set of aggregate structural parameters

A complete set of aggregate structural parameters, i.e. size, shape, density and fractal dimension was measured. The accuracy of aggregate density estimation was improved by taking into consideration the aggregate non-spherical shape. This was accomplished using the side view-drag coefficient correlation that provided a more realistic and accurate estimation of the aggregate drag coefficient and hence its density. Accordingly, estimation of fractal dimension of aggregates was more realistic compared to the cases in which aggregates were assumed to be spherical.

In most of studies published in the literature, only aggregate size and fractal dimension are monitored. In very limited cases, aggregate density was calculated, but aggregates were assumed to be spherical [4-6]. The assumption of aggregates to be spherical leads to underestimation of the drag force and the aggregate density.

6.3. Key findings

The core objective of the thesis was to investigate the response of flocculated aggregate structure to macroscopic changes in system hydrodynamic conditions. The flocculated aggregates were exposed to different average shear rates ranging from 200 to1400 s^{-1} for different shearing periods of 15 to 120 s. An important finding concerning the shear degradation of the flocculated aggregates was that the changes in the aggregate structural parameters (i.e. size, shape, density and fractal dimension) did not depend on the magnitude of shear rate when the shearing period was very short (i.e. 15s). However, at longer shearing periods (>15s), the magnitude of the shear rate became important. Exposure of aggregates to high shear rates led to a decreasing aggregate size and increasing aggregate density and fractal dimension. This indicated that aggregate breakage and compaction occurred and the aggregates experienced structural conformation upon shearing.

An additional finding in the present study was that reflocculation occurred upon reduction of shearing, which indicated that shear degradation of aggregates was not permanent. Once the high shearing was ceased and sheared aggregates were conditioned at a lower shear rate, the degraded aggregates reflocculated to some degree and a secondary structural conformation occurred. A significant degree of recovery in the aggregate structural properties, in terms of size, shape, density and fractal dimension, was observed. Reflocculation did not fully occur, meaning that the shear degradation phenomenon could be classified as “partially irreversible”. There was a slight increase in the fractal dimension of the reflocculated suspension compared to that of the flocculated suspension, measured prior to shearing. An important observation was that the extent of reflocculation did not depend on the shearing history of the suspension, for the conditions studied here.

6.4. Industrial implications

The results of the present research are not directly applicable to industrial thickening of fine tailings. Nevertheless, the key findings of the present research, the microscopic response of flocculated aggregates to hydrodynamic conditioning, provides fundamental knowledge and mechanistic insight into the rheological behavior of thickened tailings. A better understanding of the relationship connecting aggregate structure, shear conditioning and the non-Newtonian rheological characteristics of the thickened fine tailings is essential for the design, start-up, operation and maintenance of fine tailings thickeners, transport pipeline design and prediction of deposit stability [1-3].

The results of this research can partly explain changes in the rheological behavior of the thickened slurries upon shearing. The present research proves that high shear rates lead to simultaneous breakage and compaction of aggregates, which releases a portion of the water encapsulated inside the aggregate, i.e. intra-aggregate water. Additionally, previous studies indicate that shearing degrades the network formed among aggregates in a thickened slurry [7-9]. Such a network breakdown can release a portion of water captured in the void spaces of the inter-aggregates network, which decreases the superficial solid phase concentration. The summative effect of the degradation of the inter-aggregates network with individual aggregate fragmentation and compaction leads to an increase in the volume of the free water in the suspension. The released water dilutes the thickened slurry and therefore the mixture becomes thinner, which may partly explain the shear thinning behavior of thickened tailings. It is worth noting that previous studies have shown that the shear thinning behavior of flocculated slurries can be permanent and model flocculated kaolinite suspensions do not show a thixotropic behavior [10].

This research shows that there is a high degree of aggregate reflocculation after exposure to shear. It may be possible to exploit this phenomenon to improve the thickening of fine tailings. Exposure of the flocculated suspension to high shearing in pumps and transport pipelines is inevitable, which changes the rheological behavior of the slurry. Shearing of the thickened slurry before transport (e.g. in pumps and extra shearing devices) can reduce the apparent viscosity of the slurry; therefore, the transport pipeline can operate with a lower pressure drop. Moreover, the thickener can be operated to produce an underflow stream with a higher solids content by partial recirculation of slurry to the bottom of thickener after shearing. At the end of pipeline, near the disposal area, the thin slurry can be conditioned to induce reflocculation at a low shear rate. Chemical reagent addition may also be an option at this stage. The higher solids content of the final thickened slurry and partial recovery of viscoelastic properties by reflocculation (i.e. partial thixotropy) can improve the geotechnical characteristics of the deposited thickened paste.

6.5. Uncertainties and challenges

There are some uncertainties associated with this study that need to be addressed. First, the effect of the tube wall on the measured aggregate structure must be accounted for. The difference between the size of an aggregate and the tube diameter was about one order of magnitude. Under such conditions, aggregate-tube wall contact might be important and is likely comparable in magnitude to aggregate-fluid interactions. Additionally, in these tests, the average aggregate was large enough that there was a shear distribution across its surface. This might cause some degree of error in estimating the shear rates that the aggregates were exposed to. It might also cause aggregate rotation, which in turn would increase the chance of aggregate contact with the tube wall. Finally, there is a residence time distribution in laminar tube flow, due to the no-slip condition at the tube wall. In the present research, the flocculation, shearing and reflocculation times were estimated using the average volumetric flow rates and the tube length. This was relatively accurate considering the fact the tube diameters were small. However, the residence time distribution might be important for the experiments conducted at short shearing times. These uncertainties can be addressed through additional experiments using different tube sizes and also some calculations to evaluate the possibility of aggregate rotation due to the shear distribution across the aggregate surface and residence time distribution.

Experimental observation showed that at very short shearing times, the effect of shearing did not depend on the magnitude of the shear rate. Additional experiments with shorter shearing times than those studied here are recommended (e.g. at 5,10 and 20 s). It is worth mentioning that in most of the previous published studies, shearing times were much longer than those studied here.

Finally, despite the advantages of the combined image analysis and settling velocity measurement technique used in this research to provide a complete set of aggregate structural data, it is tedious, time consuming and costly. Collection of size and shape measurements using image analysis could be automated using macros and programming, but it is highly unlikely that this could be done for settling velocity measurements. Until now, the inherent complexity of the aggregate structure has not allowed for the development of a single, ideal technique that is able to quantify aggregate structure completely. Each measurement technique, including light diffraction, light scattering, electrical zone sensing, and image analysis combined with settling velocity measurements, has specific advantages and disadvantages. The search for a better method of measuring aggregate structural parameters in terms of improved accuracy, more rapid measurement and less costly analysis is a task that should be continued.

6.6. Recommendations for future work

One of the areas that future fundamental research studies should focus on is the development of mathematical models that are able to predict aggregate structural changes caused by hydrodynamic conditioning. There are numerous studies that describe the modeling of flocculation processes using population balances [11,12]. Most of these models are developed on the basis of a constant aggregate porosity and can predict only changes in the aggregate size distribution. Although these models are useful to evaluate the aggregation and fragmentation processes, they cannot predict structural conformation due to shearing and reflocculation. Moreover, these models cannot provide accurate information about aggregate shape, density and fractal dimension. Mass or volume balances must be used in conjunction with a population balance model to link total solids and fluid volume fractions with the aggregate population and to include the possibility of structural conformation.

Another simplification in population balance models is related to the estimation of the shear force acting on the aggregates. In almost any population balance model developed for studies involving a mixed tank, an average shear rate is used to determine the aggregate collision frequency and other model kernels [11,12]. However, in reality there is a shear distribution inside any shearing device. The application of laminar tube flow provides a well-defined shear field, which can be easily described by a simple mathematical term coupling the shear rate distribution with the population balance.

6.7. References

1. Boger, D.V. (2009). "Rheology and the resource industries", Chem. Eng. Sci., 64(22), 4525-4536.
2. Boger, D.V., Scales, P.F. Sofra, F., "Rheological concepts" Chap 3 in: "Paste and Thickened Tailings – A Guide", (Ed. by) Jewell, R., Fourie, A., Second Ed., Australian Centre for Geomechanics, 2010.
3. Sofra, F., "Rheological assessment – A road map for plant designers and operators", Proceedings of Paste 2006 – (Eds by) Jewell, R.J., Lawson, S., Newman, P., Australian Centre for Geomechanics, Limerick, Ireland, 2006, 13-23.
4. Huang, H. (1993). "Porosity-size relationship of drilling mud flocs: fractal structure", Clays and Clay minerals, 41, 373-379.
5. Lee, D.J., Chem. G.W., Liao, Y.C., Hsieh, C.C., (1996). "On the free-settling test for estimating activated sludge floc density", Water Res., 30, 541-550.
6. Vaezi G., F., Sanders, R.S., Masliyah, J.H., (2011). "Flocculation kinetics and aggregate structure of kaolinite mixtures in laminar tube flow", J. Colloid Interface Sci., 355, 96-105.
7. Michaels, A.S., Bolger, C.B., (1962). "The plastic flow behavior of flocculated kaolin suspensions", I & EC Fundamen., 1(3), 153-162.
8. Mills, P.D.A., Goodwin, J.W., Grover, B.W., (1991). "Shear field modification of strongly flocculated suspensions-Aggregate morphology", Colloid Poly. Sci., 269, 949-963.
9. McFarlane, A.J., Addai-Mensah, J., Bremmell, K., (2005). "Rheology of flocculated kaolinite dispersions", Korea-Australia Rheology J., 17(4), 181-190.
10. Schaan, J., Sanders, R.S., Gillies, R.G., McKibben, M.J., Litzenberger, C., Sun, R-J., Shook, C.A., "Effect of shear history on the flow properties of flocculant-dosed thickened tailings slurries", 16th International Conference on Hydrotransport, Vol. II, Santiago, Chile, 2004, 26-28 April, 403-414.
11. Thomas, D.N., Judd, S.J., Fawcett, N., (1999). "Flocculation modeling: a review", Water Res., 33(7), 1579-1592.

12. Carole Coufort, C., Bouyer, D., Lin´e, A., Haut, B., (2007). “Modeling of flocculation using a population balance equation”, Chem. Eng. Process. 46, 1264–1273.